QST-M-33

QST Takasaki Annual Report 2020

Takasaki Advanced Radiation Research Institute

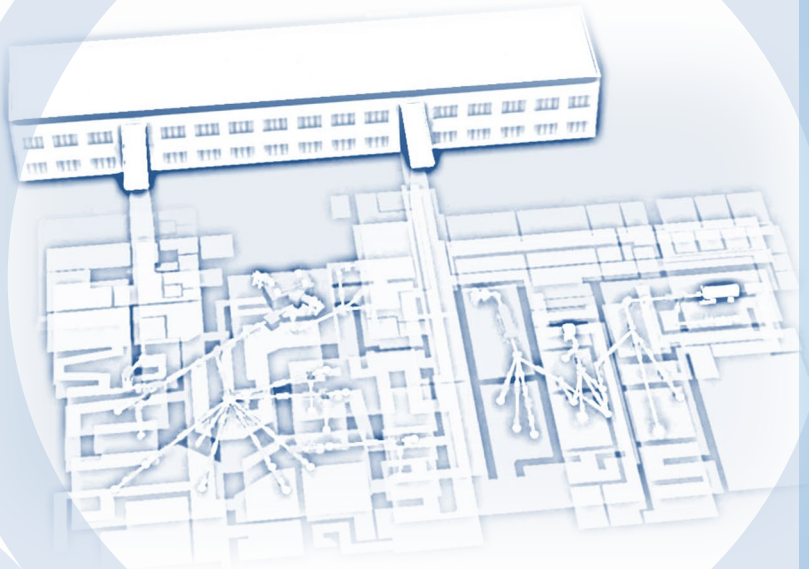

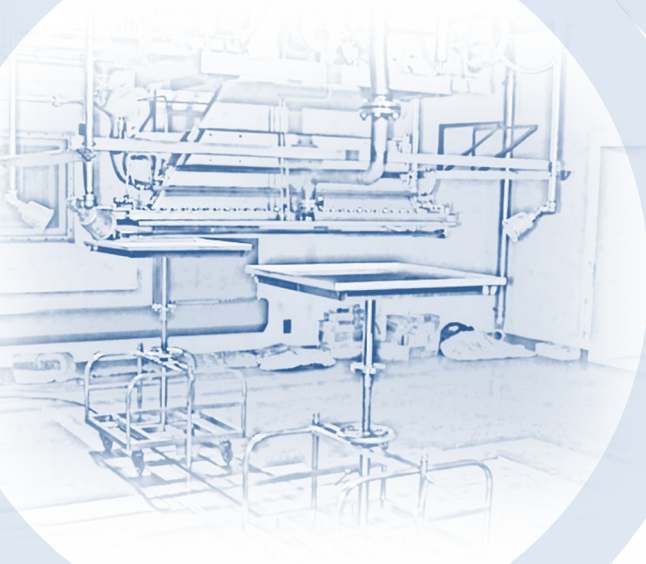

National Institutes for Quantum Science and Technology

Preface

ITOH Hisayoshi

Director General
Takasaki Advanced Radiation Research Institute
Quantum Beam Science Research Directorate
National Institutes for Quantum Science and Technology

The National Institutes for Quantum Science and Technology (QST) was established in April 2016 by combining the National Institute of Radiological Sciences (NIRS) and other institutes promoting quantum beam science and nuclear fusion research in the Japan Atomic Energy Agency (JAEA). Currently, QST has three research and development (R&D) directorates, *i.e.*, “Quantum Beam Science Research Directorate (QuBS),” “Quantum Life and Medical Science Directorate,” and “Fusion Energy Directorate.” QuBS comprises three research institutes, *i.e.*, “Takasaki Advanced Radiation Research Institute (TARRI),” “Kansai Photon Science Institute (KPSI),” and “Institute for Advanced Synchrotron Light Source (IASLS).” Using advanced beam facilities, we are performing intensive fundamental and applied research in numerous fields, such as materials science, life science, and quantum beam technology. TARRI and KPSI have two research sites, *i.e.*, Takasaki and Tokai sites for TARRI and Kizu and Harima sites for KPSI. Takasaki Ion Accelerators for Advanced Radiation Application (TIARA) at the Takasaki site, Japan Proton Accelerator Research Complex (J-PARC) at the Tokai site, Japan-Kansai Advanced Relativistic Engineering Laser System (J-KAREN) at the Kizu site, and highly sophisticated Super Photon Ring-8 GeV (SPring-8) beamlines at the Harima site are examples of typical beam facilities that we use. In IASLS, we are constructing a new advanced synchrotron light source for soft X-rays with ultrahigh intensity and coherence at the Sendai site.

In TARRI, we have 16 research projects and two research groups conducting quantum beam science R&Ds with TIARA, 2-MeV electron accelerator, ^{60}Co gamma-ray irradiation facilities, and so on, to contribute to the progress of science and technology, as well as the promotion of industries. The Advanced Functional Polymer Materials Research Group was established in 2017 under the QST’s innovation hub program to develop next-generation graft-polymer materials through the combined use of quantum beam processing and analysis techniques, as well as material informatics. The Quantum Sensing and Information Materials Research Group was established in August 2018 to conduct fundamental and applied research for realizing quantum devices, such as quantum sensors, quantum bits, and spin transistors, based on wide-bandgap semiconductors including diamonds and two-dimensional materials such as graphene. Furthermore, we are performing R&D on advanced ion beam technology at the Beam Engineering Section of the Department of Advanced Radiation Technology. Our beam facilities are available to industries, academia, and governmental

research institutes, and beam time is allocated to users based on the evaluation of their R&D programs.

This annual report covers the research activities at TARRI primarily for the fiscal year of 2020 (FY 2020). This report comprises two parts—Part I and Part II. Part I describes the recent activities of all research projects and groups, as well as the Beam Engineering Section. Part II presents the recent R&D results obtained using the quantum beam facilities of TARRI. This part contains 88 research papers in the fields of materials science and advanced quantum beam technology, as well as eight status reports on the operation/maintenance of the quantum beam facilities. The depth-resolved magnetism of Fe(001) surface was studied using a newly developed *in situ* ^{57}Fe probing layer method, which is a typical topic in the materials science field. In the upper four atomic layers, the hyperfine fields (H_{int}) exhibit a significant decrease at the surface and an oscillatory decay toward the bulk value with increasing depth. The experimentally observed H_{int} oscillations penetrating the Fe(001) surface provide direct evidence of magnetic Friedel oscillations theoretically predicted 40 years ago. The TIARA cyclotron was used to successfully develop a positron-emitting ^{127}Cs tracer for the noninvasive imaging of radiocesium dynamics *in vivo* through the ^{127}I(α, 4n)^{127}Cs reaction. The purified tracer solution was injected into the tail vein of a living rat, and the dynamics of ^{127}Cs were visualized using positron emission tomography (PET). The result showed that ^{127}Cs passed through or accumulated in the salivary glands, heart, small intestine, and kidney. The midinfrared FEL facility achieved the highest extraction efficiency (9.4%) of a free-electron laser oscillator (FEL) for advanced quantum beam technology. From the measured results, the average energy of the electron bunch was reduced from 28.5 to 25.9 MeV, which corresponds to the efficiency. This result is an important milestone for the high-extraction-efficiency FEL oscillator and will contribute to the strong-field physics of atoms and molecules.

An azimuthally varying field (AVF) cyclotron and three electrostatic accelerators in TIARA, as well as MeV electron and ^{60}Co gamma-ray irradiation facilities regarding the status of quantum beam facilities, have been continuously and safely operated. However, irradiation experiments were suspended for about a month (from the end of April to the end of May) because of the COVID-19 induced emergency. Therefore, we have introduced new data acquisition systems (named “smart module”) to the electron and ^{60}Co gamma-ray irradiation facilities. The smart module allows collecting experimental data at home through the internet, which can help in the R&D under COVID-19.

Finally, we extend our gratitude to both our domestic and foreign colleagues for cooperating, supporting, and encouraging our quantum beam science R&D, as well as technological advances in the facilities of TARRI.

Facilities

Charged particle beams and RI facilities

Takasaki Ion Accelerators for Advanced Radiation Application (TIARA) consisting of four ion accelerators, an electron accelerator, and gamma irradiation facilities are available to researchers in QST and other organizations for R&D activities on new functional and environmentally friendly materials, biotechnology, radiation effects of materials, and quantum beam analysis. We are developing microbeams, single ion hits and various shape area irradiation technique at the cyclotron. In addition, technical developments of three dimensional in-air PIXE analysis and microbeam formation of cluster ions such as C_{60} fullerene at the electrostatic accelerators are in progress.

Takasaki Ion Accelerators for Advanced Radiation Application: TIARA

TIARA facility

Cyclotron

Tandem accelerator

Single-ended accelerator

Ion implanter

Typical available ions

Accelerator	Ion	Energy (MeV)
AVF Cyclotron (K=110MeV)	H	10～ 80
	He	20～107
	C	75～320
	Ne	75～350
	Ar	150～520
	Fe	200～400
	Kr	210～520
	Xe	324～560
	Os	490
Tandem Accelerator (3 MV)	H	0.8～ 6.0
	C	0.8～18.0
	Ni	0.8～18.0
	Au	0.8～18.0
	C_{60}	0.8～9.0
Single-ended Accelerator (3 MV)	H	0.4～ 3.0
	D	0.4～ 3.0
	He	0.4～ 3.0
	e^-	0.4～ 3.0
Ion Implanter (400 kV)	H	0.02～0.38
	Ar	0.02～0.38
	Bi	0.02～0.37
	C_{60}	0.02～0.36

Energy-element range covered by the four accelerators

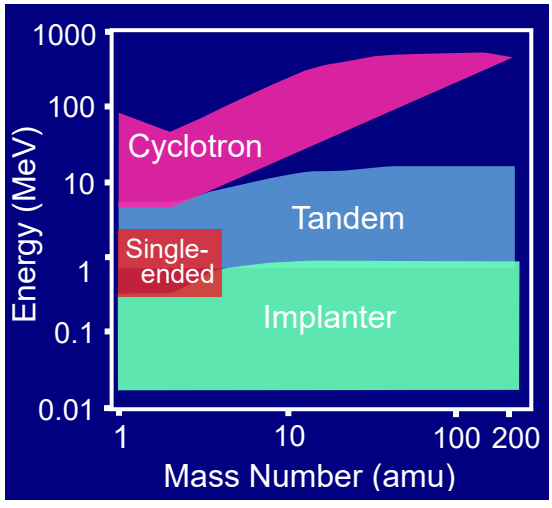

Cobalt-60 gamma-ray and electron beam irradiation facilities

Gamma-ray irradiation facility building

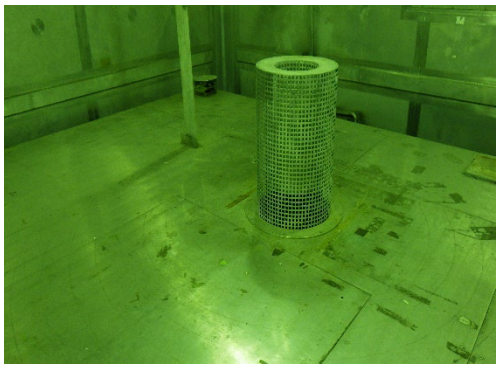

Gamma-ray irradiation room

Electron accelerator
(0.5～2.0 MeV, 0.1～30 mA)

Electron irradiation room with conveyor system

Specification

Apr. 2021

Name of facility	Cobalt-60 activity (PBq)	Number of rooms	Principal utilization
Co No.1 bld.	6.4	3	Radiation-resistance test Radiation effects on polymers
Co No.2 bld.	6.8	3	R & D on functional organic materials, inorganic materials and dosimetry
Food Irrad.	1.9	2	Radiation effects on biological substance and semiconductors

Dose-rate range

Unit : kGy/h

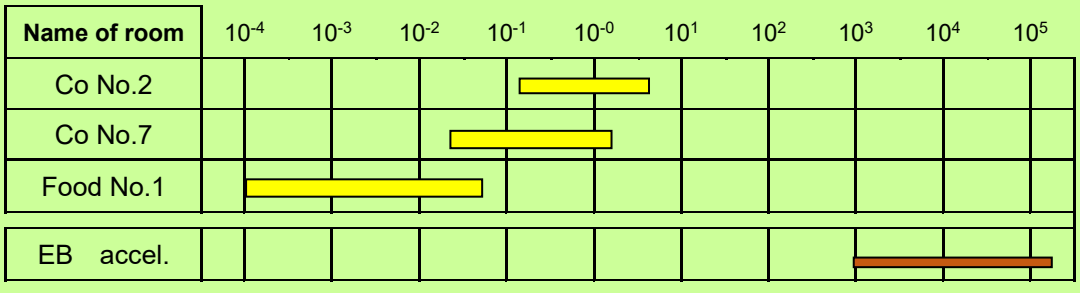

Contents

Part Ⅰ

Part Ⅰ

1. Materials Science

P1-1 Project “Functional Polymer”

Leader : MAEKAWA Yasunari

Project “Functional Polymer Research” has been developing the advanced functional polymer materials, such as polymer electrolyte materials and separation membranes for high performance fuel cells and hydrogen collection systems by using quantum beams. We have synthesized the proton- and anion-conducting electrolyte membranes (PEM and AEM) and the hydrogen permselective membranes using γ-rays and electron beams. We report herein two recent developments: poly(ethylene-co-tetrafluoroethylene) (ETFE)-based AEMs for alkaline hydrated hydrazine-fuel cells. {1-01~03, 1-34 in Part II}.

A Long Side Chain Imidazolium-based Graft-type Anion-exchange Membrane: Novel Electrolyte and Alkaline-durable Properties and Structural Elucidation using Small-angle Neutron Scattering Method [1]

Styrylimidazolium-based grafted AEMs (StIm-AEMs), in which imidazolium ionic groups are attached to styrene at the far side from the graft chains, were prepared by radiation-induced graft polymerization of *p*-(2-imidazoliumyl) styrene onto poly(ethylene-co-tetrafluoloethylene) (ETFE) films, followed by *N*-alkylation and ion-exchange reactions. StIm-AEM with a grafting degree (GD) of 18% possesses a practical conductivity (>50 mS/cm) with a very low water uptake (WU) about 10% and high stability over 600 h in a 1M KOH solution at 80 °C. There exists a critical GD (GD_c) of 20–25%, over which AEMs showed high WU and weak alkaline durability.

To clarify the detailed AEM structures, AEMs with various GDs in the range of 8 to 86% were analyzed by the small-angle X-ray scattering (SAXS) method. All AEMs showed a clear ionomer peak in q = 2 - 3 nm^{-1}, indicating the formation of ionic clusters in the conducting phase. The further analysis of this ionomer peak using the hard sphere liquid model and Porod limit analysis revealed that StIm-AEMs with GDs higher than GD_c showed “micelle” structure with graft polymer aggregates dispersed in the water matrix. On the other hand, AEM with GDs lower than GD_c showed “reverse-micelle” structure with water domains dispersed in the polymer matrix. AEMs with the “reverse-micelle” structure were more alkaline-durable owing to the lower number of water molecules around one ionic group, which resulted in a slower hydrolysis degradation, as shown in Fig. 1.

Alkaline Fuel Cells Consisting of Imidazolium-based Graft-type Anion Exchange Membranes: Optimization of Fuel Cell Conditions to Achieve High Performance and Durability [2]

In the AEM fuel cell (AEMFC) systems, water content management is very important for improved performance and durability because of the complicated water balance and transfer phenomena. The water content in AEMFC can be controlled through the dew points of flow gases. We have been developing various imidazolium-based AEMs, including 2-methyl-*N*-vinyl imidazolium, 2-styryl-*N,N*-dipropyl imidazolium, and so on. Among them, StIm-AEM have acceptable phase separation structure, resulted in very high conductivity and durability [1]. In this work, we evaluated the AEMFC performance and *in-site* durability in H_2/O_2 fuel cells at 60 °C to achieve the maximum performance by controlling the anode/cathode dew point. The results were compared with the standard benzyl trimethyl ammonium-based AEM (BTMA-AEM) in Fig. 2.

Figure 3 shows the cell voltages and power densities as a function of current density for the MEAs consisting of BTMA- and StIm-AEMs at 45/46 and 58/59 of the anode/cathode dew points, respectively. The power density of BTMA- and StIm-AEM with ion exchange capacities of 1.71 and 1.72 mmol/g reached 352 and 710 mW/cm^2 by optimizing dew points, respectively. The power density of the StIm-AEM is one of the highest performances of imidazolium-based AEMs. Furthermore, it exhibited long-term durability in H_2/O_2 fuel cell at 60 °C, maintaining 0.52 V (56%) of initial voltage after 670 h of life time test, which is better than that of the standard BTMA-AEM.

References

[1] Y. Zhao *et al.*, Soft Matter **16**, 8128 (2020).
[2] A. M. A. Mahmoud *et al.*, J. Membr. Sci. **620**, 118844 (2021).

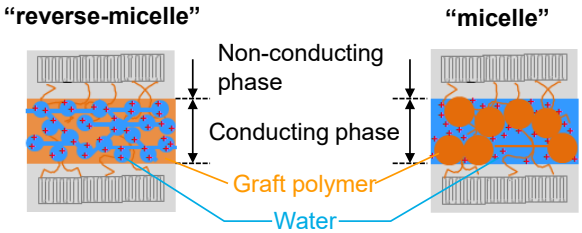

Fig. 1. Schematic illustration of the structures in StIm-AEMs.

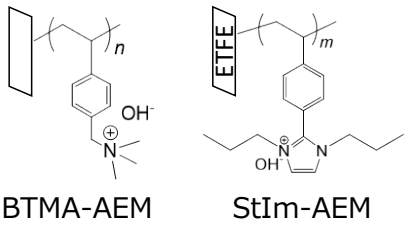

Fig. 2. Chemical structures of BTMA- and StIm-AEMs.

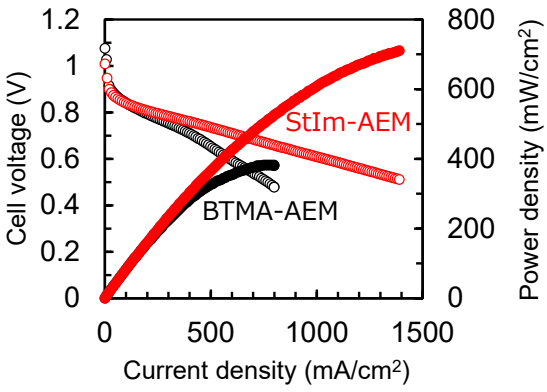

Fig. 3. Cell voltages (open circle) and power densities (closed circle) as a function of current density for BTMA- and StIm-AEMs with IECs of 1.71 and 1.72 mmol/g, respectively.

P1-2 Project “Advanced Catalyst”

Leader : YAMAKI Tetsuya

The main target of our project is development of catalytic materials for next-generation energy devices in future H_2 society by effective use of electron and ion beams. The advantage of our overarching strategy is that these quantum beams can lead to high-energy defect creation, active-site formation via non-equilibrium chemical reactions, and nano-to-micro fabrication. This report deals with R&D for highly-active electrocatalysts with low precious-metal loading in fuel cells such as direct methanol fuel cells (DMFCs) and direct ethanol fuel cells (DEFCs). {1-04~15 in Part II}

Platinum ruthenium (PtRu) alloy electrocatalysts on an irradiated defective support [1-3] {1-04, 1-06~10, 1-15}

Non- or low-Pt electrocatalysts are needed to decrease the device cost. Our advanced methods using electron and ion beams have been pursued for the preparation of highly-active platinum (Pt)-based nanoparticles (NPs) and Pt-free carbon-based catalysts [1,2]. We have so far found that the carbon support pre-irradiated with hundreds keV ions makes the deposited Pt NP catalysts more active [2].

PtRu-alloy NPs on the CeO_2-embedded carbon nanofiber support (CECNF) are known as a promising anode catalyst for DMFCs. In order to improve their methanol oxidation reaction (MOR) activity, we have attempted high-energy ion irradiation of the CECNF support [3]; the irradiation effect on the activity as well as on the CECNF’s crystalline structure was investigated.

A non-woven sheet of CECNF was prepared by using an electrospinning technique and then irradiated with 127 MeV ^{40}Ar at fluences between 5×10^{11} and 1×10^{13} ions cm^{-2}. PtRu NPs were deposited on the irradiated CECNF by a microwave-polyol method. The MOR activity was evaluated by taking a current density at 0.6 V vs. RHE in the cyclic voltammetry (CV) curves.

Figure 1 shows the activity of the Ar-irradiated samples relative to the non-irradiated samples as a function of fluence for the irradiation of the CECNF sheet. The Ar ion irradiation almost doubled the activity at a fluence of 5×10^{11} ions cm^{-2} and decreased the activity at the higher fluences. The reduction of the CeO_2 crystalline size with an increase in the fluence was observed by XRD measurements. The change in the catalytic activity was roughly correlated with an increase in the lattice distance of CeO_2, suggesting that the generated oxygen-atom vacancies could enhance the activity.

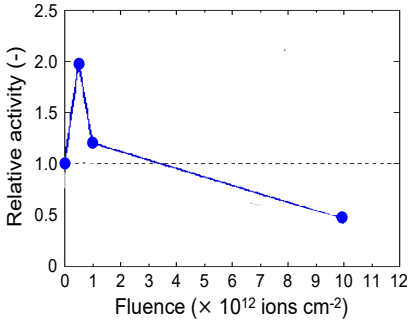

Fig. 1. Relationship between the fluence and relative MOR activity for the PtRu-alloy NPs on CECNF irradiated with 127 MeV ^{40}Ar.

Morphology-controlled electrocatalysts based on swift-heavy-ion beam technology [4-7] {1-05, 1-11~14}

Irradiation with an MeV-GeV heavy ion leaves a cylindrical track, enabling us to develop different polymer nanostructures. Some fabricated organic molecule-based nanowires by subsequent development to remove the part outside the ion tracks, while others prepared straight nanopores by preferential dissolution of the tracks. We have recently developed various nanomaterials such as cation-exchange membranes [4], blackbody materials [5], and *p-n* heterojunction structures [6].

The micro/nanocones of metals play a critical role as heterogeneous electrocatalysts endowed with high activity. We have successfully fabricated Pt cones by electrodeposition using non-penetrated porous membranes as templates [7]. This method involved the preparation of template membranes by irradiation of polycarbonate films with 150 MeV ^{40}Ar and subsequent chemical etching in an aqueous NaOH solution. The resulting conical pores had a surface diameter and depth in the range of approximately 70–1500 nm and 0.7–11 μm, respectively, which were controlled by varying the etching conditions. Field-emission scanning electron microscopy (FE-SEM) and transmission electron microscopy (TEM) (Fig. 2) demonstrated the production of controlled Pt cones with tips of a 13-nm curvature radius.

Considering the applications to DEFCs, we performed the CV for the ethanol oxidation reaction (EOR). Compared with the standard Pt plate, the Pt cone arrays exhibited up to a 3.2-fold enhanced ORR activity, which would be similar to or higher than that of the commercial products including Pt on carbon and Pt black. Such excellent activity may be exhibited by the field-induced reagent concentration. In other words, the polar ethanol molecules are likely to approach the surface of the cone electrode because the fine tips of the cones produce local high electric fields.

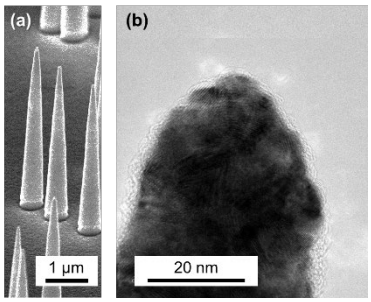

Fig. 2. Morphology of the obtained Pt cones: (a) the FE-SEM image and (b) TEM image of their tip.

References

[1] A. Idesaki *et al.*, Jpn. J. Appl. Phys. **58**, SDDF03 (2019).
[2] H. Okazaki *et al.*, J. Chem. Phys. **152**, 124708 (2020).
[3] N. Nakagawa *et al.*, Catal. Today **364**, 118 (2021).
[4] S. Sawada *et al.*, Int. J. Hydrogen Energy **45**, 13814 (2020).
[5] Y. Shimizu *et al.*, Opt. Exp. **28**, 22606 (2020).
[6] K. Kamiya *et al.*, Nat. Commun. **12**, 4025 (2021).
[7] Y. Sato *et al.*, Quantum Beam Sci. **5**, 21 (2021). (selected as a journal cover).

P1-3 Project “Positron Nanoscience”

Leader : KAWASUSO Atsuo

The aim of this project is to reveal the novel phenomena related to “spin” in solids using our original spin-polarized positron beam technologies. So far, we have been constructing the spin-polarized surface positronium spectroscopy that is substantially useful for detecting spin-polarization at the first surface layer and the spin-polarized positron annihilation spectroscopy in strong magnetic field for detecting vacancy-induced magnetism. To establish the foundation of the above spectroscopies, deep understanding of positron and positronium elementary processes is also important. We thus pursue such a basic aspect of positron physics, too. In this report, we pick up two topics in the last fiscal year (2020); one is the positronium formation process at 4H SiC surfaces reveled by the positronium time-of-flight spectroscopy and one is the development of spin-polarized positronium time-of-flight spectroscopy for probing the spin-polarized electronic states at the top-surface.

Positronium formation at SiC surface [1]

Upon the removal of natural oxide layers by hydrofluoric acid etching and heat treatment at 1000 K in ultra-high vacuum, two types of positronium were observed at 4H SiC surfaces in the positronium time-of-flight (PsTOF) measurements irrespective of conduction type and surface polarity. One type formed the major part of the PsTOF spectrum with a maximum energy of 4.7 ± 0.3 eV. This energy exceeded the theoretical value calculated with valence electrons. The PsTOF spectrum shape was different from those of metal surfaces, suggesting that the surface state electrons or conduction electrons need to be considered as the positronium source. Another positronium appeared at 1000 K in the tail of the PsTOF spectrum with a maximum energy of 0.2 – 0.5 eV. This thermally-assisted athermal positronium may be formed via the surface state positrons and electrons.

Positronium (the bound state of an electron and a positron) has been extensively investigated in fundamental physics. Positronium is also expected to be a unique probe for surface electronic states because the energy and momentum distributions of positronium formed at a solid surface reflect the surface band structure. Therefore, understanding positronium formation at solid surfaces is important.

Over the last decade, the UCR group examined positronium formation at Si and Ge surfaces. We also found strong doping and temperature dependences of positronium formation processes at Si surfaces. The positron work functions of Si and Ge are positive, and hence positrons are confined inside and in the surface mirror potentials. Whereas, the other group IV semiconductors, SiC and diamond, have negative positron work functions. It is therefore important to investigate the positronium formation at such semiconductor surfaces. In this work, we succeeded in the first observation of positronium at 4H SiC(0001) surfaces using PsTOF spectroscopy.

Development of spin-polarized positronium time-of-flight spectroscopy [2]

We have developed a spin-polarized positronium time-of-flight spectroscopy apparatus based on a ^{22}Na positron source and an electrostatic beam transportation system, which enables the sampling of topmost surface electrons around the point and near the Fermi level. We applied this technique to nonmagnetic Pt(111) and W(001), ferromagnetic Ni (111), Co(0001) and graphene on them, $Co_2FeGa_{0.5}Ge_{0.5}$(CFGG) and Co_2MnSi (CMS). The results showed that the electrons of Ni(111) and Co(0001) surfaces have characteristic negative spin polarizations, while these spin polarizations vanished upon graphene deposition, suggesting that the spin polarizations of graphene on Ni(111) and Co(0001) were mainly induced at the Dirac points that were out of range in the present measurement. The CFGG and CMS surfaces also exhibited only weak spin polarizations suggesting that the half-metallicity expected for these bulk states was not maintained at the surfaces.

Slow positrons injected into the sub-surface region of a metal diffuse back to the surface/vacuum interface and are emitted as positronium by picking up the outermost surface electrons when the positronium formation potential is negative. Because of the energy gain of the formation potential, electrons below the Fermi level with the width of formation potential can participate in the positronium formation. Hence, positronium energy spectroscopy provide information regarding the surface electron density of states (DOS). Although positronium spectroscopy is analogous to photoemission spectroscopy, a critical difference is its extremely high surface sensitivity. This owes to the fact that positronium atom is formed only at the top surface of metal, while the photoemission spectroscopy includes electrons from several surface layers. Recently, the angle-resolved positronium spectroscopy with a milli-electron-volt energy resolution has been demonstrated in a laboratory scale.

Positrons emitted from radioisotopes are longitudinally spin polarized due to the parity non-conservation in the weak interaction. Hence, spin-polarized positron beams can be easily generated. Spin-polarized positronium spectroscopy may elucidate the nature of the spin polarization of the top surface electronic states and play a valuable role in the field of spintronics.

However, existing spin-polarized positronium spectroscopies cannot resolve the positronium kinetic energy, and hence the obtained spin polarization is only an average of all electrons below the Fermi level picked up by positrons. For more detailed analysis, determination of the electron spin polarization depending on the energy level, i.e., the spin-polarized DOS, is essential. Spin-polarized and angle-resolved Ps spectroscopy with a submicron beam would be an ultimate surface spin probe that is applicable to device-scale samples. In this work, we succeeded in developing a spin-polarized positronium time-of-flight apparatus for the energy-resolved positronium spectroscopy.

References

[1] A. Kawasuso *et al.*, J. Phys.: Condens. Matter **33**, 035006 (2021).
[2] M. Maekawa *et al.*, Phys. Rev. Lett. **126**, 186401 (2021).

P1-4 Project “Semiconductor Radiation Effects”

Leader : OHSHIMA Takeshi

Quantum technologies, such as quantum computation, quantum cryptography information and quantum sensing, are expected as a game changer for our future life. Color centers of which optical and spin properties can be manipulated with high fidelity are regarded as a promising candidate for quantum bits (qubits) and quantum sensors. We create color centers in wide bandgap semiconductors such as diamond and silicon carbide (SiC) using ion and electron beams to apply such color centers to qubits and quantum sensors. In addition, the radiation effects on semiconductor materials and devices are investigated to develop radiation resistant technologies for space and nuclear applications. {1-19~23 in Part II}.

Optically and electrically excitation of silicon vacancies in SiC [1]

Silicon vacancy (V_{Si}) in SiC is known as a color center which acts as a spin qubit and a quantum sensor at room temperature (RT) since its electron spin can be manipulated even at RT [2]. Optically detected magnetic resonance (ODMR) is used to confirm spin states for V_{Si}. We intend to detect local information such as temperature, current and electric field in SiC electronic devices using V_{Si}. For this purpose, it is necessary to understand the behavior ODMR under device operation (current flowing). In this study, the effects of current (electrically excitation) on ODMR signals excited by laser. Ensemble V_{Si} centers were locally created in planar SiC pn diodes by the particle beam writing (PBW) technique. Helium (He) ions with energies of 0.5, 1.5 and 3 MeV were applied in the PBW to create V_{Si} at depths of 1, 4, and 8 μm, respectively. Figure 1 shows a photoluminescence (PL) map obtained using a home-built confocal fluorescence microscopy. In addition to laser excitation (671 nm, 100 μW), the forward current at 3 mA was flowed in the diode. Array with three PL spots is observed in the figure (the square in the figure indicates V_{Si} created by He ions with three different energies). Next, we study PL intensity under different current values. As a result, PL intensity increases with increasing current at laser powers below 30 μW although a slight decrease in PL intensity is observed at current ranges between 0 and 0.2 mA. On the other hand, in the case of the laser powers above 100 μW, PL intensity decreases with increasing current up to 0.5 mA, and shows constant values above 0.5 mA. The constant values of PL intensity are larger with larger excitation powers. Finally, ODMR contrast (the ration of the PL intensity at ODMR peak to background) is measured under current flowing. As a result, ODMR signal contrast rapidly decreases with increasing current up to 1 mA and above 1mA, the saturation of the decrease in ODMR contrast is observed when power of laser is enough high which is above 100 μW. This indicates that quantum sensing for SiC devices using V_{Si} can be realized under current flowing when power of excitation laser is adjusted.

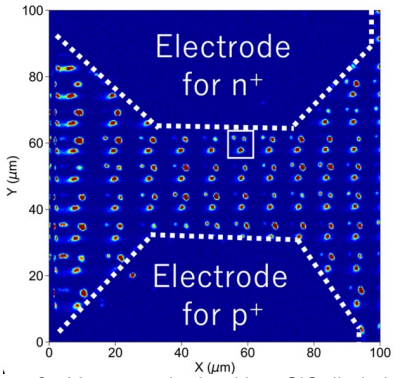

Fig. 1. PL map for V_{Si} spots obtained in a SiC diode by PBW.

Effect of hydrogen on creation of nitrogen-vacancy center in SiC [3]

Spin defects which have luminescence with near infrared regions attract attention for quantum sensing for biology and life science owing to its penetration depth. Since negatively charged nitrogen-vacancy (N_CV_{Si}) center in SiC is a spin defect with luminescence around 1300 nm, N_CV_{Si} is regarded as a candidate for this purpose. However, its creation methods have not yet been established. Here, we study the creation of N_CV_{Si} in N-doped SiC by proton irradiation and subsequent annealing. Figure 2 shows PL intensity as a function of 240 keV-proton fluence. The samples were annealed either at 900 or 1000 °C for 30 min in Ar. The concentrations of N in the samples are depicted in the figure. As shown in Fig. 2, PL intensity for SiC annealed at 1000 °C rapidly increases with fluences above $5x10^{15}$ /cm^2 whereas PL intensity for SiC annealed at 900 °C does not show such a rapid increase. Besides, further increase in PL intensity is not observed above $1x10^{16}$ /cm^2. Since hydrogen related complex defects are formed above 900 °C, the result obtained in this study can be explained in terms that hydrogen related defects are created at 1000 °C and these defects might play a role to suppress the creation of N_CV_{Si} in SiC, and as a result N_CV_{Si} cannot be observed at fluences below $5x10^{15}$ /cm^2. To clarify this, further investigations are necessary.

References

[1] Y. Yamazaki *et al.*, Appl. Phys. Lett. **118**, 021106 (2021).
[2] T. Ohshima *et al.*, J. Phys. D. **51**, 333002 (2018).
[3] T. Narahara *et al.*, Appl. Phys. Express **14**, 021004 (2021).

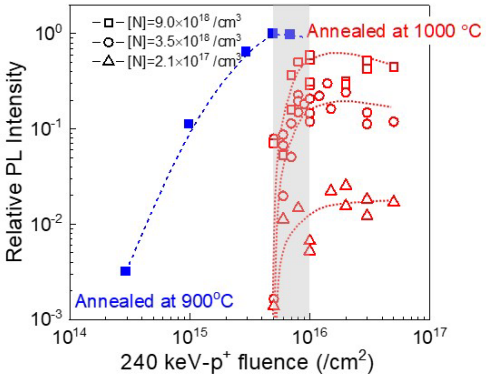

Fig. 2. PL intensity as a function of proton fluence for SiC. The intensity of PL is normalized by that for SiC with N atoms of $9x10^{18}$ /cm^2 irradiated at $5x10^{15}$ /cm^2 followed by 900 °C annealing.

P1-5 Project “Environmental Polymer”

Leader : SEKO Noriaki

Project “Environmental Polymer Research” has been developing the functional polymer fabrics for metal adsorbents by radiation induced graft polymerization technique using such as electron beams and γ-rays. The developed adsorbents can be expected for applications in removing and recovering trace metal ions from water.

Fabric adsorbents having dithiocarbamate groups for selective removal of copper ions from highly alkaline aqueous solution [1]

The high integration of semiconductor devices, which constitute a key factor that has impelled the development of modern society, has been achieved by innovations in microfabrication technology. In special, the metal contamination in chemical solution for the surface etching of Si wafers have to be less than a few μg/g (ppm). In this study, we developed a novel fabric adsorbent for removing Cu^{2+} and other ionic species from the etchants.

The fabric adsorbent with a dithiocarbamate (DTC) group was synthesized by radiation-induced emulsion grafting of glycidyl methacrylate onto a polyethylene-coated polypropylene nonwoven fabric and subsequent three-step chemical modifications consisting of amination with N-(tert-butoxycarbonyl)piperazine (N-Boc-piperazine, NBPZ), deprotection of the Boc group with HCl, and dithiocarbamation with carbon disulfide. By using the NBPZ reagent in the amination step, the self-cross-linking of piperazine (PZ) could be completely suppressed, unlike using the PZ reagent. Consequently, the PZ-DTC group density of the fibrous grafted metal adsorbent synthesized through NBPZ attained 2.12 mmol/g, which was approximately 6 times higher than that of the metal adsorbent synthesized through PZ.

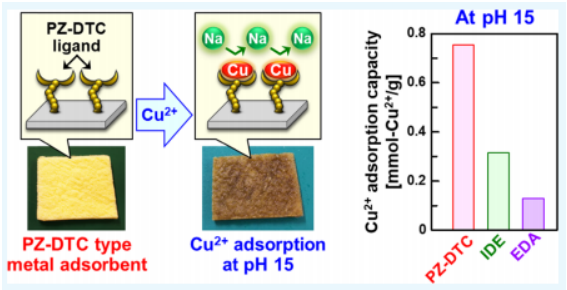

Fig. 1. The imagines of the adsorbents before and after the adsorption, and the high Cu^{2+} adsorption capacity of the adsorbent at pH15.

The fibrous grafted metal adsorbent with the PZ-DTC group selectively adsorbed heavy metal ions over light metal ions. Furthermore, it exhibited high adsorption capacity, particularly for Cu^{2+}. Figure 1 showed the fabric adsorbents before and and after the Cu^{2+} adsorption at pH15. After the adsorption, the color of the fabric adsorbent changed from yellow to dark, indicating the high concentration of copper ion loaded. The Cu^{2+} adsorption capacity was determined to be 1.90 mmol/g by a batchwise adsorption test using a single-metal-ion aqueous solution at pH 6. The order of metal ion selectivity of the fibrous grafted metal adsorbent with the PZ-DTC group was $Na^{+} < Mg^{2+}$, Ca^{2+}, Co^{2+}, $Cd^{2+} < Pb^{2+} \ll Cu^{2+}$, and $Co^{2+} \approx Ni^{2+} < Zn^{2+} \ll Cu^{2+}$. In addition, the fibrous grafted metal adsorbent with the PZ-DTC group did not lose its metal adsorption function even under highly alkaline conditions (pH 15). It could recover Cu^{2+} efficiently and selectively from a high concentration Na^{+} aqueous solution at this pH. The Cu^{2+} adsorption capacity of the fibrous grafted metal adsorbent with the PZ-DTC group was 0.75 mmol/g under a highly alkaline condition, a 10 M NaOH aqueous solution at pH 15. As shown in Fig. 1, this value was approximately 2.4 times higher than that of the other grafted adsorbent with an amine-type functional group (iminodiethanol (IDE)- and ethylenediamine (EDA)-adsorbents). Therefore, the adsorbent having DTC group is a potential material for removing metal ions from highly alkaline aqueous solution such as etching solutions for Si wafer.

Chain entanglement of 2-ethylhexyl hydrogen-2-ethylhexylphosphonate into methacrylate-grafted nonwoven fabrics for applications in separation and recovery of Dy (III) and Nd (III) from aqueous solution [2]

In this study, a nonwoven fabric adsorbent loaded with 2-ethylhexyl hydrogen-2-ethylhexylphosphonate (EHEP) was developed for the separation and recovery of dysprosium (Dy) and neodymium (Nd) from an aqueous solution. As shown in Fig. 2, the EHEP was chain entangled into the nonwoven fabrics which has the long alkyl chains induced by the radiation grafting.

The adsorbent was evaluated by batch and column tests with a Dy (III) and Nd (III) aqueous solution. As shown in Fig. 2 (right), in the batch tests, the adsorbent showed high Dy (III) adsorptivity close to 25.0 mg/g but low Nd (III) adsorptivity below 1.0 mg/g, indicating that the adsorbent had high selective adsorption. In particular, the octadecyl methacrylate (OMA)-adsorbent showed adsorption stability in repeated tests. Furthermore, in the column tests, the OMA-adsorbent was also stable and showed high Dy (III) adsorptivity and high selectivity in repeated adsorption–elution circle tests. This result suggested that the OMA-adsorbent may be a promising adsorbent for the separation and recovery of Dy (III) and Nd (III) ions.

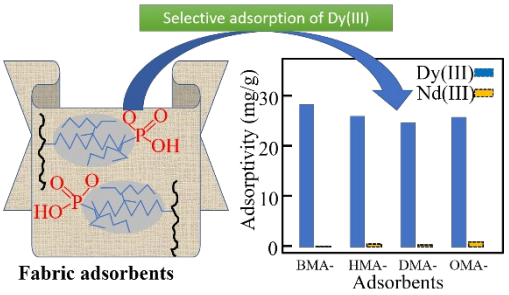

Fig. 2. Structure imagine of the fabric adsorbent and the selective adsorption of Dy(III) from aqueous solution containing Dy(III) and Nd(III) ions.

References

[1] Y. Ueki and N. Seko, ACS Omega **5**, 2947 (2020).
[2] H. Hoshina *et al.*, Polymers **12**, 2656 (2020).

P1-6 Project “Biocompatible Materials”

Leader : TAGUCHI Mitsumasa

Project “Biocompatible Materials” has been developing the functional biocompatible materials based on the radiation-induced crosslinking technique. The obtained materials can be utilized for the bio-devices in diagnostic, treatment and regenerative medicine {1-27, 1-28 in Part II}. The papers of our project are found in the attachment.

Development of magnetic resonance imaging contrast agent by radiation crosslinking [1]

MRI (Magnetic Resonance Imaging) systems are used to detect and diagnose diseases in hospitals. In addition, MRI contrast agents are used to provide more detailed imaging of blood flow conditions in organs. The contrast agents are generally composed of linear or cyclic organic ligands and gadolinium (Gd) ions to maintain higher contrast effects. Although these ligands immobilize Gd ions and inhibit their deposition in the patient's body, there is concern that these Gd-based contrast agents with low molecular weight partially enter the patient's brain through the blood cerebrospinal fluid barrier (BCFB) and the blood brain barrier (BBB) [2]. In this study, we prepared gelatin nanoparticles with appropriately controlled particle size in the range of 1-20 nm using quantum beams and loaded them with Gd complexes to develop a novel MRI contrast agent with fast renal excretion that does not pass through the BCFB and BBB. In addition, after evaluating the MRI relaxation ability of Gd ions loaded in gelatin nanoparticles, we conducted an *in vivo* study using mice to evaluate the contrast effect, renal excretion and brain persistence of Gd-loaded gelatin nanoparticles.

Three types of aqueous solutions of porcine gelatin (molecular weight=2000, 5000, 150000) with different molecular weights were irradiated with ^{60}Co γ-rays at 5-20 kGy under the air saturation condition at 25°C to produce gelatin nanogels. The size of the obtained nanogels was evaluated by a dynamic light scattering (DLS) system. The gelatin nanogels were subjected to 1,4,7,10-tetraazacyclododecane-1,4,7,10-tetraacetic acid mono-*N*-hydroxysuccinimide ester (DOTA-NHS) and gadolinium chloride to produce Gd-coordinated gelatin nanogels (GdGN). GdGN was directly imaged in water using a 200 keV transmission electron microscope with a liquid microscopy cell. The amount of Gd ions in GdGN was evaluated by Inductively Coupled Plasma Mass Spectrometry (ICP-MS). The *in vitro* cytotoxicity of GdGN was evaluated against Raji cell line (Burkitt's lymphoma). 0.3 ml of GdGN were administered to tumor-bearing mice, and the kidney, liver, and tumor sites were measured using 1H-MRI. In addition, 2 ml each of GdGN and commercially available Gd-DOTA were administered to normal mice, and choroid plexus and ventricles were imaged.

Radiation crosslinked gelatin nanogels with an average particle size of less than 100 nm were prepared by γ-ray irradiation of the gelatin solutions. The size of the nanoparticles depended on the molecular weight and concentration of gelatin and the dose rate and the dose of γ-rays. Finally, we succeeded in producing nanogels of 5 nm under the condition of 2 wt.% concentration of gelatin with a molecular weight of 2000 and 5 kGy dose. The 5-nm gelatin nanogels loaded with Gd ions were found to be stable in size in plasma but biodegradable. The GdGN showed low cytotoxicity for Raji cells and has an effective relaxability as an MRI contrast agent. Furthermore, GdGN could be concentrated up to a maximum of 20 mmol/l by centrifugation, which could be used for *in vivo* studies.

After tail vein administration of GdGN to tumor mice, MRI signal intensities in the medulla of the kidney and also in the cortex increased immediately but not altered in the liver and the tumor. After 2 hours of administration, both the former intense signals decreased to a level close to that before administration. These results indicate that the GdGN administrated from the tail vein was excreted in urine through the kidney in about 1 hour. Next, to examine the transfer into the cerebrospinal fluid, a 7-fold dose of GdGN and Gd-DOTA were administered to normal mice for comparison, and MRI imaging was performed (Fig. 1). The signals in the choroid plexus and ventricles increased with Gd-DOTA as shown in Fig. 2. The signal in the choroid plexus increased with GdGN, while the signal in the ventricles did not increase. This strongly suggests that GdGN did not migrate across the BCFB and the BBB in normal mice, thus emphasizing its safety as an MRI contrast agent.

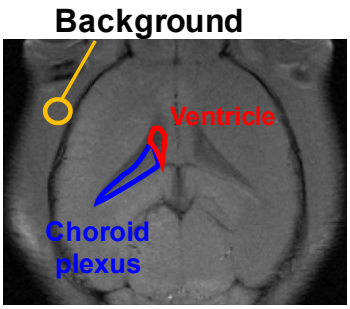

Fig. 1. MRI image in the brain of mice treated with GdGN.

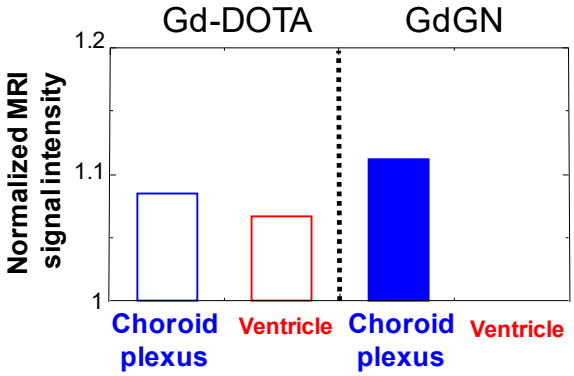

Fig. 2. MRI signal intensities of choroid plexus and ventricles in normal mice after Gd-DOTA and GdGN administration.

References

[1] A. Kimura *et al*., Acta Biomater. **125**, 290 (2021).
[2] T. Kanda *et al*., Radiology, **270**, 834 (2014).

P1-7 Project “Spintronics in Two-dimensional Materials”

Leader : SAKAI Seiji

Our project aims to develop novel spintronics devices for future information technology applications by taking advantages of the low dimensionality and quantum electronic properties of two-dimensional materials and related nanostructures. The advanced quantum beam techniques available at QST enable us to control the local atomic structure and spin-related properties in low-dimensional materials, surfaces, and interfaces. Magnetism at the surface of magnetic materials is of particular interest due to its essential role in spin-transport properties of low-dimensional spintronic devices. In 2020 we demonstrated unique magnetic oscillations at the iron surface by using a novel synchrotron Mössbauer spectroscopy technique which was developed together in partnership with the Kansai Photon Science Institute.

Discovery of magnetic Friedel oscillations at metal surface predicted 40 years ago [1]

In a magnetic material, the magnetization at the surface is not necessarily the same as it is in the bulk. At the surface, the reduced number of neighboring atoms can increase or decrease the polarization of electron spins, producing higher or lower magnetization. Theorists predicted 40 years ago that the magnetization on iron surfaces should vary with depth in the form of so-called magnetic Friedel oscillations [2]. Friedel oscillations are spatial modulations of electron spin or charge density that result from a defect or boundary in a material. So far, researchers have observed Friedel oscillations along the surface plane of films, but oscillations are also expected to occur with varying depth for certain magnetic materials. For iron, theory predicts that the (001) oriented crystal should exhibit layer-by-layer oscillations from the surface toward the bulk.

Over the past few decades, various experimental techniques have been developed to advance the study of surface and interfacial magnetism. However, few experimental studies have investigated the depth-dependent local magnetic structure of atoms. This is largely due to difficulties associated with depth-resolved spectroscopy arising from problems such as the measured signal being a result of electrons from various atomic locations within the sample. Recently, we have developed an ultrahigh vacuum system for depth-resolved synchrotron Mössbauer spectroscopy. This system enables *in situ* investigations of local magnetic structures in an atomic layer-by-layer fashion by using ^{57}Fe as a probe layer and a high-brilliance synchrotron Mössbauer source.

In this study, the depth-resolved magnetism of the Fe(001) surface was studied by using this *in situ* ^{57}Fe probing layer method [1]. Fe(001) films were fabricated by evaporating ^{56}Fe and ^{57}Fe in alternating layers onto MgO(001) substrates in ultra-high vacuum. A 0.8-ML-thick ^{57}Fe probe layer (1 ML = 0.14 nm) was embedded to the depth of the *N*th atomic layer (*N* = 1~7) below the surface of a 5.0 nm-thick ^{56}Fe(001) thin film. The Mössbauer experiments were performed under ultra-high vacuum conditions at BL11XU of SPring-8 using linearly π-polarized Mössbauer γ rays produced by the synchrotron Mössbauer source. The Mössbauer spectra were measured *in situ* by collecting the totally reflected γ rays from the sample surface under grazing incidence.

Figure 1(a) shows the Mössbauer spectra of the *N*th probe layer samples at 300 K. The spectra of the first, second, and third probe layer samples exhibited complex profiles composed of different components represented by various hyperfine fields (H_{int}), *i.e.*, small H_{int} (~28 T), large H_{int} (~36 T), and bulk-like H_{int} (~32 T). The intensities of these different components varied with the embedded depth of the ^{57}Fe probe layer. The small, large, and bulklike H_{int} components were maximized in the first, second, and third probe layer samples, respectively. In contrast, the spectra of the fourth and seventh probe layer samples exhibited a single magnetic component. Based on such systematic behavior, the prominent component with the largest area in the *N*th probe layer sample was assigned to the spectrum characterizing the ^{57}Fe atoms located in the *N*th atomic layer below the surface. Figure 1(b) plots the layer-by-layer H_{int} derived from the prominent component in each sample. The H_{int} exhibits a marked decrease at the surface and an oscillatory decay toward the bulk value with increasing depth in the upper four atomic layers. Theoretically, the observed oscillatory decay of H_{int} is strongly coupled with the Friedel oscillation of the magnetic moment caused by the surface electronic structure of Fe(001) with a large spin imbalance and d-band narrowing.

Therefore, the experimentally observed H_{int} oscillations penetrating the Fe(001) surface provide direct evidence of magnetic Friedel oscillations theoretically predicted 40 years ago. Moving forward, this *in situ* ^{57}Fe probe layer method combined with a synchrotron Mössbauer source could be used to facilitate studies on surface and interfacial magnetism in advanced spintronic materials and devices.

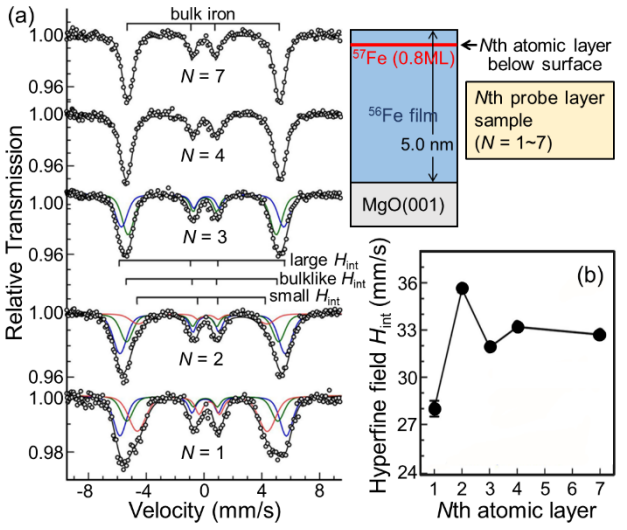

Fig. 1. (a) Mössbauer spectra of the *N*th probe layer samples measured at 300 K (b) Hyperfine fields H_{int} in the *N*th atomic layer below the surface. Inset: Schematic drawing of the samples.

References

[1] T. Mitsui *et al.*, Phys. Rev. Lett. **125**, 236806 (2020) (*Editor's Suggestion & Featured in Physics*).

[2] C. S. Wang and A. J. Freeman, Phys. Rev. B **24**, 4364 (1981).

P1-8 Project “EUV Ultra-fine Fabrication”

Chief : YAMAMOTO Hiroki

Project “EUV Ultra-fine Fabrication” has been developing the functional polymer materials such as high performance resist materials for extreme ultraviolet (EUV) and next generation EUV lithography. We have synthesized resist materials such as metal resist and block copolymer with chemical synthesis or by using quantum beams such as γ-rays and electron beam (EB). We aim to develop resist materials for EUV lithography and conduct fusion between top-down and bottom-up nanofabrication for next generation EUV lithography. We report herein two recent study: study on irradiation effects by the ultra-short pulse EUV in resist materials and development of the soft X-ray laser (SXRL) beamline for evaluation of EUV resists.

Study on irradiation effects by femtosecond-pulsed extreme ultraviolet in resist materials [1]

Short-pulse EUV of a free-electron laser (FEL) is the most potential candidate as a next-generation EUV lithography light source. Because EUV with a pulse width of less than picoseconds is a novel light born in recent scientific and technological developments, physical events and chemical reactions in resist materials induced by the short-pulse EUV are not sufficiently understood. We reported that the obtained sensitivity for picosecond EUV irradiation was approximately 50 times higher than that for typical EUV irradiation [2, 3]. Therefore, further investigation of femtosecond-pulsed EUV-induced reactions in resist materials are strongly needed for realizing EUV-FEL lithography.

In order to confirm whether the resist sensitivity of PMMA enhances or not upon exposure to femtosecond-pulsed-EUV compared with conventional EUV and SXRL, irradiation effects by femtosecond-pulsed Soft X-ray free electron laser (SXFEL) in poly(methyl methacrylate) (PMMA) were investigated.

Figure 1 shows sensitivity curve of PMMA with 66 nm film thickness after development. The sensitivity of PMMA for femtosecond-pulsed SXFEL was determined to be approximately 6–8 mJ/cm^2. PMMA can be developed with lower energy deposition for femtosecond-pulsed SXFEL than typical EUV (approximately 50 mJ/cm^2). On the other hand, the sensitivity enhancement upon exposure to femtosecond-pulsed EUV is similar to the result obtained using laser-induced-plasma based soft X-ray laser (SXRL) (2 mJ/cm^2). Surprisingly, the sensitivity enhancement is common to result obtained using picosecond-pulsed SXRL. SXRL irradiation induced the decomposition of both the main and side chains in PMMA. In femtosecond-pulsed SXFEL, the same reaction in PMMA as SXRL might be induced, so that the sensitivity of PMMA for SXFEL irradiation was enhanced compared with using typical EUV sources. These results suggest the importance of a specific resist design for next-generation EUV-FEL lithography.

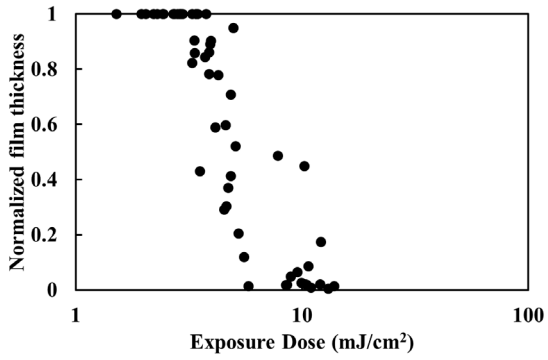

Fig. 1. Sensitivity curve of SXFEL-irradiated 66 nm thick PMMA film after development.

Development of SXRL beamline for evaluation of EUV resists [2]

We have developed the SXRL irradiation system. The SXRL with the wavelength of 13.9 nm, which is very close to the exposure wavelength of the EUV lithography system (λ = 13.5 nm). Therefore, SXRL is sufficient to be used for the evaluation of EUV resists.

In order to use the SXRL as the reliable tool for the evaluation of the EUV resists, we must correct the accurate data of the SXRL irradiation experiments. To achieve this purpose, the irradiation experiment must be carried out by use of the reliable facility and apparatus. The important parameter in the irradiation experiment is the fluence onto the target surface, which directly reflects the laser-matter interaction phenomenon.

To obtain such precise experiments, we must acquire and show the collect irradiation energy value onto the sample surface. The irradiation beamline has an intensity monitor composed by the Mo/Si multilayer beam splitter and the X-ray charge-coupled device camera. This intensity monitor provides the irradiation intensity onto the sample surface. By using the SXRL beamline, we can confirm the exact value of the ablation threshold and the durability of EUV optical elements. Finally, we performed the sensitivity evaluation of PMMA as the first experiment for the confirmation of the performance of this irradiation

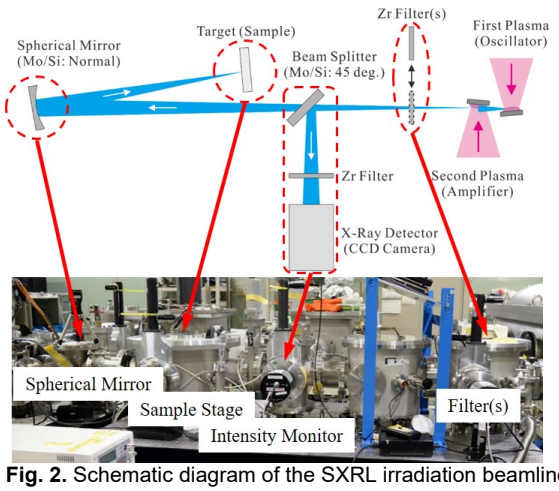

Fig. 2. Schematic diagram of the SXRL irradiation beamline.
beamline.

References

[1] Y. Hosaka *et al.*, J. Photopolym. Sci. Tech. **34**, 95 (2021).
[2] M. Ishino *et al.*, Appl. Opt. **59**, 3692 (2020).
[3] Y. Hosaka *et al.*, Appl. Phys. Lett. **115**, 073109 (2019).

P1-9 Project “Element Separation and Analysis”

Leader : OHBA Hironori

Quantum beams are versatile sources for materials processing. Our project explores basic process of the laser-matter interaction to separate elements from industrial waste liquid or analyze elements under harsh environments. For element separation, we applied a new analysis method for X-ray absorption fine structure (XAFS) spectra to elucidate the laser-induced particle formation mechanism. For element analysis, we study influences of the analysis performancel in radiation environment for the application of fiber-optic laser-induced breakdown spectroscopy. The recent results of our project are introduced as follows. {1-31 in Part II}

Application of an augmentation method to MCR-ALS analysis for XAFS and Raman data matrices in the structural change of isopolymolybdates [1]

We measured XAFS and Raman spectra of isopolymolybdates(VI), $[Mo_mO_y(H_2O)_z]^p$ (p=6m-2y) in highly concentrated HNO_3 solution (0.15 – 4.0 M), which change their geometries depending on the acid concentration as shown in Fig. 1. The simultaneous resolution of the XAFS and Raman data was performed using a multivariate curve resolution by alternating least-squares (MCR-ALS) analysis. Because the XAFS spectra were insensitive to the geometrical change of the isopolymolybdates, the MCR-ALS result of single XAFS data matrix shows a large dependence on the preparation method of the initial data matrices as shown in Fig. 2 (a). This problem is overcome by the simultaneous resolution of the XAFS and Raman data (Fig. 2 (b)): the MCR-ALS result of an augmented matrix of these data has little dependence on the initial data matrices. This indicates that the augmentation method effectively avoids the rotation ambiguities in the MCR-ALS analysis of the XAFS data.

Detection of gadolinium in surrogate nuclear fuel debris using fiber-optic laser-induced breakdown spectroscopy under gamma irradiation [2] {1-31}

Fiber-optic laser-induced breakdown spectroscopy (FO-LIBS) [3] was applied to qualitative and quantitative analysis of gadolinium (Gd) in mixed oxide samples simulating fuel debris in the damaged reactors of the Fukushima Daiichi Nuclear Power Station. The simulated debris was prepared from mixed oxide materials containing Gd_2O_3 with varying Gd concentrations. The emission spectra of the simulated debris show that the gadolinium lines at 501.5 nm and 510.3 nm are suitable for Gd detection in the fuel debris. The LIBS measurements were further performed under gamma irradiation (0–10 kGy/h), resulting in a decrease in spectral intensities due to the radiation-induced damage in the optical fiber. For quantification of Gd, robust calibration curves against gamma irradiation were established from the intensity ratio of Gd (501.5 nm)/Ce (474.5 nm) emission lines (Fig.3.), exhibiting good linearity with the Gd concentrations. The limit of detection of Gd was calculated to be less than 0.1 wt%, regardless of the radiation dose rate. These results demonstrate that FO-LIBS is a potential tool for in situ and remote analysis of nuclear fuel debris [2].

References

[1] M. Saeki, *et al*., Anal.Sci. **36**, 1371 (2020).
[2] R. Nakanishi, *et al*., Appl. Sci. **10**, 8985 (2020).
[3] M. Saeki, *et al*., J. Nucl. Sci. Technol. **51**, 930 (2014).

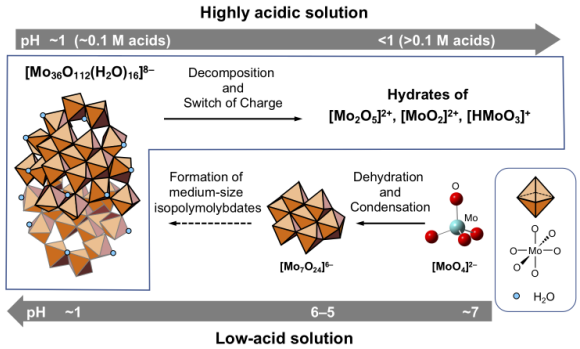

Fig. 1. Structural change of the $[Mo_mO_y(H_2O)_z]^p$ species by acidification.

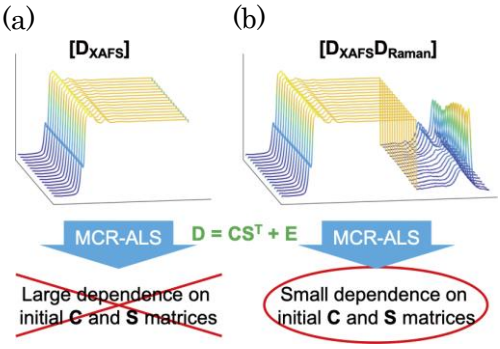

Fig. 2. Schematic drawing of the augmentation method. (a) single XAFS data matrix; (b) simultaneous resolution of the XAFS and Raman data.

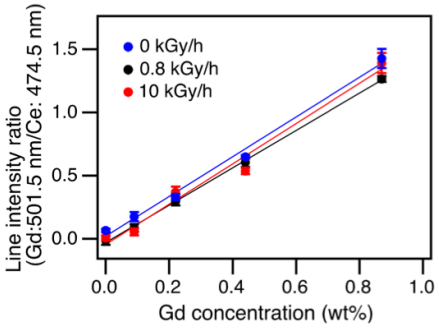

Fig. 3. Calibration curves derived from the intensity ratio of Gd 501.5 nm/Ce 475.5 nm lines. The limit of detection for Gd was calculated to be in the range of 0.03–0.08 wt%.

P1-10 Advanced Functional Polymer Materials Research Group

Leader : MAEKAWA Yasunari

The research of “Advanced Functional Polymer Materials Group” has been focused on efficient development technique for advanced functional polymer materials, which are widely used in advanced devices and construction materials. The technique includes materials informatics such as machine learning and neural network in addition to the established radiation techniques regarding to the radiation-induced graft polymerization and the X-ray/neutron structural analysis. This group has been conducting mainly the R&D for “Advanced functional polymer materials alliance” under QST innovation hub program in collaboration with participant companies. {1-34 in Part II}

Research results of “Advanced functional polymer materials alliance”

On the alliance project of the 4th year, main achievements in four research subjects are as follows.

(1) Grafting yields prediction: We are preparing functional polymer materials by the radiation-induced graft polymerization of methacrylate ester monomers on polyethylene nonwoven fabric, and trying to construct the data-set composed of the various physical values with respect to the chemical structure and electronic state of the monomers as well as the obtained grafting degrees. We investigated the effect of machine learning algorithms on prediction accuracy of the grafting degrees. It was found that ensemble methods such as "XGBoost" and "Random Forest" showed higher prediction accuracy than that of multiple linear regression.

(2) Structural data accumulation: We analyzed the hierarchical structures of the proton-conducting electrolyte membranes (PEM) using atomic force microscope and small angle X-ray/neutron scattering. The hydrophobic/hydrophilic domain structure in PEMs based on poly(ethylene-co-tetrafluoroethylene) (ETFE-PEM) were digitalized by coarse-grained molecular dynamics simulation. From the scattering profile obtained by the simulation, it was found that a polystyrene-water phase separation structure was formed in the hydrophilic domain, and the size was about 2.1 nm.

(3) Property prediction: We evaluated the properties of the PEMs, such as proton conductivity (PC) and water uptake (WU), using machine learning. In the random forest regression analysis, the PC, WU, and ionic conduction efficiency (PC/WU) were accurately predicted by optimizing the number of regression trees and the number of leaf nodes. It was found that the PC was improved by forming ion channels with good connectivity due to low crystallinity, and that the WU was suppressed by the high intermolecular force of base polymer. Accordingly, it was clarified that the PEEK-based PEM exhibited highest fuel cell performance and durability due to low crystallinity and high intermolecular force of PEEK.

(4) Database preparation: The data collected for materials informatics of the grafted polymers was integrated with FileMaker as a database management software. We designed a search operation screen and created a user interface to use the database efficiently.

Phase-separated morphology of Nafion membranes characterized by partial scattering function analysis [1]

Nafion® is a benchmark material for a proton-exchange membrane and has been commercialized in residential and automobile fuel cells. The properties of the Nafion membrane are closely related to its hierarchical structures upon hydration. However, the detailed structure (such as size, shape, and connection) is still under debate. In this study, we used a partial scattering function (PSF) analysis to identify the detailed structure of each component, and the structural correlation between two components, and hence determine hierarchical structures of the hydrated Nafion.

The hydrated Nafion membrane was treated as a three-component system: the main-chain [–(C_2F_4)$_m$–C_2F_3– with m ≅ 6.5], side-chain ($C_5F_{10}O_2$–SO_3H), and water. PSFs were quantitatively decomposed from nine I(q) profiles obtained invealed the detailed structure of each component, as shown in Fig. 1. In the large-scale (> 30 nm), structural the contrast variation SANS experiments. To elucidate the structure, we use the Debye–Bueche (DB) model to fit the small-q upturn and the Teubner–Strey (TS) model to fit the peaks in the middle- and high-q regimes. The analysis of PSF self-term of the other component with main-chain re heterogeneities with a size of > 65 nm were observed in the main- and side-chain domains but not in water domains. This structure in large-scale was supported by atomic force microscope observation. In the middle-scale (5 ~ 30 nm), as a result of the main-chain semicrystalline templating effect, bicontinuous-like structure of the crystalline domain (main-chain) and the amorphous domain (main-chain, side-chain, and water) was observed. A mean separation distance between the crystalline domains exhibited 11 nm. In the small-scale (< 5 nm), another bicontinuous-like structure exists in the amorphous phase with a mean separation distance of about 4 nm, indicating a well-connected water network responsible for the good membrane conductivity.

In order to perform a machine learning with favorable accuracy, the data-set composed of reliable experimental data is required. The PSF analysis would be useful for the collection of structural data of the graft polymer materials with specific hierarchical structures.

Reference

[1] Y. Zhao *et al*., Macromolecules **54**, 4128 (2021).

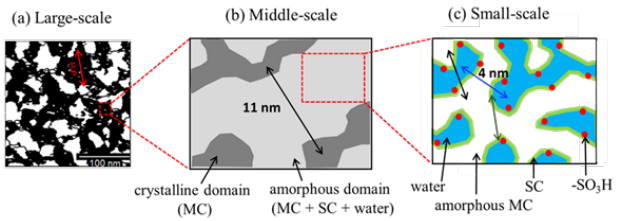

Fig. 1. Schematic of the hierarchical structure of the main-chain (MC), the side-chain (SC), and water domains in the fully hydrated Nafion membrane at (a) large-scale; (b) middle-scale; and (c) small-scale.

P1-11 Quantum Sensing and Information Materials Research Group

Leader : OHSHIMA Takeshi

Quantum technologies such as quantum sensing, quantum information and quantum computing are indispensable technologies to realize “Society 5.0” and R&D for quantum technologies are intensively carried out all over the world now. We study quantum technologies together with domestic and international Universities and Research Institutes. We focus on color centers which act as spin defects and/or single photon emitters in wide bandgap semiconductors. In addition, we propose a new technology combining spintronics with photonics “spin-photonics”. For color centers, we create such defects in wide bandgap semiconductors, *e.g.* diamond, silicon carbide (SiC) and gallium nitride using energetic particles. Then, we investigate the optical and spin properties of color centers. In addition, we intend to fabricate electronic devices with such spin defects/single photon emitters to realize quantum devices. For spin-photonics, we study technologies for new devices in which the interaction between spins and photons is applied to realize extremely low energy consumption devices. The research results that link to this group are also shown in the results obtained by the research projects “semiconductor radiation effects” and “spintronics in 2D materials”

Gradiometer using nitrogen-vacancy centers in diamond [1]

Negatively-charged nitrogen-vacancy (NV) center acts as a quantum sensor working at room temperature [2]. Since magnetometry using NV centers in diamond can achieve extremely high sensitivity in principle, competitive research and development is now in progress all over the the world. In addition to the improvement of the sensitivity of NV centers themselves, the technologies to reduce environmental noise have to be developed. Here, we fabricate a gradiometer based on two diamond pieces containing NV centers and demonstrate the reduction of magnetic noises. In this study, NV centers were created in a type Ib diamond by 2 MeV-electron irradiation at 750 °C at fluences of 1×10^{18} /cm^2. After the NV center fabrication, the diamond was cut into two pieces. Figure 1 shows the schematic diagram of gradiometer fabricated in this study. Two diamonds were used as sensor 1 and 2. AC magnetic field of 31 μT with 20 Hz is applied as an environmental noise and AC magnetic field of 10 μT with 30 Hz is applied to sensor 1 as a target magnetic field as shown in the figure. Figure 2 (a) shows the time-domain signals of detected magnetic field for sensors 1, 2 and the subtracted 2 from 1.

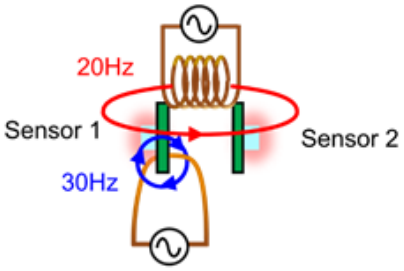

Fig. 1. Schematic diagram of gradiometer used in this study.

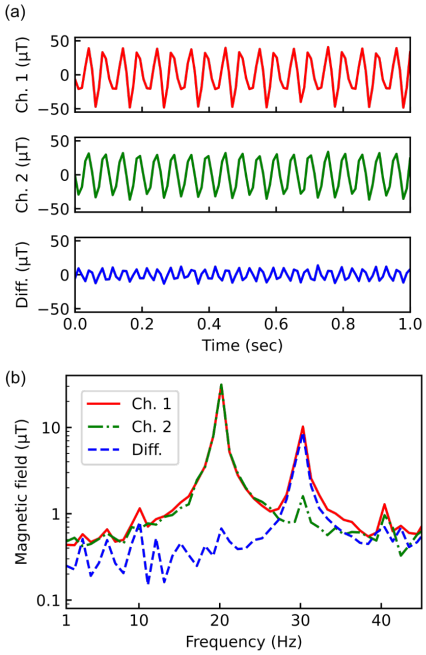

Fig. 2. (a) Time-domain signals for sensor 1, 2 and subtracted 2 from 1, referred to as “Diff.” in the figure. **(b)** Fourier-transformation of the time-domain signals shown in Fig. 2 (a).

The signal for sensor 1 shows inhomogeneous amplitude due to the modulation of the magnetic field with 30 Hz whereas sensor 2 has a signal with uniform amplitude. Figure 2 (b) shows Fourier-transformation of the time-domain signals shown in Fig. 2 (a). A peak at 20 Hz is observed for both sensor 1 and 2 although a peak at 30 Hz is obtained for only sensor 1, as shown in Fig. 2 (b). As a result, the subtracted signal shows only one peak at 30 Hz. Thus, this result indicates that the environmental noise with 20 Hz can be cancelled by the gradiometer fabricated in this study. We also confirmed the noise floor of this gradiometer. As a result, the noise floor of this gradiometer is the same as that of magnetically shielded room which is consists of three-layer permalloy shielded box.

References

[1] Y. Masuyama *et al.*, Sensors **21**, 977 (2021).
[2] J. M. Taylor *et al.*, Nat. Phys. **4**, 810 (2008).

Part Ⅰ

2. Life Science

P2-1 Project “Microbeam Radiation Biology”

Leader : FUNAYAMA Tomoo

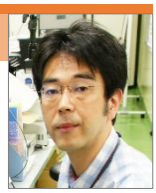

The project "Microbeam Radiation Biology" has been developing technologies to elucidate the biological response to livings exposed to high-LET radiation, which are difficult to understand as long as conventional irradiation techniques are used.

High-LET heavy-ions deposits energy to the irradiated target intensively along their trajectory, which is called as ‘ion track structure’. Irradiation of heavy ions to living organisms is known to cause severe damage to DNA, resulting in a high biological effect. However, ion track structure causes non-uniformity in the spatial distribution of deposited energy on the micrometer scale. Therefore, in the conventional broad-field irradiation, the irradiated dose is not uniform for each individual cell.

To overcome this problem, we have developed technologies to target and irradiate a single cell under a microscope using a micrometer-scale beam spot, which is the same size or smaller as a single cell [1].

This microbeam irradiation technologies had allowed us to irradiate only limited number of cells or cell populations in biological samples with heavy ions. Our technology can locally irradiate not only cultured cells, but also individuals of livings with microbeams. By irradiating a part of an individual and analyzing its response, it will become possible to understand the mechanism of biological function involved in the irradiated area. Taking advantage of this feature, we examined the effect of local irradiation of individuals on their biological activity.

Analysis of developmental control mechanisms in medaka brain nervous system [2]

The development of a mammalian fetus proceeds in the maternal uterus. Therefore, it is not possible to observe the developmental process of a single individual continuously and in detail. As a result, there are still some unresolved issues in understanding the functions of prenatal developmental control and malformation prevention. To elucidate these mechanisms, it is necessary to observe the developmental state continuously.

In this study, we investigated the mechanism of embryonic developmental process using Japanese medaka fish, which embryo has transparent eggshells. By this feature, whose developmental process can be observed in detail using a stereoscopic microscope.

We had found that irradiation causes a delay in the development of the brain nervous system, and that the delay returns to normal by the time of hatching, by irradiating blastula stage embryos of the medaka with X-rays at 2 Gy and continuously observing its developmental process. To investigate the relationship between this delay and the percentage of cells that are damaged, we used the carbon-ion microbeams ($^{12}C^{6+}$ 26.7MeV/u) of TIARA to irradiate cells of blastula stage with different beam diameters of 70, 120, and 180 μm. In embryos in which no more than 10% of the cells (70 and 120 μm beam) were irradiated, the development of the brain nervous system was temporarily delayed, as the case with 2 Gy of X-rays. This delay returned to normal by the time of hatching. However, irradiating 25% of the cells (180 μm beam) caused the remaining 75% of the cells to fail to hatch, even though they were non-irradiated.

This result indicates that the interruption of the developmental process is determined by the percentage and number of severely damaged blastula cells.

Study on mechanism of motor control in *C. elegans* [3]

The nematode *Caenorhabditis elegans*, approximately 1 mm long, is a model organism commonly used for the analysis of the nervous system and motor control. When the whole body of *C. elegans* is irradiated, the motility evaluating based on body bends is reduced temporarily. To identify the region responsible for this reduction of motility, we irradiated a 20 μm diameter area of the head, including the central nervous system (CNS), with a carbon-ion microbeam ($^{12}C^{6+}$ 15.8 MeV/u).

When the region of the CNS was irradiated with the same dose that caused decreased motility with whole-body irradiation, there was no change in motility. However, a decrease in motility was found when the dose was increased. These results indicate that the body bends of *C. elegans* is complementarily controlled by both the CNS and the autonomous regulation of muscular and motor neurons.

Furthermore, the activities of the body-wall muscle cells of *C. elegans* enclosed in a microchip (Worm Sheet) [4], was compared before and after head (CNS)-targeted irradiation of a 60-μm-diameter area. The experimental results showed that the rhythm of movement indicated by the wave of the contracting muscle cells was not ceased by the irradiation (Fig. 1). This indicates that in whole-body bending activities, the generation of motor rhythms is carried out by a mechanism that is independent of central control by the CNS.

This study revealed that the motility of *C. elegans* might not regulated by a simple top-down control mechanism by the CNS, but by a distributed control from whole nerve and muscular system.

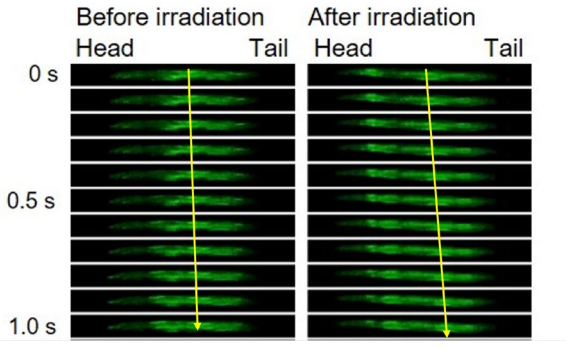

Fig. 1. Patterns of muscle cell contraction before and after CNS-targeted irradiation of a *C. elegans*.
A head region of a *C. elegans* was irradiated with 1,000 Gy of carbon-ion microbeam, then the periodic muscle contraction (fluorescent) was observed. Yellow arrows indicate moving direction of muscle contraction wave. Modified from reference [3].

References

[1] T. Funayama, Quant. Beam Sci. **3**, 13 (2019).
[2] T. Yasuda *et al.*, Biology. **9**, 447 (2020).
[3] M. Suzuki *et al.*, Biology. **9**, 289 (2020).
[4] M. Suzuki *et al.*, J. Neurosci. Methods. **306**, 32 (2018).

P2-2 Project “Ion Beam Mutagenesis”

Leader : OONO Yutaka

Ion beams are useful mutagens for plant and microbes because they are thought to cause mutations via a mechanism distinct from those of chemical mutagens or gamma rays. Our project aims to understand feature of ion-beam-induced mutations and develop applications of ion beam mutagenesis in basic and applied biotechnology. Recently, we use a next generation sequencing technique to investigate the detailed characteristics of the ion-beam- and gamma-ray-induced mutations at both genome wide and specific gene levels {2-08, 2-11 in Part II}. In addition, we try to isolate valuable mutants in ornamental plant, parasitic plants, plant growth-promoting rhizobacteria, oil-producing algae, sake yeasts, and other bacteria under collaborations with academic or industrial research organizations {2-09, 2-10, 2-12, 2-13, 2-15}. Revealing molecular basis of radiation response and resistance is another major business in our project {2-14, 2-16~18}.

Non-homologous end joining (NHEJ) is an important repair pathway that protects the genetic information in plant genome [1]

NHEJ is one of two major pathways to repair DNA double-strand breaks. Because it directly re-joins the two broken DNA ends, it is thought more mutagenic than another major DSB repair pathway, homologous recombination that uses sequence information of a homologous DNA strand for repairing. To investigate the role of NHEJ in radiation-induced mutagenesis, Yan Du, a visiting researcher from China under Nuclear Researchers Exchange Program, with collaborators including two our project members, Yoshihiro Hase and Katsuya Satoh, conducted whole genome sequencing analysis of gamma-ray induced mutations in two Arabidopsis mutants (*Ku70*$^{-/-}$ and *Lig4*$^{-/-}$) that luck NHEJ DNA repair components. A dose repose curve of survival suggested that the NHEJ-deficient mutants are hypersensitive to gamma rays and that 100 Gy for the NHEJ-deficient mutants is equivalent to 1000 Gy for wild type plants. Thus, the seeds of the NHEJ-deficient mutants were treated with 100 Gy gamma rays followed by the mutation profile in the M2 plants of the NHEJ-deficient mutants was investigated and compared with previously obtained data of the wild type plants irradiated with 1000 Gy.

As shown in Fig. 1, the mutation frequency (number of mutation / base / Gy) in the NHEJ-deficient mutants was higher than that in the wild type plants. In addition, the deletions (≥ 2 bp) and complex-type mutations were frequently detected in the both mutants. These results suggest that NHEJ deficiency results in arising severe mutations as well as increasing sensitivity to gamma rays. In other words, NHEJ is required for precise repair of broken DNA and has significant role to minimize the deleterious effects of ionizing radiations in plants.

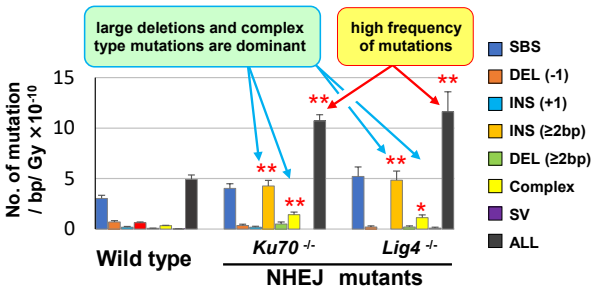

Fig. 1. Mutation frequency (number of mutation / base / Gy) in the wild type and two NHEJ-deficient mutants (*Ku70*$^{-/-}$ and *Lig4*$^{-/-}$).
Asterisks indicate significance to wild type (**p < 0.01 and *p < 0.05). SBS, single base substitutions; DEL, deletions; INS, insertions; SV. structural variants. Figures in parentheses represent size (bp) of DEL or INS.

Uncovering genome of the cesium-accumulating bacterium [2]

The bacterium *Rhodococcus erythropolis* CS98, recently reclassified as *Rhodococcus qingshengi*, is expected to be useful for removing radioactive cesium from contaminated soil because this bacterium has high ability to accumulate the cesium in the cell. Exploring cesium accumulation mechanism in this bacterium is also helpful to further improve the ability of cesium accumulation and develop practical strains for radiocesium bioremediation. In this context, Satoh *et al*. completed genome sequencing of *R. qingshengii* CS98 by both long- (GridION) and short-read (MiSeq) genome sequencing methods. Sequences obtained by GridION (1,389,142,401 bp) and MiSeq (259,666,780 bp) were assembled and polished to construct the genome of *R. qingshengii* CS98, which was comprised of one circular chromosome (6,240,414 bp) and one linear plasmid (485,693 bp). Its total length was 6,726,107 bp with 62.4% G+C content on average. Annotation pipeline predicted 6,255 protein-coding sequences (CDSs), 59 tRNAs, and 5 rRNA operons (Table 1). The linear plasmid possessed plasmid partitioning gene *parA*. The chromosome sequence of the CS98 was highly similar to that of *R. qingshengii* strains djl-6-2 (99.07% identity) and RL1 (99.09% identity). Furthermore, the linear plasmid showed a high level of similarity (99.15% identity) to the linear plasmid of the *Rhodococcus* sp. strain BH4. Further comparative genome analyses will help to elucidate the molecular basis of cesium accumulation in the bacterial cells.

Table 1
General feature of complete genome sequence of *R. qingshengii* CS98.

	Chromosome	Plasmid
Size (bp)	6,240,414	485,693
G+C content (%)	62.54	60.41
No. of CDSs	5,811	444
No. of tRNA	58	1
No. of rRNA (5S / 16S / 23S)	(5 / 5 / 5)	(0 / 0 / 0)

References

[1] Y. Du *et al*., J. Radiat. Res. **61**, 639 (2020).
[2] K. Satoh *et al*., Microbiol. Resour. Announ. **9**, e01188-20 (2020).

P2-3 Project “Medical Radioisotope Application”

Leader : ISHIOKA Noriko S.

The research objective of our project is to develop the radiopharmaceuticals labeled with useful radioisotopes (RI) for cancer theranostics (therapy and diagnosis). Our project focuses on the research of the RI drug delivery system (RI-DDS) using bioactive compounds such as antibodies and peptides in order to make the most of the ability of RI. To achieve our research objective, we also address effective RI production, the molecular mechanisms of radionuclide therapy, and dosimetry {2-20~22 in Part II}.

Electrodialytic handling of radioactive metal ions for preparation of tracer reagents [1]

Copper-64 (^{64}Cu) is a useful radionuclide for cancer diagnosis with positron emission tomography (PET) as well as radiotherapy. No-carrier-added ^{64}Cu can be produced via ^{64}Ni(p,n)^{64}Cu nuclear reaction, and separated from ^{64}Ni by chelating ion-exchange method [2]. After the separation process, the purified ^{64}Cu is obtained in hydrochloric acid (HCl). For further process of the probe synthesis, the acid matrix should be converted into biocompatible forms such as acetate buffer. Evaporation to dryness has been traditionally used for the matrix conversion. However, the evaporation to dryness is time-consuming and is a possible process leading to loss of the radioactive metal ions. The radioactivity exponentially decreases with time due to its half-life of 12.7 h. Therefore, rapid and reliable probe preparation methods are recommended. In the present study, electrodialytic radioactive metal ion handling was studied for the matrix conversion and in-line probe synthesis.

Figure 1 shows schematic flow system of the electrodialytic ion transfer device (ITD) used in this study. ITD was comprised four solution channels; anode isolator (A), donor (B), acceptor (C), and cathode isolator (D). These channels were separated with an anion exchange membrane (AEM) and a regenerated cellulose dialysis membrane (DM). The size of each channel was 5 mm width and 40 mm length. The thin solution layers (0.13 mm each) created strong electric fields and short distance for the transfer. Both of the cathode and anode electrodes consist of platinum mesh. Aqueous solution was continuously flowed into each channel. The donor solution of ^{64}Cu in HCl were introduced into the donor channel. The acceptor solution was desired acids after conversion such as acetic acid (CH_3COOH). The voltage of 10 V was applied to the electrodes during the flow. The effluent of ITD was collected and analyzed with a gamma counter. As a result, it was confirmed that the matrix can be transferred from HCl into CH_3COOH under optimized conditions, even though the radioactive metal ions were at the tracer level.

When a ligand was dissolved in the acceptor solution, the transferred metal ions from the donor were well mixed and formed a complex with the ligand in-line. Herein, we demonstrated electrodialytic synthesis of pseudo-PET diagnosis probe using the ligand 1,4,7,10-tetraazacyclo-dodecane-1,4,7,10-tetraacetic acid (DOTA), which was widely used for the ^{64}Cu PET probe. Results of the in-line probe synthesis using the acceptor solution, 1 μM DOTA in 1 mM CH_3COOH, are shown in Fig. 2. The syntheses of ^{64}Cu-DOTA were evaluated with radio-TLC (a) and radio-HPLC (c). As shown in Fig. 2b, the recovery of ^{64}Cu transferred from donor into acceptor, which was indicated by the green bar, was obviously improved by addition of DOTA in acceptor. The red bar represents that the transferred ^{64}Cu ions were quantitatively reacted with DOTA in acceptor.

Additionally, we found that ITD made possible not only transfer but also enrichment of the radioactive metal ions by the relatively larger flow rate of donor to acceptor. When the flow rates for donor and acceptor solutions were 1.0 and 0.10 mL/min, respectively, it was proved that the concentration of ^{64}Cu transferred from donor into acceptor was enriched 10 times.

In summary, the electrodialytic ion handling method can achieve simultaneous matrix conversion, probe synthesis, and enrichment even at the ultra-trace concentration level. This new method can treat RI in closed system rapidly without contamination and loss of RI.

References

[1] Y. Sugo *et al.*, Anal. Chem. **92**, 14953 (2020).
[2] S. Watanabe *et al.*, Nucl. Med. Biol. **36**, 587 (2009).

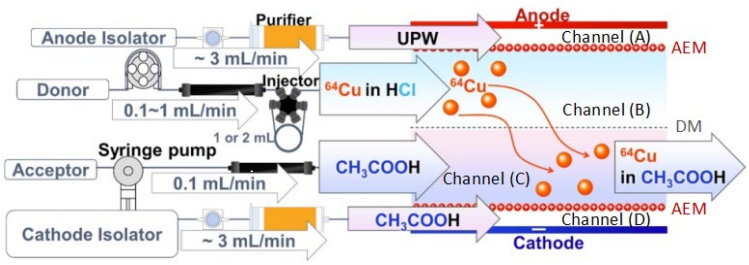

Fig. 1. Schematic flow system of ITD for matrix conversion of ^{64}Cu solution from HCl into CH_3COOH.

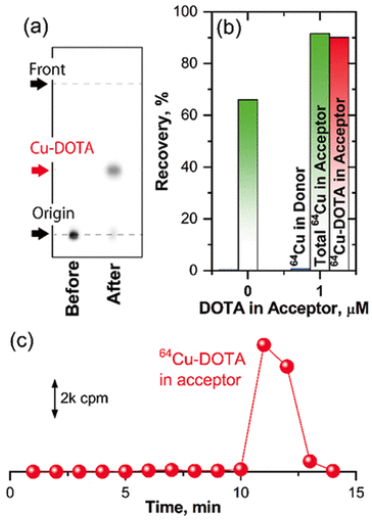

Fig. 2. In-line synthesis of ^{64}Cu-DOTA complex by the ITD treatment. (a) radio-TLC images before and after the treatment, (b) recoveries of ^{64}Cu obtained with and without DOTA in the acceptor, and (c) radio-HPLC chromatogram after the treatment.

P2-4 Project “Radiotracer Imaging”

Leader : KAWACHI Naoki

The aim of “Radiotracer Imaging Research” project is to measure, visualize the radiation sources quantitatively, and characterize the biological processes and functions, using radioisotopes and imaging devices such as positron emitting tracer imaging system (PETIS). We will establish systematized the most advanced techniques for live-imaging using radiotracers and these production methods, nuclear imaging apparatus, imaging techniques using each apparatus, and kinetic analytical methods for understanding the elements and molecules transport functions related to agriculture, environmental problems and medicine within living systems. {2-23, 2-24, 3-01 in Part II}

Development of the positron-emitting ^{127}Cs tracer for non-invasive imaging of radiocesium dynamics *in vivo*

Visualizing the dynamics of cesium (Cs) is desirable to elucidate the mechanism of radiocesium transport in animals, plants, and humans. Therefore, we aimed to develop the production and purification methods of the positron-emitting nuclide ^{127}Cs (half-life of 6.25 h) and also to verify the suitability of ^{127}Cs as a tracer for non-invasive imaging of radiocesium dynamics *in vivo*.

^{127}Cs was produced using the ^{127}I (α, 4n) ^{127}Cs reaction, which was induced by irradiation of sodium iodide with a ^{4}He^{2+} beam from a cyclotron. We excluded sodium ions by using a material that specifically adsorbs Cs as a purification column [1] and successfully eluted ^{127}Cs by flowing a solution of ammonium sulfate into the column. We injected the purified ^{127}Cs tracer solution into living rats and the dynamics of Cs were visualized using positron emission tomography (PET). This revealed that ^{127}Cs was localized in the saliva glands, heart, small intestine, and kidney (Fig. 1). The distribution was the same tendency as the results of previous studies using disruptive methods Thus, the ^{127}Cs tracer is useful for the non-invasive investigation of radiocesium in living organisms [2].

Development of new imaging method for plant rhizosphere research

The release of the photoassimilated carbon (C) into the rhizosphere, which extends several millimeters from the plant roots into the surrounding soil is estimated that approximately 50% of the root biomass, therefore, it is cost to plants. However, the released C compounds have important roles on enhance the plant’s ability to adapt the rhizosphere environment. A method to measure and quantitatively analyze C partitioning between the root system and the soil is desirable for clarifying the regulatory mechanisms of the C release into the rhizosphere. In this study we developed a new method to visualize and evaluate the movement of photoassimilated C into the root system and its release into the soil coupled with positional information by using $^{11}CO_2$ and PETIS.

A new type rhizobox was specifically designed for the PETIS imaging experiment to separate the released ^{11}C from that of the root (Fig. 2 (a)). The $^{11}CO_2$ gas was fed to the aerial part of a test plant and the PETIS imaging was started immediately to monitor the ^{11}C-photosynthates movement into the root system in real time (Fig. 2 (b) and (c) middle). Then, the plant root was removed from the rhizobox and the PETIS imaging resumed to visualizing the distribution of ^{11}C signals released into the rhizosphere soil (Fig. 2 (b) and (c) right). The release capability of whole root system showed the same order in white lupin than that of soybean, however its characteristics of distribution showed a hotspot in locally high level which differed with soybean that was showed uniform. Our imaging method will be a powerful tool for characterization of C partitioning and provide accurate spatial information for sampling of the rhizosphere soil coupled with roots, and which can greatly useful for improvement of the rhizosphere research [3].

References

[1] T. Shibata *et al.*, Radiat. Phys. Chem. **119**, 247 (2016).
[2] N. Suzui *et al.*, Sci. Rep. **10**, 16155 (2020).
[3] Y.-G. Yin *et al.*, Sci. Rep. **10**, 8446 (2020).

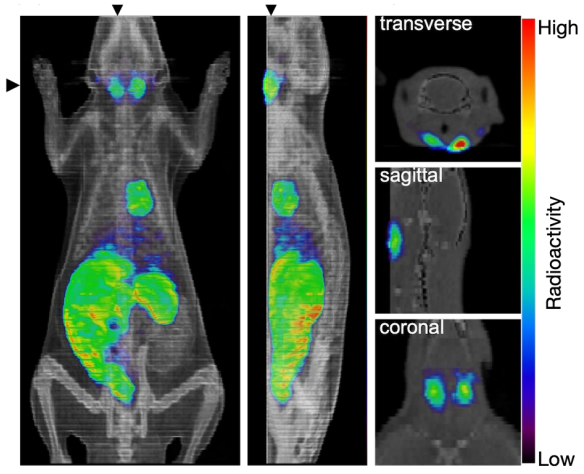

Fig. 1. PET-CT fusion images in a living rat. PET images were integrated for 4 hours after injection of ^{127}Cs tracer.

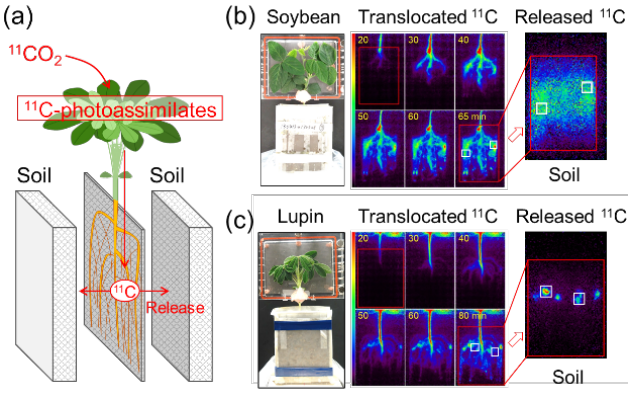

Fig. 2. (a) Configuration of a new rhizobox and PETIS imaging experiment. (b) PETIS image data of ^{11}C distributions in roots and (c) the rhizosphere soil.

P2-5 Project “Generation of Radioisotopes with Accelerator Neutrons

Leader : HASHIMOTO Kazuyuki

In our project, we have developed the production of medical radioisotopes (RI) for cancer diagnosis and therapy such as ^{99}Mo/^{99m}Tc, ^{90}Y, ^{47}Sc, ^{64}Cu, and ^{67}Cu using fast neutrons from a cyclotron accelerator. The neutrons were obtained by irradiating 40-50 MeV deuterons to beryllium or carbon. A separation and purification method of aimed radioisotope from the target materials and radioactive impurities has also been developed. We also investigate the production of medical RI such as ^{211}At and $^{95, 96}$Tc by the tandem accelerator in Tokai (Japan Atomic Energy Agency). Aiming to build a domestic production system of medical RIs using accelerator driven neutrons, we have begun to develop innovative medical RI production facilities.

Development of innovative medical radioisotope production facilities [1]

A new project “Deuteron Accelerator for Theranostics mEdicine (DATE) project” started in 2020 in collaboration with Cyclotron and Radioisotope Center (CYRIC) at Tohoku University, Sumitomo Heavy Industries, Ltd and Chiyoda Technol Corporation. The main aim of this project is to install a negative deuteron ion source and a stripper foil in the existing AVF cyclotron of Tohoku University to accelerate the deuteron beam of 25-40 MeV with an intensity of 100 μA. By so doing, innovative medical radioisotope production facilities (an irradiation system by accelerator neutrons, a transport system of irradiated samples and radioisotope separation system) can be achieved within 2 years. The deuteron beam intensity will be twenty-times stronger than the currently available beam intensity of 5 μA, but only one-twentieth of that, which will be obtained at the new system proposed for the Generation of Radioisotopes with Accelerator Neutrons by Deuterons (GRAND) [2]. These facilities will produce large quantities of copper-64 ($T_{1/2}$= 12.7 h, ^{64}Zn(n,p)^{64}Cu) for diagnosis and copper-67 ($T_{1/2}$= 61.9 h, ^{68}Zn(n,np/d)^{67}Cu) for therapy, which can be used as radiopharmaceuticals for personalized medicine, and contribute to the development of new radiopharmaceuticals. This project is a part of Program on Open Innovation Platform with Enterprises, Research Institute and Academia (OPERA).

Separation of astatine from irradiated lead targets based on dry distillation in a glass test tube [3]

In general, the ^{211}At radionuclide, which is a prospective candidate for utilization in targeted alpha therapy, is produced via the ^{208}Bi(^{4}He,2n)^{211}At reaction. We proposed that complementary and unique production routes of astatine were obtained by ^{7}Li ion beams [4]. The ^{nat}Pb(^{7}Li,xn)$^{207-210}$At reaction provides gamma emitters of astatine. One of the gamma emitters, ^{210}At is unsuitable for medical use due to its high radiotoxicity, but suitable for fundamental studies owing to the convenience of gamma-ray detection. To use astatine radionuclides produced in the ^{nat}Pb(^{7}Li,xn)$^{207-210}$At reaction, we developed a procedure for the preparation of no-carrier-added astatine tracer solutions based on dry distillation in a glass test tube [4, 5]. The procedure was simple and readily conducted without specific apparatuses in a conventional laboratory. In this work, we aim to study optimized conditions of the separation of astatine from the lead target by dry distillation.

The production of astatine radionuclide was carried out by using 60 MeV ^{7}Li^{3+} ions supplied from the JAEA tandem accelerator. The beam current of 80–200 nA was employed during the irradiation for 0.5–2.0 h. Dry distillation was performed for 15 min in a glass test tube (length 1 80 mm; inner diameter 16 mm) with an electric furnace at 650 ℃, as described in [3,5]. The amounts of radioactivity in the lead target were 90–220 and 31–140 kBq for ^{210}At and ^{209}At, respectively. Two cadmium-zinc-tellurium (CZT) gamma-ray spectrometers measured astatine radioactivity to study the heating time required to separate astatine from the irradiated lead target as well as radioactivity distributions in the glass test tube after dry distillation. The temperature of the outer wall of the glass test tube were measured with two thermocouples.

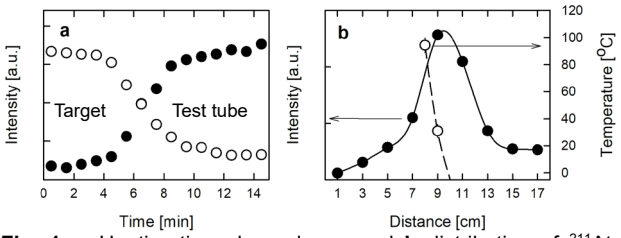

Fig. 1. a Heating-time dependence and **b** distribution of ^{211}At, radioactivity produced via ^{nat}Pb(^{7}Li,xn)$^{207-210}$At and temperature across the length of the test tube in the dry distillation.

Results in a dry distillation trial are shown in Fig. 1. Dependence of astatine radioactivity on heating time at the target position (open circle) and the portion near the test tube opening (solid circle) are shown in Fig. 1a. This shows that the lead target conducted heat and melted in ~4 min, and then astatine escaped from melted lead and rapidly transport to the test tube opening in ~10 min. Fig.1.b shows distribution of astatine radioactivity (solid circle and line) and temperatures (open circle and dashed line). Cooling the 10–14 cm portion at –5 ℃ with a thermoelectric cooler provided a large temperature gradient from 650 ℃ to –5 ℃ in the range of 3–10 cm as well as an effective adsorption of astatine at ~9.5 cm. The adsorption temperature of astatine on the glass was estimated at 20 ℃ from the temperature at the peak of astatine radioactivity distribution.

The obtained adsorption temperature was compared with the reported data owing to fundamental interest of volatile astatine species [3].

References

[1] Press release of CYRIC at Tohoku University and QST on October 19, 2020.
[2] Y. Nagai *et al.,* J. Phys. Soc. Jpn. **82**, 064201 (2013).
[3] I. Nishinaka *et al.*, J. Radioanal. Nucl. Chem. **327**, 869 (2021).
[4] I. Nishinaka *et al.*, J. Radioanal. Nucl. Chem. **304**, 1077 (2015).
[5] I. Nishinaka *et al.*, J. Radioanal. Nucl. Chem. **326**, 743 (2020).

Part Ⅰ

3. Advanced Quantum-Beam Technology

P3-1 Project “LCS Gamma-ray”

Leader : HAJIMA Ryoichi

The research objective of LCS Gamma-ray Research Project is developing the technologies of high-brilliance γ-ray generation and exploring its scientific and industrial applications such as nuclear physics, nuclear astrophysics and non-destructive measurement of nuclear material. The γ-ray source is based on laser Compton scattering (LCS), which enables one to generate energy-tunable mono-energetic γ-rays. In the research project, we are developing critical components for electron accelerators to achieve small-emittance and high-average current beams, γ-ray optics and a Monte Carlo simulation code.

Bandwidth of a Compton radiation source with an electron beam of asymmetric emittance [1,2]

Compton scattered radiation sources have been utilized in a broad range of experiments from fundamental science to industrial applications for their unique features, the generation of energy-tunable, nearly monoenergetic polarized photon beams. In the Compton radiation sources, the radiation bandwidth can be controlled by a collimator to restrict the scattering angle, but the bandwidth is also affected by the emittance and energy spread of the electron beam. In this study, we discussed collimator optimization to obtain narrow-band radiation from a Compton source with an electron beam having asymmetric emittance in the horizontal and vertical planes. A Monte Carlo simulation code based on Geant4 has been developed and used to compare circular and rectangular collimators for shaping the radiation spectrum of Compton sources. The developed code was benchmarked with CAIN, a Monte Carlo code to calculate interactions of high-energy electrons, positrons and photons including Compton scattering. Figure 1 shows Compton radiation spectra calculated by Geant4 and CAIN for the collision of 1-GeV electrons and 10-μm laser photons. Each plot contains 6 spectra corresponding to different collimator settings: no collimator, collimators with opening angles of 1 mrad, 0.5 mrad, 0.3 mrad, 0.1 mrad and 0.03 mrad. The results of Geant4 simulations are consistent with the results of CAIN.

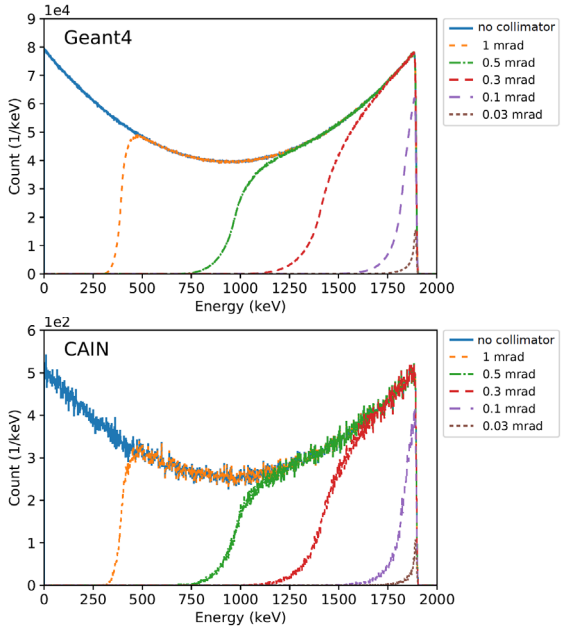

Fig. 1. Radiation spectra calculated by Geant4 and CAIN. Each plot contains 6 spectra corresponding to different collimator settings: no collimator, collimators with opening angles of 1 mrad, 0.5 mrad, 0.3 mrad, 0.1 mrad and 0.03 mrad.

Utilizing the developed code, we performed collimator optimization for the Compton radiation sources at the NewSUBARU operated for 1-MeV gamma beam generation, in which the electron beam emittance is asymmetric in the horizontal and vertical planes. Figure 2 shows calculated radiation spectra for a circular collimator and a rectangular collimator with an aspect ratio of 5. We can compare two specific cases with similar areas: a circular collimator of 0.5 mrad (green curve) in Fig. 2(a) and a rectangular collimator of 1 × 0.2 mrad (orange curve) in Fig. 2(b). Two cases have the same spectral density at the maximum energy, but the spectral shapes are different. The ratio of collimated photons with respect to the incident photons is 47% and 36%, respectively. The latter case benefits physics applications of the gamma-ray beam for a narrower FWHM and a smaller number of collimated photons with keeping the spectral density at the maximum energy. The longer tail in the energy region below 500 keV seen in the latter case is less of a practical concern, because background signals arising from the low-energy gamma-ray photons can be efficiently reduced by shielding the detector with a lead sheet of a few millimeters.

In conclusion, it has been suggested that a rectangular collimator with an optimum dimension shows excellent performance in the spectral shaping, elimination of the low-energy background with keeping the peak spectral density.

Selective Isotope CT Imaging Based on Nuclear Resonance Fluorescence Transmission Method [3]

In this study, selective isotope CT imaging based on nuclear resonance fluorescence (NRF-CT) was demonstrated for a sample where two different isotope-

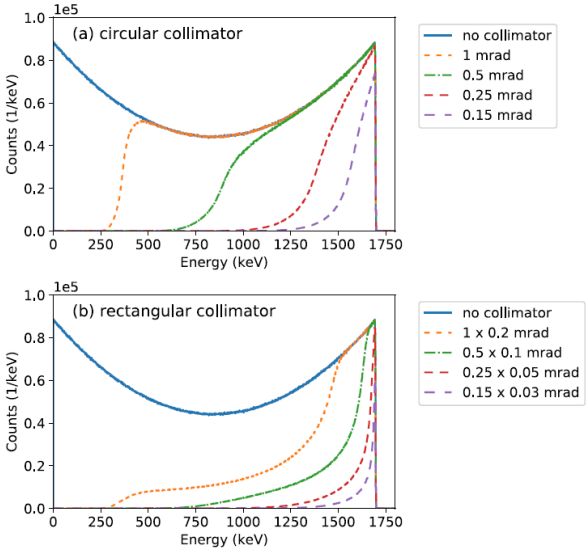

Fig. 2. Calculated radiation spectra for (a) a circular collimator and (b) a rectangular collimator with an aspect ratio of 5.

enriched rods (^{206}Pb in purity >93.3% and ^{208}Pb in purity >97.8%) were installed in a thick aluminum holder. Since the isotope rods have an approximately the same atomic composition, the rods cannot be distinguished by the standard CT technique based on photon attenuation measurement.

For the selective isotope CT imaging, we employed a “transmission method”, in which a gamma-ray beam passing through a sample for the measurement is transported to the second target, a witness target, which includes the same isotope of interest as shown in Fig. 3 The isotopic abundance in the sample can be evaluated from the NRF yield of the witness target, because the NRF yield is affected by the resonance absorption in the sample.

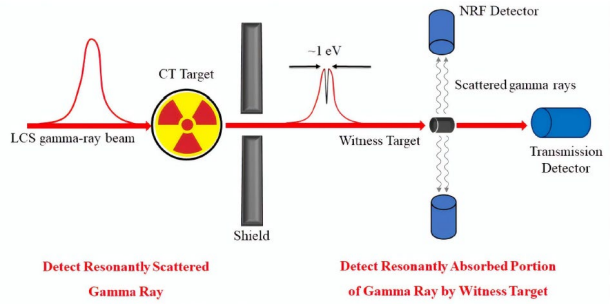

Fig. 3. Geometry of the NRF transmission method.

Figure 4(a) depicts the geometry of the sample, while Fig. 4(b) shows the reconstructed image of the OFF-resonance attenuation measurement. The figure clearly shows the positions of the ^{208}Pb and ^{206}Pb rods but it was practically impossible to distinguish between these two isotopes. Fig. 4(c) shows the distribution of the ON-resonance gamma-ray attenuation and Fig. 4(d) shows the distribution of the NRF attenuation induced only by the ^{208}Pb isotope (pure NRF). In the reconstructed image, the ^{206}Pb rod that is marginally visible in Fig.4(c) is not visible in Fig. 4(d), while the ^{208}Pb rod can be clearly observed.

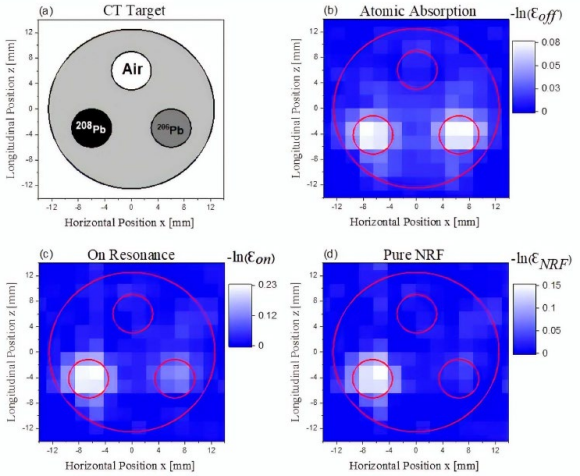

Fig. 4. (a) Geometry of the CT target. Reconstructed CT images of (b) atomic, (c) ON-resonance, and (d) pure NRF.

Record high extraction efficiency of free electron laser oscillator [4]

The highest extraction efficiency (9.4%) of a free electron laser (FEL) oscillator has been achieved at the midinfrared FEL facility of Kyoto University. Because of the interaction between the electron beam and FEL electromagnetic field, a maximum electron energy decrease of 16% was observed. The measured energy decrease was consistent with the measured FEL spectrum. An FEL micropulse energy of ~100 μJ with the expected few-cycle pulse duration at a wavelength of 11 μm was observed.

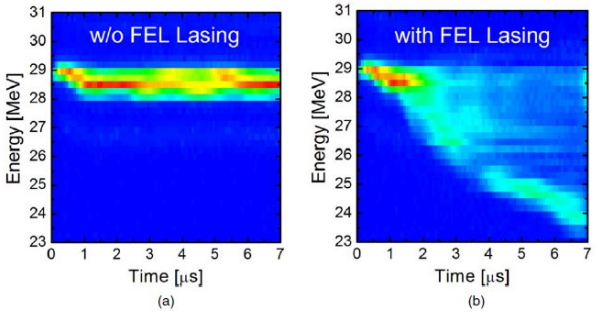

Fig. 5. The measured evolution of the energy distribution in a macropulse. (a) Without FEL lasing. (b) With FEL lasing

High-efficiency lasing was achieved by introducing the dynamic cavity desynchronization (DCD) method. With the DCD method, we can switch the FEL lasing mode from the high-gain, low saturation mode to the low-gain, high-saturation mode within a macropulse. The low-gain, high-saturation mode corresponds to superradiant FEL lasing under perfect synchronization. The energy evolutions of the electron bunch in a macropulse with and without FEL lasing are shown in Fig. 5. Clearly, a large fraction of the electrons in bunches are greatly decelerated in the latter part of the macropulse. The maximum energy decrease was 16%. From the measured result of energy evolution, the average energy of the electron bunch at each moment in the macropulse can be calculated. The average energy of the electron bunch was gradually reduced from 28.5 to 25.9 MeV, which corresponds to the extraction efficiency of 9.4% as shown in Fig. 6.

This is the world’s highest recorded extraction efficiency observed in an FEL oscillator. This result is an important milestone for the high-extraction-efficiency FEL oscillator and will contribute to the strong-field physics of atoms and molecules.

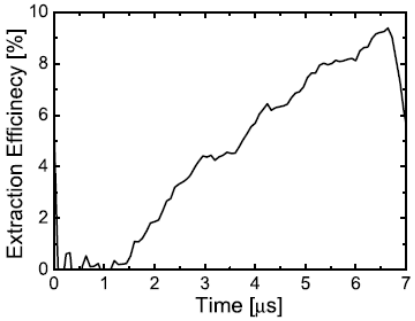

Fig. 6. The extraction efficiency of the FEL evaluated from the results shown in Fig.5.

References

[1] R. Hajima, Nucl. Instrum. Meth. Phys. Res. A **985**, 164655 (2021).
[2] R. Hajima, Proc. 17th Annual Meeting of Particle Accelerator Society of Japan, Sept. 2-4, 2020, Online Virtual Conference, 724 (2020).,
[3] K. Ali et al., IEEE Trans. Nucl. Sci. **67**, 1976 (2020).
[4] H. Zen et al., Appl. Phys. Exp. **13**, 102007 (2020).

P3-2 Beam Engineering Section

Section Manager : ISHII Yasuyuki

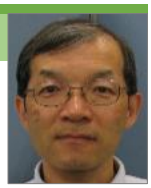

The research objectives in our section are development of various accelerator-related-techniques including ion-beam-irradiation-techniques and ion-beam-analyses. Each member has been engaged in individual research more than one. Recent remarkable studies are shown as follows; the first article is refractive index change and thermo-optic effect in polydimethylsiloxane nanocomposites with oxide nanoparticles induced by proton beam writing, and the second one is delivery and effectiveness of carboplatin via targeted delivery compared to passive accumulation of intravenously injected particles releasing carboplatin upon irradiation. {1-32, 1-33, 2-25~29, 3-02~06, 3-08~16 in Part II}

Refractive index change and thermo-optic effect in polydimethylsiloxane nanocomposites with oxide nanoparticles induced by proton beam writing [1]

Proton beam writing (PBW) is a direct writing technique of waveguides in various polymeric materials such as polydimethylsiloxane (PDMS) and polymethylmethacrylate (PMMA). We demonstrated optical switching by a Mach-Zehnder interferometer embedded in these polymer optical waveguides using thermo-optic (TO) effects. The advantage is to use the nanocomposite materials for transparent, high refractive index materials for optical applications with PBW. Inorganic/organic hybrid materials can combine the light weight and cost-effective features of the polymeric component as high refractive index materials. The TiO_2 nanocomposite is one of the promising candidates to achieve high refractive index and maintain high transparency, a high refractive index (n ~ 2.45 and 2.7 for anatase and rutile, respectively) and a very low absorption coefficient in the visible range. The TiO_2/PDMS composite has been also studied for photocatalytic activity under UV irradiation to realize self cleaning surface and microfluidic photocatalytic device.

In Fig. 1, we show the near field patterns observed at the output end of waveguides at two different angles (a) and (b). With increasing width of optical waveguides, we observed a transition from single-mode (1) to multi-mode waveguides (2) and (3) for the TiO_2/PDMS nanocomposites.

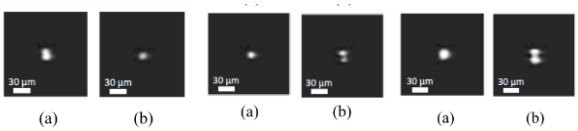

Fig. 1. Near field patterns of output end of waveguides.

Refractive index can be controlled by varied concentration of TiO_2. For low proton fluence of less than 100 nC/mm^2, the refractive index has increased due to PDMS compaction. Optical waveguides were written on the TiO_2/PDMS nanocomposite by PBW and the waveguide mode was changed from single- to multi-mode with increasing width around 10 μm.

Delivery and effectiveness of carboplatin via targeted delivery compared to passive accumulation of intravenously injected particles releasing carboplatin upon irradiation [2]

Radiosensitive particles that release their core contents in response to radiation using alginate polymerized with Fe^{2+} and hyaluronic acid have previously been developed. Radiation causes conversion of hyaluronic acid into acetyl-glucosamine, whereas alginate-Fe^{2+} is depolymerized, changing Fe^{2+} to Fe^{3+}. Thus, the microparticles release their core contents in response to radiation.

To treat tumors in deep-sited organs, radiation-sensitive particles containing a platinum-based anticancer drug (carboplatin) were refined in the order of nanometers. Then, the nanoparticles were intravenously (i.v.) injected into the tail vein of mice, and the efficacy of this method at accumulating nanoparticles in the tumor was evaluated. Finally, the antitumor effect and adverse effects of the anticancer drug administered after irradiation in vivo in C3He/N mice were tested.

In this study, micro-PIXE camera, imaging and analysis was used to measure trace elements in nanoparticles. This image was used in observing the kinetics of nanoparticles when they were i.v. injected into mice. In the irradiated nanoparticle, three types of nanoparticles were observed: Type I: no observable morphological changes (Fig. 2(A)); type II: release of the liquid core with detectable contour of the microcapsules; and type III: release of the liquid core with no detectable contour of the microcapsules (Fig. 2(C)). The type I nanoparticles were considered to not be ruptured. Type II and III nanoparticles were considered to be ruptured. From the relationship between the dose and the bursting rate of the capsules, a significant rise in burst rate was observed with increasing radiation dose. The maximum rupturing rate was 67% at 40 Gy irradiation, but the difference between the bursting rate at 30 and 40 Gy was not significant.

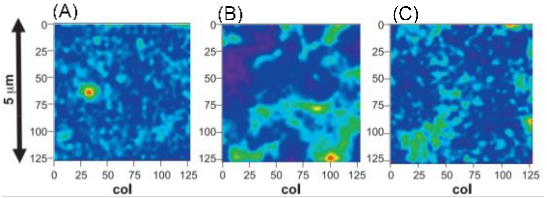

Fig. 2. Distribution images of platinum as carboplatin by micro-PIXE camera.

By performing this study including the results obtained by the micro-PIXE, we succeeded in refining radiation-sensitive particles containing a platinum-based anticancer drug in the order of nanometers, which resulted in increased accumulation of particles to tumor and antitumor effect as well as reduced adverse effect of carboplatin, under intravenous injection of particles. {2-27}

References

[1] Y. Kaneko *et al*., Nucl. Instrum. Meth. Phys. Res. B **459**, 94 (2019).
[2] T. Segawa *et al*., Radiat. Res. **193**, 263 (2020).

Part Ⅱ

Part Ⅱ

1. Materials Science

1 - 01 Development of gas permselective membranes by radiation-induced graft polymerization into ion-beam irradiated polymer films II

S. Hasegawa, A. Hiroki, S. Sawada and Y. Maekawa

Department of Advanced Functional Material Research, TARRI, QST

Separation and purification of gas molecules with similar physical and chemical properties are an important matter in industry. Since current systems for the gas separation and purification accompanies a large energy loss, permselective membranes are required to reduce the energy loss [1].

Radiation-induced graft polymerization is a useful technique for introducing new functional polymers into polymer substrates. We previously reported that the hydrogen permselective membranes were prepared by the graft polymerization with γ-irradiated polyvinylidene fluoride films [2]. On the other hand, when polymer films are irradiated with heavy ion beam instead of γ-rays, radicals are produced in the latent track. The graft polymerization of vinyl monomers proceeds from the radicals, generated in the latent track to produce the perpendicularly aligned cylindrical graft-polymer region with several hundred nm diameter. In this work, we propose development of gas permselective membranes by the combination of the ion-beam irradiation and the graft polymerization (Fig. 1).

Ethylene tetrafluoroethylene copolymer (ETFE) films (AGC Inc. 25 μm thickness) were irradiated with 560 MeV Xe ions ($^{129}Xe^{26+}$) at a fluence of 3×10^8 ions/cm^2 at TIARA. The irradiated ETFE films were immersed into vinylethoxysilane (VESI) or 3-methacryloxypropylmethyl diethoxysilane (3-MPMDS) solution (VESI or 3-MPMDS 50 vol% in solvent) at 60 °C to obtain VESI- or 3-MPMDS-grafted ETFE (Table 1). The obtained VESI- and 3-MPMDS-grafted ETFE films showed grafting degrees (GDs) of 0.9 and 2.7%, respectively (Table 1). Permeabilities of hydrogen (H_2) and methane gas (CH_4) through the grafted membranes were conducted by a differential pressure method.

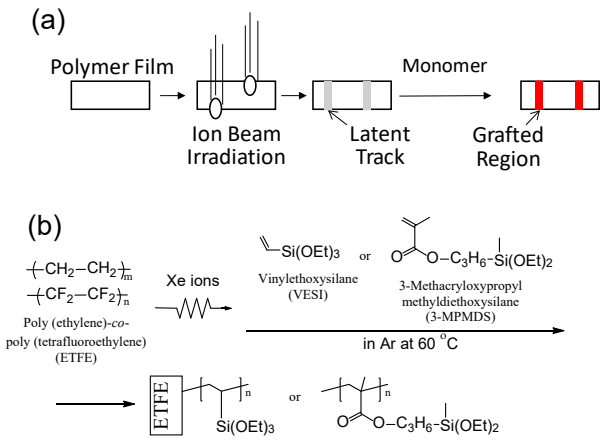

Fig. 1. Synthetic illustration (a) and chemical scheme (b) of gas permselective films prepared by the combination of ion-beam irradiation and graft polymerization.

The H_2 and CH_4 permeability through the original ETFE film was quite low (0.8×10^{-11} and 0.1×10^{-11} mol/sec·m^2·Pa). The H_2 and CH_4 permeabilities of the ion-beam irradiated (non-grafted) ETFE film showed 4.1×10^{-9} and 3.9×10^{-9} mol/sec·m^2·Pa, which are 513 and 3900 times higher than the original ETFE film, respectively. On the other hand, VESI-*g*-ETFE film (GD:0.9%) showed lower CH_4 gas permeability (1.0×10^{-9} mol/sec·m^2·Pa), and the selective permeation ratio (H_2/CH_4) was 4.5. The H_2 and CH_4 permeabilities of the 3-MPMDS-g-ETFE film (GD:2.7%) were 119×10^{-9} and 53×10^{-9} mol/sec·m^2·Pa, respectively, with a H_2/CH_4 ratio of 2.2. It was found that the gas permeability as well as gas permselectivity were improved by the grafting on the ETFE films irradiated with Xe ions. Taking accounts of the diameters of hydrogen and methane (0.28 nm and 0.37 nm) [3], the H_2 gas permselectivity of these grafted ETFE films should be induced by an affinity effect originated from the interaction between the graft chains and the gas molecule rather than a molecular sieve effect.

Table 1
GD, gas permeability, and H_2/CH_4 ratio of ion-beam irradiated and grafted ETFE films.

Grafted chain	Ion Beam Irradition*	GD (%)	Gas permeability ($\times 10^{-9}$ mol/sec・m^2・Pa)		H_2/CH_4
			H_2	CH_4	
-	-	-	0.008	0.001	8
-	○	-	4.1	3.9	1.0
VESI	○	0.9	4.5	1.0	4.5
3-MPMDS	○	2.7	119	53	2.2

Acknowledgments

This work was supported by the Japan Society for the Promotion of Science (JSPS) KAKENHI Grant Number 16K06785.

References

[1] R.W. Baker *et al.*, Ind. Eng. Chem. Res. **41**, 1393 (2002).
[2] S. Hasegawa *et al.*, Quantum Beam Sci. **4**, 23 (2020).
[3] H. Kuno *et al.*, The Piping Engineering **54**, 28 (2012).

1 - 02 Modification of polymeric materials by quantum beam irradiation

A. Idesaki, A. Hiroki, S. Hasegawa and Y. Maekawa

Department of Advanced Functional Materials Research, TARRI, QST

The Basic Hydrogen Strategy was formulated by Hydrogen and Fuel Cell Strategy Council in March 2019. In the Basic Hydrogen Strategy, efforts for popularization of fuel cell vehicles (FCVs) and hydrogen station (HRSs) are declared as one of the most important issues in the field of mobilities. The main components installed in the FCVs are fuel cells and high pressure-hydrogen tanks so that the costs of them should be reduced in order to realize the popularization of FCVs and HRSs. In the case of the high pressure-hydrogen tanks, the cost of ¥700,000 for one current tank is required to be reduced to around ¥300,000. The common high pressure-hydrogen tank for FCVs, type IV tank, is composed of plastic liners and carbon fiber reinforced plastics (CFRPs). It is effective to reduce the amount of expensive carbon fiber in order to realize the low cost-tank, therefore, novel high performance-polymeric materials which can be alternative to the CFRPs have been strongly desired.

The materials in the type IV tank are exposed repeatedly to severe conditions such as high pressure of 70 MPa, wide temperature range of -40 °C to 85 °C. Especially, the materials must retain sufficient durability against the high pressure-hydrogen; the materials with low hydrogen gas permeability and high mechanical properties are desirable. Professor Nishimura at Kyushu University has summarized relationship between hydrogen gas permeability and elongation at break for various polymeric materials as shown in Fig. 1. Although the polymeric materials should maintain the capability of elastic deformation against the repetitive loading and unloading in the practical use, the elongation can be one of the indicators for the screening of materials. Hard polyamides, which exhibit low hydrogen gas permeability and low elongation at break, cannot afford large deformation. Polyethylenes, which exhibit high elongation at break, can afford large deformation, however, cannot suppress the hydrogen gas permeation. According to the relationship as shown in Fig. 1, our goal for development of polymeric materials with low hydrogen gas permeability and high mechanical properties is to achieve the “TARGET ZONE”. We have examined introduction of crosslinking structure into the polymeric materials, which is expected to reduce the hydrogen gas permeability and enhance the mechanical properties, utilizing quantum beam irradiation technique. In this work, polyethylenes were irradiated by ^{60}Co gamma-rays up to dose of 1000 kGy under vacuum at ambient temperature. After the irradiation, the gel fraction measurements, tensile tests, exposure tests for high pressure-hydrogen gas, and so on, were conducted. It was found that the gel fraction increased rapidly in the dose range of 10-100 kGy due to the crosslinking to produce insoluble component. Other measurements have been under conducting. These data will be summarized as a database and we will discuss the guideline for development of high pressure-hydrogen-resistant polymeric materials.

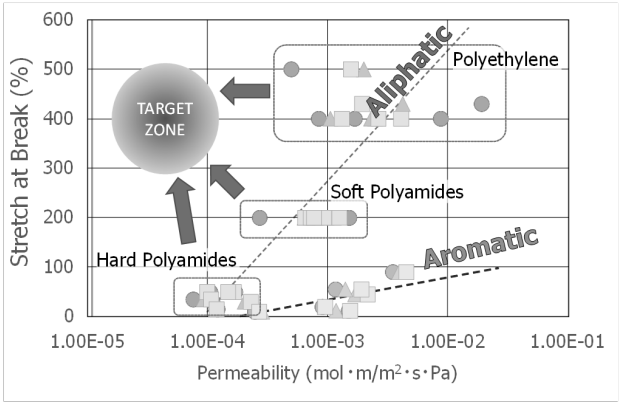

Fig. 1. Relationship between H_2 permeability and tensile property for various polymeric materials.

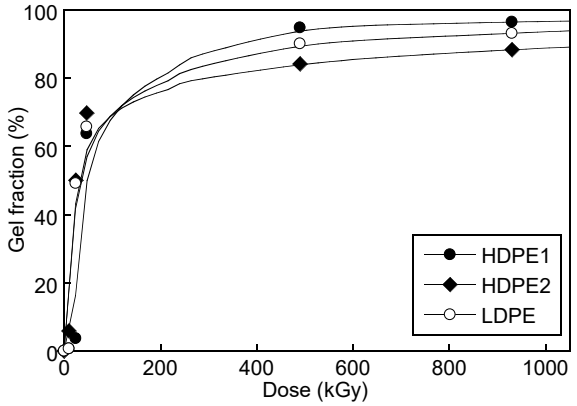

Fig. 2. Change of gel fraction of polyethylene after gamma-ray irradiation.

Acknowledgments

This work is based on results obtained from a project, JPNP20003, commissioned by the New Energy and Industrial Technology Development Organization (NEDO). This is a collaboration work with Kyushu University (Prof. Shin Nishimura) and The University of Shiga Prefecture (Prof. Katsuhisa Tokumitsu).

1 - 03 Synthesis and properties of anion conducting solid polymer electrolyte membranes prepared by radiation-induced grafting

K. Yoshimura[a)], H. Takamatsu[a,b)], Y. Zhao[a)], A. Hiroki[a)] and Y. Maekawa[a)]

[a)]Department of Advanced Functional Materials Research, TARRI, QST
[b)]Graduate School of Science and Technology, Gunma University

Anion conducting solid polymer electrolyte membranes (AEMs) have been established as a key component in energy conversion and storage systems including fuel cells, redox flow batteries, and rechargeable zinc-air batteries [1]. Even though an alkaline fuel cell is significantly attractive because of non-precious metals used as active catalysts, there is no commercially available AEMs due to severe alkaline operating condition [2].

Recently, we have developed poly(ethylene-co-tetrafluoroethylene) (ETFE) based *N*-vinylimidazolium-type AEMs by radiation-induced grafting. During this research, it has been found that the copolymerization of styrene (St) affects the nanoscale phase separation of AEMs and increases alkaline stability; the AEMs degraded via the initial *β*-elimination and following ring opening reactions of the imidazolium unit. In this time, we synthesized the AEM based on a co-poly(2-(4-ethenylphenyl)-1-propyl-1-H-imidazole (2StIm)/St) grafts to exclude *β*-hydrogen from the structure and suppress ring opening reactions.

The ETFE films were irradiated with a ^{60}Co γ-ray source (QST Takasaki) at room temperature in argon atmosphere with an absorption dose of 50 kGy. The pre-irradiated ETFE films were immediately immersed into the argon-purged monomer solution consisting of a mixture of 2StIm/styrene (50/50 to 95/5 vol. ratio) in 1,4-dioxane (50 vol%). The imidazole groups in the grafted-ETFE were *N*-alkylated using propyl iodide. The resultant AEMs (an iodide form) were immersed in 1 M HCl solution, followed by 1 M KOH solution at room temperature for 16 h to give the OH^- forms of the AEMs, as shown in Scheme 1.

The ionic conductivity was measured by two-point probe AC impedance spectroscopy at 100% relative humidity in N_2-purged deionized water. The ion exchange capacity (IEC) was measured using standard back titration methods.

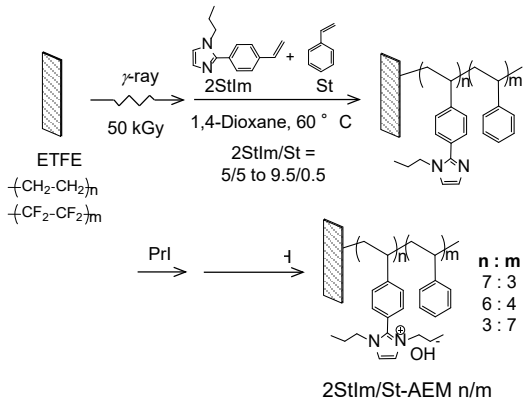

Scheme 1. Preparation scheme for 2StIm/St AEMs.

Since IEC was targeted to be ~0.9 mmol/g, the total number density of imidazolium groups is expected to be same for all AEMs. The AEMs showed almost same ion conductivities (46 to 60 mS/cm). To examine the effects of the hydrophobicity of graft-copolymers on AEMs, alkaline durability tests were performed in 1M KOH at 80 ºC. The degradation rate of anionic groups in AEMs increased the order of AEM 7/3 > AEM 6/4 > AEM 3/7. This indicates that the alkaline stability of the AEMs decreased with increasing of the amount of St (Fig.1). A reverse relationship that higher hydrophobicity results in lower alkaline durability was found.

As a result of the small-angle neutron scattering, the size of polymer micelles consisting of imidazolium cation increased with the increase of the St ratio. This increase in micelle size apparently made the cation more exposed to alkaline solution, resulting in acceleration of ring-opening reaction of the imidazolium ring (Fig. 2).

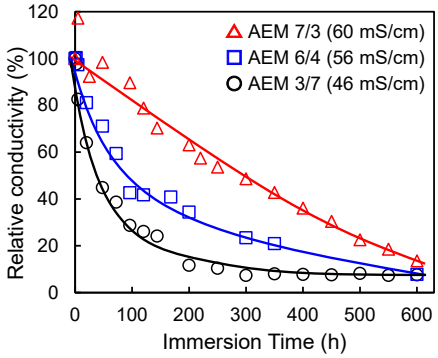

Fig. 1. The AEM conductivities after being immersed in 1 M KOH at 80 °C.

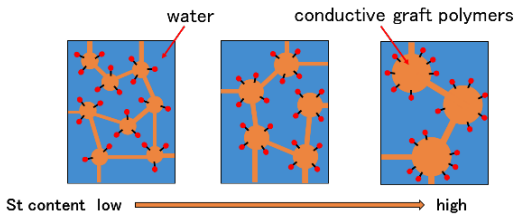

Fig. 2. Schematic illustrations of the morphology of 2StIm/St AEMs.

References

[1] N. Sun *et al.*, J. Membr. Sci. **605**, 118113 (2020).
[2] T.B. Ferriday and P. H. Middleton, Int. J. Hydrogen Energy **46**, 18489 (2021).

1 - 04 Effects of activation methods on the durability of carbon electrodes for vanadium redox flow battery

R. Obata[a,b], H. Doki[a], H. Ishitobi[a], H. Okazaki[b], T. Yamaki[b] H. Koshikawa[b], S. Yamamoto[b] and N. Nakagawa[a]

[a]Graduate School of Science and Technology, Gunma University
[b]Department of Advanced Functional Materials Research, TARRI, QST

Introduction

The vanadium redox flow battery (VRFB) is one of the energy storage systems suitable for the use of renewable energy applications. VRFBs can be designed with independent power and capacity, and the state of charge can be accurately measured. However, it has the disadvantage of lower battery current due to high internal resistance such as the kinetic resistance. Previous studies have reported that surface activation of the electrode material can improve the electrochemical activity [1]. Therefore, we have been conducting electron irradiation to carbon cloth (CC) as an electrode material. This treatment can add oxygen functional groups (OFGs) to the surface without surface etching. In this study, we evaluated the durability of electron-beam irradiated CC in comparison with air-oxidized CC. Also, change in the surface elemental fraction before and after the charge-discharge was clarified using X-ray photoelectron spectroscopy (XPS).

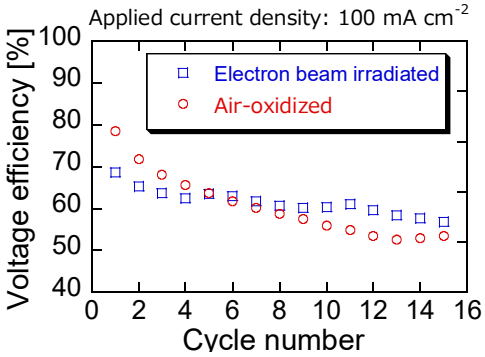

Fig. 1. Voltage efficiency of EB-irradiated CC and Air-oxidized CC.

Experimental

As the electrode material, 0.55 mm-thick CC (Nihon carbon Co.) was irradiated with electron beams (EB) in an air atmosphere at an acceleration current of 10 mA at an irradiation dose of 8.34×10^{16} e cm^{-2} at 2 MeV. In comparison, the air-oxidized CC was prepared by heating under air in a muffle furnace at 500 °C for 3 h.

The CC electrode with an area of 3.24 cm^2 and Nafion117 as the electrolyte membrane is used as cell components. 1 M V ion in 3 M H_2SO_4 was used as the electrolyte, and flowed into the cell at 20 mL/min. A battery test system (PFK2011 Kikusui Electronics Co.) was used for the measurement, and 15 cycles were performed at a constant current of 100 mA cm^{-2}. The voltage efficiency (VE) was calculated in the same way at elsewhere [2].

XPS was performed using an X-ray photoelectron spectrometer PHI5000Versaprobe II (ULVAC PHI, Japan) to analyze the O *1s* spectra.

Results and discussion

Figure 1 shows the VE of EB-irradiated CC and Air-oxidized CC. Although the initial VE was higher for the air-oxidized CC, the EB-irradiated CC showed higher VE after

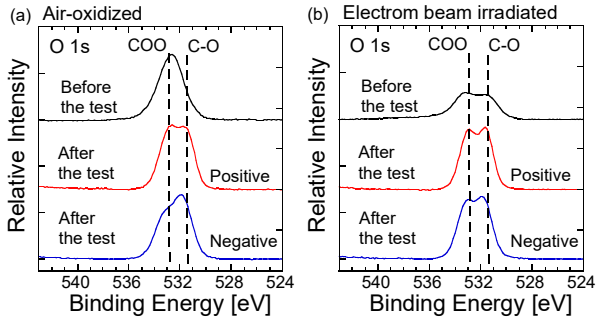

Fig. 2. O *1s* spectra of (a)Air-oxidized CC and (b)EB-irradiated CC.

the 5th cycle because the decay of efficiency was smaller for the EB-irradiated CC. Figure 2 shows the O *1s* spectra before and after the cycling test. In the air-oxidized CC, the peak shape changed significantly on the positive electrode after the cycling test. It is considered that the COO-bond is decomposed by the charge-discharge reaction. On the contrary, there is no significant change in the peak shape in EB-irradiated CC. It is clear that EB irradiation suppresses the decomposition of the OFGs by the charge-discharge reaction more than the air-oxidation. This is because, in air-oxidization, OFGs with low durability may be added with pores, in contrast, there are no surface etchings in EB irradiation, and stable OFGs may be added, which suppresses the decomposition by the electrochemical oxidation and reduction. In summary, EB-irradiated CC have stable OFGs those do not decompose easily and exhibit excellent durability.

Acknowledgments

The authors thank Ms. Chihiro Suzuki of QST for her help with the TEM observations. This research was supported by JSPS KAKENHI Grant Number JP18K14048. The authors appreciate this foundation.

References

[1] Z. He *et al.*, Carbon **127**, 297(2018).
[2] H. Ishitobi *et al.*, J. Electrochem. En. Conv. Stor. **17** 031001 (2020).

1 - 05 Formation of precious metal nanoparticles inside ion-track-etched capillaries formed in polyimide films

S. Yamamoto, H. Koshikawa, T. Taguchi, A. Idesaki, H. Okazaki and T. Yamaki

Department of Advanced Functional Materials Research, TARRI, QST

Aligned and high-aspect-ratio capillaries (diameter: several hundreds of nm, length: several tens of μm) containing nanoparticles of precious metals (e.g., Ag, Au) can be expected to be applied to plasmonic absorber materials in visible light region. Plasmonic absorbers have the ability to convert light energy into heat energy[1]. Aligned capillaries made of flexible films (e.g., polyimide) can allow unidirectional gas flows and act as filters. By adding to capillaries type plasmonic absorbers also catalytic qualities (e.g., Pt, Pd nanoparticles), it would be possible to apply them to gas-reforming materials. A key process in this context is the precipitation of homogeneous and highly dispersed precious metal nanoparticles inside the capillaries. Ion-track-etched capillaries created in polymer films by ion beam irradiation and chemical etching[2]. Precious metal nanoparticles can be obtained by precipitating them from a solution using ionizing radiations (e.g., high-energy electron beams, γ-rays)[3]. In our previous work, Pt nanoparticles inside heat-treated ion-track-etched polyimide capillaries was fabricated by these methods [4].

In this work, we demonstrated the preparation of ion-track-etched polyimide capillaries containing Pt, Ag and Au nanoparticles. Polyimide films (thickness: 25 μm) were irradiated with 350 MeV $^{129}Xe^{23+}$ ions at a fluence of 3×10^7 ions/cm^2 using an AVF cyclotron accelerator. The irradiated films were etched in a sodium hypochlorite (NaClO) aqueous solution to create the capillaries with diameters of ~500 nm. The films in an aqueous solution containing 0.5 mmol/L metal complexes (H_2PtCl_6, $AgNO_3$, $AuCl_4$) and 0.5 vol% ethanol (C_2H_5OH) were irradiated with 2 MeV electron beam of 500 kGy using a 2-MV electron accelerator. The nanoparticles in capillary inside were characterized by transmission electron microscope (TEM). Cross-sectional TEM samples were prepared with an ion slicer (IB-090600CIS, JEOL) and a ultramicrotome (UC6, Leica).

Figure 1 shows cross-sectional TEM image of ion-track-etched capillaries in the polyimide films which were precipitated (a) Pt, (b) Ag and (c) Au by the electron-beam radiation method. TEM observations confirmed the formation of Pt nanoparticles with isolated aggregates into ion-track-etched capillaries in polyimide films. The isolated aggregates were composed of Pt nanoparticles with sizes < 5 nm. Also, the formation of Ag and Au nanoparticles with sizes < 10 nm were confirmed. The results suggested that a combination of ion and electron beam irradiation techniques can be applied to the production of high aspect-ratio capillaries containing metal nanoparticles in flexible polymer films. In the next step, we will optimize the synthesis conditions (e.g., metal complexes concentration in aqueous solution, electron beam fluence) to form homogeneous and highly dispersed metal nanoparticle precipitation inside the capillaries for development of plasmonic absorbers materials.

Acknowledgments

This work was financially supported by JSPS KAKENHI Grant Number 18K04739. The authors thank Ms. Chihiro Suzuki for her help with the TEM observations.

References

[1] L. Zhou *et al*, Sci. Adv. **2**, e150127 (2016).
[2] H. Koshikawa *et al*, J. Membr. Sci. **327**, 182 (2009).
[3] J. Belloni, Catal. Today **113**, 141 (2006).
[4] S. Yamamoto *et al*, Quantum Beam Sci. **4**, 8 (2020).

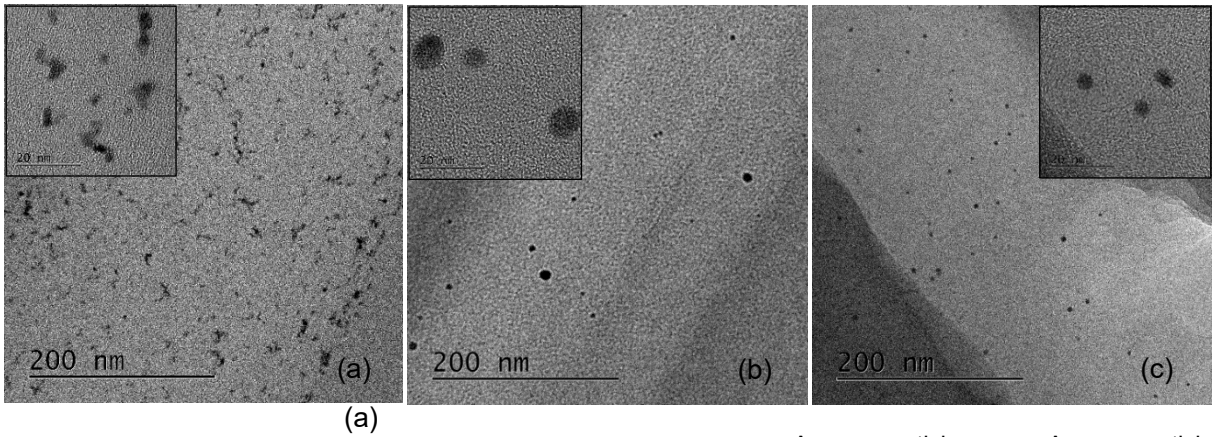

(a)

Fig. 1. Low- and high-magnification cross-sectional TEM images (a) Pt nanoparticles, (b) Ag nanoparticles and (c) Au nanoparticles formed into an ion-track-etched capillaries.

1 - 06 Utilization of ion implantation technique for introduction of Fe nanoparticles into a carbon precursor polymer (2)

A. Idesaki, S. Yamamoto, M. Sugimoto and T. Yamaki

Department of Advanced Functional Materials Research, TARRI, QST

Nitrogen (N)-doped carbon catalysts, which exhibit catalytic activity for an oxygen reduction reaction ($O_2 + 4H^+ + 4e^- \rightarrow 2H_2O$), are expected to be applied for the cathode in the fuel cells as non-precious metal catalysts. The N-doped carbon catalysts are generally synthesized by pyrolysis of mixtures of precursor polymers and metal compounds at 800-1000 °C in an inert atmosphere. In the pyrolysis process, metal nanoparticles (NPs) with size of 20-200 nm derived from the metal compounds act as a catalyst for the graphitization of the precursor polymers in the temperature range of 800-1000 °C; carbon atoms dissolve into the molten metal NPs and precipitate to form the graphitic structure. On the other hand, nitrogen atoms are eliminated during the pyrolysis above 700 °C that means simultaneous N-doping and graphitization are hard to be achieved in the conventional method. In order to synthesize the N-doped carbon catalysts with high performance, the pyrolysis temperature should be low as possible to achieve sufficient graphitization and N-doping simultaneously. The possible resolution for this problem is to introduce fine metal NPs in the precursor polymers because the finer metal NPs melt at lower temperature [1]. Thus, we have proposed the metal-ion implantation technique where 100 keV Fe^+ ions were implanted into a phenolic resin (PhR) [2]. We have reported that the particle size of Fe NPs after the heat treatment at 800°C was controlled in the range of 5-30 nm by the fluence of Fe^+ ions and that the smaller Fe NPs promoted the graphitization of the PhR. However, in this case, the distribution of Fe^+ was not uniform in the depth direction. In order to realize highly efficient graphitization of the PhR, it is important to control the depth distribution of Fe^+ as well as the particle size of Fe NPs. Then, we have examined multi energy-ion implantation in this work (see Fig.1). The PhR film was implanted by 40/60/100 keV Fe^+ sequentially to the total fluence of 1×10^{15} ions/cm^2 as same as the 100 keV-implantation. The implanted PhR film was immersed into methanol to remove non-implanted part, dried, and finally heat-treated at 800°C in N_2 atmosphere. Figure 2 shows depth profile of Fe in the PhR just after the implantation measured by transmission electron microscope-energy dispersive X-ray spectroscopy (TEM-EDS). The dotted line in the figure shows the result of calculation by SRIM2013 code. In the case of 100 keV-implantation, the distribution of Fe was similar to the calculation result. On the contrary, the intensity of Fe in the depth range of 40-70 nm was weak in the case of 40/60/100 keV-implantation comparing with the result of calculation. We have not been able to clarify the reason for this phenomenon, however, we can find a broader distribution of Fe in the depth direction in the case of 40/60/100 keV-implantation than that of 100 keV-implantation. After the heat treatment at 800°C, the average particle size of Fe NPs obtained with 40/60/100 keV-implantation was 16.5 ± 8.0 nm including the fine Fe NPs with the size of less than 5 nm. The introduced Fe NPs is smaller than that of 100 keV-implantation (18.5±6.3 nm, not including Fe NPs with the size of less than 5 nm). Furthermore, the Raman spectra indicated that the graphitization was promoted in the case of 40/60/100 keV-implantation. As a conclusion, it was found that the multi energy-ion implantation technique is useful for uniform introduction of fine Fe NPs and highly efficient graphitization of the PhR.

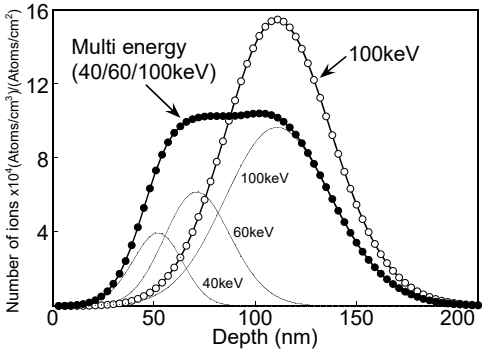

Fig. 1. Depth profile of Fe^+ in the PhR calculated by SRIM2013 code. The Fe^+ ions are introduced more uniformly in the depth direction by the multi energy-implantation than that of 100 keV-implantation.

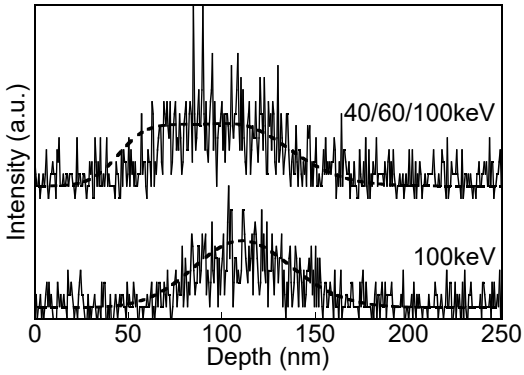

Fig. 2. Depth profile of Fe in the PhR just after the ion implantation measured by TEM-EDS.

Acknowledgments

This work was supported by JSPS KAKENHI Grant Number 18K11938.

References

[1] A. Moisala *et al.*, J. Phys.: Condens. Matter **15**, S3011 (2003).

[2] A. Idesaki *et al.*, Quantum Beam Sci. **4**, 11, (2020).

1 - 07 Ubiquitous organic molecule-based free-standing nanowires with ultra-high aspect ratios

K. Kamiya[a)], K. Kayama[a)], M. Nobuoka[a)], S. Sakaguchi[a)], T. Sakurai[a)], A. Idesaki[b)], H. Koshikawa[b)], M. Sugimoto[b)] and S. Seki[a)]

[a)]Department of Molecular Engineering, Graduate School of Engineering, Kyoto University
[b)]Department of Advanced Functional Materials Research, TARRI, QST

The critical dimension of nanostructures fabricated by top-down nanolithography techniques is approaching the true nano-sized regime (single-nm scale), and a variety of practical devices have been designed and targeted for production this decade. Planar devices fabricated by these protocols, however, are reaching the intrinsic limit of aggregation onto 2-dimensional planes because the critical dimension is comparable to the size of molecules; there is no room for further integration. A way to overcome this limit is the 3-dimensional integration of nanostructures, and such implementation has been initiated by a facile “piling up” superposition method based on 2D nanolithography techniques.

Nanopatterning not only of “soft” organic materials but also hard metal oxide/Si based materials has always had problems in its extension into 3D spaces, because the interaction between the structures, surfaces, and molecules becomes considerable enough in nanospace to deform the structures, even though such interactions are negligible or relatively small in the bulk state, as represented by statistical thermodynamics. This makes it hard to directly form nanostructures with aspect ratios over ~10 by conventional processing methods.

We have developed a unique technique to produce uniform 1-dimensional nanostructures with extremely high aspect ratios, borrowing from the technology used in cancer radiotherapy with high-energy charged particles. Previously, protein nanowires with aspect ratios of ~100-1000 were reported for the first time in 2014 [1]. Crosslinking reactions of protein molecules were the key processes used to confine the molecules in 1-dimensional cylindrical nanospace, and one single nanowire could be produced by a reaction induced by an atom. Unlike in the case of traditional nanolithography with “beams of photons/electrons” focused into a smaller area than the targeted size of the structure, the proposed method does not need this focus, because an atom is always a particle along its trajectory, releasing its energy for chemical reactions. Polymeric molecules are advantageous to amplify the effects of these chemical reactions; however, the size of molecules is equivalent to the size of nanostructures targeted in this decade.

To address these issues of dimensions, aspect, interactions, and molecules in the formation of nanostructures, herein we report an unprecedented protocol to produce standing 1D nanowire arrays with following features [2]:

1) Free-standing,
2) Single-nm radius,
3) Ultra-high aspect ratio over 100, and
4) Based on a wide variety of organic molecules.

As shown in the following figure, completely isolated, ultra-high aspect nanowires are free-standing on a substrate, and like mowed lawns, the perfect uniformity of the nanowire plexus clearly illustrates the high feasibility of the present protocol in terms of dimensional (size) control.

Two-component free-standing nanowires based on distinct molecules were also demonstrated to insert “one heterojunction in one nanowire,” of which the position was also perfectly under control.

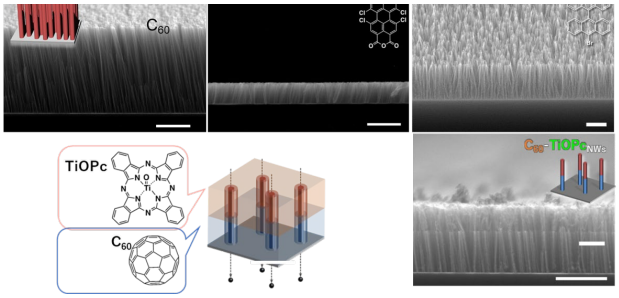

Fig. 1. A SEM image of free-standing nanowire plexus based on C_{60} nanowires formed by the present protocol and isolated by sublimation (top, left). Cross-sectional image of nanowire plexus prepared from 1,6,7,12-tetrachloro-3,4,9,10-perylenete-tracarboxylic dianhydride (PTCDA-Cl_4, top. center) and from 10,10’-dibromo-9,9’-bianthracene (top, right). Schematic illustration of double-segment nanowires (bottom, left-center). A SEM image of free-standing double-segment nanowires from C_{60} and PTCDA-Cl_4 (bottom, right).

Acknowledgments

This work was supported in part by a Grant-in-Aid for Transformative Research Areas (20H05862) from MEXT, Scientific Research (A) and (B) from JSPS. High-energy charged particle irradiation was carried out at the Takasaki Advanced Radiation Research Institute, QST under the Facility Sharing Program.

References

[1] M. Omichi *et al*., Nat. Commun. **5**, 3718 (2014).
[2] K. Kamiya *et al*., Nat. Commun. **12**, 4025 (2021).

1 - 08 Development of metal oxide-catalysts utilizing quantum beam irradiation technique

A. Idesaki and S. Yamamoto

Department of Advanced Functional Materials Research, TARRI, QST

According to the Basic Hydrogen Strategy formulated in March 2019, efforts for popularization of 800,000 fuel cell vehicles (FCVs) by 2030 are declared as one of the goals in the field of mobilities in Japan. In order to achieve this goal, the cost of polymer electrolyte fuel cells (PEFCs) for the FCVs should be reduced; the cost of about 20,000 yen/kW for the current PEFCs is required to be reduced to about 5,000 yen/kW. In the PEFCs, platinum of several tens grams is used as a catalyst to enhance the reaction at the cathode as shown in Fig. 1. Therefore, non-precious metal catalysts have been desired to reduce the cost of the PEFCs. An oxygen reduction reaction (ORR; $O_2 + 4H^+ + 4e^- \rightarrow 2H_2O$) occurs at the cathode in the PEFC. This ORR proceeds through production of some intermediates (*OOH, *O, *OH) as shown in Fig.1. The adsorption energy of the intermediates on the catalyst surface dominates the performance of the catalysts, therefore, appropriate adsorption energy of each intermediate should be controlled to realize the highest performance. However, theoretical calculation has revealed that the equilibrium potential (E^0 = 1.23 V vs. RHE) cannot be achieved in the case of platinum catalysts because the adsorption energy of the intermediates is independently uncontrollable on the platinum catalysts [1]. On the other hand, another theoretical calculation has predicted that titanium oxide (TiO_2) with oxygen defects and/or doped heteroatoms exhibit the possibility to realize the equilibrium potential of 1.23 V vs. RHE [2]. Additionally, similar possibility has been predicted for zirconium oxide (ZrO_2) with stable oxygen defects. These predictions suggest that non-precious metal catalyst for the cathode in the PEFCs would be realized by using metal oxides. As far, there is no reports on the metal oxides which exhibit the equilibrium potential for the ORR. Therefore, development of technique to produce metal oxides with the ideal catalytic performance is desired. Here, we propose the quantum beam irradiation technique as a method to form ideal catalytic sites in the metal oxides, utilizing the effects of knocking out, heteroatom doping, and so on. In this work, TiO_2 powder was irradiated by 2 MeV electron beam with dose of 100 MGy as maximum under vacuum at temperature range of room temperature to 500 °C. After the irradiation, it was found that the white TiO_2 powder was colored gray due to the oxygen defects. Other measurements such as ORR activity, X-ray diffraction (XRD) measurements, and so on, have been under conducting. We will investigate the possibility of quantum beam irradiation for development of metal oxide-catalysts. with the ideal catalytic performance.

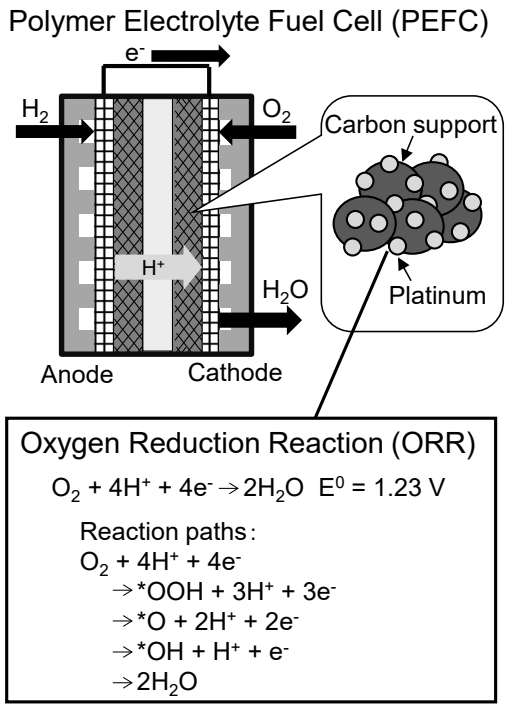

Fig. 1. Scheme of the polymer electrolyte fuel cell (PEFC) and oxygen reduction reaction (ORR) at the cathode.

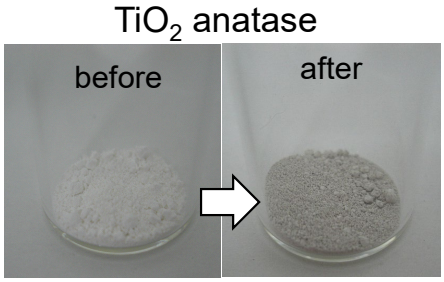

Fig. 2. TiO_2 sample before and after the electron beam irradiation under vacuum at 500 °C.

Acknowledgments

This work is based on results obtained from a project, JPNP20003, commissioned by the New Energy and Industrial Technology Development Organization (NEDO). This is a collaboration work with Fukuoka University, Chiba University, Osaka University, Kyushu University, Oita University, Kochi University of Technology, and Utsunomiya University.

References

[1] A. Kulkarni *et al.*, Chem. Rev. **118**, 2302 (2018).
[2] Y. Yamamoto *et al.*, J. Phys. Chem. C **123**, 19486 (2019).

1 - 09 Characterization of the irradiation defects produced by Au-ions in $GdBa_2Cu_3O_y$ superconducting tapes using a slow positron beam

T. Ozaki[a], A. Yabuuchi[b], H. Okazaki[c], H. Koshikawa[c], S. Yamamoto[c] and T. Yamaki[c]

[a] Department of Nanotechnology for Sustainable Energy, Kwansei Gakuin University
[b] Institute for Integrated Radiation and Nuclear Science, Kyoto University
[c] Department of Advanced Functional Materials Research, TARRI, QST

Introduction

The rare-earth (RE)-based cuprate superconductors, $REBa_2Cu_3O_y$ (REBCO), exhibits superconducting transition temperatures T_c with approximately 90 K and is expected to be useful for magnetic coils above the boiling point of liquid nitrogen (77.3 K). Critical current properties in magnetic fields are improved by introducing lattice defects using ion-irradiation techniques. Due to their high sensitivity to vacancies, positrons are useful for characterizing irradiation-induced defects. In this study, $GdBa_2Cu_3O_y$ (GdBCO) coated conductors (CCs), which were industrially produced superconducting tapes, were irradiated with Au ions at 2 or 10 MeV and probed using a slow positron beam.

Experiment

The GdBCO CCs were irradiated with 2 MeV Au^{2+} at fluences of 5.0×10^{11} and 4.0×10^{12} ions cm^{-2} or 10 MeV Au^{4+} at fluences of 7.3×10^{11} and 5.5×10^{12} ions cm^{-2}. The 2 MeV ions stop in the 500-nm thick GdBCO layer, while 10 MeV ions penetrate it. The pristine and irradiated samples were probed using a slow positron beam at the Kyoto University Research Reactor. The Doppler broadening of annihilation radiation (DBAR) spectra was acquired with incident positron energies E_+ varying from 0.03 to 25 keV. The sharpness of the DBAR spectra is evaluated by the *S*-parameter, which becomes generally lower when positrons annihilate in a perfect lattice, and higher when positrons are trapped into vacancies [1].

Results and Discussion

Figure 1 displays the *S*-parameters of the GdBCO CCs before and after the irradiation as a function of the incident positron energy [2]. The *S*-parameters for all the irradiated samples were clearly lower than that for the unirradiated sample. This reduction is opposite to the generally expected tendency of the *S*-parameter change caused by ion irradiation. Moreover, the DBAR spectra normalized to the calculated defect-free GdBCO spectrum revealed existence of vacancy clusters in both of the pristine and heavily-irradiated samples. These results indicate that the size of the irradiation-induced defects is smaller than that of the vacancy clusters initially contained in the GdBCO CC samples. The relationship between the *S*-parameter of the GdBCO layer obtained from the VEPFIT analysis and the value of T_c is plotted in Fig. 2 [2]. We found that irradiation-induced vacancy-type defects caused a degradation of T_c, demonstrating that a slow positron beam could be a useful tool for characterizing the effects of ion irradiation on commercial superconducting tapes that contain vacancy clusters.

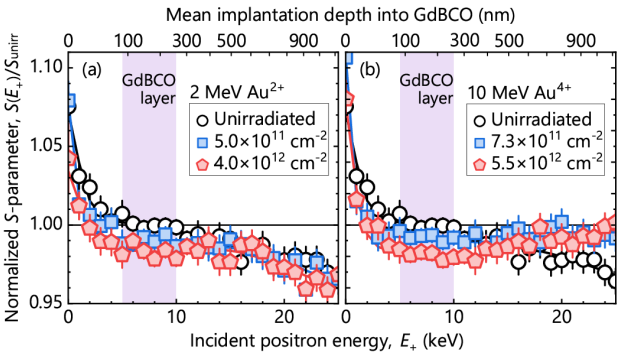

Fig. 1. Normalized *S*-parameters as a function of the incident positron energy for (a) 2 MeV Au^{2+} and (b) 10 MeV Au^{4+} irradiated GdBCO superconducting tapes [2].

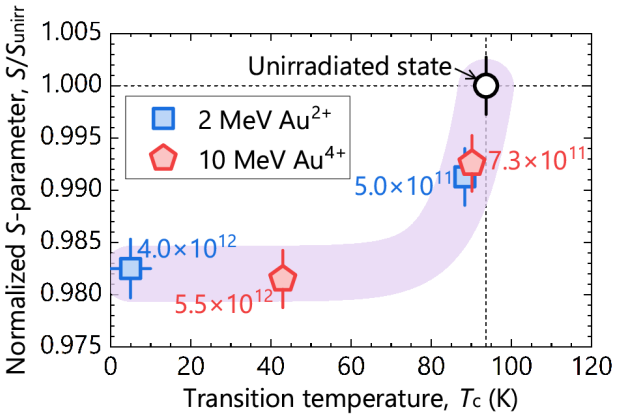

Fig. 2. Normalized *S*-parameters as a function of the incident positron energy for (a) 2 MeV Au^{2+} and (b) 10 MeV Au^{4+} irradiated GdBCO superconducting tapes [2].

References

[1] R. W. Siegel, Annu. Rev. Mater. Sci. **10**, 393 (1980).
[2] A. Yabuuchi *et al.*, Appl. Phys. Express **13**, 123004 (2020).

1 - 10 Fabrication of advanced power FET devices for harsh environment applications

T. Kawae[a)], H. Okazaki[b)] and T. Yamaki[b)]

[a)]College of Science & Engineering, Kanazawa University
[b)]Department of Advanced Functional Materials Research, TARRI, QST

Introduction

Wide-gap semiconductors offer a large application potential for use in next-generation power devices. For electrical equipment used in outer space, the power devices must use the limited power source efficiently and operate in extremely harsh environments exposed to radiation and heat rays. Diamond with a bandgap of 5.47 eV is expected as a next-generation power device material with excellent radiation resistance. However, it is difficult to activate the carriers in diamond at room temperature due to the large activation energies for dopants. Thus, we proposed the use of ferroelectrics as a gate insulator because of its huge polarization, and have produced ferroelectric gate diamond FET (FeFET), which showed typical properties such as a high current on/off ratio and efficient carrier inducing at room temperature [1,2]. As another advantage, ferroelectrics have superior radiation resistance. Based on these advantages, our focus is that the diamond FeFET will be a key device that contributes to the development of the space industry [3].

We have started a basic study on radiation resistance of the FeFET structure. As a preliminary experiment to identify its vulnerable parts in γ-ray environments, the FeFET structure using similar materials, *i.e.*, wide-gap semiconductor ZnO and inorganic ferroelectric $Pb(Zr,Ti)O_3$ (PZT) was prepared, and the degradations of its device characteristics during the course of γ-ray irradiation were investigated.

Experimental procedure

A ferroelectric PZT back-gate structure was prepared on the $Pt/SiO_2/Si$ and $SrRuO_3$-coated $SrTiO_3$ substrates. Each PZT gate was prepared by chemical solution deposition (CSD) and pulsed laser deposition (PLD), respectively. An Al-doped ZnO (Al-ZnO) channel was deposited on the PZT back-gate. Then, source and drain electrodes were prepared using photolithography and lift-off techniques. For comparison of ferroelectricity of the gate structure, PZT film capacitors were prepared on the same substrate.

The prepared FeFETs were irradiated with γ-rays at Co-60 irradiation facility of TARRI, under the conditions of dose rate of 2 to 20 Gy/h and of an irradiation time of 1 h. Their electrical properties were compared before and after the irradiation.

Results and discussion

The prepared FeFETs and film capacitors on each substrate exhibited clear n-channel FeFET operation and ferroelectricity. Figure 1 shows I_D-V_G properties of prepared FeFETs before/after γ-ray irradiation with 20 Gy/h. As changes before and after γ-ray irradiation, a decrease of on-current and shift of the characteristic curve to positive bias side were observed. On the other hand, the insulating resistance of the PZT gate was maintained since the increase of off-current did not occur in both the specimens. Also, after γ-ray irradiation, no degradation in the ferroelectricity of PZT, such as a decrease in the saturation polarization and remnant polarization values, was observed in the P-V curves of each film capacitor.

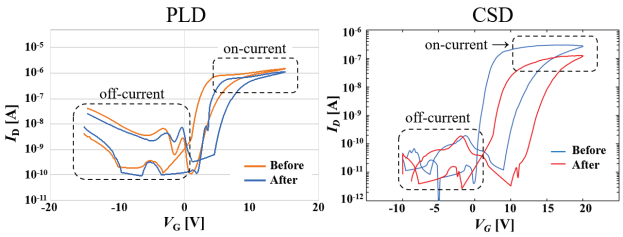

Fig. 1. I_D-V_G curves of prepared FeFETs before/after of gamma-ray irradiation.

From the above results, a decrease in carrier mobility of Al-ZnO channel and formation of the interface state between the Al-ZnO channel and PZT gate are considered to be the main γ-ray-induced degradations. In order to avoid the observed degradations and realize the advanced power FeFETs for harsh environments, it became clear that the suppression of elements diffusion at the interface must be solved immediately. To suppress element diffusion at the interface, there are device process approaches such as (A) creation of a barrier layer and (B) giving a thermal history. Especially, approach (A) will be made by introducing an insulating layer (SiO_2 or Al_2O_3) for a large band offset between diamond and inorganic ferroelectric with a bandgap of 3-4 eV.

Although elements diffusion at the interface due to γ-ray irradiation was observed, there was no degradation of insulating and polarization properties of the PZT gate, which is the most important factor for stable device operation. These results indicate the superiority of the device structure composed of wide-gap semiconductors and ferroelectrics with excellent radiation durability.

Acknowledgments

This work was supported by JSPS KAKENHI Grant Number JP 20K04595 and Kanazawa Univ., SAKIGAKE project 2020.

References

[1] T. Kawae *et al.*, Appl. Phys. Lett. **108**, 242101 (2016).
[2] T. Kawae *et al.*, Jpn. J. Appl. Phys. **56**, 10PF06 (2017).
[3] Vision for Space industry2030, Cabinet Office of Japan https://www8.cao.go.jp/space/vision/mbrlistsitu.pdf

1 - 11 Fabrication of flat-plate perfect blackbody materials using etched high-energy-ion tracks

K. Amemiya[a)], Y. Shimizu[a)], H. Koshikawa[b)], M. Imbe[a)] and T. Yamaki[b)]

[a)]National Metrology Institute of Japan, AIST
[b)]Department of Advanced Functional Materials Research, TARRI, QST

We have been developing a novel flat-plate perfect blackbody material [1,2] based on etched ion tracks [3]. Poly allyl diglycol carbonate (CR-39 in trade name) plastic plates were irradiated with energetic heavy ion beam from AVF cyclotron of TIARA; then the samples were etched in NaOH solutions to fabricate randomly arrayed optical micro-cavities (etch pits) on their surface, followed by replica molding. The resultant blackbody sheet from poly dimethyl siloxane (PDMS) with carbon black fillers exhibited ultralow reflectance of $\lesssim 0.5\%$ in UV–VIS-NIR-MIR, notably $\lesssim 0.1\%$ in MIR while maintaining good mechanical durability [2]. This ultra-low reflectance relies on the multiple reflections of incident light inside the micro-cavities on the blackbody sheet surface.

Our blackbody sheet would be used as a flat-plate standard infrared radiator, whose emission spectrum is determined only by the temperature of the sheet according to Planck's law. Thereby, highly accurate calibration of radiation thermometers including thermographic devices would be possible. With the pandemic of the COVID-19, non-contact thermometers and thermography have become widespread, and a high-emissivity and large-area flat-plate blackbody source is required. In this paper, we report the fabrication of the blackbody sheet with a large area for temperature reference applications.

We have fabricated a 100 mm x 80 mm PDMS blackbody sheet. We confirmed that the large-area blackbody sheet exhibited ultralow reflectance of < 0.2% (emissivity of > 0.998) at thermal infrared wavelengths (8-15 μm) when the radius *r* and the aspect ratio *h*/*r* of the micro-cavity were 5.3 μm and 4.0 (Fig. 1). The reflectance values at six separate positions on the blackbody sheet agreed with each other (Fig. 2), which implied that the blackbody sheet would have high in-plane uniformity [4].

Figure 3 shows a conceptual image of the flat-plate blackbody infrared radiation source, which would work as a temperature reference for thermographic device correction in real time. Currently, we are investigating the temperature accuracy of the prototype of a flat-plate blackbody source.

Acknowledgments

This work was partially supported by KAKENHI JP18K11940 and AMED JP20he0822011.

The ion beam irradiation experiment was conducted at TIARA of QST, which was supported by the Inter-University Program for the Joint Use of JAEA/QST Facilities.

References

[1] K. Amemiya *et al.*, Nucl. Instrum. Meth. Phys. Res. B **356–357**, 154 (2015).
[2] K. Amemiya *et al.*, J. Mater. Chem. C **7**, 5418 (2019).
[3] S. Kodaira *et al.*, Radiat. Meas. **46**, 1782 (2011).
[4] Y. Shimizu *et al.*, Opt. Express **28**, 22606 (2020).

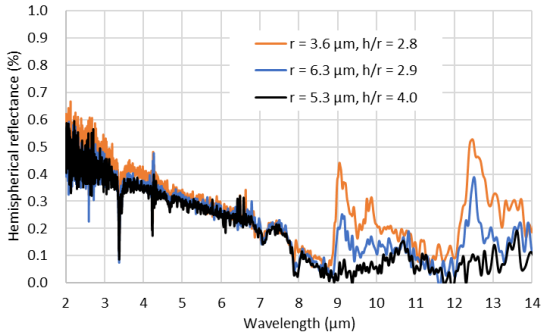

Fig. 1. Micro-cavity geometry dependence of the spectral reflectance of the blackbody sheet

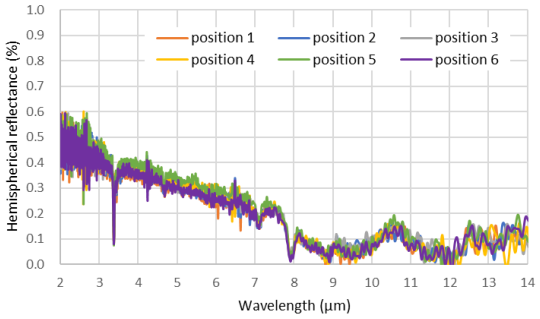

Fig. 2. In-plane uniformity of the spectral reflectance of the blackbody sheet.

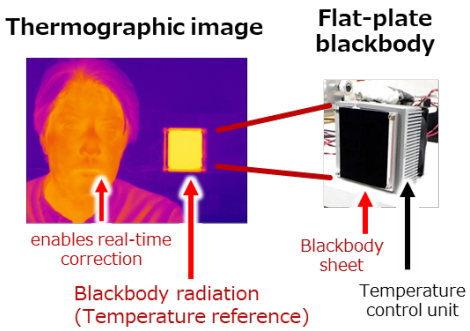

Fig. 3. Conceptual image of the flat-plate blackbody infrared radiation source.

1 - 12 Development of proton exchange membranes for hydriodic acid concentration by ion-track grafting technique

N. Tanaka[a)], S. Sawada[b)], C. Sugimoto[a)] and T. Yamaki[b)]

[a)]HTGR Research and Development Center, JAEA
[b)]Department of Advanced Functional Materials Research, TARRI, QST

The hydrogen (H_2) production with no CO_2 emission should address global-warming issues. A promising method for this purpose is the thermochemical water-splitting iodine–sulfur (IS) process with high-temperature nuclear or solar heat sources. It is composed of the following three key reactions:

(i) $2H_2O + SO_2 + I_2 \rightarrow 2HI + H_2SO_4$ (100 °C)
(ii) $H_2SO_4 \rightarrow SO_2 + 0.5O_2 + H_2O$ (600-900 °C)
(iii) $2HI \rightarrow H_2 + I_2$ (500 °C)

HI gas is separated from a hydriodic acid solution produced by the Bunsen reaction (i) for the subsequent decomposition reactions (ii) and (iii). Before the separating operation, the HI solution should be pre-concentrated to prevent the azeotropic phenomena, which is carried out by electro-electrodialysis (EED) using a proton exchange membrane (PEM). The PEMs are required to show both high proton (H^+) conductivity and high H^+ selectivity to reduce the electric power consumption.

We developed the PEMs by a radiation grafting method [1], which involves the irradiation of the base polymer film by γ-rays or an electron beam and the graft polymerization to introduce the cation exchange groups. The prepared PEMs with the high ion exchange capacity (IEC) were found to show a higher H^+ conductivity than that of the conventional PEMs, thereby reducing the cell voltage for EED. However, these PEMs showed lower H^+ selectivity and unexpected chemical species such as I^- and H_2O were permeated. The decreased selectivity is originated from the excessive swelling of the ion channels composed of the hydrophilic graft chains and absorbed water. Therefore, a proper PEM structure which prevents the excessive swelling must be considered to improve the H^+ conductivity and selectivity.

Most recently, we started to develop the novel PEMs by an ion-track grafting technique using MeV-GeV heavy ions, instead of γ-rays or the electron beam. Such a high-energy ion beam can create the one-dimensional cylindrical ion tracks, which chemically modified the ion channels by the graft polymerization. The cylindrical ion channels efficiently transport H^+ to increase the high conductivity, while the surrounding unmodified regions restrict the excessive swelling of the ion channels to increase the H^+ selectivity.

In order to verify the practical applicability to EED, the PEM was prepared by irradiation of the base poly(ethylene-*co*-tetrafluoroethylene) film with 560 MeV ^{129}Xe at a fluence of 3.0×10^8 ions/cm^2, graft polymerization of styrene monomers into the ion tracks, and sulfonation of the grafted styrene units. The IEC of the PEM was measured to be 1.9 mmol/g by an acid-base titration. For the HI concentration test, the EED cell with an effective electrolysis area of 5 cm^2 was used. An aqueous HI/I_2 solution at the molality of [HI] = [I_2] = 10 mol/kg was supplied to both the cathode and anode sides. The EED was conducted at 40 °C by applying a constant current of 200 mA/cm^2.

Figures 1 and 2 show the time dependence of the catholyte and anolyte compositions, respectively. In the catholyte, the HI molality increased with time; conversely the I_2 molality decreased. In contrast, the HI and I_2 molalities decreased and increased, respectively, in the anolyte. These results indicate that the ion-track grafted PEM can proceed the HI concentration. An investigation for further improvement in the EED performance is in progress by optimizing the ion beam irradiation conditions.

Acknowledgments

This work was supported by JSPS KAKENHI Grant Number JP20K05203.

References

[1] N. Tanaka, Chem. Eng. Sci. **237**, 116575 (2021).
[2] S. Sawada, Bull. Soc. Sea Water Sci., Jpn. **73**, 208 (2019).

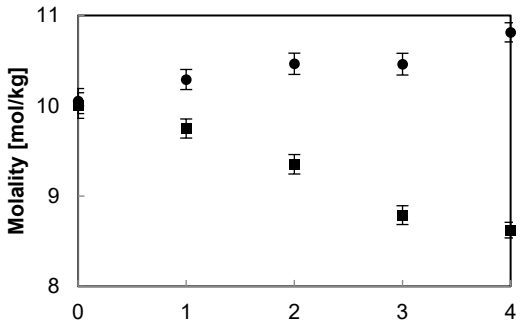

Fig. 1. Time course of compositions in catholyte solution: HI (●), I_2 (■).

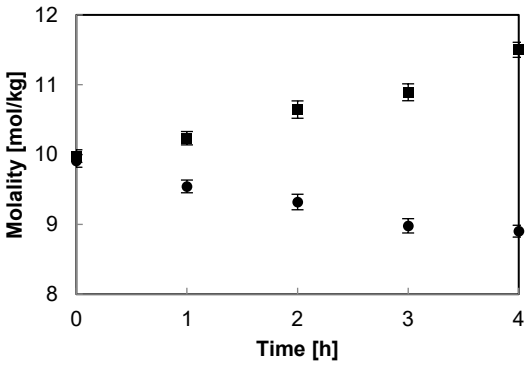

Fig. 2. Time course of compositions in anolyte solution: HI (●), I_2 (■).

1 - 13 Ion and water transport properties of nanostructured cation exchange membranes prepared by ion-track grafting

S. Sawada, H. Koshikawa and T. Yamaki

Department of Advanced Functional Materials Research, TARRI, QST

In Japan, table salt is produced *via* condensation of salt in saline water by electrodialysis and subsequent water evaporation. An electrodialysis system has repeating pairs of cation exchange membranes (CEMs) and anion exchange membranes (AEMs), through which Na^+ and Cl^- are transported respectively to condense salt. The membranes for this application require the two properties: low ion-conduction resistance to reduce electric power consumption and low osmotic-pressure-driven water permeation flux not to hamper salt condensation [1-3].

In spite of the establishment of commercial electrodialysis process, the development of novel membranes that meet these requirements is still of great interest to improve its performance. One promising way to prepare CEMs and AEMs is a heavy-ion-track grafting method [1-3], which involves the irradiation of a base film with heavy ions to create the latent tracks and the subsequent graft polymerization. The graft chains with ion exchange groups are introduced only in the cylindrical latent tracks to form hydrophilic ion channels, and the surrounding non-irradiated parts are not modified. It is expected that the resulting one-dimensional cylindrical ion channels should efficiently transport ions to reduce ionic resistance, while non-modified parts should restrict the excessive water swelling of the ion channels and the water permeation.

In this study, we prepared the nanostructured CEMs by the ion-track-grafting method for the application to saline water electrodialysis. Their membrane resistance and water flux were evaluated and compared with those of Selemion CSO (AGC Seimi Chemical Co., Japan), the benchmark electrodialysis CEM. The characteristic transport properties of Na^+ and water in the nanostructured CEMs are discussed.

Ethylene-*co*-tetrafluoroethylene (ETFE) films with a thickness of 25 μm (DuPont Co., USA) were irradiated with 310 MeV ^{84}Kr ions from an AVF cyclotron at the Takasaki Ion Accelerators for Advanced Radiation Application facility. The number of irradiated ions per 1 cm^2, namely the ion fluence, was fixed at 4.0×10^8 ions/cm^2. The irradiated ETFE film was immersed in a styrene solution at 60 °C for 1.5-12 h. Then, the styrene-grafted film was sulfonated by chlorosulfonic acid to prepare the CEM. The ion exchange capacities (IECs) of the CEMs were measured by acid-base titration. The membrane resistance in a 0.5 mol/L NaCl aqueous solution was measured by a two-probe AC impedance technique. The water flux was measured under the osmotic pressure difference between pure water and a 3 mol/L NaCl aqueous solution.

The prepared CEMs showed the IECs ranging from 0.58 to 0.94 mmol/g. As the IEC became high, the membrane resistance decreased, and conversely the water flux increased. Fig. 1 shows the relationship between the membrane resistance and water flux. The CEM whose data point is closer to the origin is more suitable for practical saline water electrodialysis. The water flux increased with decreasing the membrane resistance for the nanostructured CEMs; in other words, these two transport properties were in a trade-off relationship with each other. Interestingly, one CEM, indicated by an arrow in the figure, showed two-thirds the membrane resistance and four-fifths the water flux of CSO. Its IEC and water uptake were 0.72 mmol/g and 7.8%, respectively, both of which were far lower than those of CSO (2.2 mmol/g and 26%). Low membrane resistance even at low IECs was surely attributed to the efficient Na^+ transport in one-dimensional ion channels, while low water flux was directly attributed to very low water uptake. Adjustment of the IEC and water uptake at a moderate level balanced the ion and water transport properties appropriately.

The saline water electrodialysis experiment using our nanostructured CEM is now in progress.

Acknowledgments

This work was partially supported by the salt science research foundation (Grant number: 1623, 1717 and 1817).

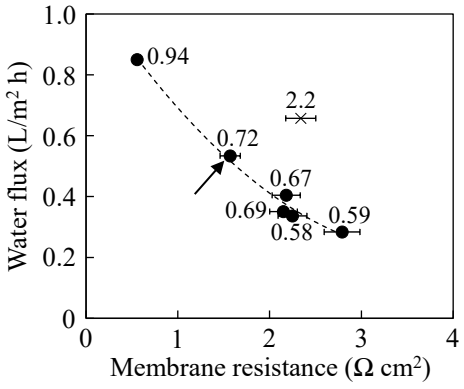

Fig. 1. Relationship between the membrane resistance and water flux for the nanostructured CEMs (●) and Selemion CSO (×). The numbers next to the data points are the IECs (mmol/g).

References

[1] S. Sawada *et al*., Bull. Soc. Sea Water Sci., Jpn. **73**, 208 (2019).
[2] S. Sawada *et al*., Sep. Sci. Tech. **55**, 2211 (2020).
[3] S. Sawada *et al*., Salt Seawater Sci. Tech. **1**, 61 (2021).

1 - 14 Fabrication of titanium oxide nanocones using polymer ion-track membranes as templates

H. Koshikawa, S. Yamamoto, M. Sugimoto, S. Sawada and T. Yamaki

Department of Advanced Functional Materials Research, TARRI, QST

Chemical etching of a polymer film irradiated with swift heavy ions that stop in the middle leads to the formation of ion-track membranes with non-penetrating conical pores. These porous membranes have been used as templates for inorganic nanocones with various sizes and shapes [1]. Titanium dioxide (TiO_2) nanocones have been applied to the process of hydrogen production by photocatalytic water splitting based on the theoretical prediction that the photocatalyst having nanocone-shaped protrusions on its surface absorbs light more efficiently than the flat one [2]. We report here a new method for preparing TiO_2 nanocones, which involves the sol-gel synthesis of TiO_2 microcrystals, filling the conical pores of the ion-track membrane with the TiO_2 microcrystals, and heat treatment.

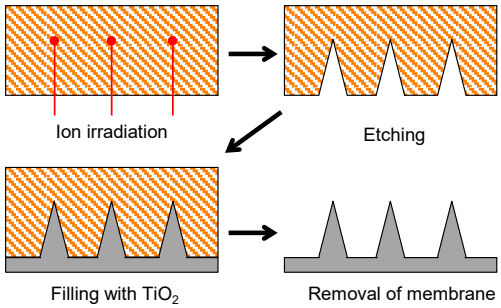

Fig. 1. The procedure for preparing the TiO_2 nanocones.

Figure 1 shows the procedure for preparing TiO_2 nanocones. A stack of two 25-μm-thick polyimide films (Kapton, Du Pont-Toray Co., Ltd.) was irradiated with 127 MeV ^{40}Ar ions at a fluence of 3.0×10^7 ions/cm^2 using the TIARA AVF cyclotron, QST-Takasaki. The stopping depth was 41 μm from the front surface, meaning that the impinging ion penetrated through the first film and stopped in the second film. The second film was etched in a sodium hypochlorite (NaClO) solution (5.0% available chlorine, as supplied by FUJIFILM Wako Pure Chemical Corporation) at 60 °C. Next, the suspension of TiO_2 microcrystals was synthesized according to the previously report [3] and dropped on the pore-open side of the etched membrane. The subsequent vacuum drying and heat treatment in air at 400 °C for 3 h made the TiO_2 deposited inside the conical pores. Finally, the track-etched membrane was dissolved with the NaClO solution, leaving the TiO_2 nanocones. The shape of the nanocones was observed with a scanning electron microscope (SEM), and the cross section of the nanocones in the template membrane was observed with a transmission electron microscope (TEM).

The SEM image of the nanocones is shown in Fig. 2 (a). The TiO_2 nanocones had a base diameter of 1.0 μm and a height of 2.4 μm, both of which agree well with the surface diameter and depth of the pores, respectively. A cross-sectional TEM image of the TiO_2 nanocones in the template membrane is shown in Fig. 2 (b). Although the white part in the image probably indicates the nanocones broken during the sample preparation for our TEM observations, we can confirm filling the pores with TiO_2 and sharp nanocone tips. Figure 2 (c) shows a TEM image of the same nanocones after the heat treatment, demonstrating that the nanocone tip remained sharp.

References

[1] H. Koshikawa *et al.*, 26th Annual Meeting of MRS-Japan, D3-P21-016 (2016).

[3] T. Kurosaki *et al.*, Electrochemistry **70**, 860 (2002).

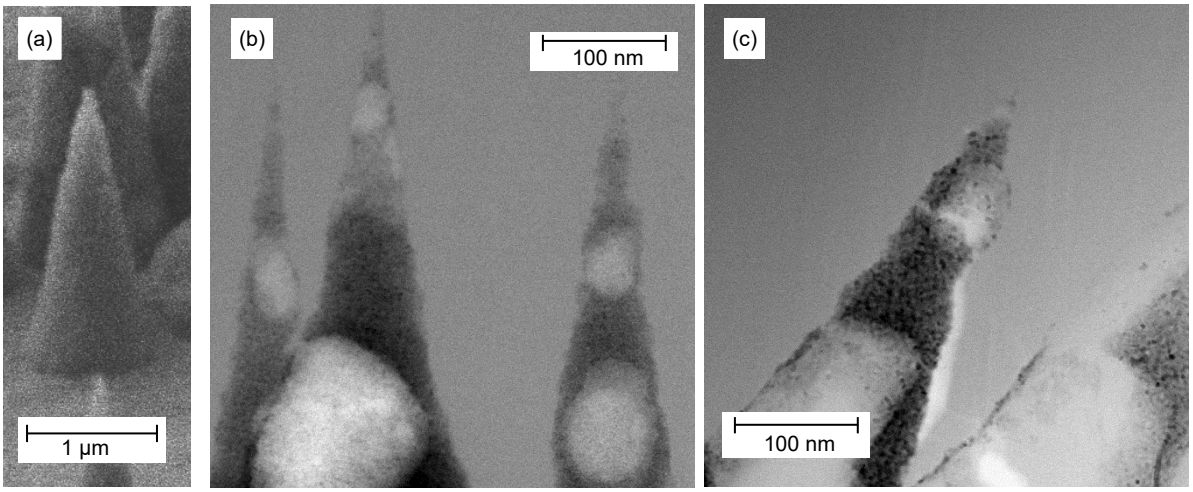

Fig. 2. (a) SEM image of the TiO_2 nanocones after the dissolution of the template membrane. TEM images of the TiO_2 nanocones in the template membrane (b) before and (c) after the heat treatment in air at 400 °C for 3 h.

1 - 15 Weakened bonding of oxygen with the Pt nanoparticle catalyst on an ion-beam-irradiated carbon support

H. Okazaki[a)], A. Idesaki[a)], H. Koshikawa[a)], D. Matsumura[b)], S. Yamamoto[a)], and T. Yamaki[a)]

[a)]Department of Advanced Functional Materials Research, TARRI, QST
[b)]Materials Sciences Research Center, JAEA

The oxygen reduction reaction (ORR) activity of the Pt nanoparticles (NPs) was found to become higher on the glassy carbon (GC) substrate irradiated with 380 keV Ar^+ [1]. This finding suggests that the Pt NPs would be electronically modified by vacancy introduction in the GC. The X-ray absorption fine structure (XAFS) analysis of the Pt L-edge [2] and C K-edge [3] recently yielded sufficient information concerning the effect of the vacancy on the electrocatalyst-support (Pt-C) interaction, and the thereby-changed microscopic structure of Pt NPs. However, it has not yet been revealed how these electronic and structural changes of Pt NPs through the Pt-C interaction can affect the actual electrocatalytic reaction. Thus, we performed *in situ* XAFS measurements in an O_2 atmosphere to clarify the electronic states of the Pt NPs upon O_2 adsorption, which is the first step of the ORR process.

GC substrates were irradiated with 380 keV Ar^+ at a fluence of 7.5×10^{15} ions/cm^2 at the Takasaki Ion Accelerators for Advanced Radiation Application (TIARA). We deposited the Pt NPs on the irradiated substrate by RF magnetron sputtering (Pt/irrad. GC). The Pt NPs deposition was also performed on the pristine GC substrates (Pt/GC) for comparison. The XAFS spectra of the Pt L-edge were measured at BL14B1 in SPring-8. After the H_2 reduction at 100 °C for 10 min for initialization, the *in situ* measurements were performed at room temperature in He gas and subsequently O_2 gas. Finally, we obtained a difference spectrum (called $\Delta\mu$ spectrum) in these two atmospheres to examine the effect of adsorbed O_2.

Figure 1 shows the $\Delta\mu$ spectra for the Pt/irrad. GC and Pt/GC together with the results of peak fitting using the Lorentzian function. We observed the positive intensity around 11562 eV due to new Pt electronic states formed by O_2 exposure. The $\Delta\mu$ spectrum for Pt/GC was fitted with one peak at 11561.9 eV (denoted as peak 1). On the other hand, we obtained the best fitting result for Pt/irrad. GC using the peak 1 at 11561.2 eV plus another minor peak in a higher energy of 11564.4 eV (denoted as peak 2). The energy of peak 1 was comparable to that of the white-line peak at 11562.3 eV for both the samples. Lytle *et al.* [4] previously performed similar experiments; in other words, the Pt NPs on Al_2O_3 were examined by the *in-situ* XAFS while reduced in H_2 for measuring a bare surface and subsequently exposed to O_2. They observed the white-line increase with no significant shift in response to O_2. Therefore, peak 1, a main component of the $\Delta\mu$ spectra, can be assigned to the O_2 adsorption on the Pt surface.

We then discuss the origin of peak 2. Such a higher

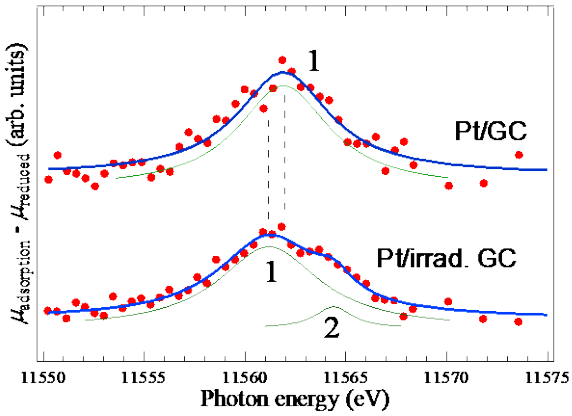

Fig. 1. The results of the peak fitting for the $\Delta\mu$ spectra of Pt/GC and Pt/irrad. GC.

energy peak can generally be assigned to the Pt oxide because PtO_2 formation is known to shift the white-line peak in the XANES spectrum to higher energies and increase its intensity as a consequence of carrying a positive charge on Pt atoms. But the energy of peak 2 was too high for PtO_2, which exhibited the positive peak at 11563.5 eV in the $\Delta\mu$ spectrum of the PtO_2 powder versus the Pt foil (result not shown). Thus, the peak 2 might come from a kind of the Pt oxide, probably the surface oxide-like layer of Pt involving the vacancies in GC.

It is worth pointing out that the energy of peak 1 was 0.7 eV lower for the Pt/irrad. GC than for the Pt/GC. This shift indicates that the Pt-O antibonding level were lowered in energy and became close to the Fermi level; thus, the Pt-O bond in the Pt/irrad. GC would be weakened.

We will compare the above-obtained results with those of theoretical calculations using density functional theory and molecular dynamics simulation. This would enable us to obtain a structural snapshot of the interface among the vacancy and C atom in GC, and the Pt atom with O_2 adsorbed weakly and, ultimately, energy and mechanistic diagrams in the overall ORR pathways.

Acknowledgments

This work is partially supported by a Grant-in-Aid for Scientific Research (KAKENHI) Grant Number 18H01923 and KAKENHI is funded by the Ministry of Education, Culture, Sports, Science and Technology (MEXT), Japan.

References

[1] K. Kakitani *et al.*, QST Takasaki Annu. Rep. 2015, **QST-M-2**, 42 (2016).
[2] K. Kakitani *et al.*, Rad. Phys. Chem. **153**, 152 (2018).
[3] H. Okazaki *et al.*, J. Chem. Phys. **152**, 124708 (2020).
[4] For example, F. W. Lytle *et al.*, J. Chem. Phys. **70**, 4849 (1979).

1 - 16 Characterization of embedded nanocomposites in solid synthesized by dual ion irradiation

F. Hori[a)], T. Yamada[a)], Y. Morikuni[a)], H. Obayashi[a)], A. Iwase[a,b)], T. Matsui[a)], M. Maekawa[c)] and A. Kawasuso[c)]

[a)]Graduate school of Engineering, Osaka Prefecture University
[b)]Wakasa-wan Energy Research Center
[c)]Department of Advanced Functional Materials Research, TARRI, QST

Recently, metallic nanomaterials have attracted tremendous attention due to their unique properties, such as luminescence, absorption, magnetic property, catalytic activity and hydrogen absorption. These properties come from their size, shape, alloy system and complex electronic state which is not appear in bulk materials. In addition, non-equilibrium state of nanoparticles may have curious properties. In general, metal nanoparticles are fabricated by chemical reduction methods due to their industrial advantages. However, the chemical method is not suitable for the synthesis of non- equilibrium structure and phased nanomaterials. Ion irradiation method is a method that is highly controlled impurity injection with high density of energy into solid. We suppose this method is useful to synthesize the new functional nanomaterials. So far, we have successfully synthesized new functional nanoparticles in glassy solid by using this method [1,2]. In this paper, the result of synthesis of metal nanocomposites, which is not solid solution, by dual ions irradiation is shown.

Amorphous silica glass (SiO_2: 5 × 5 × 1 mm^3) was prepared as an irradiation target. The target was irradiated with 380 keV Ag ions and 200 keV Ni ions at room temperature by using ion implanter at TIARA, National Institutes for Quantum and Radiological Science and Technology (QST-Takasaki). Dual irradiation with Ag and Ni ions has done by changing irradiation order (AN: is irradiated firstly with Ag ions and followed by Ni ions, NA: is vice versa). The irradiation fluence of Ag ion is 5×10^{15} to 7×10^{16} /cm^2 and that of Ni ions was 1×10^{15} to 1×10^{17} /cm^2. After each ion irradiation, these samples were examined by X-ray photoelectronic spectroscopy (XPS) at KEK, positron annihilation, UV-vis, Grazing Incidence X-ray Diffraction (GIXD).

The intensity and position of UV-vis absorption peak originated from surface plasmon resonance (SPR) of synthesized nanoparticles AN and NA are clearly different, as shown in Fig. 1. This result indicates that the structure and electronic state of these nanoparticles formed by irradiation in the reverse order are not same. Fig. 2 shows the GIXD patterns of both samples. As seen in this figure, diffraction peaks around 44 degrees for NA is a single peak but splited for AN. Also, both peaks do not match that of pure Ag and Ni. This result shows that the formed nano materials may be a composite with lattice distortion. These results well agree with the result of XPS measurement. That is the peak which indicates metal bonds are observed, but the peak intensity ratio of Ni 2p and Ag 3d has reverse relationship between AN and NA. Essentially, Ag and Ni is not solid solution in thermally. Therefore, it is considered that this method produces non-equilibrium nanocomposites in which Ag and Ni were not in a thermal equilibrium state, but in different states depending on the irradiation order.

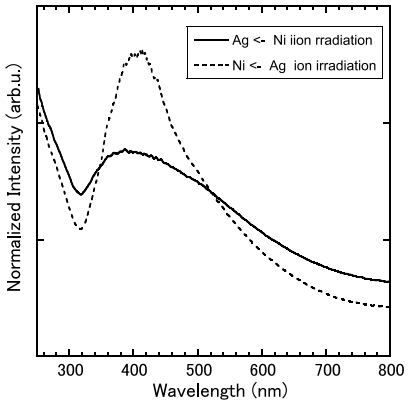

Fig. 1. UV-vis spectra of Ag and Ni ions irradiated samples.

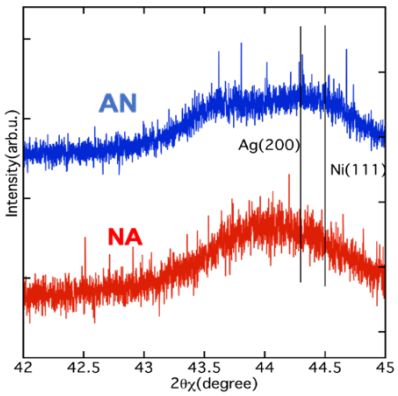

Fig. 2. GIXD profile of Ag and Ni irradiated samples.

Acknowledgments

We would like to thank to Dr. Y. Baba and Dr. N. Usami for the X-ray measurement at KEK-PF.

References

[1] T.Yamada *et al.*, Nanotechnology **31**, 455706 (2020).
[2] T. Yamada *et al.*, Trans. Mater. Res. Soc. Jpn **45**, 127 (2020).

1 - 17 Study of induced magnetism caused by vacancy clusters in Gd-implanted GaN by spin-polarized positron annihilation spectroscopy

M. Maekawa, S. Sakai, A. Miyashita and A. Kawasuso

Department of Advanced Functional Materials Research, TARRI, QST

Diluted magnetic semiconductors (DMSs) is a key material for the development of the spintronics devices. Gadolinium-doped gallium nitride (GaGdN) is known as a DMS that exhibits ferromagnetism at room temperature [1]. Although each Gd atom has a magnetic moment of 7 μ_B, the anomalous large magnetic moment as high as 4000 μ_B/Gd ('colossal' magnetization) has been reported [2]. The origin of the anomalous magnetization is still unclear. Some possible candidates are proposed such as the vacancy-type defects [3]. From our recent studies, the single Ga vacancies in GaN show very weak magnetism [4], however, the colossal magnetism might be due to the vacancy clusters [5]. In this study, we investigated what type of vacancy clusters are generated and how they are related to the colossal magnetism.

Samples were MBE-grown undoped GaN films with the thickness of 2 μm on sapphire substrates. Using a 400 keV ion implanter, Gd ions were implanted at 370 keV at a room temperature to the maximum dose of 1×10^{15} cm^{-2}. After implantation, samples were annealed at 1173 K in N_2 atmosphere. Using a conventional positron beam apparatus, the coincidence Doppler-broadening (CDB) annihilation radiation spectra were obtained. Furthermore, using a spin-polarized positron beam apparatus the magnetic DBAR (MDB) intensities were also obtained in the magnetic fields of ±0.91 T.

Figure 1 shows the CDB spectra for the sample with dose of 10^{15} Gd^+ /cm^2. The curves denote the theoretical calculations assuming nitrogen vacancy (V_N), gallium vacancy (V_{Ga}), 8-vacancy (V_8) and 12-vacancy (V_{12}), respectively. This result shows that the small vacancies such as V_{Ga} does not reproduce the experimental result. It seems that V_{12} is more suitable because it reproduces the experimental data around 0 m_0c, since this momentum region reflects the annihilation with valence electrons.

Figure 2 shows the MDB spectrum. The calculations (solid lines) showed that small vacancy defects (V_{Ga} and V_N) have spontaneous magnetizations (3 and 1μ_B, respectively). V_{12} cluster detected by the CDB experiment does not show magnetism. However, isolated V_{12} has no magnetization, two close V_{12} clusters separated by an interatomic distance simulating the high-density condition shows spontaneous magnetization of 2 μ_B due to the formation of partially-filled states. As shown in Fig. 2, the calculated spectrum for V_{Ga} has downward peak at the centers, which is because of the preferential annihilation of positrons with spin-polarized N valence electrons. This is completely different from the experimental upward-peak spectrum. Contrarily, V_N and V_{12} have upward-peak spectra because of the spin polarization of Ga valence electrons. The intensity of V_N is not sufficient because of the weak localization of the positron wave function and is not comparable to the experiment. Both the intensity and curve shape of V_{12} are comparable to the experiment. Thus, spin-polarized V_{12} clusters may be the major positron trapping centers and the ferromagnetism is explained by electron spins associated with high-density V_{12} vacancy clusters.

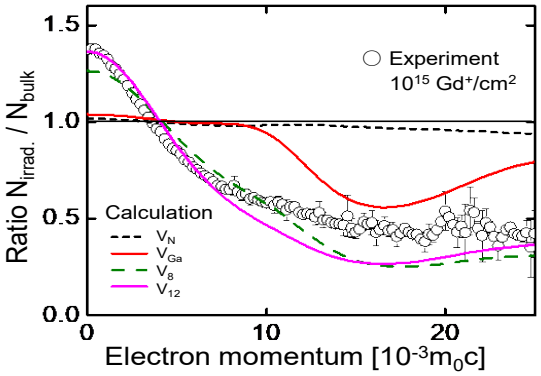

Fig. 1. The coincidence Doppler broadening of annihilation radiation (ratio) spectra for the samples with doses of 10^{15} Gd^+/cm^2.

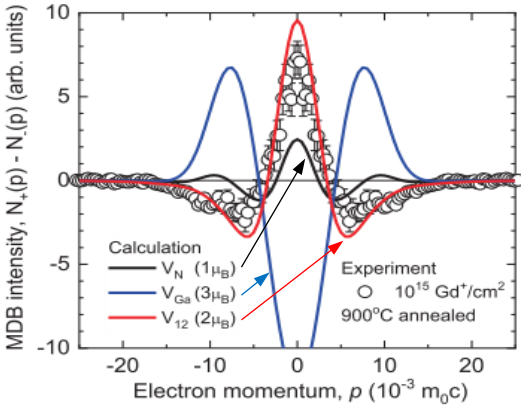

Fig. 2. MDB spectrum measured at 300 K for the Gd-implanted sample with a dose of 10^{15} cm^2 after annealing at 1173 K (open circles). The solid curves denote the theoretical calculations assuming V_N, V_{Ga}, and V_{12} cluster.

References

[1] N. Teraguchi *et. al.*, Solid State Comm.**122**, 651 (2002).
[2] M. A. Khaderbad *et. al.*, Appl. Phys. Lett. **91**, 072514 (2007).
[3] S. Dhar *et. al.*, Phys. Rev. Lett. **94**, 037205 (2005).
[4] M. Maekawa *et. al.*, e-J. Surf. Sci. Nanotech. **16**, 347 (2018).
[5] M. Maekawa *et. al.*, QST Takasaki annual report 2019, **QST-M-29**, 45 (2020).

1 - 18 Search for an acceptor in β-Ga_2O_3 with an ion implantation technique

K. Miki[a)], M. Maekawa[b)], R. Iimura[c)], M. Miyamoto[a)], R. Shimazu[a)], S. Miki[a)], Yi Tang[a)], A. Kawasuso[b)], S. Yamakoshi[c)], K. Sasaki[c)] and A. Kuramata[c)]

[a)]Department of Electrical Material and Engineering, University of Hyogo
[b)]Department of Advanced Functional Materials Research, TARRI, QST
[c)]Novel Crystal Technology, Inc.

Recently, large energy consumptions have arisen due to the spread of wireless information communication and electric devices. To solve this problem, it is required to improve the performance of power devices that are indispensable for electrical equipment. Therefore, their next generation materials, SiC and GaN, and the more future material β-Ga_2O_3 are attracting attention as alternatives of Si. Among them, β-Ga_2O_3 has a high performance that can be expected to have low cost, high breakdown voltage, and low power loss [1,2]. However, since the p-type dopant of β-Ga_2O_3 has not been discovered, it is difficult to develop a power device with high withstand voltage [3,4]. For overcoming this difficulty, we are searching for the demanded p-type dopant using the ion implantation method.

In this work, we chose Ba as an acceptor element candidate. We doped Ba into β-Ga_2O_3(010) substrate with the 4 densities of 3×10^{20} cm^{-3}, 1×10^{20} cm^{-3}, 3×10^{19} cm^{-3}, and 1×10^{19} cm^{-3}. All the ion implantation areas are box profile in the depth of 15-75 nm as indicated in Fig. 1. For example, 3×10^{20} cm^{-3} box profile was fabricated with 4 ion implantations: 1.7×10^{15} cm^{-2} (370 keV); 5.4×10^{14} cm^{-2} (190 keV); 3.6×10^{14} cm^{-2} (110 keV); 2.6×10^{14} cm^{-2} (50keV) at TIARA facility, QST. After the Ba ion implantation, each sample was cut into 6 ones with an area of 5mm × 5mm. Those samples were annealed in pure nitrogen gas ambient for 30 min at various temperature in 600 - 1100 °C by 100 °C step. Electrochemical capacitance-voltage (ECV) measurements were performed to estimated effective carrier concentrations, N_d-N_a for all the samples, using dielectric constant of 10. It is noted that all the β-Ga_2O_3 sample has non-intentional donor, Si with the donor density of around $1\text{-}2\times10^{17}cm^{-3}$.

Figure 2 shows the ECV results for various Ba dose samples. With increase of anneal temperature from 600 °C to 1000 °C, N_d-N_a increases, then, toward 1100 °C, decreases. This decrease means possibility of Ba as p-type. We checked Ba SIMS profile inside the sample after the anneal of 1100 °C. the peak of Ba dopant decreased to be under 10^{17} cm^{-3}. Therefore, origin of the decrease of N_d-N_a in 1000 -1100 °C is different from realization of the p-type.

Acknowledgments

A part of this work is on results obtained a project commissioned by the New Energy and Industrial Technology Development Organization (NEDO).

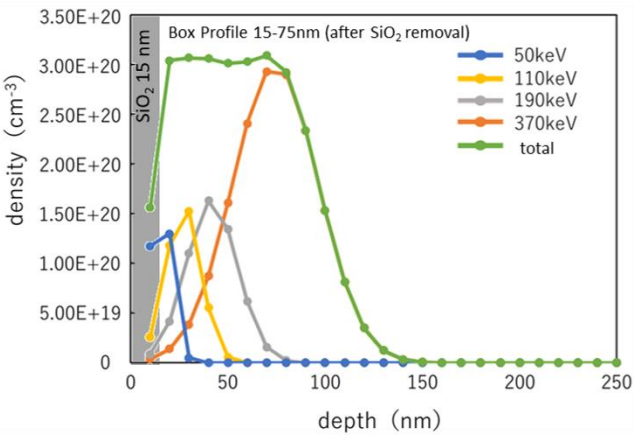

Fig. 1. Box profile of Ba in the case of implantation of $3\times10^{20}cm^{-3}$.

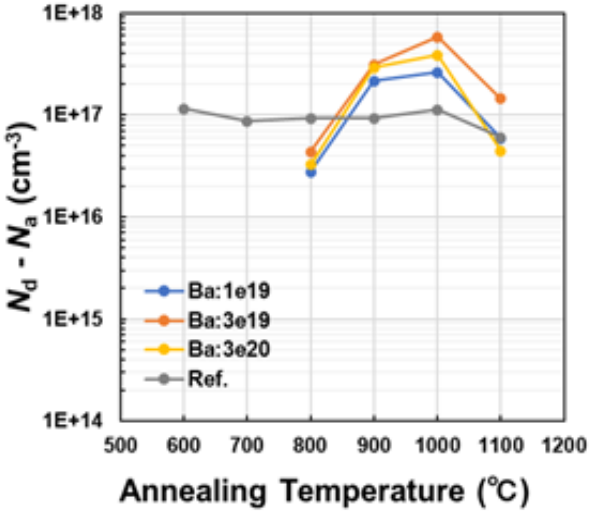

Fig. 2. Effective donor density as a function of anneal temperature for various Ba dose samples.

References

[1] M. Higashiwaki *et al.*, Semicond. Sci. Technol. **31**, 034001 (2016).
[2] G. Jessen et al., 75th Annual Device Research Conference (DRC), 1 (2017).
[3] A. T. Neal *et al.*, Appl. Phys. Lett. **113**, 062101 (2018).
[4] A. Kyrtsos *et al.*, Appl. Phys. Lett. **112**, 032108 (2018).

1 - 19 Optical characterization of Nd ions implanted into nanoscale regions in GaN toward biological applications

S.-I. Sato[a)], M. Deki[b)], T. Nishimura[c)], H. Watanabe[d)], S. Nitta[d)], Y. Honda[d)], B. C. Gibson[e)], A. D. Greentree[e)], H. Amano[d)] and T. Ohshima[a)]

[a)]Department of Advanced Functional Materials Research, TARRI, QST
[b)]Venture Business Laboratory, Nagoya University
[c)]Research Center of Ion Beam Technology, Hosei University
[d)]IMaSS, Nagoya University
[e)]ARC CNBP, RMIT University

Gallium nitride (GaN) is an attractive material for lifescience applications such as bioimaging and sensing due to its biocompatibility, relatively mature fabrication and chemical functionalization [1]. Neodymium (Nd)-doped GaN is of particular interest because of its extremely stable near infrared luminescence at 0.9~1.1 μm with narrow linewidth (a few nm) at room temperature (RT), which is suitable characteristics for optical imaging in biological tissues [2]. To realize the potential of Nd-doped GaN for bioimaging/sensing, small ensembles of Nd ions must be optically detectable at RT with a high signal-to-noise ratio.

This paper reports photoluminescence (PL) properties of small ensembles of Nd ions in a GaN epilayer at RT. Implantation of Nd ions into nanoscale regions in GaN was performed using lithographically-defined masks to mimic the spatial dimensions of Nd-doped GaN nanoparticles as fluorescent probes. The resonant excitation wavelength for Nd ions was determined to be around 619 nm from the photoluminescence excitation spectrum.

The Nd-doped GaN sample was fabricated using following steps: (1) electron beam lithography, (2) Nd ion implantation (100 keV, 1.0×10^{14} cm^{-2}), and (3) thermal annealing for activation (1250 °C for 2 min under N_2 atmosphere). The thickness (half width) of the implanted layer was estimated to be 21 nm, according to TRIM calculation. Figure 1(a) shows the confocal laser scanning microscope (CFM) image of Nd-doped GaN at RT. The excitation laser wavelength was 620 nm and the luminescence from Nd ions centered at 916 nm was selectively collected using an avalanche photodiode and a 900 nm long pass filter. The results show that the Nd implanted square regions with the side of 200 nm were optically detected. PL spectrum from the implanted regions were also characterized as shown in Fig. 1(b). Three peaks originating from the $^4F_{3/2} \rightarrow {}^4I_{9/2}$ transition in Nd^{3+} appeared at 916.3 nm, 934.6 nm, and 944.0 nm from all the implanted regions while no peak was found in the unimplanted regions. The smallest volume optically detected in this study was 8×10^4 nm^3 (60 nm square) and the minimum detected ensemble of Nd ions was 4×10^3, although not all of implanted Nd ions activated as luminescence centers. This value is comparable with ceramic nanoparticles which have been used for fluorescence probes (less than 100 nm in diameter) [3] and thus, this study opens the door to lifescience and bioimaging applications of Nd-doped GaN [4]. Further smaller number of Nd ions can be detected by the reduction of undesired defect luminescence.

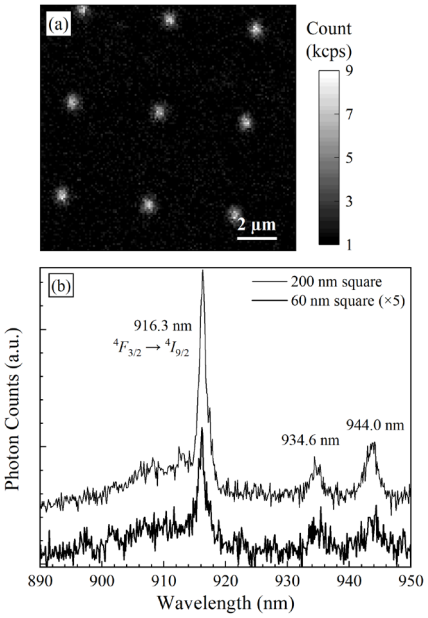

Fig. 1. (a) CFM image of the Nd-GaN at RT. The implanted area was 200 nm square (200 nm × 200 nm) and the grid interval was 5 μm. (b) PL spectra of 200 nm and 60 nm square implanted regions.

Acknowledgments

This study was supported by QST President's Strategic Grant (“Exploratory Research”, “QST International Research Initiative”), JSPS KAKENHI (JP17KK0137, JP18H01483), and the Australian Research Council (CE140100003, LE140100131, FT160100357). A part of this work was conducted at the AIST Nano-Processing Facility, supported by "Nanotechnology Platform Program" of the Ministry of Education, Culture, Sports, Science and Technology (MEXT), Japan, Grant Numbers JPMXP09F18AT0061 and JPMXP09F19AT0040.

References

[1] A. M. Smith *et al.*, Science **4**, 710 (2009).
[2] S. A. Jewett *et al.*, Acta Biomater. **8**, 728 (2012).
[3] E. Hemmer *et al.*, Nanoscale **5**, 11339 (2013).
[4] S.-I. Sato *et al.*, Opt. Mater. Express **10**, 2614 (2020).

1 - 20 Ion-beam assisted synthesis of new graphene compounds

S. Entani[a)], M. Takizawa[b)], K. Harii[a)], Y. Yamazaki[a)] and T. Ohshima[a)]

[a)]Department of Advanced Functional Materials Research, TARRI, QST
[b)]Department of Physical Sciences, Faculty of Science and Engineering, Ritsumeikan University

Two-dimensional materials such as graphene and hexagonal boron nitride (*h*-BN) have attracted wide attention for nanoelectronics and spintronics. The characteristics are strongly affected by atomic-scale local structure of the two-dimensional material. It is expected that the nano-structural control by heteroatom doping leads to tailoring of the electronic and physical properties of the two-dimensional material. Ion irradiation is one of the effective techniques to introduce these local atomic structures in the two-dimensional material [1].

In the present work, a new non-chemical method for synthesizing new graphene compounds was inspected by high-energy ion irradiation to the heterostructure of graphene and the dopant material layer. Here, we report the synthesis of iodographene (graphene iodide) by high-energy ion irradiation to the KI/graphene heterostructure. Graphene was grown by conventional thermal chemical vapor deposition on a polycrystalline Cu foil. After the growth, the graphene sheet was transferred on SiO_2 by etching the Cu foil with a $FeCl_3$ solution [2]. Graphene/SiO_2 was then introduced to an ultrahigh vacuum chamber and a 100 nm-KI film was deposited at room temperature. The specimen was irradiated with 3.0 MeV Ni^+ ions at Takasaki Ion Accelerators for Advanced Radiation Application (TIARA), TARRI, QST. The Ni ion fluence was varied from 10^{13} to 10^{15} ions·cm^{-2}. The ion irradiations were performed at room temperature. After the ion irradiation, the KI overlayer was removed by water-rinsing. The atomic and electronic structure of ion-irradiated KI/graphene/SiO_2 were characterized using micro-Raman spectroscopy, near edge X-ray absorption fine structure (NEXAFS) and X-ray photoelectron spectroscopy (XPS). NEXAFS measurements were performed at the BL-27A station of the Photon Factory in High Energy Accelerator Research Organization (KEK-PF) and at the BL-8 of the SR center in Ritsumeikan University.

Figure 1 shows C *K*-edge and I L_3-edge NEXAFS spectra of 10^{15} ions·cm^{-2} ion-irradiated KI/graphene/SiO_2. Several significant features are observed in Fig. 1 (a); a sharp peak at 285.4 eV (C1), structures at around 286-289 eV (C2) and two peaks at 297.2 and 299.8 eV (C3). C1 and C2 are assigned to C 1*s* to π^* and σ^* transitions, respectively. C3, which is absent in pristine graphene/SiO_2, may be associated with the iodine doping. It is found that the intensity of C1 decreases significantly compared with that of C2 in ion-irradiated KI/graphene/SiO_2, which is expected for the sp^2-sp^3 transition induced by iodination. In the I L_3-edge NEXAFS spectrum shown in Fig. 1 (b), we see a shoulder at around 4560.4 eV (I1), a peak at 4567 eV (I2) and broad structures at around 4578-4589 eV (I3). These spectral features in ion-irradiated KI/graphene have certain amount of similarity to those of organoiodine compounds [3]. I1 is assigned to 2*p* to 5*d* transitions. I2 and I3 are assigned to the transitions from 2*p* to empty states of *s*- and *d*-like character, which is associated with the hybridization of carbon and iodine electronic states to form π^* and σ^* orbitals. The NEXAFS results lead to the conclusion that in KI/graphene/SiO_2 the high-energy ion irradiation causes iodination of graphene by the formation of the C-I bond. The quantitative analysis of iodination was carried out using the core-level XPS spectra (not shown here). It is calculated that the 10^{15} ions·cm^{-2} irradiation of KI/graphene/SiO_2 causes 5-7% iodination from the peak intensity ratio between C 1*s* and I 3*d*. It has been reported that iodographene is unstable and spontaneously decomposing compound [4] and that the iodine doping has been performed as elemental iodine in the form of triiodide (I_3^-) and pentaiodide (I_5^-) [5]. In contrast to these reports, with consideration of the absence of Raman signals of elemental iodine in ion-irradiated KI/graphene/SiO_2, it can be said that we successfully obtained iodographene with the C-I bond in this study. We propose that the high-energy ion irradiation can be useful as a novel tool for heteroatom doping into the two-dimensional material.

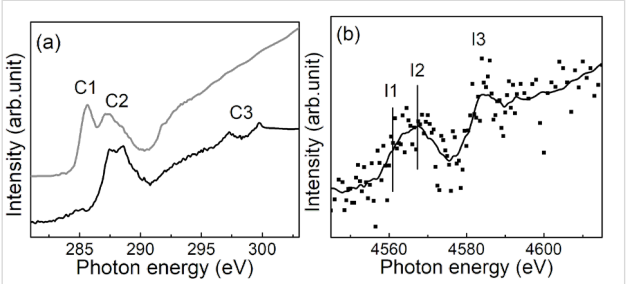

Fig. 1. (a) C *K*-edge and (b) I L_3-edge NEXAFS spectra of 10^{15} ions·cm^{-2} irradiated KI/graphene/SiO_2 (black) and pristine graphene/SiO_2 (grey). The KI layer was removed by water-rinsing before NEXAFS measurements.

Acknowledgments

XAFS experiments were performed as part of the projects accepted by the Photon Factory Program Advisory Committee (PF-PAC Nos. 2018G518, 2020G589).

References

[1] S. Entani *et al.*, RSC. Adv. **6**, 68525 (2016). S. Entani *et al.*, Nanotechnology **31**, 125705 (2020).
[2] S. Entani *et al.*, Surf. Sci. **704**, 121749 (2021).
[3] M. L. Schlegel *et al.*, Geochim. Cosmochim. Acta **70**, 5536 (2006).
[4] R. Zbořil *et al.*, Small **6**, 2885 (2010).
[5] G. Kalita *et al.*, J. Mater. Chem. **21**, 15209 (2011).

1 - 21 Saturation of collected charge induced by heavy ions on SiC-SBDs

M. Takahashi[a)], M. Iwata[a)], A. Takeyama[b)], T. Ohshima[b)], T. Makino[b)] and H. Shindou[a)]

[a)]Research Unit I, Research and Development Directorate, JAXA
[b)]Department of Advanced Functional Materials Research, TARRI, QST

Introduction

Silicon carbide (SiC) power devices are promising candidates for next generation space applications due to the attractive physical properties of SiC material. Many studies of SiC device behaviors under heavy ion irradiations have been reported and Kuboyama reported that a degradation mode having three characteristic regions in accordance with the bias voltage was observed by heavy ion irradiations with SiC Shottoky Barrier diode (SBD) as shown in Fig.1 [1].

However, it is needed to realize the SiC devices having higher breakdown voltage even in harsh radiation environment for applying practical use. The authors have a hypothesis that if the amount of collected charge observed in Region 1 reduces, the start voltage of Region 2 may be increased. Therefore, we aimed to confirm the LET dependence of the collected charge under low bias condition (Region 1) in this study.

Experimental

The device under test (DUT) was C4D10120 which is commercial SiC-SBD manufactured by CREE. Collected charge induced by heavy ions on the DUT measured in the same manner as [1]. ORTEC 142B charge sensitive pre-amplifier was used.

These experiments were evaluated by using TIARA at QST. A monoenergetic heavy ion beam was used for the evaluation. Table 1 lists ions used in this study and related information. Linear energy transfer (LET) and the ion range in SiC were calculated by SRIM [2]. All the irradiations were performed at normal incidence and at room temperature.

Results and Discussions

Figure 2 shows the results of collected charge as a function of the reverse bias voltage observed with Xe, Kr and Ar ion species. All data was taken from the same device. As shown in Fig.2, the saturation of collected charge was confirmed with Xe, Kr ions at 2~3 pC under the same bias voltage. In other words, collected charge did not increase in proportion to the LET with Kr or Xe ions. The saturation of collected charge was lower than the ideal generated charge calculated using the values of energy. It has been reported that similar phenomenon is observed in diamond, Si, and SiC detectors; it is called "Pulse Height Defect (PHD)".

The saturation of collected charge induced by heavy ions on commercial SiC-SBD was observed as the same of detectors in this study. In the future, we plan to demonstrate the hypothesis by investigating the effect between the amount of collected charge observed in Region 1 and the starting voltage of Region 2. In addition, since a phenomenon seemed to be PHD also occurred in SiC-SBD, we plan to compare the amount of collected charge with SBDs of other materials.

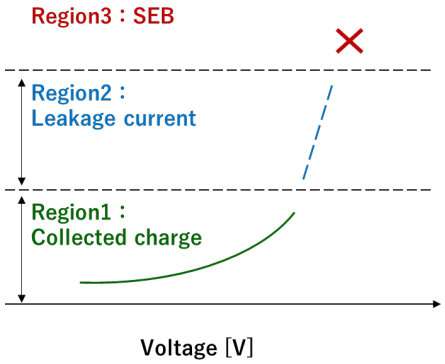

Fig. 1. Characteristic regions observed by heavy ion irradiations on SiC Schottky diodes.

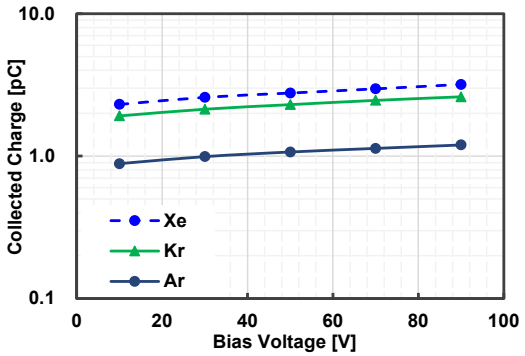

Fig. 2. Collected charge under low reverse bias voltage observed with Xe, Kr and Ar ion species.

Table 1
Characteristics of ion species used in this study.

Ions	Initial Energy [MeV]	LET at SiC surface [MeV/(mg/cm^2)]	Range in SiC [μm]
^{129}Xe	454	73.2	25.2
^{84}Kr	322	42.3	26.7
^{40}Ar	150	16.3	25.8

References

[1] S. Kuboyama *et al.*, IEEE Trans. Nucl. Sci. **53**, 3343 (2006).
[2] J. F. Ziegler *et al.*, "The Stopping and Range Ions in Matter," 2010.
[3] N. Iwamoto *et al.*, IEEE Trans. Nucl. Sci. **61**, 3732 (2014).
[4] E. F. Aguilera *et al.*, IEEE Symposium Conference Record Nucl. Sci. **2**, 784 (2004).

1 - 22 Effects of hydrogen storage characteristics of hydrogen absorption materials by ion irradiation

H. Abe[a)], R. Morimoto[b)] and H. Uchida[b)]

[a)]Department of Advanced Functional Materials Research, TARRI, QST
[b)]Course of Applied Science, Graduate School of Engineering, Tokai University

The effect of ion irradiation on the rate of electrochemical hydrogen absorption by Pd, which is used as a negative electrode of the nickel-metal hydride battery, was investigated. In previous studies, surface modifications are crucial to improve the reactivity of hydrogen materials because the dissociation of H_2 molecules in a gas phase or the dissociation of H_2O molecules in an electrochemical process is the first step of the overall hydrogen absorption reaction rate in materials [1]. The dissociation of H_2 or H_2O molecules is markedly influenced by surface conditions of the material. The induction of vacancy in materials was found to be effective for an increase in the hydrogen absorption rate [2,3]. For the surface modification of materials, ion implantation with low energy is known to be a quite useful method. So far, we have systematically investigated the effects of surface oxide layers on the kinetics of hydrogen absorption in hydrogen-absorbing metals [1]. These facts give the possibility that the hydrogen absorptivity in Palladium (Pd) is improved by surface modification due to ion irradiation.

Experimental

The samples used in this study were Pd sheets (99.99% purity) with a size of 15 × 15 × 0.1 mm^3. Regarding Pd, before irradiation, all samples were annealed for an hour at 1173 K in a flowing pure N_2 gas (99.9998% purity). Ion irradiation was made with argon ion (Ar^+) in acceleration energy of 350 keV, doses range from 1×10^{14} to 1×10^{17} cm^{-2} at room temperature using the 400 kV ion implanter at the TIARA. The temperature of the samples increased up to 353 K at a beam current of ~10 μA, and almost no annealing effect took place during the irradiation. For the electrochemical measurements of the hydrogen absorption rate of Pd (cathode), a Pt sheet with a size of 30mm x 30mm x 0.3mm and a purity of 99.98 wt.% was used as an anode. A Hg/HgO electrode was also used as the reference electrode in an open cell [4]. The rate of hydrogen absorption in the Pd samples was evaluated as a change in the current density mA(*g-alloy*)$^{-1}$ in 6M(*mol/l*)-KOH at room temperature. During the measurements, a constant voltage of -0.93 V was applied to the samples. In all experiments, no gas bubbles were observed during hydrogen absorption. Details of the electrochemical measurements have been reported elsewhere [4].

Results and discussion

Figure 1 shows hydrogen absorption curves of Pd samples before and after 350 keV Ar^+ irradiation. Typical electrochemical hydriding curves, non-irradiated, doses range from 1×10^{14} to 1×10^{17} cm^{-2} are measured at 298 K. The hydrogen reaction rate can be determined from a temporal change in the [H]/[Pd] value. The value of non-irradiated, 1×10^{14}, 1×10^{15}, 1×10^{16} and 1×10^{17} cm^{-2} samples were estimated to be [H]/[Pd] = 0.0018, 0.0035, 0.0037, 0.0052 and 0.0108 respectively for the initial stage at reaction time from 0 to 350 minutes. The hydrogen reaction rate of the ion irradiated sample was six times (max.) higher than that of the non-irradiated one. These results also support the assertion that the initial hydrogen absorption rate of Pd is enhanced by the introduction of vacancies due to ion irradiation.

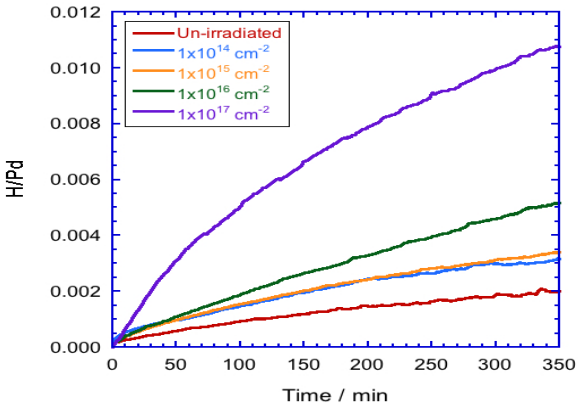

Fig. 1. Hydrogen absorption curves of Pd samples irradiated with 350 keV Ar^+ at doses range from 1×10^{14} to 1×10^{17} cm^{-2}.

Conclusion

The ion irradiation treatment of the surface of Pd using Ar^+ was found to enhance the initial rate of electrochemical hydrogen absorption in Pd. Ion irradiated Pd sample was found to induce a higher absorption rate than that of the non-irradiated one. The initial hydrogen absorption rate was also found to increase with increasing irradiation energy.

These results suggest that defects introduced in Pd by ion irradiation facilitate the rate of nucleation and growth of hydride.

Further studies are required to elucidate the role of each ion in the improvement of the hydrogen absorption in Pd.

References

[1] H. Uchida, Int. J. Hydrogen Energy **24**, 861 (1999).
[2] H. Abe *et al.*, Mater. Sci. Forum **363-365**, 156 (2001).
[3] H. Abe *et al.*, Nucl. Instrum. Meth. Phys. Res. B **206**, 224 (2003).
[4] H.H. Uchida *et al.*, J. Alloy. Comp. **231**, 679 (1995).

1 - 23 Analysis of alfa-ray degradation characteristics of an InGaP solar cell for dosimeter application

M. Imaizumi[a)], T. Nakamura[a)], T. Sumita[a)], S.-I. Sato[b)] and T. Ohshima[b)]

[a)]Research and Development Directorate, JAXA
[b)]Department of Advanced Functional Materials Research, TARRI, QST

We have proposed to use a solar cell as a dosimetry device for the radiation measurement in the destroyed nuclear reactor vessels at Fukushima 1F [1]. One good candidate is InGaP solar cell, because its high radiation resistance against electrons and protons has been demonstrated as a space solar cell [2]. On the other hand, α (helium ion), β (electron), and γ-ray (photon) are the prior radiations in the nuclear vessels to be measured. Therefore, radiation resistance of InGaP solar cells against α and γ-ray has to be studied. Last year, we have reported potential resistance of InGaP solar cell to γ-ray [3]. In this study, we performed helium ion irradiation to an InGaP solar cell to investigate the α-ray resistance. The degradation characteristics of output parameters of the InGaP solar cell were analyzed and compared with degradation by electrons and protons.

Single-junction InGaP solar cells were prepared for this study. The InGaP cell was not specially designed for a dosimeter device but already used for a radiation study elsewhere [4]. The InGaP solar cells were subjected to helium-ion (He^+) irradiation tests at QST Takasaki. The irradiated helium-ion energies were 1 and 5 MeV, which were estimated to be an equivalent energy of α–ray particles in the vessels. Current-voltage output characteristics of the cells under AM0, 1sun simulated solar light were measured before and after the He^+ irradiation.

The degradation tendency of three output parameters, short-circuit current (Isc), open-circuit voltage (Voc) and maximum power (Pmax) of the InGaP solar cell were obtained from the He^+ ion irradiations and the results were compared with those from electron and proton irradiations reported in Ref.[4]. To compare the degradation characteristics due to He^+ ion, electron and proton directly, we employed the displacement damage dose (DDD) for the radiation parameter instead of fluence. DDD is basically a product of fluence and the non-ionization energy loss (NIEL). First, we calculated the NIEL values of InGaP (In : Ga : P = 1 : 1 : 2) for He^+ ion, electron and proton [5], and then DDD values were deduced for 1 and 5 MeV He^+ ions, 1 nad 2 MeV electrons, and 0.2 and 3 MeV protons, which were irradiated on the InGaP solar cells.

The degradation characteristics of the InGaP solar cell as a function of DDD are depicted in Fig. 1. It is found that the damage by He^+ ion is not catastrophic despite that the mass of He^+ ion is four times heavier than that of proton (H^+), and the remaining factors are fairly equivalent with those by electrons and protons.

This study firstly revealed the α-ray resistance of InGaP solar cell. The results indicate that InGaP solar cells can be used as a dosimetry device for harsh radiation environment such as Fukushima 1F.

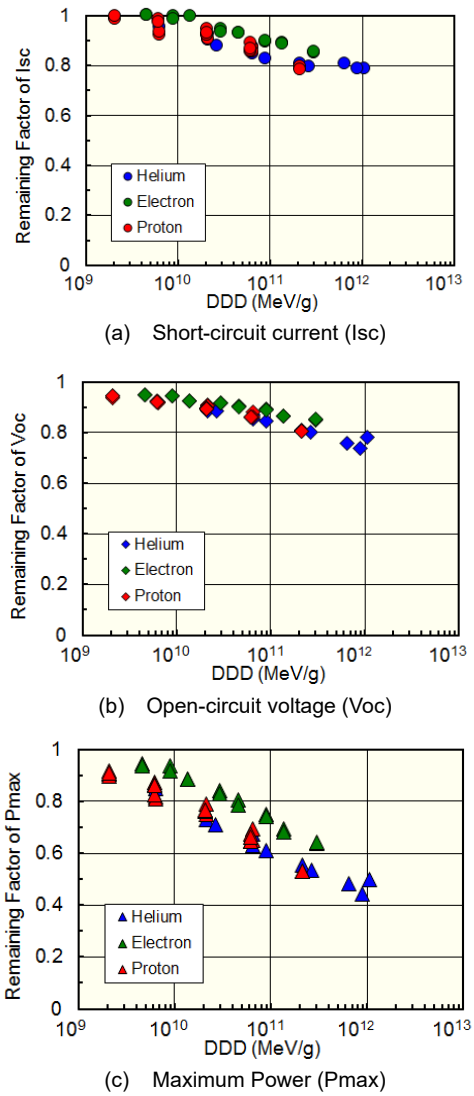

Fig. 1. Degradation characteristics of output parameters of the InGaP solar cell by helium, electron and proton irradiations expressed as a function of displacement damage dose (DDD).

References

[1] Y. Okuno *et al.*, J. Nuc. Sci. Tech. **56**, 851 (2019).
[2] M. Yamaguchi *et al.*, Appl. Phys. Lett. **70**, 1566 (1997).
[3] Y. Okuno *et al.*, J. Nuc. Sci. Tech. online (2019).
[4] M. Imaizumi *et al.*, Prog. Photovoltaics: Res. Appl. **25**, 161 (2017).
[5] https://sr-niel.org, Istituto Nazionale di Fisica Nucleare, Italy.

1 - 24 Separation of Dy and Nd using a fibrous adsorbent synthesized by radiation induced graft polymerization

H. Hoshina, J. Chen, H. Amada and N. Seko

Department of Advanced Functional Materials Research, TARRI, QST

Rare earths, including scandium, yttrium, and 15 types of lanthanoids, have become indispensable materials for the high-tech industry in recent years. Almost all the demand for rare earths is dependent on imports from a limited number of countries, as sources of rare earths are unevenly distributed throughout the world. Therefore, it is necessary to recycle used rare earths to ensure a stable supply of this material. Demand is particularly high for dysprosium (Dy) and neodymium (Nd), raw materials used in permanent magnets found in computers, home appliances, and hybrid cars. As a result of this demand, techniques for recycling Dy and Nd from used materials, such as permanent magnets, have been investigated. The most common method of recycling Dy and Nd from solids involves the use of an acidic solution to leach metals from the used materials, followed by solvent extraction purification. Metal purification by solvent extraction requires a large number of separation steps, a long processing time, and a large space for all of the necessary equipment. Hence, an adsorbent capable of efficiently separating metals in a short time has been developed in this study.

The adsorbent for the separation of Dy and Nd was synthesized by introducing octadecyl methacrylate with an alkyl chain that will act as a graft chain onto non-woven fabric with Radiation induced graft polymerization (RIGP), followed by the loading of 2-ethylhexyl hydrogen-2-ethylhexylphosphonate (EHEP) as a functional group by the hydrophobic interaction of the alkyl chains in both the graft chain and EHEP.

The adsorption performance of the adsorbent and the stability of the loaded EHEP was evaluated by column adsorption and elution tests. The column adsorption tests were carried out using a solution of 100 mg/L Dy and Nd at a space velocity (SV) of 100 h^{-1}. The SV is calculated by dividing the flow rate of the solution by the volume of adsorbent in the column. The adsorption curves of Dy and Nd were obtained by plotting C/C_0, where C_0 is the concentration of Dy or Nd in the feeding solution and C is the concentration of Dy or Nd in the effluent, versus the bed volume (BV). The results of adsorption tests are shown in Figure 1. In the case of Dy adsorption, all the Dy that passed through the column was adsorbed up to a BV of 80. After that, C/C_0 gradually increased and reached 0.98 at a BV of 400. In contrast, C/C_0 in Nd adsorption was 0 until a BV of 40, then it rapidly increased. Since the adsorbed Nd was replaced with Dy, the concentration of Nd in the effluent was greater than the initial concentration, and C/C_0 reached 1.3 at a BV of 144. The adsorption capacities of Dy and Nd in the column adsorption test were 43.6 and 4.2 mg/g adsorbent, respectively. The elution test was conducted with a 1 mol/L HCl aqueous solution, after the adsorbent packed in the column was thoroughly washed by passing deionized water through the column. The HCl solution was added to the column at an SV of 100 h^{-1}. The maximum concentrations of Dy and Nd in the effluent of the elution test were 373 and 38 mg/L, and elution ratio of Dy and Nd were 99 and 98%, respectively. Almost all the Dy and Nd were eluted within a BV of 80. After the elution test, the adsorbent was thoroughly washed with deionized water before the adsorption test was repeated. The repeated adsorption test was performed with the same conditions as the first adsorption test. The breakthrough curves of Dy and Nd adsorption for the repeated adsorption test showed a similar behavior as the first adsorption test, and the adsorption capacities of Dy and Nd were 43.0 and 5.2 mg/g adsorbent. These results indicated that the desorption of EHEP can be suppressed by introducing a long alkyl chain that creates strong hydrophobic interactions as a graft chain, and that high adsorption performance can be maintained throughout repeated adsorption testing.

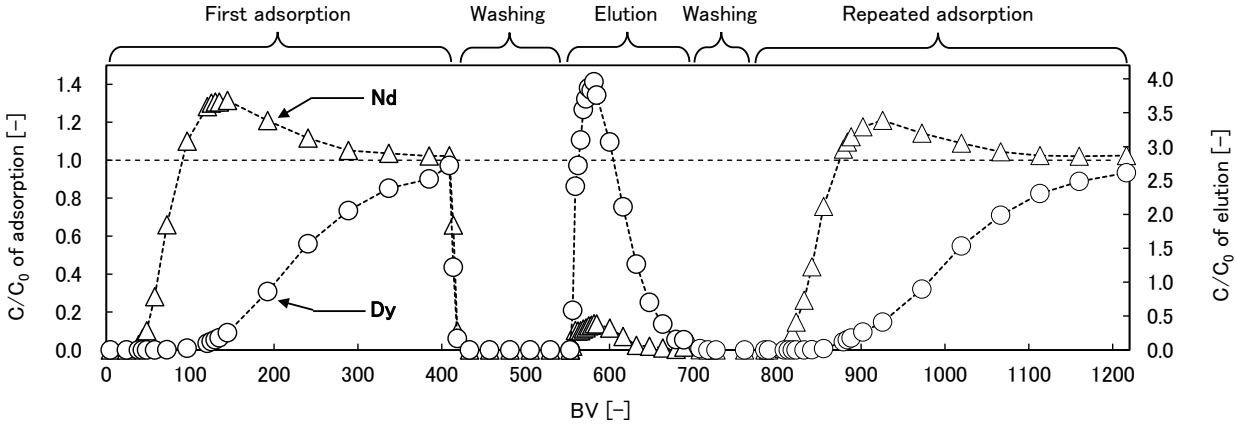

Fig. 1. The adsorption/elution profiles of Dy and Nd with fibrous adsorbent containing EHEP at SV 100 h^{-1}.

1 - 25 Prediction of grafting yield by multiple linear regression analysis

Y. Ueki, N. Seko and Y. Maekawa

Department of Advanced Functional Materials Research, TARRI, QST

Radiation-induced grafting can impart desired functions into trunk polymers without degrading their physical and chemical properties. However, in conventional grafting, researchers formulate hypotheses based on experience and intuition, and repeatedly verify them through experiments to obtain new materials. Therefore, conventional methods require long research periods, which in turn result in large amounts of labor and expenses for the commercialization of new materials. To solve the above problems, we believe that it is necessary to renew the conventional and inefficient processes based on precedent or on experience and intuition to a high-speed and highly efficient process that integrates experimental science with data science. The objective of this study is to predict grafting yields by using machine learning and quantify the importance of explanatory variables on the grafting yield.

Figure 1 shows a simple analytical flowchart from data collection to the evaluation of the grafting yield prediction model. Of the 49 methacrylate ester monomers, 41 monomers were selected as training data, and the rest 8 monomers were used in experiments as test data. The grafting yield, which is the objective variable, was obtained by actual grafting experiments. The explanatory variables for building the machine learning dataset were calculated by quantum chemical (QC) calculations using Spartan'18 software. 28 explanatory variables were employed based on the monomer structure information, natural bond orbital (NBO) charges of the methacrylate group, NMR chemical shifts of the methacrylate group, and FT-IR vibrational frequencies and intensities. Multiple linear regression (MLR) analysis was adopted as the machine learning method to build the grafting yield prediction model, and R-Studio was used for its calculation. The MLR model was performed using the "glmnet" algorithm. The prediction accuracy of the grafting yield prediction model was evaluated through the coefficient of determination (R^2) and the root mean square error (RMSE).

The MLR model with all 28 explanatory variables could not build a model with sufficient predictive accuracy because both the R^2 and RMSE values of the training and test data showed great deviations, i.e., R^2 and RMSE of the training data were 0.8321 and 52.11, respectively, whereas those of the test data were 0.4343 and 105.31, respectively. This is probably because those unnecessary explanatory variables were forcibly incorporated into the prediction model. Therefore, to exclude explanatory variables with low contribution, L1 regularization (Least Absolute Shrinkage and Selection Operator, LASSO) was applied as an explanatory variable selection criterion in model building. Two explanatory variables, NMR shift-related and FT-IR-related, were excluded by the application of LASSO. As shown in Fig. 2 (A), the prediction accuracy of the MLR model with LASSO was improved, and the application of LASSO was found to be effective in building the grafting yield prediction model. The R^2 and RMSE values of the MLR/LASSO model were 0.8313 and 52.23 for the training data, and 0.6635 and 79.62 for the test data.

The importance of explanatory variables on the grafting yield prediction was evaluated through the standard partial regression coefficient (β). The β values range from −1 to 1, providing the insight into the prediction model. Regardless of the absolute value, the explanatory variables with larger β values indicate a higher contribution to the prediction model, and conversely, the explanatory variables with β values close to zero indicate a lower contribution to the prediction model. Additionally, the positive β value leads to the increase of the grafting yield, whereas the negative β value leads to the decrease of the grafting yield. As shown in Fig. 2 (B), it was found that the explanatory variables such as the polarizability and the O1 NMR shift exhibited relatively high importance to the prediction of the grafting yield. Judging from the positive or negative signs of the β values, it was found that lower polarizability and $\nu_{C1=C2,\ s}$ showed to higher grafting yields, whereas higher O1 NMR shift and O2 NBO charge exhibited higher grafting yields.

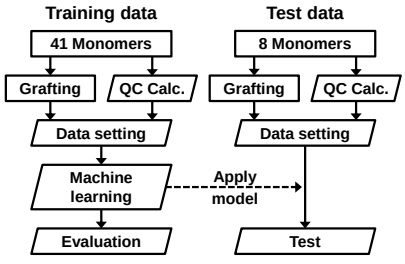

Fig. 1. Simple analytical flowchart from data collection to the evaluation of prediction model.

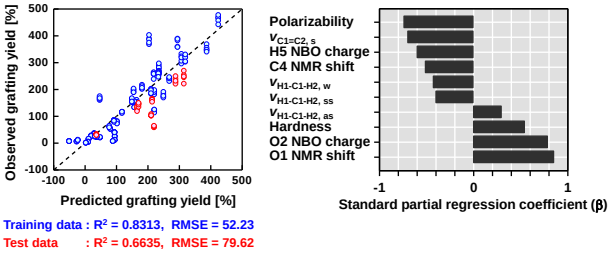

Fig. 2. MLR/LASSO results. (A) Predicted versus observed grafting yields plot. (B) The top 10 most important explanatory variables in the predictive MLR/LASSO model.

1 - 26 Surface Passerini three component reaction on cellulosic fabrics grafted with polymers featuring lignin-based components

K. Matsubara[a)], R. Kakuchi[a)], M. Omichi[b)] and N. Seko[b)]

[a)]Division of Molecular Science, Faculty of Science and Technology, Gunma University
[b)]Department of Advanced Functional Materials Research, TARRI, QST

Introduction

Because of a growing importance of material sciences, surface decoration of fabrics (or textiles) has been playing an indispensable role in modern science because they can lead to purpose-oriented applications. In addition, considering that the chemical sustainability has become also important factor, the use of bio-sourced compounds for material fabrication has been attracting methodology. For this, we have turned our attention to the employment of wood-biomass-sourced chemicals, where cellulose serves as a matrix material and a lignin-sourced vanillin as a reactive monomer unit. To take advantage of the vanillin as a reactive group, the Passerini three component reaction (Passerini-3CR) was successfully utilized as a surface modification protocol. In this work, lignin-derived methacrylated vanillin (MV) was graft polymerized from the matrix cellulose to anchor the poly(methacrylated vanillin) (PMV) on the cellulose surface (Cell-g-PMV). Then we aimed to accomplish the Passerini-3CR modification of the Cell-g-PMV, which can lead to sustainable surface chemistry of the Cell-g-PMV (Scheme 1).

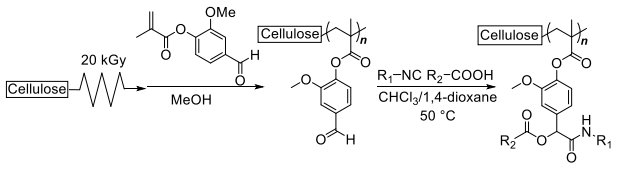

Scheme 1. Schematic overview of the radiation-induced graft polymerization of methacrylated vanillin and the surface Passerini-3CR with isocyanides and carboxylic acids.

Results and Discussion

As mentioned in the introduction, we focused on the surface Passerini-3CR of Cell-g-PMV. Thus, the Passerini-3CR reactivity of PMV was analyzed in the solution to ensure the successful surface Passerini-3CR. For this, PMV was subjected to the Passerini-3CR with model reactants of 1-adamantyl isocyanide and 1-hexanoic acid. Specifically, the PMV was reacted in $CHCl_3$ at 50 °C for 40 hours, where the reactant concentration of $[CHO]_0/[NC]_0/[COOH]_0$ was set as 1/3/3. ^1H NMR measurements revealed the high conversion of PMV aldehyde as evidenced by the significant decrease in the CHO peak at 9.9 ppm. In a clear contrast, peaks due to the 1-adamantyl isocyanide and 1-hexanoic acid newly developed. These observations revealed that the PMV aldehydes were converted into the corresponding α-acyloxy amides via the Passerini-3CR. In the same fashion to the above ^1H NMR measurements, FT-IR measurements also supported the amide generation via the Passerini-3CR. These results guaranteed that the Passerini-3CR showed feasibly high reactivity on the PMV polymer and thus their use as the surface reaction should be also feasible.

Finally, we thus targeted Passerini-3CR of Cell-g-PMV. For this, MV was graft polymerized from the cellulosic fabrics using radiation-induced graft polymerization technique. To demonstrate our proof of concept, bio-sourced chemicals were used for the surface modification of the Cell-g-PMV. Precisely, *N*-Boc-L-methionine and ethyl isocyanoacetate were selected as amino-acid-derived surface modifier. In the same fashion with the model solution reaction, *N*-Boc-L-methionine and ethyl isocyanoacetate were immobilized on the Cell-g-PMV surface with 50% aldehyde conversion via the Passerini-3CR. This reaction process was evidenced by nitrogen and sulfur atoms detected in the SEM-EDX measurements (Fig. 1). Based on our approach, fully bio-sourced fabrication of functional materials can be achieved without the use of additional catalysts or activators, taking advantage of the high compatibility between multicomponent reactions and bio-based compounds [1].

Fig. 1. SEM image and the corresponding SEM-EDX spectrum of the PMV after the Passerini-3CR with ethyl isocyanoacetate and *N*-Boc-L-methionine.

Conclusions

In this work, we have proved that the combination of radiation-induced graft polymerization and the Passerini-3CR should pave a way to sustainable material fabrics only sourced from bio-based components.

Reference

[1] R. Kakuchi *et al*., Polym. J. **53**, 523 (2021).

1 - 27 Radiation crosslinking gelatin gel applied as a scaffold with high transparency for tissue engineering

A. Kimura[a)], F. Yoshida[b)], M. Ueno[b)] and M. Taguchi[a)]

[a)]Department of Advanced Functional Materials Research, TARRI, QST
[b)]Graduate School of Science and Technology, Gunma University

Gelatin is a well-known biomaterial and used in several applications, including food, cosmetics, medicine, and pharmaceutical industries. It requires modification of the 3-dimensional mesh structure via chemical crosslinking techniques prior to its use as a biomaterial because the gelatin gel exhibits low resistance to heat and dissolves at human body temperatures. Glutaraldehyde (GA) is generally used as a chemical crosslinker and reacts with an amino group of gelatin to form a Schiff base structure connecting gelatin molecules. Chemically crosslinked gelatin has been used as a cell scaffold for tissue engineering. However, the bright field of the cell microscopic image of the chemically crosslinked gelatin becomes darker because the Schiff base moiety is yellow-colored. Therefore, to ensure that tissue engineering applications can be easily observed under a microscope, there remains a need for a highly transparent cell scaffold material. In this study, the potential of the radiation crosslinking technique to develop a gelatin scaffold for tissue engineering was evaluated by comparing with scaffolds made via chemical crosslinking [1].

The transparency of the gelatin crosslinked with radiation is higher than that of gelatin crosslinked via chemical crosslinking with GA, as shown in Figure 1. The lower transparency of the GA crosslinked gelatin was attributed to the formation of the Schiff base moieties. Transmittances of chemically crosslinked gelatin at GA concentrations of 0.2, 0.3, and 0.6 wt% were 99, 94, and 82% at 440 nm, respectively. The transmittance of the radiation-crosslinked gelatin at the concentration from 1 to 15 wt% in and around the visible region of the spectrum was higher than 95%, which is higher than that of GA crosslinked gelatin and similar to that of a polystyrene dish.

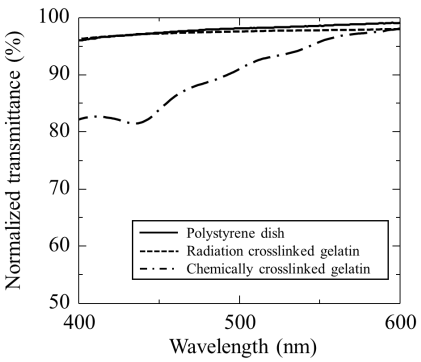

Fig. 1. Transmittance of polystyrene dish (solid line), radiation-crosslinked gelatin (dashed line, 15 wt% of gelatin, 30 kGy), and chemically crosslinked gelatin (dash-dotted line, 15 wt% of gelatin, 0.6 wt% glutaraldehyde aqueous solution).

The reason for the higher transparency of the radiation-crosslinked gelatin has not yet been clarified.

Radiation crosslinking mechanisms for gelatin have been discussed qualitatively [2], but quantitative studies are required to understand its higher transparency, as well as its potential for applications as a biomaterial. The composition ratio of the 15 amino acid residues in the gelatin before and after irradiation were analyzed and the proportions of phenylalanine, tyrosine, and histidine residues decreased significantly with increasing absorbed dose, as shown in the inset of Fig. 2. The proportions of the other 12 amino acids were nearly unaffected by γ–ray irradiation, as shown in Fig. 2, and these amino acids were considered not to have participated in the crosslinking reactions. Conversely, the amount of the cell adhesion active sequence in the radiation-crosslinked gelatin did not decrease, indicating that cell adhesion would be maintained even after γ–ray irradiation.

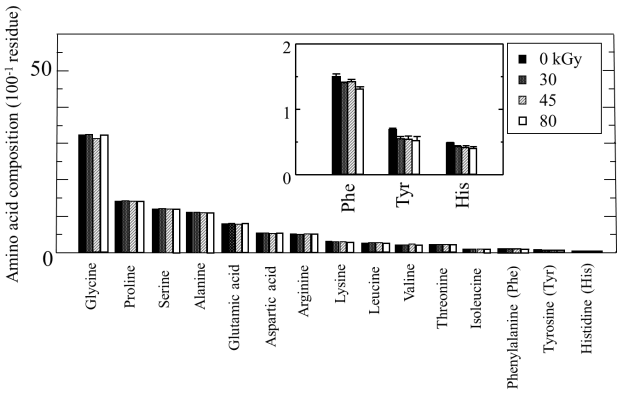

Fig. 2. Composition ratios of 15 amino acid residues in gelatin after γ–ray irradiation. Insert: Composition ratios of phenylalanine (Phe), tyrosine (Tyr), and histidine (His) as a function of doses absorbed.

Irradiation products were detected for a 10 wt% aqueous gelatin solution by HPLC analysis. 6 species were identified and quantified including 3,4-dihydroxyphenylalanine, *p*-tyrosine, dityrosine, *o*-tyrosine, *m*-tyrosine, and phenylalanine. These oxidized products have no absorption bands in the visible region; therefore, the radiation crosslinking technique can modify the gelatin while maintaining high transparency, in contrast to chemical crosslinking techniques.

References

[1] A. Kimura *et al.*, Radiat. Phys. Chem. **180**, 109287 (2020).
[2] W.M. Garrison, Chem. Rev. **87**, 381 (1987).

1 - 28 Application of radiation crosslinked peptide nanoparticles for tumor imaging

A. Kimura[a)], M. Ueno[b)], T. Arai[b)], K. Oyama[a)] and M. Taguchi[a)]

[a)]Department of Advanced Functional Materials Research, TARRI, QST
[b)]Graduate School of Science and Technology, Gunma University

There are various diagnostic methods for tumors in medical treatment, however, some of them impose drug side effects on the patients. Drug delivery systems (DDS) that efficiently deliver drugs to tumors have made great development in solving these problems. Nanoparticle-based contrast agents that can be applied to common biomedical imaging devices such as fluorescence imaging, MRI, CT, PET, and SPECT have also been developed. The size of the nanoparticles is adjusted to target the tumor cells and to allow them to pass through the perforated blood vessel of the tumor. The size-controlled particles attach to the tumor cells with a positive or negative charge and are subsequently taken up into the cells mainly via endocytosis. Therefore, techniques that synthesize nanoparticles with precisely controlled particle sizes, surface charge, and particle stability are required in order to accumulate nanoparticles to the tumor for safer diagnostics. This study aimed to form a peptide nanoparticle suitable for diagnostics by the use of the radiation crosslinking technique. The peptide particles with a size of ~100 nm, controlled surface potential, and particle stability in vivo were developed by γ-ray irradiation [1].

The peptides comprised radiation crosslinking amino acid residues; phenylalanine (Phe), tyrosine (Tyr), and histidine (His), which formed a crosslinked structure by the radiation-induced bimolecular reaction [2]. Glycine (Gly), which is the major component of native protein but not related to radiation crosslinking, was also selected as a peptide component. Therefore, we employed five amino acid residues per peptide, designed and synthesized six peptides to form a radiation-crosslinked nanoparticle platform as listed in Table 1.

Table 1
Composition of the designed peptides.

Abbreviation	Peptide Sequence
HGHGH	His-Gly-His-Gly-His
YGYGY	Tyr-Gly-Tyr-Gly-Tyr
FGFGF	Phe-Gly-Phe-Gly-Phe
FG4	Phe-Gly-Gly-Gly-Gly
FG3F	Phe-Gly-Gly-Gly-Phe
G5	Gly-Gly-Gly-Gly-Gly

Aqueous solutions of G5, FGFGF, FG4, FG3G were irradiated at 2.5 kGy and analyzed by LC-MS. In the case of G5 and FG4, only the monomer peak was detected and no multimerization reaction was observed. For FG3F, both the monomer and dimer peaks were observed. In addition, monomer, dimer, and trimer peaks were observed for FGFGF. Peptides containing one or two amino acid residues that contribute to the crosslinking reaction are unlikely to undergo multimerization. Therefore, the peptides containing three residues, namely Phe, Tyr, and His, were more suitable for the production of nanoparticles and used in the subsequent experiments.

Diameters of HGHGH, YGYGY, and FGFGF nanoparticles in water after γ-ray irradiation in the dose range from 5 – 15 kGy were investigated by dynamic light scattering measurement. The particle size range of YGYGY was controlled in the range 130 – 550 nm by the absorbed dose, while these of FGFGF and HGHGH were 140 – 220 nm and 80 – 90 nm, respectively. The stabilities of these nanoparticles were investigated in phosphate-buffered saline to simulate in vivo conditions. The HGHGH nanoparticles were stable for 6 days, while YGYGY and FGFGF were not. Moreover, the measured surface potential of the HGHGH nanoparticles after fluorescent labeling was -14 mV by electrophoretic light scattering, revealing that the electrostatic repulsion between these nanoparticles hindered their aggregation.

The cellular uptake test of the fluorescent-labeled HGHGH nanoparticles with a size of 80 nm was carried out using HeLa human cancer cells (Fig. 1). The confocal images revealed that the HGHGH nanoparticles were distributed inside the cells. The negative surface of the fluorescent-labeled HGHGH nanoparticles allows them to attach to the surface of the HeLa cells, whereby they are uptaken into the cell via endocytosis [3]. The radiation crosslinking technique can be employed to create a nanoparticle with great potential for application as nanosensors for tumor diagnosis.

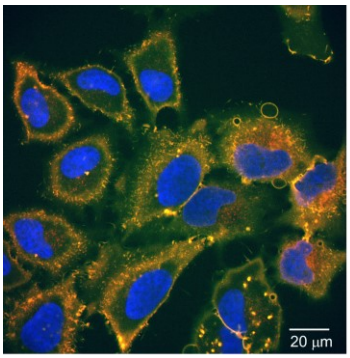

Fig. 1. Confocal image of red-fluorescent 80 nm HGHGH nanoparticles in HeLa cells. Blue: nuclei, yellow: cell membranes, and red: nanoparticles.

References

[1] A. Kimura *et al*., Nanomaterials **11**, 714 (2021).
[2] A. Kimura *et al*., Radiat. Phys. Chem. **180**, 109287 (2020).
[3] C. He *et al*., Biomaterials **31**, 3657 (2010).

1 - 29 NOx production in gas-liquid two-phase radiolysis - 1. Experimental setup -

K. Hata[a)], A. Kimura[b)], T. Sato[a)], C. Kato[a)] and M. Taguchi[b)]

[a)]Materials Evaluation Research Group, Nuclear Safety Research Center, JAEA
[b)]Department of Advanced Functional Materials Research, TARRI, QST

In the long-term debris removal operation at the Fukushima Daiichi Nuclear Power Station (1F), radionuclides (dissolved and particulate) eluted from debris may cause radiolysis of air as well as contaminated water. Because of the large volume of gas phase in the reactor buildings, gas-phase radiolysis could affect the production of radiolytic oxidants and the corrosion behavior of structural materials. Especially, nitrogen oxides (NOx), which is dominant species produced from gas-phase radiolysis, are known as strong oxidants. These nitrogen oxides are mainly produced by the reaction of excited nitrogen and oxygen in the air [1, 2]. However, it is also considered that NOx is produced from the reaction of excited nitrogen and water vapor without oxygen [3]. If water vapor makes a significant contribution to the NOx production, the anti-corrosion effect of purging the building with nitrogen may be overestimated. The purpose of this study is to elucidate the effect of γ-ray irradiation to gas-liquid two-phase systems on the production of oxidants including NOx to provide the basic data for the corrosive environment based on radiolysis in the 1F containment.

To maximize the effect of gas-phase radiolysis in a gas-liquid two-phase sample in the experiment, an irradiation method was considered. The ^{60}Co γ-ray irradiation facility, TARRI, QST was used for the irradiation. The sample in a glass irradiation vial was put on a lead block, which was laid on a height-adjustable lab jack. The sides and the front of the irradiation vial was also covered with lead blocks. These lead blocks divided the vial into two parts, an upper irradiated (unshielded) part and a lower shielded part. Figure 1 (above) shows the layout of the sample vial, shielding lead blocks, and the position of the pellet-shaped alanine dosimeter for dose evaluation. To measure dose distribution, the vial without aqueous solution and the dosimeters were set at a position of 1 kGy/h in the irradiation room and then irradiated with γ-rays for 0.5 to 2 h. Dose distribution in the height direction of the sample vial was determined by the ESR signal of the alanine dosimeters. Square points in Figure 1 (bottom) show the absorption dose measured when the upper end of the shielding lead was adjusted at the position of 50 mm below the upper end of the ^{60}Co source. It was confirmed that the upper part without shielding was irradiated as planned and that the dose at the lower part was lowered by more than one order of magnitude compared to the upper part. The experimental results of dose evaluation were in agreement with the simulated one by PHITS code [4] (Figure 1 below, line) although there is a slightly difference at the boundary of the shield (33-45 mm). The results of the PHITS analysis

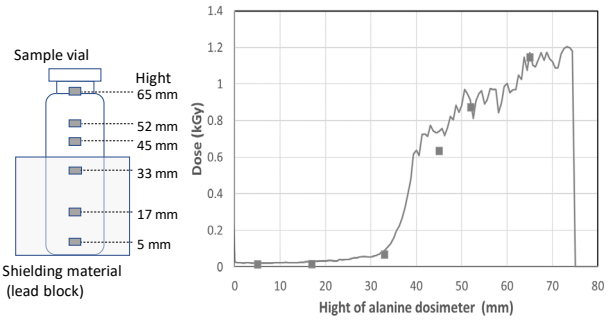

Fig. 1. The layout of the sample vial, shielding lead block and the position of the pellet-shaped alanine dosimeter for dose evaluation (left). Dose evaluation of alanine dosimeter (■) and simulation by PHITS code (line)(right).

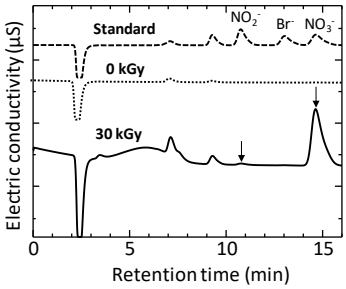

Fig. 2. Ion chromatogram of anion standard solution and air-saturated water before and after γ-ray irradiation at 30 kGy.

show that the low dose region from the bottom of the sample vial to 20 mm was affected by γ-rays through the lead block, and the increase in the dose from 30 to 50 mm was responsible for the scattered γ-rays from the top of the lead.

As a preliminary experiment for the analysis of the oxidizing products generated in the gas phase, air-saturated Mill-Q water was irradiated with γ-rays at 30 kGy and analyzed with ion chromatography connected to an anion analysis column. Qualitative and quantitative analysis was performed using an anion standard reagent as shown in Figure 2. The concentration of NO_2^- and NO_3^- was estimated to be about 10 and 15 μmol / L, respectively.

In the future, radiolysis experiments of gas-liquid two-phase systems will be carried out, and the effect of irradiation conditions, such as purge gas(atmosphere) and dose rate, will be investigated.

References

[1] G.R. Dey, Radiat. Phys. Chem., **80**, 394 (2011).
[2] O. Tokunaga *et al.*, Radiat. Phys. Chem. **24**, 145 (1984).
[3] A.R. Jones, Radiat. Res. **10**, 655 (1959).
[4] T. Sato *et al.*, J. Nucl. Sci. Tech. **55**, 684 (2018).

1 - 30 Synthesis of polycrystalline and amorphous double-thick-walled silicon carbide nanotubes

T. Taguchi[a)], S. Yamamoto[b)] and H. Ohba[a)]

[a)]Tokai Quantum Beam Center, TARRI, QST
[b)]Department of Advanced Functional Materials Research, TARRI, QST

Silicon carbide (SiC) is a promising non-oxide ceramic material used in a wide range of applications. SiC has been utilized as a wide-bandgap semiconducting material and structural material under high temperatures, owing to its attractive chemical, physical, and mechanical properties. Conversely, nanomaterials may possess excellent and novel properties that differ from those of their bulk materials. In particular, we succeeded in synthesizing nanometer-sized single-phase SiC nanotubes with engrossing geometries [1]. Photoluminescence energy peaks were observed for these SiC nanotubes, which were higher than in the case of bulk SiC, indicating bioactivity for the first time and demonstrating a novel microstructural change by ion irradiation that differed from bulk SiC materials [2, 3]. Thus, SiC nanotubes have novel properties relative to bulk SiC materials. Therefore, the synthesis of new structured SiC nanomaterials with novel properties is required. Herein, we report the successful synthesis of polycrystalline and amorphous double-thick-walled (DTW) SiC nanotubes from multi-walled carbon nanotubes (MWCNTs) first time.

The MWCNTs (GSI Creos Corporation, Tokyo, Japan) were heated with Si powder (The Nilaco Corporation, Tokyo, Japan) at 1,200 °C for 30 h in a vacuum. The samples were then heated at 800 °C for 4 h in the air to remove unreacted MWCNTs and carbon layers. The samples heated in the air were immersed in a 5 M NaOH and then a 0.2 M HCl solutions to eliminate the thin SiO_2 layers. The molybdenum grid holder, which deposited the DTW SiC nanotubes, was irradiated with 200 keV Si^+ ions from 400 kV ion implanter at room temperature in TEM (Model JEM-4000FX, JEOL Ltd., Japan) to synthesize amorphous DTW SiC nanotubes. In-situ TEM observation of DTW SiC nanotube under Si^+ ions irradiation was carried out. The ion fluence was up to 9.2×10^{20} ions/m^2, and the corresponding irradiation damages for the SiC were calculated by SRIM 2008 to be 24.0 dpa.

Figure 1 shows the TEM images and selected area electron diffraction pattern of a typical polycrystalline DTW SiC nanotube [4]. These TEM images indicate that the SiC nanotube possesses a double-walled (DW) structure in which a thinner nanotube is enclosed within a thicker nanotube. Both outer and inner nanotubes had a wall thickness of more than 20 nm, regardless of their outer diameter. The average distance between the outer and inner nanotubes was found to be higher than 7 nm. No connected areas were observed in the DTW SiC nanotube with a spacing of more than 30 nm between the outer and inner nanotubes. According to Fig. 1 (a), the DTW SiC nanotube has an open-end structure. However, the DTW SiC nanotubes with the closed-end structure were also observed. When all the carbon was transformed into SiC, the volume of carbon swelled up to 2.2 times its initial size. Therefore, DTW SiC nanotubes with a perfect DW structure could not be synthesized without a wall thickness of at least 50 nm or more in MWCNTs [4].

The amorphous DTW SiC nanotubes were also successfully synthesized by the ion irradiation with 200 keV Si^+ at room temperature of polycrystalline DTW SiC nanotubes. The TEM images and selected area electron diffraction pattern of typical amorphous DTW SiC nanotube are shown in Fig. 2. The degree of crystallinity of the SiC nanotube was decreasing with growing irradiation damage, and the SiC crystals were completely amorphized when irradiated at 3.2 dpa. According to these TEM images, the DW structure in the amorphous SiC nanotube was maintained even after ion irradiation. When the irradiation damage increased up to 24.0 dpa, the amorphous DTW SiC nanotube altered to the amorphous SiC nanowire.

References

[1] T. Taguchi *et al*., J. Am. Ceram. Soc. **88**, 459 (2005).
[2] T. Taguchi *et al*., Appl. Surf. Sci. **403**, 308 (2017).
[3] T. Taguchi *et al*., Acta Mater. **154**, 90 (2018).
[4] T. Taguchi *et al*., Appl. Surf. Sci. **551**, 149421 (2021).

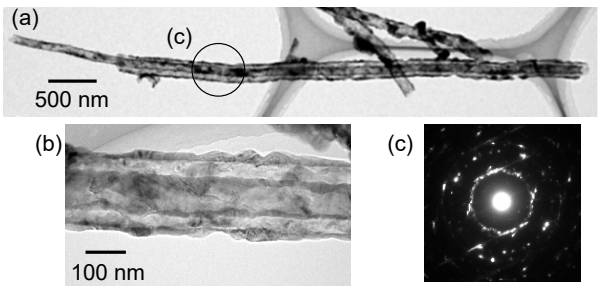

Fig. 1. (a) Low and (b) middle magnifications TEM images and (c) selected area electron diffraction pattern of typical polycrystalline DTW SiC nanotube.

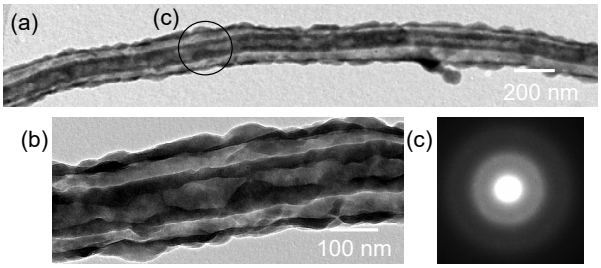

Fig. 2. (a) Low and (b) middle magnifications TEM images and (c) selected area electron diffraction pattern of typical amorphous DTW SiC nanotube.

1 - 31 Detection of gadolinium in surrogate nuclear fuel debris using fiber-optic laser-induced breakdown spectroscopy under gamma irradiation

R. Nakanishi[a)], M. Saeki[a)], I. Wakaida[b)] and H. Ohba[a)]

[a)]Tokai Quantum Beam Science Center, TARRI, QST
[b)]Collaborative Laboratories for Advanced Decommissioning Science, JAEA

Decommissioning of TEPCO Fukushima Daiichi nuclear power station (F1-NPS) needs information on the post-accident environment inside the nuclear reactor core. In the F1-NPS, molten fuel debris (mixture of melted fuel core (UO_2), fuel cladding (Zr), and construction materials (Fe)) might be submerged in water inside the reactor core. Besides, the debris contains gadolinium (Gd) as a key element. The relative abundance of Gd in the debris is an important factor for criticality control of the debris and a risk assessment of the retrieval process. Although it is crucial to determine its elemental compositions, nuclear fuel debris is currently inaccessible and has yet to be identified because of the high radioactivity in the reactor vessels. Thus, there is a compelling need for methods to remotely analyze the debris and detect the above elements in a high-radiation field.

For the internal surveillance of the damaged reactor in F1-NPS, we have proposed fiber-optic LIBS (FO-LIBS) and confirmed that the light transmission of the employed fiber optics is not degraded by the radiation exposure in the near-infrared region, which is used for the laser and emission transmission. In addition to the radiation resistivity, we have demonstrated underwater LIBS using simulated debris [1]. However, it is unknown how the LIBS emission is observed in an environment of high-dose radiation. In the present work, we reveal Gd emission lines applicable to Gd identification in the simulated nuclear fuel debris and obtain calibration curves that will prove robust against gamma irradiation.

As real fuel debris is not available as a sample, the LIBS measurements were performed using surrogate debris synthesized from mixed oxide materials containing Gd, Ce, Zr, and Fe with varying Gd concentrations (0 ~ 0.87 wt%). Cerium was employed as a surrogate for uranium based on the similarity of their electronic structures. Laser-induced breakdown plasma from the simulated fuel debris was generated by irradiation of a focused Nd:YAG laser beam (1064 nm, 7 ns, 5 Hz) through a 30 m fiber-optic cable. The laser energy was set to 10 mJ at the target. Emission spectra were acquired using an Echelle spectrograph ($\lambda/\Delta\lambda > 50{,}000$) equipped with an EMCCD (1 μs Delay time, 2 μs Exposure time) at the laser shots of 500. The dose rates tested were 0, 0.8, and 10 kGy/h, which were controlled by adjusting the distance between the ^{60}Co emitter and probe head installed on a motorized linear stage.

Figure 1 displays the representative LIBS spectra of the surrogate debris (Gd 0 wt%) measured before and during gamma irradiation. The spectrum during irradiation was recorded when the accumulated dose reached 5.4 kGy at 10 kGy/h. The spectral profiles appear congested, originating from the prominent lines of Ce and Zr, along with the minor lines of Fe and N. As shown in Fig. 1, gamma irradiation decreased the LIBS signal, particularly in the UV-Vis region (λ < 800 nm). The emission spectra of the surrogate debris show that the optical emission lines at 501.5 nm and 510.3 nm are suitable for Gd detection in nuclear fuel debris. For quantification of Gd, robust calibration curves against gamma irradiation were established from the intensity ratio of Gd (501.5 nm)/Ce (474.5 nm) emission lines as shown in Fig.2, exhibiting good linearity with the Gd concentrations. The limit of detection of Gd was calculated to be less than 0.1 wt%, regardless of the radiation dose rate. These results demonstrate that FO-LIBS is a potential tool for in situ and remote analysis of nuclear fuel debris [2].

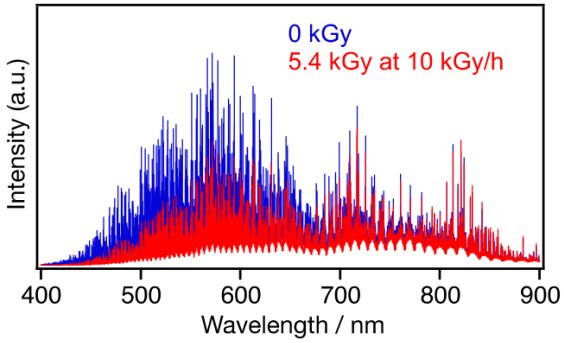

Fig. 1. Emission spectra of the surrogate nuclear fuel debris with and without gamma irradiation at a dose rate of 10 kGy/h.

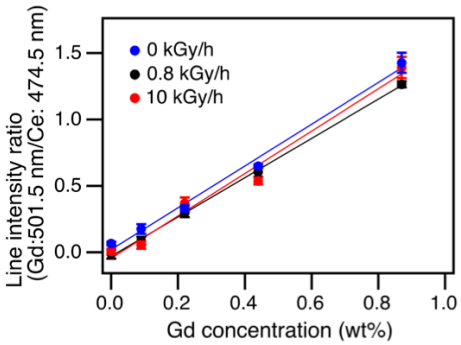

Fig. 2. Calibration curves derived from the intensity ratio of Gd 501.5 nm/Ce 475.5 nm lines.

References

[1] M. Saeki *et al.*, J. Nucl. Sci. Technol. **51**, 930 (2014).
[2] R. Nakanishi *et al.*, Appl. Sci. **10**, 8985 (2020).

1 - 32 Quantitative evaluation of lithium concentration in all-solid-state battery electrode cross sections using micro-PIGE elemental analysis

Y. Yamada[a)], G. Fukunishi[b)], K. Suzuki[a)], R. Kanno[a)], T. Satoh[c)], M. Finsterbusch[d)], T. Kamiya[e)] and K. Mima[f)]

[a)]Institute of Innovative Research, Tokyo Institute of Technology
[b)]Department of Chemical Science and Engineering, Tokyo Institute of Technology
[c)]Department of Advanced Radiation Technology, TARRI, QST
[d)]Institute of Energy and Climate Research, Forschungszentrum Jülich GmbH
[e)]Graduate School of Science and Technology, Gunma University
[f)]Institute of Laser Engineering, Osaka University

Introduction

In all-solid-state batteries, contact between solids forms a reaction field for charge transfer; thus, an electrode structure design is essential for controlling the battery performance. Micro-PIGE analysis using a micro proton beam capable of measuring two-dimensional lithium distribution visualizes dynamic behavior of charge carriers at the electrode cross-section of a practical battery. This technique promises to contribute to the elucidation of localized phenomena in electrodes.

Variation of lithium distribution, which depends on the state-of-charge (SOC) for the battery, has been successfully visualized by micro-PIGE [1]. However, quantification analysis of the lithium in a composite electrode has not been demonstrated yet. Therefore, as the initial step, lithium distribution at the electrode cross-sections of all-solid-state batteries, which have different SOC, were measured by the micro-PIGE techniques in this study.

Experimental setup

We performed micro-PIGE analysis using the 3.0-MeV proton ion beam at TIARA. The spatial lithium distribution in the cross-section near the anode layer was obtained by γ-rays of $^{7}Li(p,p'\gamma)^{7}Li$. The pellet-type battery was composed of cathode ($LiNbO_3$-coated $LiCoO_2$ + $Li_{10}GeP_2S_{12}$), solid electrolyte ($Li_{10}GeP_2S_{12}$) and anode (amorphous TiS_3). The batteries having different SOC (0%, 75% and 100%) were prepared by galvanostatic charge/discharge process with a current density of 0.12 mA/cm^2. The cross-sections of the pellets were smoothed by Ar ion beam milling (IM4000, Hitachi high-tech) and set in a sealed measurement cell with a 5-μm-thick Kapton film window. After that, a micro proton beam was scanned over a 100 μm × 100 μm area near the anode, and the γ-ray information signals were integrated for 20 minutes for each sample.

Results

Figure 1 shows the γ-ray intensity profiling near the interlayer between the anode and solid electrolyte layer. Since the lithium concentration in the $Li_{10}GeP_2S_{12}$ solid electrolyte region did not change during the charging process, the γ-ray intensities from all samples are comparable. In contrast, in the amorphous TiS_3 anode region, the difference in γ-ray intensity was observed according to the SOC, suggesting that it reflected the difference in lithium concentration in the electrode.

Figure 2 shows the relationship between the average γ-ray intensity in the anode region and the anode composition estimated from the electrochemical capacity. The lithium amount in the anode layer estimated from the γ-ray intensity showed a proportional relationship with the estimated one from the electrochemical capacity. This suggests that the SOC can be estimated from the γ-ray intensity using a linear relationship. Since the accurate estimation of the SOC is extremely important in operating in-situ observation, we plan to investigate the lithium quantification accuracy in detail.

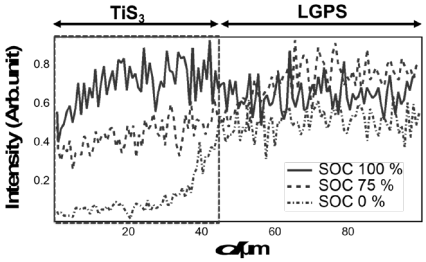

Fig. 1. The SOC dependent γ-ray intensity profile near the interlayer between the anode and solid electrolyte. (100 μm × 100 μm)

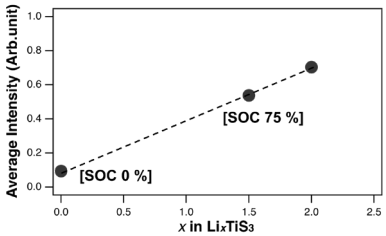

Fig. 2. The interrelationship between the average γ-ray detection intensity in the anode region and the anode composition estimated from the electrochemical capacity.

Acknowledgments

This project has been supported by the NEDO-BMBF Japan-German collaboration program.

Reference

[1] Y. Yamada *et al.*, Electrochemistry **88**, 45 (2020).

1 - 33 IBIL spectra obtained by different ion beams

S. Watanabe[a)], M. Nakahara[a)], Y. Yuri[b)], T. Yuyama[b)], Y. Ishii[b)], M. Koka[c)] and N. Hagura[d)]

[a)]Nuclear Fuel Cycle Engineering Laboratories, JAEA
[b)]Department of Advanced Radiation Technology, TARRI, QST
[c)]Beam Operation Co., Ltd.
[d)]Atomic Energy Research Laboratory, Tokyo City University

Introduction

Ion beam induced luminescence (IBIL) analysis is one of promising technologies to evaluate structure of complexes consists of cations and organic compounds. Our group has already shown its applicability to structural analysis of complex formed in adsorbent for the reprocessing technology [1, 2]. In the previous studies, luminescence of various complexes of Eu^{3+} were observed, and profile of the luminescence depended on specie of ligands coordinating around Eu^{3+}. The characteristic line spectra were assigned to be $^5D_0 \rightarrow {}^7F_J$ (J = 0,1,2,3,4,5,6) transition of 4f electron in Eu^{3+} [3], and some of them are known to be sensitive to symmetry of ligands around Eu^{3+} ion. If the number and kind of spices coordinating around an attracting light source is known, information of symmetricity of the ligands must be evaluated by the analysis. Therefore, combination of IBIL and other technology such as Extended X-ray Absorption Fine Structure would be a powerful tool to investigate the complexes.

So far, the luminescence induced by H^+ irradiation have been observed. However, influence of species irradiated on samples was not evaluated. High LET ion beam is expected to bring different electron excited states and different transition spectra, and those must give further information about structure of the complexes. In this study, IBIL spectra induced by 2 different ion beams were obtained and influence of the beam was discussed.

Experimental

N,N,N',N',N'',N''-hexaoctylnitrilotriacetamide (HONTA) was impregnated into styrene-divinyl benzene copolymer coating around porous particles, and Eu^{3+} was loaded into the adsorbents from 0.01 M nitric acid solution.

The IBIL measurements were performed using the ILUMIS system equipped in the light-ion microbeam line connected to a 3-MV single-ended accelerator in TIARA [4] and LB beamline of AVF cyclotron in TIARA. In the ILUMIS and cyclotron systems, 3 MeV proton beam and 107 MeV Ar^{8+} beam were irradiated on the adsorbent attached to a sample holder, respectively. The IBIL Spectra were observed by an UV-vis spectrometer (Solid Lambda CCD, Spectra CO., Ltd.).

Results and discussion

The IBIL spectra obtained by 3 MeV H^+ and 107 MeV Ar^{8+} irradiations are shown in Fig. 1, where intensity of the profile was normalized. 3 characteristic line spectra were observed in 3 MeV H^+ system at 580 ($^5D_0 \rightarrow {}^7F_1$), 620 ($^5D_0 \rightarrow {}^7F_2$) and 690 ($^5D_0 \rightarrow {}^7F_4$) nm. In the 107 MeV Ar^{8+} system, spectra at 740 ($^5D_0 \rightarrow {}^7F_5$) and 820 ($^5D_0 \rightarrow {}^7F_6$) nm were also observed. The $^5D_0 \rightarrow {}^7F_5$ and $^5D_0 \rightarrow {}^7F_6$ transition peaks were not clearly observed in previous studies, and discussion about the transition has not been important. Irradiation of the high energy particle enable to observe those peaks, precise investigation on the spectra and accumulation of spectroscopic data of known compounds might bring beneficial information about the structural analysis.

A broad peak at 350 nm was newly observed by the Ar^{8+} irradiation, and the peak is assigned to be transition from $^5H_3$ state whose energy is higher than that of $^5D_0$ to ^7F_J (J = 0,1,2,3,4,5,6) states. The high energy particle is considered to contribute the new emission, and high LET might be effective to obtain emissions. Database of the emission from various compounds is required to evaluate the experimental data.

Influence of LET of ion beam on IBIL spectra was experimentally observed, and new peaks were revealed to be obtained by high energy particle irradiation. Collection of emission data from standard samples is expected to contribute interpretation of the spectra.

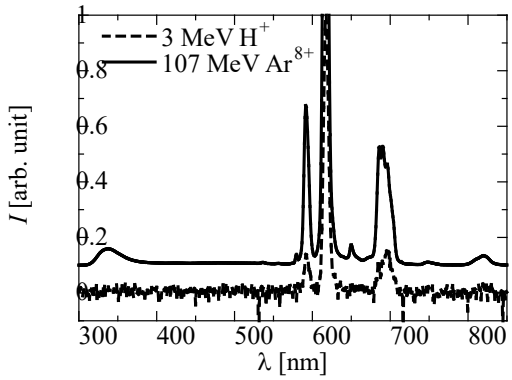

Fig. 1. IBIL spectra of Eu(III) loaded adsorbents

Acknowledgments

A part of this work is supported by the Innovative Nuclear Research and Development Program from the Ministry of Education, Culture, Sports, Science and Technology of Japan.

References

[1] S. Watanabe *et al.*, Nucl. Instrum. Meth. Phys. Res. B **450**, 61 (2019).
[2] S. Watanabe *et al.*, Nucl. Instrum. Meth. Phys. Res. B **477**, 60 (2020).
[3] K. Binnemans, Coord. Chem. Rev. **295**, 1 (2015).
[4] W. Kada, *et al.*, Nucl. Instrum. Meth. Phys. Res. B **332**, 42 (2014).

1 - 34 Three-component domains in fully hydrated Nafion membrane characterized by partial scattering function analysis

Y. Zhao, K. Yoshimura, T. Motegi, A. Hiroki and Y. Maekawa

Department of Advanced Functional Materials Research, TARRI, QST

Perfluorosulfonic acid polymer membranes, such as Nafion®, are benchmark materials for a proton-exchange membrane and have been commercialized in residential and automobile fuel cells and electrolytic synthesis of chlorine and sodium hydroxide owing to their excellent proton conductivity and thermomechanical properties [1]. The properties of the Nafion membrane are closely related to its hierarchical structures upon hydration [1].

Hydration-induced phase-separated morphology of Nafion membranes has been extensively studied in the past decades using small-angle X-ray scattering (SAXS) and neutron scattering (SANS) methods. However, the detailed structure (such as size, shape, and connection) is still under debate and the quantitative assignment of the characteristic structure (such as the composition of the scattering objects) is ambiguous. This is because the traditional analysis depends on intensity profiles, $I(q)$, with q being the scattering vector, which can only qualitatively give the possible structures of all components, but not the quantitative structure information of each component in the membrane. Partial scattering function (PSF) analysis for each component in Nafion is a potential method to identify the detailed structure of each component, and the structural correlation between two components, and hence determine hierarchical structures of the hydrated Nafion [2].

Nafion membrane (NR-212, mass density = 1.97 g/cm^3) with a thickness of 50.8 μm was purchased from DuPont. The hydrated Nafion membrane was treated as a three-component system: the main-chain [–(C_2F_4)$_m$–C_2F_3– with $m \cong 6.5$], side-chain ($C_5F_{10}O_2$–SO_3H), and water. PSFs were quantitatively decomposed from nine $I(q)$ profiles obtained in the contrast variation SANS experiments using eq. (1) [2].

$$I(q) = (b_{MC} - b_{SC})(b_{MC} - b_W)S_{MC-MC}(q) + (b_{SC} - b_{MC})(b_{SC} - b_W)S_{SC-SC}(q) + (b_W - b_{MC})(b_W - b_{SC})S_{W-W}(q) \quad (1)$$

where b_i and S_{ii} are the scattering length density (SLD) and PSF self-term of the i component with i = MC: main-chain, SC: side-chain, and W: water. S_{ii} reflects the exact structure of the i component, and the cross-term S_{ij} ($i \neq j$) deduced from S_{ii}, gives the interaction between the i and j components and their positions relative to each other.

S_{ii} are plotted as a function of q in Fig. 1. It comprises three features in the representative q-regimes. To elucidate the structure, we use the Debye–Bueche (DB) model to fit the small-q upturn and the Teubner–Strey (TS) model to fit the peaks in the middle- and high-q regimes. The analysis of S_{ii} revealed the detailed structure of each component as shown in Fig. 2. In the large-scale (> 30 nm), structural heterogeneities with a size of > 65 nm were observed in the main- and side-chain domains but not in water domains. This large-scale structure was supported by AFM observation. In the middle-scale (5 – 30 nm), bicontinuous-like structure of the crystalline main-chain phase and the amorphous phase composed of the amorphous main-chain, graft and water, with a mean separation distance of 11 nm was observed, as a result of the main-chain semicrystalline templating effect. In the small-scale (< 5 nm), another bicontinuous-like structure exists in the amorphous phase with a mean separation distance of about 4 nm, indicating a well-connected water network responsible for the good membrane conductivity. PSF cross-term analysis for every two components suggested the location of each component, in that the main-chain domains tend to phase-separate from either the side-chain or water domains, but the side-chain and water domains are closely attached through sulfonic acid groups.

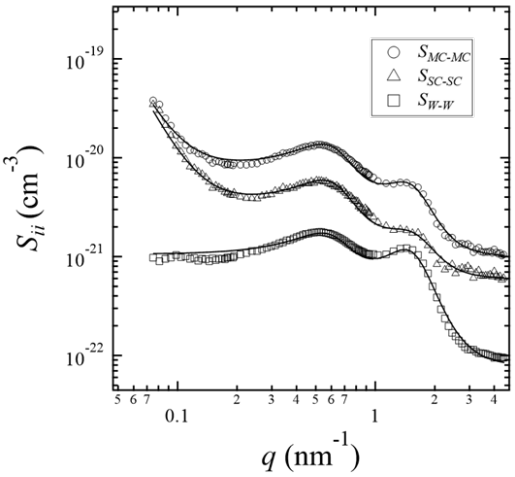

Fig. 1. PSF self-terms S_{ii} of fully hydrated Nafion (symbols) and the best-fitting results from structure models (solid lines).

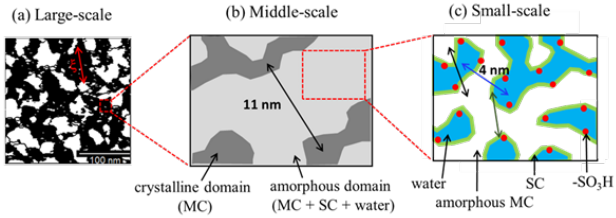

Fig. 2. Schematic of the hierarchical structure of the MC, SC and water domains in the fully hydrated Nafion membrane at (a) large-scale; (b) middle-scale; and (c) small-scale.

References

[1] A. Kusoglu *et al.*, Chem. Rev. **117**, 987 (2017).
[2] Y. Zhao *et al.*, Macromolecules. **54**, 4128 (2021).

1 - 35 Study on fusion neutron irradiation effects using multiple ion-beam irradiation

M. Ando[a)], J. Yu[a)], T. Nozawa[a)], H. Oka [b)] and N. Hashimoto [b)]

[a)]Department of Fusion Reactor Materials Research, RFI, QST
[b)]Faculty of Engineering, Hokkaido University

Reduced activation ferritic/martensitic steels (RAFMs) such as F82H and Eurofer97 are candidates for the blanket structural material for DEMO fusion reactors. It is especially important to evaluate the effects of 14MeV neutron irradiation on the mechanical properties of this material. However, fusion neutron irradiation facilities are not yet available. Therefore, irradiation data is mainly obtained by irradiation experiments (without He and H effects) in fission reactors. One of the irradiation features for the blanket structure material is the high-dose and high-energy neutron irradiation that leads to an accumulation of displacement damage along with high levels of He and H production. Therefore, our study is to obtain information about a particular behavior that is a specific part of the response under fusion neutron irradiation. Recently, we have conducted a series of ion irradiation experiments of RAFMs in the temperature range of 300 to 500 ˚C for doses ranging from 20 to 80 dpa in the TIARA facility. We are performing the post-irradiation examination (PIE) to obtain data on dose and temperature dependences of void swelling along with irradiation hardening using irradiated F82H specimens. On the other hand, micro-mechanical tests of ion-irradiated F82H are being performed using μ-tensile and μ-pillar test methods. Also, an evaluation of the sink strength for dislocation loops and helium bubbles on several grain boundaries in ion-irradiated RAFM is started by collaboration research with Hokkaido University.

The materials used in this study were F82H variants and Eurofer97. The irradiations were carried out with 10.5 MeV Fe^{3+} ions plus 0.38 MeV H^+ and/or 1.05 MeV He^+ ions. In multiple ion-beam irradiation, He and H implantation rates were fixed to be 10 and 40 appm/dpa, respectively.

Figure 1 shows the irradiation matrix achieved during the series of irradiation campaigns using the TIARA facility as of the end of 2020. Irradiation experiments have been almost conducted in the temperature range of 300 to 500 ˚C. The irradiation matrix is mostly fulfilled for single (Fe^{3+})/dual ($Fe^{3+}+He^+$) /triple ($Fe^{3+}+He^++H^+$) beam irradiation with the doses in 20 dpa incremental steps up to 80 dpa. On the other hand, it is necessary to perform some dual-H ($Fe^{3+}+H^+$) ion-irradiation experiments to evaluate the synergistic effect of He and H for microstructural evolution. Thus, dual-H irradiation has also been started in this irradiation campaign.

In parallel with these irradiation experiments, the PIE campaign has been started and part of the irradiation hardening behavior and microstructure evaluation data has been obtained.

Figure 2 shows examples of tensile properties obtained by μ-tensile testing for single ion-irradiated F82H at 300 ˚C, up to 10 dpa. In this time, μ-tensile properties could be obtained at the single-block F82H before/after irradiation. For without notches specimens, μ-yield stress (μ-YS) and μ-ultimate tensile strength (μ-UTS) of ion-irradiated F82H at 300 ˚C, 10dpa were higher than these of unirradiated F82H. On the other hand, the maximum strength values of μ-tensile specimens with notches are the almost same level for both the unirradiated and irradiated specimens. Since the local plastic constraint occurs around notches, it is considered that a kind of fracture stress (μ-FS) for a single-block F82H can be obtained by using μ-tensile specimens with notches. The data obtained in these activities will contribute greatly as simulated irradiation data by multiple ion-beam irradiation under the Japan-EU collaboration BA Phase-II program.

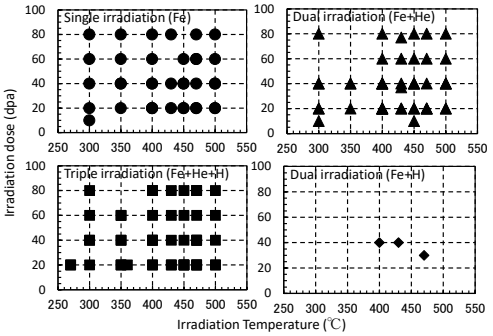

Fig. 1. Irradiation matrix achieved so far during the series of irradiation campaign using TIARA facility up to 2020.

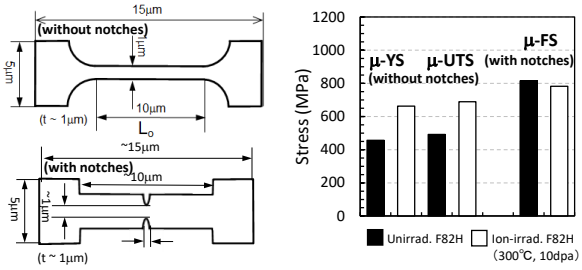

Fig. 2. Examples of the μ-tensile properties obtained by μ-tensile testing for irradiated F82H at 300 ˚C, 10dpa using with/without notched specimens.

Reference

[1] D. Hamaguchi *et al.*, QST Takasaki Annu.Rep. 2019, **QST-M-23**, 64 (2021).

1 - 36 Effects of self-ion irradiation on microstructure in tungsten

Ju-Hyeon Yu, M. Ando, T. Nozawa and H. Tanigawa

Department of Fusion Reactor Materials Research, RFI, QST

Powder-metallurgically-processed hot-rolled tungsten (PM-HR-W) is one of the strong candidates as divertor tile materials of fusion DEMO reactor considering the manufacturing capability, uniformity, and reproductivity. The low-temperature and grain boundary embrittlement caused by the recrystallization of the PM-HR-W is important to maintain the soundness of the cooling performance and the structures of the divertor components. Fine-grain structure as a result of hot-rolling (HR) and removal of elastic strain by stress-relieved (SR) heat treatment is advantageous in not only improving low-temperature embrittlement but also strengthening [1]. Particularly, the SR heat treatment on the pure W material with a lamella-like layered grain structure induced through the rolling process may enhance the resistance of embrittlement. Of particular importance is to understand the irradiation effect on such unique microstructure as well as mechanical properties. This study aims to investigate the effects of self-ion irradiation on tungsten materials as an initial assessment.

The effect of irradiation hardening was evaluated for three kinds of ITER-grade pure tungsten (IGW) with different manufacturing processes, i.e., original IGW, moderately cross-rolled W (CLW), and highly cross-rolled W (CHW) [2]. 18 MeV W^{6+} ions were irradiated to the maximum 18 dpa at 500 and 800 °C. Nano-indentation tests were conducted on the irradiated surface of W.

Figure 1 shows indentation hardening as a function of dose, clearly indicating irradiation temperature dependence of the saturation dose and hardness. For irradiation at 500 °C, a saturation of irradiation hardening was identified in the early stage (0.3 to 1.0 dpa) and the irradiation hardness did not exceed 7.5 GPa. By contrast, for irradiation at 800 °C, irradiation hardening was saturated at 3.4 dpa and hardness exceeded 7.5 GPa. Note that no marked difference in the trend was identified by W grade variation. The possible explanation for such difference will be evaluated by following microstructural observation by the transmission electron microscope.

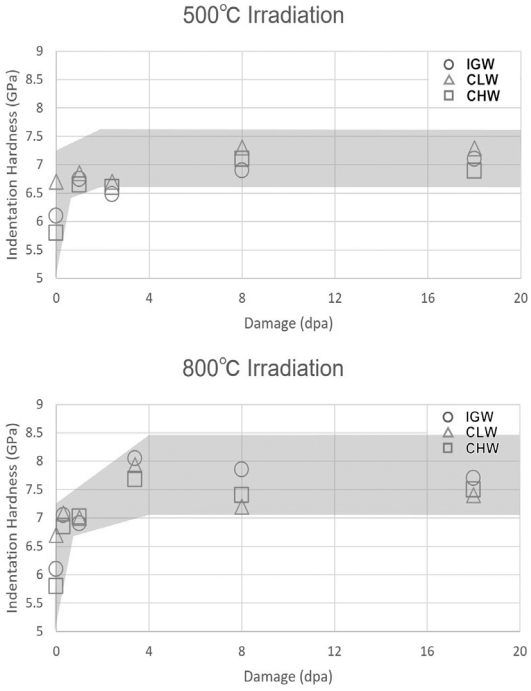

Fig. 1. Dose dependence of hardness of pure W.

In addition, irradiation hardening will be evaluated by the alternative way, i.e., micro-tensile test. The micro-tensile test is a method of testing that can be conducted generally using the focused ion-beam apparatus. This technique can be applied for ion irradiation specimens with a narrow irradiation area and micro-scall strength of the unique microstructure that cannot be obtained from the hardness test can be directly evaluated.

Figure 2 shows the fracture behavior of 2 types of tensile test methods (small specimen tensile test and micro-tensile test) using the non-irradiation tungsten specimens. The former clearly indicates that the bulk W specimen shows a brittle fracture in nature. It was however surprising that the micro-deformation of pure W materials was considerably large (ranged from 30 to 70%) depending on microstructure (approximately 50% in the figure). This implies that the key deformation mechanism of single grain and multi-grains with grain boundaries is different. From this aspect, it is suggested that the micro-tensile testing is more beneficial to evaluate the key mechanism of the irradiation effect on the pure deformation of the W grain and it is also advantageous that the grain boundary interaction can be separately evaluated. Further experiments for ion-irradiated W will be conducted as a next step.

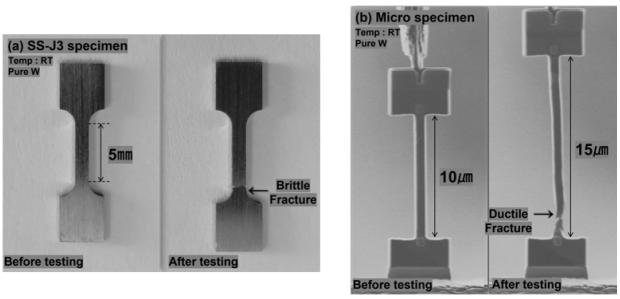

Fig. 2. Fracture behavior of (a) SS-J3 (small) specimen tensile test and (b) micro tensile test.

References

[1] S. Nogami *et al.*, Fusion Eng. Des. **140**, 48 (2019).
[2] J-H. Yu *et al.*, Fusion Eng. Des. **157**, 11679 (2020).

1 - 37 Irradiation tests of radiation hard components and materials for ITER blanket remote handling system

M. Saito, Y. Kawai, K. Nakata, Y. Noguchi and N. Takeda

Department of ITER Project, NFI, QST

Introduction

The ITER blanket remote handling system (BRHS) will replace the first walls in a gamma radiation environment having a dose rate of 250 Gy/h to 500 Gy/h. BRHS components have a radiation hardness requirement of 1 MGy, however, we set a radiation hardness target value of 5 MGy to increase the availability of the system. In this study, we investigated the radiation hardness of welded duplex stainless steel and bellows composed of thermoplastic polyurethane, PEEK, and SUS304.

Results

Samples (30 mm W × 70 mm L × 12 mm H) were made of SUS329J4L, a candidate material for the ITER BRHS articulated rail. Welding beads were deposited to fill a 5-mm-deep, 60° single bevel groove on each sample (manual GTAW, 1G). Samples were irradiated at 1,850 Gy/h up to 5 MGy in Gamma-ray irradiation facility. The atmosphere around the samples was kept at 30 °C and 43.2% relative humidity by using a thermostatic chamber within which a K_2CO_3 saturated salt solution was placed. Photos of the samples before and after irradiation are shown in Table 1. No corrosion was observed on sample surfaces nor on welds after 5 MGy of irradiation. SEM-EDX analysis was also performed, and no change in element mass concentration was observed in any sample even after 5 MGy of irradiation (Fig. 1).

The telescopic arm of the BRHS must be covered by bellows to prevent radioactive dust from infiltrating into the system. A bellows mock-up (410 mm W × 550 mm H, compressed length of 110 mm, extended length of 805 mm) was manufactured. The mock-up was irradiated at 1260 Gy/h at the side nearest the radiation source. The dose rate at the side opposite the radiation source was measured to be 280 Gy/h. The mock-up was rotated at the halfway point of the irradiation test to ensure that both sides of the mock-up were evenly irradiated up to 1 MGy. A 450-stroke expansion test was performed by using the test machine shown in Fig. 2. The appearance of the bellows after 450 strokes is shown in Fig. 3. The corners and adhesion zones of the bellows were illuminated and observed every 10 strokes; no cracks were observed. The differential pressure outside the bellows relative to inside the bellows was also measured. No sudden drops in pressure were observed, thus, we determined there were no cracks in the bellows.

Table 1
SUS329J4L samples at various irradiated doses.

Sample (welding method)	Irradiated dose [MGy]			
	0	1	2	5
Weld bead SUS329J4L (GTAW)	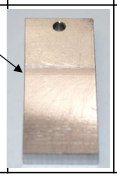			

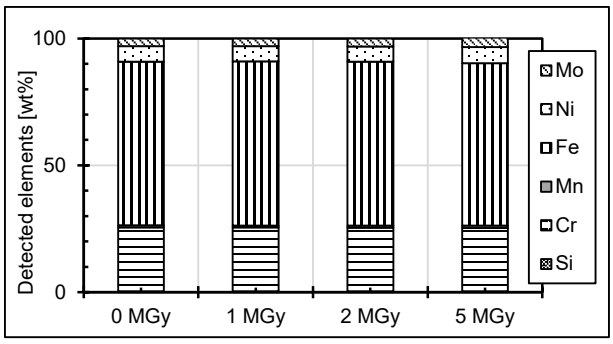

Fig. 1. EDX Element mass concentration.

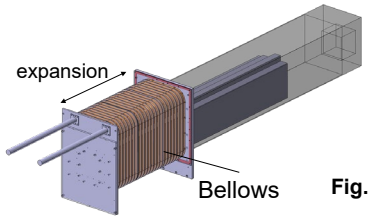

Fig. 2. Bellows test machine.

Fig. 3. Bellows after 450 strokes.

Conclusion

After irradiation up to 5 MGy under approximately 40% relative humidity at 30 °C, no corrosion was observed on all welded SUS329J4L samples. Welded SUS329J4L is unlikely to corrode owing to gamma irradiation in a humid environment, at least up to 5 MGy, therefore, we determined that SUS329J4L is suitable for use in the BRHS. The bellows mock-up was irradiated up to 1 MGy and satisfied the 450-stroke expansion test without cracking, thus, we determined that the bellows are radiation hard up to 1 MGy. In future work we will irradiate the bellows mock-up up to 2 MGy.

Acknowledgments

The authors would like to acknowledge M. Fujibayashi of Nabell Corporation; K. Mizuhashi, K. Takeuchi, K. Saga, and E. Nakamura of Beam Operation Co., Ltd.; and H. Seito from the Takasaki Advanced Radiation Research Institute who supported the irradiation experiments.

1 - 38 Gamma-ray irradiation experiment for ITER diagnostic systems in JADA III

S. Kitazawa, T. Hatae, M. Ishikawa, T. Oikawa, R. Imazawa, E. Yatsuka, H. Ogawa, K. Nojiri, T. Ushiki, T. Sugie, H. Murakami, K. Shimizu, T. Kikuchi and T. Yokozuka

Department of ITER Project, NFI, QST

JADA (ITER project Japan Domestic Agency) are developing to procure five diagnostic systems, microfission chamber (MFC), poloidal polarimeter (PoPola), Edge Thomson Scattering (ETS), divertor impurity monitor (DIM) and divertor infrared thermography (IRTh).

The reliability under the ITER radiation conditions of relevant equipment to be installed in the vacuum vessel, in the interspaces (IS) between the vacuum boundary and the biological shield and in the port cells (PC) outside the biological shields should be evaluated. In this study, we launched gamma-ray irradiation experiments in QST Takasaki Advanced Radiation Research Institute from 2018. The results obtained in the experiments are used important basses for showing that components can maintain their performances under the ITER radiation environment in the design review for each diagnostic system

In the experiments, optical and electrical components on DIM, IRTh, ETS, PoPola and MFC were irradiated up to 10 MGy for IS items or up to 200 kGy for PC items in 6th Cell at Co-60 2nd Building. Some optical fibres on DIM were irradiated in 1st cell at Food irradiation Building.

For DIM items, lens and some optical materials were verified [1], and then optical fibres for transmission of collected light from plasma and plasma faced metal mirrors are on-going to test. For IRTh items, change of transmittance by gamma-ray irradiation for optical elements (CaF_2, ZnSe (no coated and Anti-reflection (AR) coated), ZnS (no coated and AR coated), Si (no coated and AR coated)) were tested. For ETS items, four kinds of cerium-doped glasses (BK7G18, LF5G19, SF6G05 and LAK9G15 manufactured by Schott) were investigated their spectral transmissions. The samples were irradiated up to 10 MGy. For PoPola items, a Piezo actuator was tested to confirm its durability. For MFC items, pieces of mineral insulated (MI) cable were tested to observe the surface coating.

Several interesting results were obtained in the experiments. For DIM system, several optical fibres that are expected to possess radiation resistance have been selected from previous experiments [1]. These results contribute to evaluate the DIM measurement performance, and thus the further irradiation experiments are continuing to select the optimum materials with high irradiation resistance. Another experiment evaluates the deterioration on reflectance of metal mirrors due to corrosion by gamma-ray irradiation in humid environments, assuming introduction of moist air when breaking vacuum during maintenance in ITER. Mo specimens were irradiated with gamma-ray under various humidity environments to evaluate the deterioration of the reflectance. The Mo specimen could not maintain their reflectance under any of the humid conditions. The effect of corrosion on the mirror material should be investigated to optimize its optical performance. In IRTh system, no significant change in transmittance of the CaF_2 and Si was observed with gamma-ray irradiation up to about 5.9 MGy. On the other hand, ZnSe and ZnS showed several % degradation in the transmittance in the wavelength range of 1.2 μm to 20 μm when 5.9 MGy gamma-ray was irradiated. According to the SEM analysis, this degradation seems to be caused not by absorption but by surface oxidation or hydration. AR coating of ZnSe or ZnS mitigated the degradation in transmittance except near 3.0 μm. In ETS system, four types of glasses were tested. Figure 1 shows the comparison of spectral transmission between irradiated and non-irradiated samples. LF5G19 and BK7G18 had almost the same spectral transmission as when they were not irradiated. On the other hand, SF6G05 and LAK9G15 were colored and their spectral transmission decreased after gamma-ray irradiation. Since ETS uses signals with a wavelength of 590-1070 nm, the effect of changes in the spectral transmission of SF6G05 on measurement performance is minor.

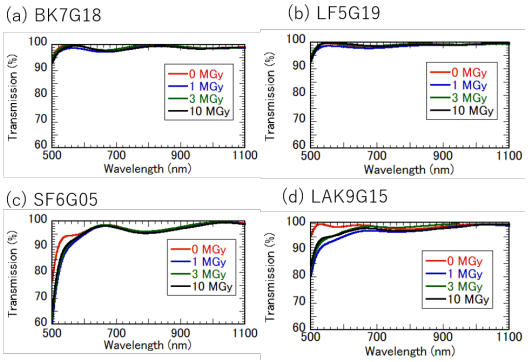

Fig. 1. Comparison of spectral transmission between 10-MGy irradiated and non-irradiated samples.

Acknowledgments

We would like to thank Naotsugu Nagasawa, Hajime Seito, Hiroyuki Okazaki, Shunya Yamamoto and Hiroshi Koshikawa (QST Takasaki) and Masahiro Shimoyama and Sakiko Haruyama (RADA) for their cooperation in the irradiation and observation.

Reference

[1] S. Kitazawa *et al.*, J. Plasma Fusion Res. **14**, 3405089 (2019)

1 - 39 Structural analysis of complex formed in adsorbent for gravity driven extraction chromatography

S. Watanabe[a)], Y. Sano[a)] and H. Matsuura[b)]

[a)]Nuclear Fuel Cycle Engineering Laboratories, JAEA
[b)]Atomic Energy Research Laboratory, Tokyo City University

Introduction

Trivalent minor actinides (MA(III): Am and Cm) contained in high level liquid waste (HLLW) generated from reprocessing of spent nuclear fuel possess radiotoxicity, and partitioning and transmutation of those elements are important strategy for sustainable nuclear energy [1]. In order to recover MA(III) from HLLW with practical process, our group is proposing a hybrid process consist of solvent extraction and extraction chromatography which is expected to reduce amount of secondary wastes and to have advantages in safety and economy over the processes of only the solvent extraction or the extraction chromatography. In this technology, MA(III) and lanthanides (Ln(III)) are recovered from high level liquid waste by the solvent extraction with centrifugal contactors, and MA(III) is separated from Ln(III) by gravity driven extraction chromatography. Existing extraction chromatography utilize porous silica support made by sol-gel method, and small pore and particle size generate large pressure drop of packed columns. The gravity driven extraction chromatography requires a new support for adsorbents, and we are conducting optimization in structure of the support to achieve efficient flow of mobile phase in columns and separation performance. In this study, local structure of complexes formed in adsorbent with various supports are investigated by Ion beam induced luminescence (IBIL) and Extended X-ray absorption fine structure (EXAFS) techniques to give beneficial information to the optimization study.

Experimental

Silica based porous supports were prepared by sol-gel or liquid column cutting method. Chemical composition of the liquid column was changed, and totally 3 kinds of support powders were obtained. N,N,N',N',N'',N''-hexaoctylnitrilotriacetamide (HONTA) was impregnated into styrene-divinyl benzene copolymer coating around those particles, and Eu was loaded into the adsorbents from 0.01 M nitric acid solution.

Eu-L_{III} edge (6.98 keV) EXAFS measurements were carried out at the BL5S1 beamline of Aichi Synchrotron Radiation Facility, Japan. The adsorbent was put in a SUS flat washer with 1 mm thickness and 10 mm inner diameter, and then sealed by two Kapton films.

The IBIL measurements were performed using the ILUMIS system equipped in the light-ion microbeam line connected to a 3-MV single-ended accelerator in TIARA [2]. A few particles of the adsorbent were put on a Kapton film attached to a sample holder, and sealed by a Kapton film. The samples were irradiated by 3 MeV proton beam with a beam current of about 100 pA. The IBIL Spectra were observed by an UV-vis spectrometer (Solid Lambda CCD, Spectra CO., Ltd.).

Results and discussion

EXAFS analysis showed that the coordination number of the nearest oxygen around the Eu(III) ion slightly changed depending on adsorption amount of Eu(III). However, distinct change in the local structure was not observed.

IBIL spectra obtained for the Eu(III) loaded adsorbents are shown in Fig. 1. Those line spectra were attributed to be $^5D_0 \rightarrow {}^7F$ transition of 4f electron in Eu(III) [3], and profile the $^5D_0 \rightarrow {}^7F_4$ transition spectra observed at 700 nm depended on the support particles. The $^5D_0 \rightarrow {}^7F_4$ transition profile is known to be sensitive to symmetry of atoms around Eu(III), therefore change in symmetry of the complex must be observed by the IBIL measurement.

Quantum chemical calculation on Eu(III)-HONTA complex showed that stability of complex depend on its symmetry, and change in the stability is considered to relate with adsorption/elution reactions. In order to select an appropriate support particle, relationship of chemical reaction with the structure of complexes will be precisely investigated.

Acknowledgments

This work is supported by the Innovative Nuclear Research and Development Program from the Ministry of Education, Culture, Sports, Science and Technology of Japan.

References

[1] IAEA, Technical Reports Series No. **435**, IAEA, Vienna (2004).
[2] W. Kada, *et al.*, Nucl. Instrum. Meth. Phys. Res. B **332**, 42 (2014).
[3] K. Binnemans, Coord. Chem. Rev. **295**, 1-45 (2015).

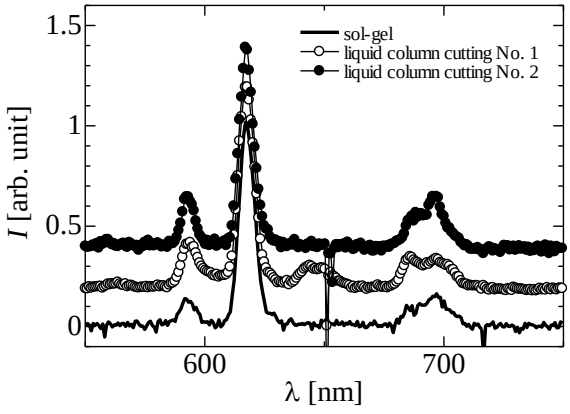

Fig. 1. IBIL spectra of Eu(III) loaded adsorbents.

1 - 40 Characterization of growth and composition control in $Ti_{1-x}Al_xN$ thin films on monocrystalline AlN by reactive CVD

Y. Kasukabe[a,b], H. Shimoda[b] and S. Yamamoto[c]

[a]Global Learning Center, Tohoku University
[b]Department of Metallurgy, Tohoku University
[c]Department of Advanced Functional Materials Research, TARRI, QST

Films of $Ti_{1-x}Al_xN$ have been known as the material which exhibits superior mechanical and thermal properties, and those are widely used as coatings for industrial applications such as cutting tools. Irrespective of those attracting performance, little is studied on the growth mechanism as well as the chemical process. In this work, $Ti_{1-x}Al_xN$ thin films have been prepared by reactive Chemical Vapor Deposition (CVD) and analyzed by Field Emission Gun Scanning Electron Microscopy (FEG-SEM), Transmission Electron Microscope (TEM) [1], and X-ray Diffraction (XRD).

Recently, it has been reported that $Ti_{1-x}Al_xN$ films have been grown by use of the titanium tetra chloride, $TiCl_4$, and c-plane (0001) monocrystalline hexagonal aluminum nitride, AlN, as precursors [2]. The AlN has been prepared at 1500 °C with the gas mixture of NH_3 and $AlCl_3$ on c-plane (0001) monocrystalline hexagonal sapphire. During the $Ti_{1-x}Al_xN$ growth, hydrogen (H_2) gas is used as carrier gas of $TiCl_4$. The growth has been performed on the 100-nm-thick monocrystalline AlN on sapphire.

In order to characterize the effect of H_2 carrier gas flux on the $Ti_{1-x}Al_xN$ film morphology, the surface morphologies of the $Ti_{1-x}Al_xN$ layers deposited at 1200 °C for 15 minutes with H_2 carrier gas flux fixed (a) at 100 sccm (Standard Cubic Centimeter per Minute), (b) at 1000 sccm and (c) 2000 sccm on monocrystalline AlN substrates, were observed as shown in Fig. 1. Fig. 1 (a) indicates there are many grains grown in a columnar shape. These columnar grains grow randomly. However, the surfaces of the layers fabricated with H_2 gas flux at more than 1000 sccm (shown in Fig. 1 (b) and (c)) are much flatter than that of the layer with 100 sccm. It can be considered that this phenomenon results from the transportation of $TiCl_4$ by H_2 gas flux and the reaction between $TiCl_4$ and AlN. If fewer H_2 carrier gas flux, which means fewer $TiCl_4$, exists in the reactor, these react to each other, because of the high reactivity between $TiCl_4$ and AlN, as soon as $TiCl_4$ reaches the AlN surface. Therefore, the surface tends to be rough in this condition. However, if enough amounts of H_2 gas flux exist, $TiCl_4$ can be carried effectively and easily diffuse on the surface, leading to the flatter surface. This indicates that surface morphologies of the grown $Ti_{1-x}Al_xN$ films can be controlled by changing the H_2 carrier gas flux.

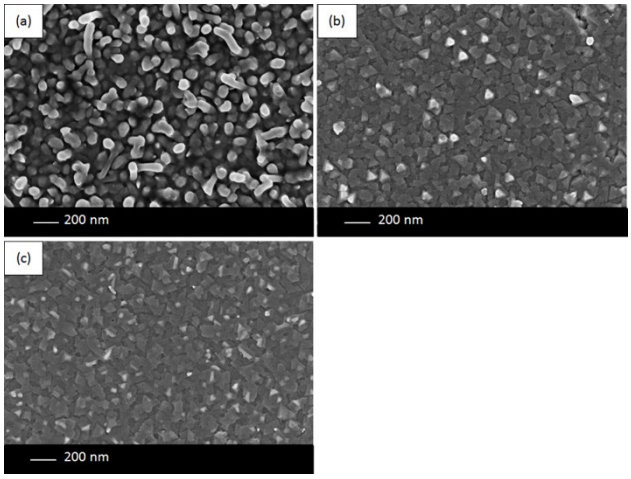

Fig. 1. Surface morphologies of the layers fabricated on monocrystalline AlN at 1200 °C with H_2 gas flux fixed at (a) 100 sccm, (b) 1000 sccm, (c) 2000 sccm observed by FEG-SEM.

X-ray diffraction patterns of the layers deposited with H_2 carrier gas fixed at 100−2000 sccm on monocrystalline AlN substrates are shown in Fig. 2. The shift of the position of the peak $Ti_{1-x}Al_xN$ (222) marked by * can be found according to the Vegard's law. Moreover, it can be recognized that H_2 carrier gas promotes the growth of $Ti_{1-x}Al_xN$ film which leads to the increase in the intensity of $Ti_{1-x}Al_xN$ (222) peak. These indicate that more H_2 carrier gas leads to the growth of of Ti-rich $Ti_{1-x}Al_xN$ films. Therefore, it can be concluded that the H_2 carrier gas promotes the growth of Ti-rich $Ti_{1-x}Al_xN$ films and the surface flatness.

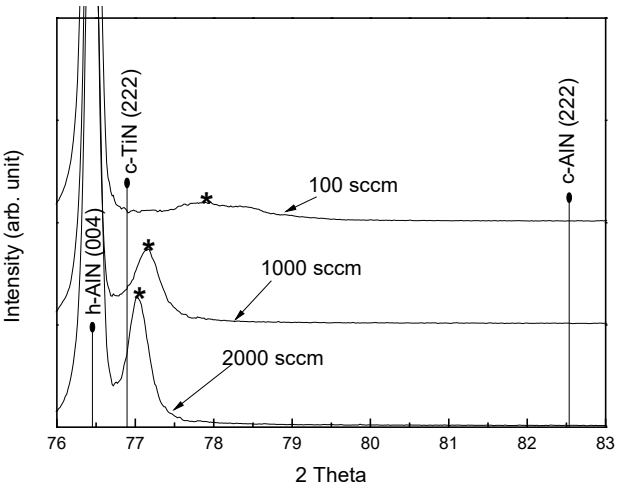

Fig. 2. X-ray diffraction patterns of the layers fabricated on monocrystalline AlN at 1200 °C with H_2 gas fixed at (a) 100 sccm, (b) 1000 sccm, (c)2000 sccm. The marks of * indicate the position of the peak of $Ti_{1-x}Al_xN$ (222).

References

[1] H. Abe *et al.*, JAERI-Research **96-047**, 1 (1996).
[2] R. Boichot *et al.*, Surf. Coat. Technol. **205**, 1294 (2010).

1 - 41 Gamma-irradiation effect on ESR signals derived from hydrothermally altered minerals and its application to fault dating

T. Fukuchi

Faculty of Education, Graduate Faculty of Interdisciplinary Research, University of Yamanashi

For the purpose of earthquake disaster prevention, it is significant to evaluate the activity during the Quaternary period on unrecognized active faults in the regions without clear tectonic landform or Quaternary overlying sediments. In case of the 2018 Osaka earthquake (M6.1), an unrecognized active fault caused serious earthquake disaster. At the present stage, we have no evaluation method but to estimate the absolute age of fault rocks produced in faulting. The ESR (electron spin resonance) dating technique is available in estimating the absolute age of fault rocks using radiation defect radical centers derived from fault-rock-forming minerals [1]. Among the fault-rock-forming minerals, there often exist hydro-thermally altered minerals subjected to frictional heat by faulting, and then the ESR signals derived from such hydrothermally altered minerals may give the absolute age of fault movement.

I carried out ESR and XRD analyses of hydrothermally altered minerals in fractured Hoo-type granite distributed along the Hakushu fault, a part of the Itoigawa-Shizuoka Tectonic Line (ISTL) Active Fault System, using sodium poly-tungstate (SPT) heavy solution. The ESR and XRD analyses revealed that the hydrothermally altered minerals lighter than 2.59 g/cm^3 mainly consist of potash feldspar (orthoclase) and have quartet signals which are often detected from montmorillonite, whereas those heavier than 2.59 g/cm^3 mainly consist of quartz and/or plagioclase (albite) and have no quartet signals (Fig.1). On the other hand, although the fresh minerals lighter than 2.59 g/cm^3 in fresh Hoo-type granite mainly consist of potash feldspar (orthoclase), they have no quartet signals (Fig. 1).

These results show that the quartet signals detected from the hydrothermally altered potash feldspar (orthoclase) may have been formed by the chemical reaction of fresh potash feldspar (orthoclase) with H_2O caused by frictional heating in faulting. Therefore, the quartet signals derived from the hydrothermally altered potash feldspar (orthoclase) may give the absolute age of fault movement. The ESR age (T) is calculated by dividing the equivalent dose (D_e) to which the fault rock has been subjected since the formation of the quartet signals by the annual radiation dose (D); $T = D_e/D$. The D_e is obtained by extrapolating the growth curve calculated from the intensities of the quartet signals before and after artificial gamma-irradiation. The D is calculated from the concentrations of ^{238}U, ^{232}Th and K_2O contained in the fault rock, which is determined by chemical analysis such as ICP-MS, using the conversion table [1].

The gamma-irradiation effect on the quartet signals (A, B, C and D signals) obtained from the fractured Hoo-type granite is shown in Fig. 2. The artificial gamma-irradiation for determining the D_e was carried out with a ^{60}Co source at 2 cell irradiation facility in the Food Irradiation Building, Takasaki Advanced Radiation Research Institute, QST. The irradiation dose rate is 380.7 Gy/h. The quartet signals increase with gamma-irradiation although the C signal among the quartet signals overlaps with the Ge center in quartz, which is detected only by artificial gamma-irradiation [1]. Since the B signal increases with increasing radiation dose, I preliminary have determined the D_e from it; D_e = 6.00 ± 1.24 kGy (the coefficient of determination R^2 = 74.9%). The D has been estimated as 4.36 ± 0.49 Gy/ka. Consequently, the B signal give the ESR age of 1.38 ± 0.32 Ma, implying that the Hakushu fault has moved in the Early Pleistocene during the Quaternary period.

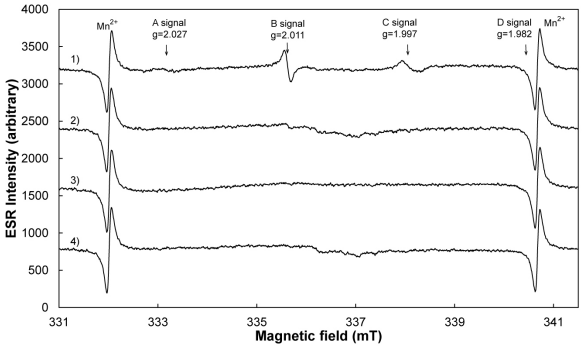

Fig. 1. ESR spectra obtained from the hydrothermally altered minerals (1 and 2) and fresh ones (3 and 4). 1) < 2.59 g/cm^3, 2) > 2.59 g/cm^3, 3) < 2.59 g/cm^3, 4) > 2.59 g/cm^3. The ESR spectra were measured at a microwave power of 1 mW under RT.

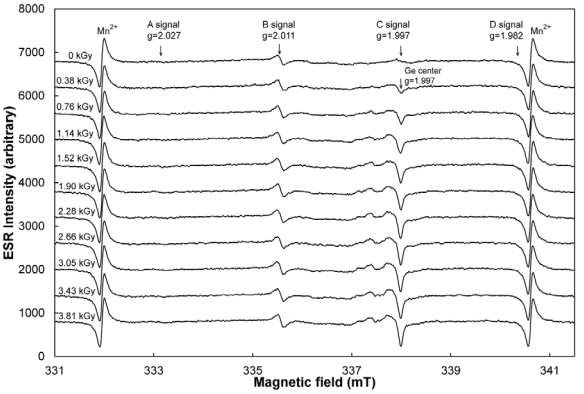

Fig. 2. Gamma-irradiation effect on the quartet signals obtained from the hydrothermally altered minerals. The ESR spectra were measured at a microwave power of 1 mW under RT. The irradiation dose rate is 380.7 Gy/h.

Reference

[1] T. Fukuchi, Radioisotopes **70**, 131 (2021).

Part Ⅱ

2. Life Science

2 - 01 Further analysis of penumbra area of neon and argon ions in DNA thin sheet perpendicularly exposed to ion beams

K. Urano[a,b], A. Ito[a], M. Ide[a], Y. Takano[a,c,d], S. Yoshida[a], R. Hirayama[d],Y. Furusawa[d], Y. Yokota[e] and T. Funayama[e]

[a]School of Engineering, Tokai University
[b]Nuclear Safety Research Center, JAEA
[c]Graduate School of Med. Pharm. Sci., Chiba University
[d]Department of Charged Particle Therapy Research, IQMS, QST
[e]Department of Radiation-Applied Biology Research, TARRI, QST

Introduction

In the continuing effort to evaluate the contribution of indirect action in the biological effects of high-LET radiation, we have been focusing on the measurement of the area of oxidative DNA damage induced by OH radicals that are the main species in the indirect action. In term of a track structure of high-LET radiation, penumbra region that is caused by secondary electron delta rays with low-LET nature probably corresponds to such oxidative DNA damage region. To visualize DNA oxidative region, we developed a method to detect the location of 8-hydroxydeoxyguanosine (8-OHdG) by immunostaining method using fluorescence antibody against 8-OHdG generated in DNA-lipid complex sheet, hereafter referred to as DNA sheet, with water-insoluble nature. The use of such DNA sheet enabled irradiation under water environment. In our previous study we measured the area of fluorescence dots due to the binding locations of 8-OHdG antibody in the perpendicular irradiation of carbon ions to DNA sheet [1]. The results showed that with increasing LET, that is decreasing particle energy, the dot area decreased, which was in consistent with the theoretical study evaluating penumbra region by Chatterjee and Schaefer [2].

In the present study, we extended ion species to neon and argon with higher LET than the case of carbon ion, using TIARA and HIMAC at IQMS for comparison.

Materials and Methods

The heavy ion species used is shown in Table 1. TIARA and HIMAC beams were used for the higher LET and the lower LET, respectively.

Table 1
List of ion species used.

Ion species	Energy (MeV/u)	LET (keV/μm)	Facilities
Ne	400	31	HIMAC
	26	437	TIARA
Ar	500	90	HIMAC
	29	1370	TIARA

Before irradiation DNA sheet made on a coverglass was pretreated with Bouin fixative, and then set to an irradiation position perpendicular to the ion direction. During irradiation, the DNA sheet on which water was dropped was covered with mylar film to maintain water environment around the DNA sheet. Irradiated DNA sheet was treated with the procedure of immunofluorescence method using 8-OHdG antibody (Santa Cruz Biotech. Inc., USA). The obtained image of fluorescence dots was analyzed using ImageJ software. In the previous study we developed a possible discrimination method of background fluorescence dots from dots caused by ions [1]. The same procedure was applied to the present data.

Results and Discussion

Figure 1 shows LET dependence of area size of the fluorescence dots for neon and argon ions. The size decreased with increasing LET for both ions. For comparison, the previous data for carbon ions [1] were inserted, which showed the similar LET dependence. These results are in consistent with the mathematical formula by Chaterjee and Schaefer as described above. In addition, at the same LET, the dot area was increased with increasing atomic number, which also in accord with the result by Chaterjee and Schaefer.

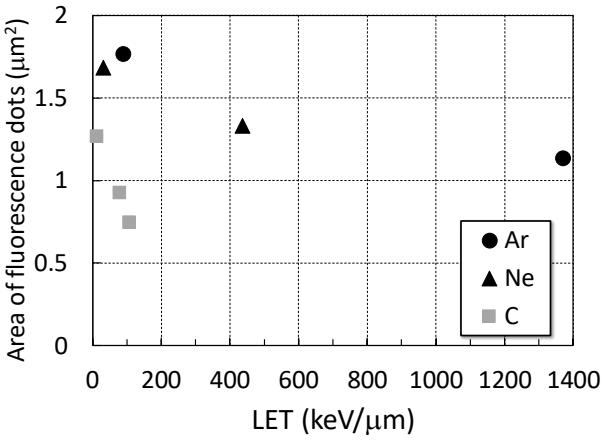

Fig. 1. LET dependence of area of fluorescence dots for argon, neon and carbon ions.

References

[1] K. Urano *et al.*, QST Takasaki Annual Report 2019, **QST-M-29**, 84 (2021).
[2] A. Chatterjee and H. J. Schaefer, Radiat. Environ. Biophys. **13**, 215 (1976).

2 - 02 Analysis of the effects of EGFR signaling on radiation effects

T. Hara[a], T. Aoki[a], H. Sato[b], T. Funayama[c], Y. Nakagami[d], A. Okazaki[e], T. Ohno[b] and Y. Suzuki[f]

[a]Department of Radiological Technology, Gunma Prefectural College of Health Sciences
[b]Department of Radiation Oncology, Gunma University Graduate School of Medicine
[c]Department of Radiation-Applied Biology Research, TARRI, QST
[d]Department of Radiology, Dokkyo Medical University
[e]Department of Radiation Oncology, Tsuboi Cancer Center Hospital
[f]Department of Radiation Oncology, Fukushima Medical University School of Medicine

Introduction

We have been studying the analysis of the effects of EGFR signaling on the effects of radiation.

Among them, we found that EGFR signal pathways could be a target for a triple-negative breast cancer (TNBC) for which an effective treatment has not yet been established. So far the results obtained were summarized as follows;

(1) The EGFR inhibitor increased radiosensitivity to the triple-negative breast cancer cell line MDA-MB-231.
(2) The enhancing effect was seen when the EGFR inhibitor was treated before irradiation.
(3) No enhancing effect was observed when the EGFR inhibitor was treated after irradiation.

From the above results, we considered that the EGFR signal pathway is a target of radiation sensitization effect, and that the effect of radiotherapy can be enhanced by inhibiting the EGFR signal pathway with a drug before irradiation.

Methods

The protocol for the combined use of radiation and drug was as follows: pre-treat, in which the drug was added 24 hours before irradiation, and post-treat, in which the drug was added 24 hours after irradiation (Fig.1).

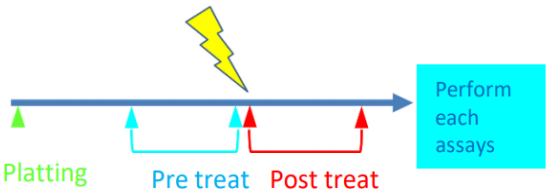

Fig. 1. Protocol for irradiation procedure.

We used cetuximab as an EGFR inhibitor in this experiment.

After radiation, samples were collected in Lysis buffer and quantified. For each sample, 20 μg of protein was separated by sodium dodecyl sulfate–polyacrylamide gel electrophoresis. The proteins were transferred onto a PVDF membrane. The membrane was incubated with the primary antibody for 1 h (EGFR 1:1000, pEGFR 1:1000, GAPDH 1:1000; Cell Signaling Technology (CST)) and then with a secondary antibody for 0.5 h (IgG, HRP-linked Antibody 1:2000; Cell Signaling Technology (CST)). The immunocomplex was visualized using the ECL Plus kit (GE Healthcare Life Sciences, MA), and images were developed with C-DiGit chemiluminescent scanner (LI-COR, NE).

Result

The result of experiment by Western blot is shown in Fig. 2. GAPDH was used as the internal control. The numbers in the figure were normalized by GAPDH in control and indicated the expression levels of each protein. The total expression level of EGFR was not different between irradiation alone, pretreat, and post-treat. However, focusing on the state of activated EGFR, that is, pEGFR, it was found that pre-treat and post-treat significantly suppressed the quantity of pEGFR as compared with irradiation alone.

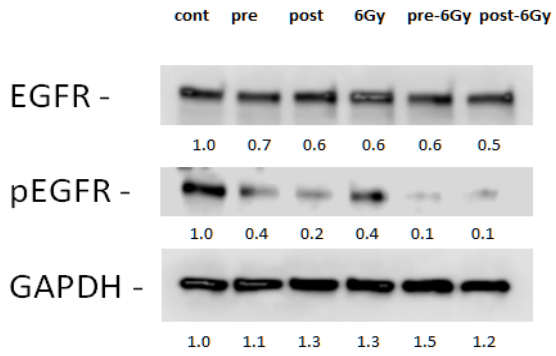

Fig. 2. Western blot analysis for investigating the intracellular EGFR status.

Conclusion

From the above results of experiment, it is suggested that MDA-MB-231 cells of the TNBC cell line enhances the radiation effect by suppressing the repair pathway of DNA damage controlled by the EGFR with cetuximab before irradiation [1, 2].

Therefore, we consider that chemoradiotherapy targeting the EGFR pathway can be an effective treatment for TNBC.

References

[1] T. Fang *et al.*, Blood. **136**, 441 (2020).
[2] S. Wu *et al.*, Clin. Cancer Res. **26**,1395 (2020).

2 - 03 Foci formation of DNA damage repair proteins after simulated-space radiation exposure

T Oizumi[a], R Ohno[a], T. Funayama[b] and AJ. Nakamura[a]

[a]College of Science, Ibaraki University
[b]Department of Radiation-Applied Biology Research, TARRI, QST

Exposure to ionizing radiation is one of the problems associated with human activities in space. Heavy ion beams with high linear energy transfer (LET) in space radiation are known to cause cluster DNA damage in which multiple DNA damage occurs within 1–2 helix turns of a DNA molecule [1]. Furthermore, radiation exposure would occur under the microgravity environment in space that might induce different responses for radiation exposure from that on the ground. Since the failure of DNA damage repair may induce genomic instability and increase the risk of developing cancer, it is important to understand the difference of DNA damage response after space radiation exposure. Therefore, in this study, we evaluate the DNA damage responses after radiation exposure by immunostaining for phosphorylated H2AX (γ-H2AX) and 53BP1 to assess the biological impact of those stresses in space.

Histone H2AX, which is a key protein in DNA repair, is rapidly phosphorylated at the site of DNA double-strand breaks (DSBs) following DNA damage induction [2-3]. Upon DNA DSB induction by ionizing radiation (IR), the accumulation of hundreds of molecules of various DNA repair proteins including γ-H2AX and 53BP1 can be visualized as a large focus at the DNA DSB site which is known as Ionizing Radiation-Induced Foci (IRIF) [4]. The γ-H2AX foci serve as sites of accumulation of DNA repair proteins and may also induce chromatin remodeling possibly to aid access of repair proteins to the DSB sites. Therefore, the formation of γ-H2AX foci is critical for efficient DNA repair and the maintenance of genome stability.

Here, we analyzed the kinetics of γ-H2AX and 53BP1 foci formation after exposure of proton beam (20 MeV, 2.73 keV/μm), helium ion beam (63 MeV, 13.2 keV/μm) and carbon ion beam (190 MeV, 124 keV/μm) that are considered as a component of cosmic rays. Moreover, we investigated the foci formation after the combination of helium ion beam and carbon ion beam exposure.

TIG-3 (normal human diploid skin fibroblast) were plated on chamber slides and exposed to radiation. Cells were fixed by 2% paraformaldehyde and immunostained for γ-H2AX and/or 53BP1. Carbon ion beam, which causes more complex DNA damage than the helium ion, induced a larger size of γ-H2AX foci than helium ion beam at one hour after exposure [5]. Not only one hour after the exposure, LET-dependent foci size expansion was clearly shown by four-hour post-irradiation, indicating more complex DNA damages were induced in a LET-dependent manner [5]. Consistent with γ-H2AX, the 53BP1 focus size at one hour after irradiation increased in a LET-dependent manner [5]. Interestingly, in the proton and helium irradiated groups, the mean 53BP1 focus size was slightly increased from 1–4 hour after irradiation [5]. It has been reported that the repair of DSBs, characterized by large 53BP1 foci, was a slow process within the biphasic kinetics of DSB repair, suggesting non-homologous end joining with error-prone end resection [6]. Therefore, it is reasonable to assume that the LET-dependent specific DNA damage repair switching is occurred after radiation exposure.

Finally, we evaluated whether DNA damage induction differed in the order of beams of exposure from C-ion to He-ion and He-ion to C-ion. Both large and small size of foci formation was observed in carbon and helium ion mixed beam irradiated cells regardless the order of beam for exposure (Fig. 1).

In conclusion, our data suggest that the biological effects of space radiation may be significantly influenced by the dose as well as the type of radiation exposure.

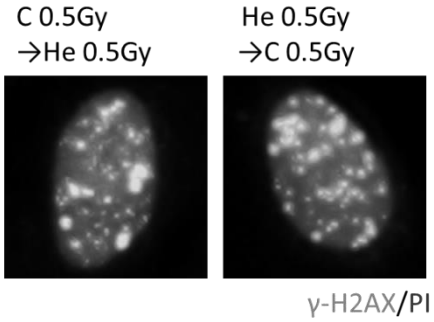

Fig. 1. γ-H2AX foci per cell after radiation exposure.TIG-3 cells were exposure to both C-ion (0.5Gy) and He-ion (0.5Gy), and then fixed at 1 hour post irradiation.

References

[1] Y Lorat *et al.*, Radiother. Oncol. **121**, 154 (2016).
[2] E. Rogakou *et al.*, J. Cell Biol. **146**, 905 (1999).
[3] E. Rogakou *et al.*, J. Biol Chem. **273**, 5858 (1998).
[4] T. T. Paull *et al.*, Curr. Biol. **10**, 886 (2000).
[5] T. Oizumi *et al.*, Life **10**, 341 (2020).
[6] A. Shibata *et al.*, Mutat. Res. **803**, 55 (2017).

2 - 04 An attempt to induce developmental arrest of the silkworm eggs at cleavage stage by depth-controlled irradiation

T. Takahashi[a)], Y. Soma[a)], R. Isoyama[a)], T. Fumayama[b)], M. Suzuki[b)] and K. Shirai[a)]

[a)]Faculity of Textile Science and Technology, Shinshu University
[b)]Department of Radiation Applied Biology, TARRI, QST

In general, to carry out rapid cell (or nuclear) cleavage, there are no or incomplete checkpoint system in the early embryo of animals. We reported a dose-dependent developmental delay of the silkworm eggs at early developmental stage after heavy ion irradiation. These results suggest that the silkworm eggs in the early developmental stage have developmental arrest mechanisms by checkpoints.

However, the radiation response of the silkworm egg is quite complicated. Early embryonic development is under control of the maternally derived components. Moreover, the silkworm egg at cleavage stage is a polynuclear cell (syncytium). So, there are still lots of questions of the radiation response of the silkworm egg to be answered. There is no delay in development of the egg when ~10% of nuclei of an egg at cleavage stage (syncytium) were irradiated with 500 Gy of carbon ions. However, the irradiation to 40 - 50% of nuclei induced developmental arrest. These results indicate the execution of the developmental arrest of the egg is determined by the ratio of damaged and normal nuclei. To investigate the complex mechanisms of the radiation-induced developmental arrest requires lots of irradiated eggs, the targeted irradiation using HZ1 port microbeam cannot process many eggs. Carbon ion beams can control the irradiation depth by shielding with an appropriate material. Mylar film have often been used for shielding beams. In the study, we tried to attempt to induce developmental arrest of the egg by the depth-controlled irradiation using HY1 port broad field irradiation facility.

Materials and Methods

The silkworm (*Bombyx mori)* strain used in the experiments was the pigmented non-diapause strain, *pnd pS.* The silkworm eggs were collected and irradiated with 20 Gy of carbon ions (190 MeV, HY1 port) at 8 hours after oviposition. The irradiated eggs were incubated at 25 °C, then the eggs were fixed by Carnoy's solution. Depth control of the irradiation were carried out by using stacked mylar films (100 μm/sheet).

Results and Discussion

The thickness of egg was 0.551 ± 0.022 mm at the thickest part (anterior part). On the other hand, the irradiation depth of the carbon ion beam is about 0.9 mm. So, we decided to use 7 to 2 layers of Mylar film to make the irradiation depth 0.2-0.7 mm.

As a result, no clear delay in development was observed in the carbon ion irradiated eggs covered with 4 to 7 layers of Mylar film. However, delayed development might occur in the irradiated eggs shielding with 3-layer mylar film. While control eggs progressed to cycle 9 or 10, all of the irradiated eggs were at cycle 9 (Table 1).

Table 1
Developmental delay of the irradiation eggs shielding with 3-layer film.

	developmental stage	
	cycle 9	cycle 10
control	5	4
20 Gy (3-layer film)	5	

Moreover, in the irradiated egg covered with 2 layers of Mylar film, developmental arrest was observed. The irradiated egg clearly has fewer nuclei than the control egg, (Fig. 1). Since the developmental stage of the irradiated eggs is estimated to be cycle 6 or 7, it is considered to stop their development immediately after irradiation (Table 2).

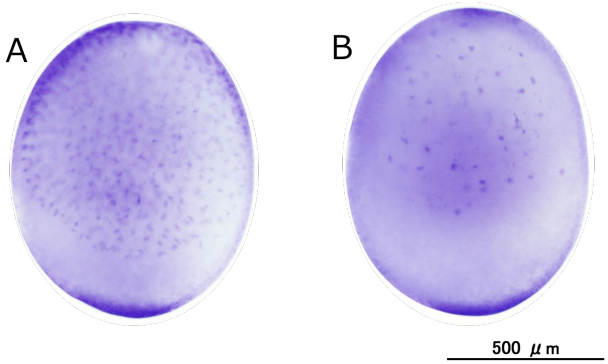

Fig. 1. Developmental arrest of the irradiation eggs shielding with 2-layer film. A: control, B: irradiated egg (shielding with 2-layer film).

Table 2
Developmental arrest of the irradiation eggs shielding with 2-layer film.

	developmental stage		
	cycle 6	cycle 7	cycle 11
control			7
20 Gy (2-layer film)	6	8	

In this study, we succeeded in inducing the developmental arrest of the silkworm eggs by depth-controlled irradiation using Myler film. However, when using a two-layer film, the resultant range of the beam in water is about 0.7 mm, which is longer than the thickness of the silkworm egg. This result is considered to be due to the shielding effect of the eggshell. Further research should be conducted on the method of depth-controlled irradiation for the silkworm egg.

2 - 05 Visualization of microglial activation by targeted irradiation with carbon ion microbeam in embryonic brain of transgenic medaka (*Oryzias latipes*)

S. Oda[a)], T. Yasuda[a)], D. Li[a)], M. Yuan[a)], T. Endo[a)], S. Mori[a)], E. Sha[a)], Q. Jia[a)], M. Suzuki[b)], T. Funayama[b)], Y. Kobayashi[b)] and H. Mitani[a)]

[a)]Department of Integrated Biosciences, The University of Tokyo
[b)]Department of Radiation-Applied Biology Research, TARRI, QST

Long-lasting inflammation is frequently induced in the irradiated brain for radiotherapy of cranial tumor and its mitigation and/or prevention has been an issue of medicine. When vertebrate brain is irradiated, microglia, residential immune cells in brain, are activated, removing injured and dead cells, maintaining tissue homeostasis of the brain. Irradiation-induced excessive activation of microglia might further damage normal cells even after they have removed injured/dead cells, resulting in radiation-induced brain injury (RIBI). Elucidation of the mechanism and the dynamics of microglial activation is expected to contribute to new therapeutic methods for RIBI. In this study, we aimed to elucidate the dynamics of microglial activation by irradiation in model animal, medaka (*Oryzias latipes*).

Apolipoprotein E (ApoE) is expressed during the late phase of phagocytosis (24 hours after irradiation) in irradiation-activated microglia of medaka embryo, which can be used as an indicator of activated microglia [1]. We successfully established a transgenic medaka line that express fluorescent Kaede protein driven under the promoter of medaka apolipoprotein E (ApoE) [2]. Using TIARA, we conducted targeted irradiation of only the right lobe of optic tectum with collimated microbeam (diameter = 250 μm) of carbon-ion ($^{12}C^{5+}$, 26.7 MeV). When 3 days-post fertilization embryos of the transgenic medaka was irradiated, apoptosis was induced only in the irradiated area (right lobe of the optic tectum) and only microglia located there were activated after the irradiation [3].

Fluorescent protein Kaede emits green fluorescence with a peak of 518 nm and its emission maximum shifts to 582 nm (orange fluorescence) after irradiated with UV. Newly expressed Kaede protein can be distinguished from the preexisted Kaede protein, since only the newly expressed Kaede emitted green fluorescence after UV irradiation (4). In this study, we irradiated the Kaede-expressing transgenic embryos with UV under fluorescence microscope, making preexisted Kaede protein in the embryos red-shifted, and successfully visualized microglia that were activated and newly expressed ApoE after the irradiation with carbon ion microbeam *in vivo*.

In the transgenic embryos at 2, 3 and 4 days after the irradiation with carbon ion microbeam, green fluorescent cells localized only in the right lobe of optic tectum, where the carbon-ion microbeam (10 Gy) was irradiated. When the green fluorescent cells were exposed to UV light, green fluorescence changed to orange fluorescence, indicating that the green fluorescent cells were activated microglia and expressed Kaede protein in response to the targeted irradiation with carbon-ion microbeam.

We have observed that almost the same number of microglia as in wild-type embryos were activated after gamma irradiation in a p53-deficient medaka embryos, although apoptotic cells death was not induced by the irradiation in the p53-deficient medaka embryos, suggesting that gamma-ray irradiation could directly activate microglia in embryonic medaka brain [1]. It can be expected that the method developed here will advance the elucidation of the regulatory machinery of microglial activity by irradiation.

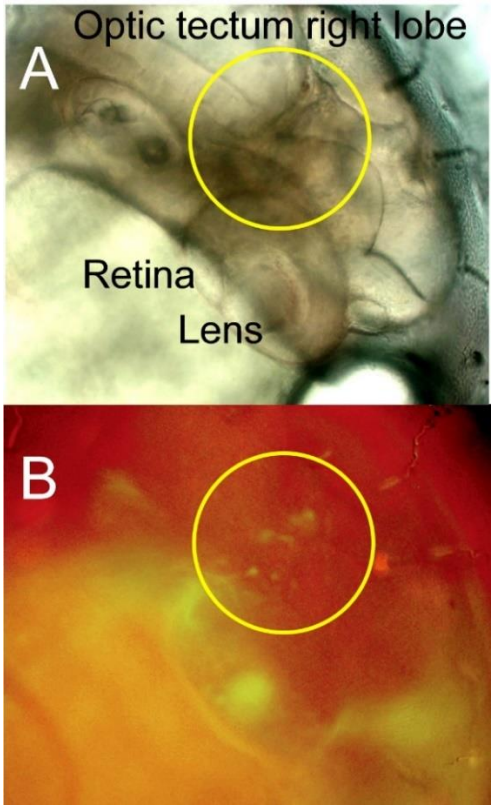

Fig. 1. Localized microglia activation in the irradiated area (right lobe of optic tectum) of transgenic medaka embryo 2 days after the irradiation (A: bright field image, B: fluorescent image).

References

[1] T. Yasuda *et al.*, PLos One **10**, e0127325 (2015).
[2] A.C.G. Peh, Master Thesis, The University of Tokyo (2018).
[3] T. Yasuda *et al.*, Int. J. Mol. Sci. **18**, 1428 (2017).
[4] R. Ando *et al.*, PNAS **99**, 12651 (2002).

2 - 06 Metabolomics in carbon-ion-induced bystander effects on normal human fibroblasts (2)

M. Suzuki[a)], T. Funayama[b)], M. Suzuki[b)], Y. Yokota[b)] and Y. Kobayashi[b)]

[a)]Department of Charged Particle Therapy, IQMS, QST
[b)]Department of Radiation-Applied Biology Research, TARRI, QST

We have been studying the bystander cellular effects in normal human fibroblasts or human tumor cell lines using the carbon-, neon- and argon-ion microbeams. We can summarize from the obtained results as follows;

(1) The observed bystander effects induced in normal human fibroblasts were dependent on radiation quality, showing clear bystander effects induced by the lower-Linear-Energy-Transfer (LET) carbon ions but not the higher-LET neon and argon ions.
(2) Gap-junction mediated cell-to-cell communication was an essential role for inducing the aforesaid effects.
(3) The bystander effect via secreted factor(s) at 24h after irradiation was induced by argon ions but not carbon and neon ions in cell death, and by neon and argon ions not carbon ions in gene mutation.
(4) The secreted factor-induced bystander effects were suppressed by ascorbic acid but not dimethyl sulfoxide.
(5) In the case of communication between tumor and normal cells, the medium from the irradiated human tumor cells enable to induce damage in the neighboring non-irradiated normal cells via the secreted factor-induced bystander effects.

Thus heavy-ion induced bystander effects varied radiation quality such as ion species and LET, and also differed from an inducing pathway. Studies of bystander cellular responses induced by different radiation types using a microbeam can provide us an important scientific evidence to understand radio-biological responses induced by low-fluence irradiations. Especially, the study of such biological responses can surely provide the critical information for evaluating risk such low-dose exposure as the accident of Fukushima Daiichi Nuclear Power Plants caused by the Great East Japan Earthquake and developing tumor radio-therapy. However, there are a lot of unknown phenomena concerning cellular responses induced by low-fluence irradiations of heavy ions and still unclear their mechanism.

Now our target is to identify mechanism(s) of pathways for heavy-ion induced bystander effects. We've just started the experiment forcing on metabolome level in order to examine metabolite concerning bystander effects using the metabolome analysis. This year we try to examine metabolome analysis against carbon-ion irradiated normal human fibroblasts, which showed the bystander cellular effects via gap-junction mediated cell-cell communication, and report the preliminary data.

Normal human skin fibroblasts, which were distributed by the RIKEN BioResource Center Cell Bank in Japan, were irradiated with carbon-ion microbeams (190 MeV,114 keV/μm) generated at the HZ1 port. Irradiations were carried out using the 256-cross-stripe method [1]. Briefly, the beam size of each irradiation point of the microbeam was 20 μm in diameter and the irradiations in each point were performed to deliver 7 ions. Immediately after irradiation, the medium was removed from the dish, methanol containing 2-isopropylmalic acid was added, the cells were scraping from the dish and collecting the cell suspension into the 15 mL polypropylene tube. The sample was washed twice in methanol, homogenized, centrifuged at 3000 rpm for 5 min and collected supernatant. After drying the solution containing methoxyamine hydrochloride and pyridine was added and shaking for 30 min. And then in the sample N-methyl-N-(trimethylsilyl)trifluoroacetamide was added, shaking for 30min, centrifuged at 16000 × g for 1 min and collected supernatant. The sample was analyzed using the gas chromatography-mass spectrometry. The obtained data was calculated and analyzed using the SHIMAZU Smart Metabolites Database.

The heatmap representation from the result of hierarchical clustering after principal component analysis of 229 candidates showed that metabolic fluctuations occurred between control and irradiation, and almost all of compounds of the irradiated sample with the specific inhibitor of gap junction tended to reduce when comparing to control (Fig.1). We continue to study in order to understand mechanism or mechanisms for heavy-ion induced bystander effects.

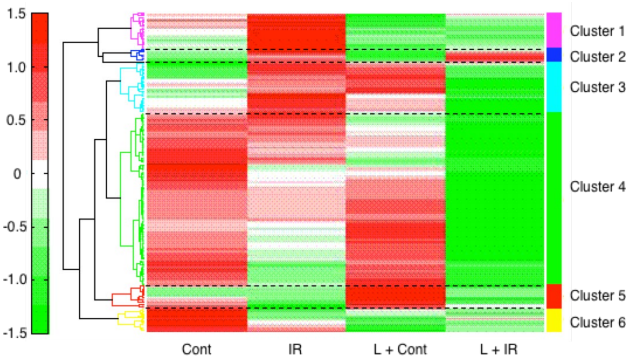

Fig.1. Heatmaps of the samples from carbon-ion-microbeam irradiated cells. "Cont" shows unirradiated samples, "IR" shows carbon-ion-microbeam irradiated samples and "L" means to use together with a specific inhibitor of gap junction.

Reference

[1] M. Suzuki *et al.*, JAEA Takasaki Annu. Rep. 2006, **JAEA-Review 2007-060**,107 (2008).

2 - 07 Effects of targeted central nervous system irradiation of *Caenorhabditis elegans*

M. Suzuki[a)], Z. Soh[b)], H. Yamashita[c)], T. Tsuji[b)] and T. Funayama[a)]

[a)]Department of Radiation-Applied Biology Research, TARRI, QST
[b)]Graduate School of Adv. Sci. & Eng., Hiroshima University
[c)]Graduate School of Eng., Hiroshima University

The nematode *Caenorhabditis elegans* is a powerful model for investigating biological mechanisms. We can use radiation, which can be controlled precisely and finely, as an external stimulus, and recorded responses that differ from normal by perturbing biological functions. So far, we found that motility of *C. elegans* in crawling on agar was significantly reduced after whole-body irradiation with ^{60}Co gamma rays or heavy ions, in a dose-dependent manner [1, 2]. Furthermore, we found that targeted irradiation of a 20-μm-diameter area of head including the central nervous system (CNS) with 500 Gy did not affect motility [3]. This suggested that radiation inhibits motility by a whole-body mechanism rather than affecting motor control via the CNS or a stimulation response. However, whether irradiated area-dependent and dose-dependent effects on motility by targeted irradiation occur remain unknown.

Therefore, in the present study, we aimed to investigate irradiated area-dependent and dose-dependent effects on motility. We generally followed previously described method [3, 4]. Briefly, targeted microbeam irradiation was delivered using a collimating microbeam system at HZ1 port of TIARA. To target to a specific region, animals were enclosed in straight channels of a microfluidic chip, Worm Sheet [4] during irradiation. A track-averaged value of the linear energy transfer (LET) of carbon ions used was 125 keV/μm. The nerve ring, corresponding to the entire CNS, was targeted and irradiated with carbon ions. The whole nerve ring at a Ø 60-μm micro-aperture region or the center of that at a Ø 20-μm micro-aperture region was targeted and irradiated with an exact number of carbon ions corresponding to 500 or 1,000 Gy at the irradiation area. For example, 95,000 particles correspond to a dose of 500 Gy at a Ø 60-μm region. For comparison, we conducted the whole-body broad-beam irradiation at HY1 port of TIARA. Immediately after irradiation, we collected and washed animals and transferred them to a fresh agar plate. Motility was evaluated using “body bends”, defined as the mean value of bends in the anterior body region at 20-s intervals in six animals. Mean values from five experiments were calculated for each irradiation condition and then divided by the mean value of non-irradiated animals.

As shown in Fig. 1a, the motility of whole-body irradiated animals was reduced in a dose-dependent manner. Irradiation with 500 Gy targeted to the CNS within either of 60- and 20-μm-diameter areas did not induce an irradiation area-dependent effect on motility. In contrast, significant effects between non-irradiated animals were observed with irradiation of 1,000 Gy targeted to 60- and 20-μm-diameter areas (Fig. 1b–c). Regarding irradiation region-dependent effects, the reduction of motility by 1000-Gy irradiation was greater for whole-body irradiation and CNS-targeted irradiation of a 60-μm-diameter area compared with CNS-targeted irradiation of a 20-μm-diameter area. These results indicated a dose-dependent effect of CNS-targeted irradiation and an irradiated area-dependent effect of 1,000-Gy irradiation on motility. Although a dose of 500 Gy was sufficient to reduce motility using whole-body irradiation, 1000-Gy CNS-targeted irradiation was required to induce the same effects as whole-body irradiation [5].

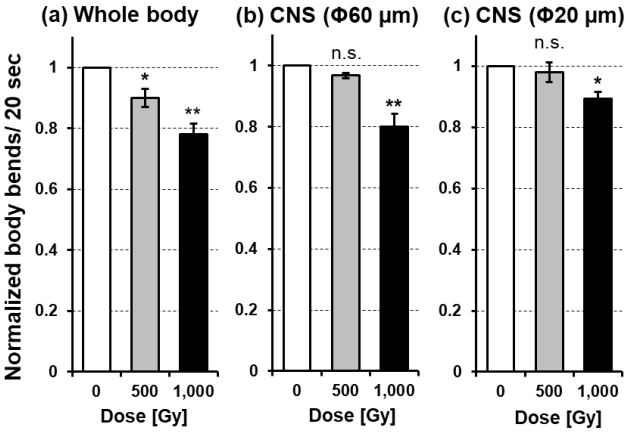

Fig. 1. Motility of *C. elegans* after carbon-ion irradiation.
(a) Motility in animals after whole-body irradiation. (b) Motility of animals after CNS-targeted irradiation of a 60-μm-diameter area. (c) Motility of animals after irradiation CNS-targeted irradiation of a 20-μm-diameter area. The error bar represents the SEM of independent 5 experiments. All data were analyzed using one-way ANOVA at 0.05 (*) and 0.01 (**) significance levels.

Acknowledgments

We thank the crew of the cyclotron of TIARA for their kind assistance; and the Caenorhabditis Genetic Center of the University of Minnesota for providing strains of *C. elegans* and *E. coli*. This study was supported in part by JSPS KAKENHI, grant numbers JP15K11921, JP18K18839, JP15H03950; and MEXT KAKENHI, grant number JP18H04991.

References

[1] M. Suzuki *et al*., J. Radiat. Res. **50**, 119 (2009).
[2] T. Sakashita *et al*., Sci. Space. **26**, 7 (2012).
[3] M. Suzuki *et al*., J. Radiat. Res. **58**, 881 (2017).
[4] M. Suzuki *et al*., J. Neurosci. Methods **306**, 32 (2018).
[5] M. Suzuki *et al*., Biology **9**, 289 (2020).

2 - 08 Consideration of conditions for extremely deep sequencing to detect mutations in plant DNA

Y. Oono, S. Kitamura and K. Satoh

Department of Radiation-Applied Biology Research, TARRI, QST

To establish an easy and quick method for evaluating frequency of mutations occurred in plant DNA, we have tried to apply maximum-depth sequencing (MDS), an extremely deep sequencing method that enables to detect extremely rare mutations through next generation sequencing (NGS) with an error correction [1]. The procedure of the MDS was previously described in [2]. Briefly, each molecule of a target DNA extracted from plants was labelled with a distinct DNA barcode, lineally amplified using a single primer and DNA polymerase, and subjected to NGS. Because original mutations that existed in plant DNA will be conserved among NGS reads harboring identical barcodes, they can be distinguished from erroneous mutations caused by PCR or NGS. In this work, we have prepared 4 test reactions to test 1) dual targeting in one reaction, 2) effect of pre-treatment of DNA repair enzymes, and 3) sensitivity of this method by inputting low amount of DNA with a known mutation.

Genomic DNA (1.25 µg) extracted from 7-d-old wild-type *Arabidopsis* light-grown seedlings was used for each reaction. To evaluate sensitivity for mutation detection, low amount (0.125 ng) of genomic DNA from *axr1-3* mutants was mixed to wild-type DNA (reaction #3 and 4). The DNA samples were treated with DNA repair enzymes (PreCR) before digested with restriction enzymes in reactions #2 and 4. Target specific primers with N14 random barcodes (BAR) were mixed to the restriction enzyme-digested DNA and hybridized to target genes (*HY1* and *HY2* for #1 and 2, *AXR1* for #3 and 4) followed by synthesizing the complementary DNA strand by Q5 polymerase (NEB), amplifying DNA linearly for 12 times and 30 cycles of PCR. The PCR products were purified with Size-Selective DNA Purification System (ProNex, Promega) and subjected to paired-end sequencing of MiniSeq NGS system (Illumina). The reads obtained by the NGS were confirmed by checking presence of sequences for the target specific primer and BAR as well as identity of each paired reads. The confirmed reads were classified by the sequence of the BARs. The number of reads (R) classified under the same BAR sequence and the number of BARs linked with equal or more than 2 reads (R≥2) were counted. If mutant reads (r) account for equal or more than 60% of total reads in a BAR (r≥60%), the BAR is considered as that it represents a mutation originated from the plant DNA.

The result of the analysis is summarized in Table 1. We have made dual targeting (*HY1* and *HY2* genes) reactions in duplicate and obtained 48% and 50% *HY1* and 33% and 31% for *HY2* confirmed reads from raw reads (100%) in the reaction #1 and 2, respectively. The presence of enough number of confirmed reads for both *HY1* and *HY2* genes suggests that the dual targeting reaction worked as expected although the efficiency seems to depend on the initial reaction between the specific primer and the target sequence. A smaller number of reads and BARs in the *AXR1* reactions (#3 and 4) than in the *HY1*&*HY2* reactions (#1 and 2) indicates the initial reaction for *AXR1* did not work effectively. On the other hand, we detected a greater number of mutations (No. of BARs with R≥2 and r≥60%) in the *AXR1* reactions than in the *HY1*&*HY2* reactions. Reason why greater number of mutations detected in the *AXR1* is unknown. Regarding effect of repair enzymes, because there is no remarkable difference in the results between reactions #1 and 2, and between reactions #3 and 4, the addition of repair enzymes seems not to improve the reaction. Finally, we successfully detected 3 and 7 of the *axr1-3* sequences (G to A mutation at position 16) in 43 and 28 BARs tagged with putative mutant reads among 9,661 and 15,927 BARs with R ≥ 2 in the reaction #3 and 4, respectively, suggesting the rare mutation sequences can be detected by this method. We hope large scaling of this method with further fine tuning of the conditions for polymerase reactions as well as the mutation detection program will enable us to practically detect extremely rare mutations in plant DNA.

References

[1] J. Jee *et al.*, Nature **534**, 693 (2016).

[2] Y. Oono *et al.*, QST Takasaki Ann, Rep. **QST-M-29**, 90 (2020).

Table 1

Summary of the result of the MDS.

Reaction #	1	2	3	4
Target gene(s)	*HY1*&*HY2*	*HY1*&*HY2*	*AXR1*/ *axr1-3*	*AXR1*/ *axr1-3*
repair enzymes	-	+	-	+
No. of raw reads	585,910	557,705	391,610	453,618
No. of confirmed reads	*HY1*: 282,901 *HY2*: 192,339	*HY1*: 278,401 *HY2*: 171,710	159,200	225,172
No. of BARs	*HY1*: 191,992 *HY2*: 172,746	*HY1*: 196,049 *HY2*: 136,462	11,512	19,174
No. of BARs with R≥2	*HY1*: 56.780 *HY2*: 24,346	*HY1*: 58,134 *HY2*: 30,564	9661	15,927
No. of BARs with R≥2 and r≥60%	*HY1*: 5 *HY2*: 7	*HY1*: 7 *HY2*: 7	43 (*axr1-3*: 3)	28 (*axr1-3*: 7)

2 - 09 Inactivation of CCD4 gene by ion beam irradiation in Azalea

K. Ureshino[a)], K. Satoh[b)] and Y. Oono[b)]

[a)]Faculty of Agriculture, University of the Ryukyus
[b)]Department of Radiation-Applied Biology Research, TARRI, QST

Evergreen azaleas are one of the representative ornamental woody plants. Cultivated varieties have been derived from natural and artificial hybridization and selection among evergreen species belonging to subgenus Tsutsusi in the genus *Rhododendron*. The flower colors of cultivated varieties are mainly variations of white, pink, red, or purple. However, no yellow-flowered cultivar of evergreen azaleas has been produced till date.

Creating yellow-flowered cultivars is one of the important breeding objectives for evergreen azaleas. *R. japonicum* f. *flavum* is a yellow-flowered deciduous species belonging to the subgenus Pentanthera [1]. The yellow petals contain carotenoid compounds such as β-carotene and lutein as the main pigments [2]. To create yellow-flowered evergreen azaleas, we have conducted intersubgeneric three-way crosses between an interspecific hybrid of white-flowered evergreen azaleas (‘Miyamasatsuki’) and *R. japonicum* f. *flavum*, and many progenies were obtained [3]. The petal color of the buds on the progenies was light yellow just before anthesis, and these petals contained carotenoid pigments [4]. However, the light-yellow color of the petals was not stable, and it faded as the flower developed.

In a previous report, we compared the concentration and composition of carotenoids and the expression patterns of carotenoid biosynthesis and cleavage genes during petal development in a yellow-flowered deciduous azalea (*Rhododendron japonicum* f. *flavum*), a white-flowered evergreen azalea (‘Miyamasatsuki’), and their progeny, to determine the factors that cause discoloration as the petals of the progeny develop [2]. The progeny has a relatively high expression of carotenoid biosynthetic genes inherited from *R. japonicum* f. *flavum*. Carotenoid degradation in the petals of the progeny was mediated by a high CCD4 gene expression inherited from white-flowered evergreen azalea [2]. Thus, inactivation of CCD4 gene during petal development is useful to avoid discoloration of petals in the progenies.

Heavy-ion beam irradiation is one of the useful methods for inactivation of target genes. The present study was conducted to clarify an efficient dose of heavy-ion beam irradiation for azalea seeds.

Materials and methods

Seeds from the three-way crosses between a white-flowered evergreen hybrid from *R. kiusianum* × *R. eriocarpum* (‘Miyamasatsuki’) and yellow flowered deciduous species, *R. japonicum* f. *flavum* were used. They were irradiated with various doses of the 320 MeV carbon ion ($^{12}C^{6+}$) using a TIARA AVF cyclotron. After irradiation, seeds were sterilized in 5% sodium hypochlorite solution for 15 min followed by three washes in sterile distilled water. After sterilizing, about 100 seeds were sown on the petri-dish (Ø 9.0 cm) filled with 25 mL of Anderson’s rhododendron medium [5] supplemented with 30 g·l^{-1} sucrose having pH 5.0 and solidified with 3.5 g·l^{-1} gellangum. Three replicates were conducted per each treatment. The cultures were incubated at 25 °C in a growth chamber in the light (ca. 44.73 μmol·sec^{-1}·m^{-2}) of 16 h daylength. After one month, the germination rate and leaf color of progenies were observed. The seedlings were then, transplanted into the medium with 10 mg·l^{-1} of N6-(2-isopentenyl) adenine (2ip) to induce multiple shoots. After one month, survival rate of seedlings was observed.

Results

Seedlings were obtained nevertheless of irradiation. Germination rate of seeds and frequency of green plant appearance were not significantly different among treatments. On the other hands, survival rates of seedlings significantly decreased at 83 Gy, and 49.4% of seedlings were died at one month after transplanting into 2ip medium (Table1).

Now, the seedlings were multiplicated into 2ip medium. After acclimatization, we will check the morphological characteristics of them.

Table 1
Effect of carbon ion beam irradiation on seed germination, leaf color and survival rate of seedlings.

Dose (Gy)	% of germination	% of green plant appearance	% of seedlings survived
0	35.8[a]	51.1[a]	84.9[a]
8.3	38.6[a]	51.0[a]	87.2[a]
25	54.6[a]	48.1[a]	77.7[a]
50	37.0[a]	41.6[a]	63.4[a]
83	44.1[a]	35.8[a]	50.6[b]

Values marked with different letters indicate statistically significant difference (Tukey’s test, 1% significance).

References

[1] T. Yamazaki, A revision of the genus Rhododendron in Japan, Taiwan, Korea and Sakhalin. Kokusai Bunken Insatsusha, Tokyo. (1996).
[2] K. Ureshino *et al.*, Euphytica **207**, 401 (2016).
[3] K. Ureshino *et al.*, Euphytica **999**, 113 (1998).
[4] I. Miyajima *et al.*, J. Jpn. Soc. Hort. Sci. **69**, 280 (2000).
[5] W.C. Anderson, J. Am. Soc. Hort. Sci. **109**, 343 (1984).

2 - 10 Construction of mutant lines of the parasitic plant *Cuscuta campestris* Yuncker by carbon ion irradiation, and development of experimental systems for screening

R. Yokoyama[a)], K. Satoh[b)] and Y. Oono[b)]

[a)]Graduate School of Life Sciences, Tohoku University
[b)]Department of Radiation-Applied Biology Research, TARRI, QST

Cuscuta species is one of the most widespread group of parasitic plants that subsist on various plant species. Since their host plants include economically important crops, understanding the molecular basis of parasitism of *Cuscuta* species is of critical importance to crop production. Until now, however, the molecular mechanisms underlying the parasite infection using an invasive organ, called a haustorium, remain largely unknown.

We selected *C. campestris* as a model parasitic plant to elucidate the molecular mechanism of parasite infection, because *C. campestris* is broadly sympatric in the world, and therefore is one of the most studied species of the genus *Cuscuta* [1]. We sequenced the genomes of the homozygous lines of *C. campestris*, which we established for identical genotype by self-pollination. Following the sequencing of *C. campestris* genome, we now promote to produce ion-beam irradiated *C. campestris* populations on a large scale for finding the various mutants in the same genetic background.

To use screening assays for parasitism mutants in *C. campestris*, we also developed an *in vitro* experimental system (Fig. 1a). Some studies reported that tactile stimuli induced the formation of haustoria, and far-red light or blue light irradiation promoted parasitism in *Cuscuta* seedlings. We demonstrated that both of tactile stimuli and blue light irradiation were simultaneously required for haustorial induction and formation, and subjected to haustorial induction for 24 h, and haustorial formation for 48 h. *In vitro* regulation of the haustorium development by tactile stimuli and blue light irradiation should be useful in high-throughput screening assays for mutants involved in various aspects of haustorium (Fig. 1b).

Using this *in vitro* experimental system, we further showed that application of host plant tissues to the developing haustorium stimulated vascular cell differentiation in haustorium. This result suggests the involvement of contact between *Cuscuta* and the host tissues in the regulation of vascular cell differentiation during haustorium development [2]. Additionally, we demonstrated that *C. campestris* utilizes host-produced ethylene for the proper growth of search hyphae during haustorium development [3].

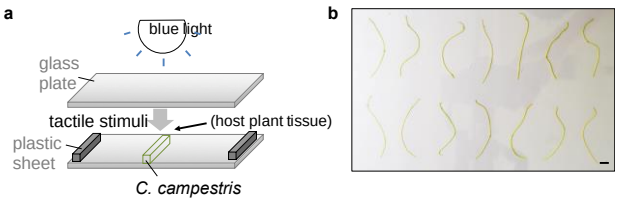

Fig. 1. The experimental system that *in vitro* regulates the haustorium development in *C. campestris*. (a) Schematic images of the *in vitro* experimental system for haustorium induction. (b) High-throughput screening assays for *C. campestris* mutants involved in the haustorium development. Bar = 1 cm.

We previously investigated the dose-response relationship of the rates of seed germination, seedling growth and parasitism to determine the ion-beam irradiation dose suitable for producing a large scale of population harboring mutants. We irradiated *C. campestris* seeds with carbon ions (190 MeV, $^{12}C^{6+}$) accelerated by an AVF cyclotron at TIARA, QST, within a 30 to 3000 Gy range, and showed that parasitism was clearly inhibited when the seeds were irradiated at a dose higher than 100 Gy. Unexpectedly, however, there was little inhibition of seed germination by irradiation, although seedling growth was affected by higher doses of irradiation [4].

To elucidate the different response of parasitism, seed germination and seedling growth by high doses of irradiation, we investigated the effects of irradiation using the *in vitro* experimental system. The results showed that high doses of irradiation had an especially severe impact on the formation of the haustorial primordia with a high level of DNA replication (Fig. 2). High doses of irradiation seemed to have no or less effect on seed germination and seedling growth. Since ion-beam irradiation causes an inhibition of accurate DNA replication, the findings suggest that the seed germination and seedling growth of *C. campestris* may be less involved in DNA replication.

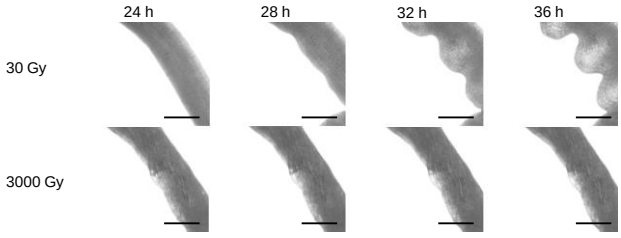

Fig. 2. Visualization of haustorial primordia induced by tactile stimuli and blue light irradiation. The *in vitro* experimental system was used to image haustorial primordia in 7-day-old *C. campestris* seedlings when the seeds were irradiated at a dose 30 Gy (upper) and 3000 Gy (lower). Time points on the top indicate the elapsed time from the start of the induction. Bar = 0.5 mm.

References

[1] R. Yokoyama, Agri Biotech **3**, 57 (2019).
[2] Y. Kaga *et al.*, Front. Plant Sci. **11**, 193 (2020).
[3] H. Narukawa *et al.*, Plant Physiol. **185**, 491 (2021).
[4] R. Yokoyama *et al.*, QST Takasaki Annu. Rep. 2018, **QST-M-23**, 74 (2020).

2 - 11 Large DNA alterations detected in gamma-ray-irradiated Arabidopsis M1 plants

S. Kitamura, K. Satoh and Y. Oono

Department of Radiation-Applied Biology Research, TARRI, QST

Mutations have a potential to change gene functions, which give impact on various biological aspects including speciation, evolution, as well as breeding. Therefore, detection and characterization of mutations are important to accelerate our understanding the fundamental mechanisms that are widely related to plant biology. Since ionizing radiations can induce various types of mutations throughout whole genomes without obvious target sequences, they are recognized as one of the good mutagens for scientific and breeding purposes. Next-generation sequencing (NGS) has been recently developed, and whole-genome sequencing with NGS makes it possible to detect mutations that occurred in whole genome qualitatively and quantitatively. However, such analyses have been exclusively performed using plants in M2 (obtained by self-pollination of mutagenized plants) or later generations, to which large DNA alterations such as large deletions and chromosomal rearrangements are hardly transmitted. Therefore, in order to detect genome-wide mutations including large DNA alterations, NGS using M1 (the mutagenized generation) genomic DNA was conducted in this study.

We constructed Arabidopsis plants that were heterozygous for three anthocyanin genes. If either of three wild-type alleles at the heterozygous loci is mutated, the cells harboring such a mutation would result in loss of ability to produce anthocyanins, leading to the formation of anthocyanin-less sectors in mutagenized plants [1]. Triple heterozygous Arabidopsis seeds were irradiated with gamma-rays (1,000 Gy) at the gamma-ray irradiation facility, and the germinated seedlings were examined regarding anthocyanin accumulation in aerial parts. Seven of the 163 irradiated plants produced anthocyanin-less sectors in leaves, whereas such sectors were not observed in 168 non-irradiated plants.

Using genomic DNA extracted from the 7 sectors, whole-genome sequencing was conducted. Although visual screening enriched a single cell-population exhibiting anthocyanin-less phenotype in the sector, other cell populations having different genotypes would be mixed to unknown extent. To evaluate mutations occurred in M1 sectors correctly, therefore, relatively minor mutations should be detected. For this purpose, we intended to obtain larger NGS data than the standard M2 analyses. After purification of raw sequence data, 769 mutations with allele frequencies of 0.1 – 0.7 were detected from the 7 sectors. Among them, 25 large DNA alterations, such as structural variations (inversion and translocations) and >100 bp deletions were found. There have been several reports concerning whole-genome sequencing of gamma-ray-irradiated M2 or later generations in plants, but the large DNA alterations were rarely detected. Therefore, these large DNA alterations were further characterized.

Twenty-six junctions of the 13 structural variations (SVs) (an example of SVs is shown in Fig. 1) could be divided into 4 types; 6 no insertion/deletion (indel) sites, 11 only-deletion sites, 1 only-insertion site, and 8 indel sites. Among 19 deletions and 9 insertions, 9 and 6 were 5 bp or less in length, respectively. Thus, the rejoined sites possessing 0–5 bp indels were overrepresented in SV (>60%). SVs are formed by incorrect rejoining of two ends of DNA double-strand breaks (DSBs) distally located each other. Because classical non-homologous end-joining (c-NHEJ) can rejoin two DSB ends without indel or with very short indels, the junction patterns in SV suggest that c-NHEJ is crucial for repairing gamma-ray-induced DSBs, and is consistent with the fact that DSBs in Arabidopsis are primarily repaired by the c-NHEJ pathway [2].

Sequence analysis on twelve >100 bp deletions indicated that 3 rejoined sites harbored insertions, one of which was larger than 10 bp. Similar large insertions were found at two rejoined sites of SV. We found highly homologous sequences to the respective large insertions and their flanking regions around their junctions. Because these relatively large sequences are potentially used as templates for generating insertions by DNA polymerase θ (Polθ) at the rejoined sites of DSBs [3], Polθ-mediated repair might work in some junctions of large DNA alterations.

In conclusion, whole-genome sequencing of M1 plants is effective to detect large DNA alterations, and their characterization provides valuable information related to the nature of gamma-ray-induced DSB repair in plants.

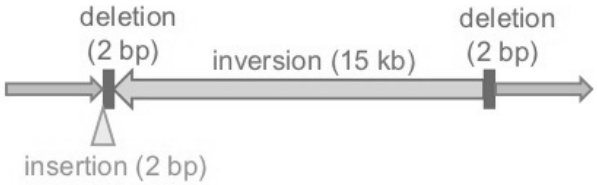

Fig. 1. An example of structural variations (inversion). Arrows represent direction of genome sequence. Deletions and an insertion are indicated as boxes and triangle, respectively.

Acknowledgments

This work was partially supported by JSPS KAKENHI 19K12333.

References

[1] S. Kitamura *et al.*, QST Takasaki Annu. Rep. 2019, **QST-M-29**, 92 (2021).
[2] C. Schmidt *et al.*, Plant J. **98**, 577 (2019).
[3] H. Shen *et al.*, G3 **7**, 193 (2017).

2 - 12 Mutagenesis of the oil-producing algae by heavy ion irradiation

H. Araie[a)], Y. Hase[b)], Y. Iwata[c)], Y. Oono[b)] and I. Suzuki[d)]

[a)]Department of Biosciences, Kanto Gakuin University College of Science and Engineering
[b)]Department of Radiation-Applied Biology Research, TARRI, QST
[c)]Research Institute for Advanced Electronics and Photonics, AIST
[d)]Faculty of Life and Environmental Sciences, University of Tsukuba

Biofuel production by microalgae, is attracting attention as a candidate for next-generation energy, because it does not compete with food production. However, it is necessary to improve and create useful strains which have high oil content or high growth rate that are more suitable for oil production. In this study, we focused on very-long-alkyl ketones so-called alkenone (Fig. 1), which are thought to be good candidates for biofuels [1]. We selected one of the alkenone-producing haptophytes, *Tisochrysis lutea* (Strain T-Iso), because some molecular biotechnological methods and information are available [2, 3]. We have been trying heavy ion beam irradiation to create useful mutant strains that are more suitable for oil production.

Here, we focused on cerulenin which is known as inhibitor of fatty acid synthesis. In sake yeast, it is reported that fatty acid synthesis enhanced mutants were obtained by adding cerulenin to the medium when heavy ion beam was irradiated [4]. Therefore, we performed a similar experiment with microalgae to get fatty acid and alkenone synthesis enhanced mutants.

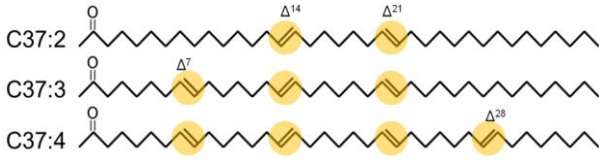

Fig. 1. Alkenone structures. The carbon number of these alkenones is 37 and they have two to four *trans*-type double bonds and a keto group at a C2 position.

In this experiment, we irradiated 0, 10, 20, 30 and 40 Gy of 320 MeV carbon ions to wild-type cells with 0, 5, 7.5, 10, 12.5 or 15 mg/L cerulenin. Total 2678 surviving colonies were cultivated in 96-well plates and lipid content was measured after 1, 2, 3 and 4-week incubation at 20°C. For detection of neutral lipids, we stained cells with Nile Red (final conc. 1 μg/mL) and measured fluorescence of the neutral lipids by a microplate reader (SYNERGY HTX, BioTek). At the same time, we also measured fluorescence of chlorophyll and optical density by a microplate reader.

As the results, histogram of lipid fluorescence intensity showed that 5 ~ 10 mg/L cerulenin were suitable for obtaining mutants with high lipid fluorescence intensity (data not shown).

We picked up mutants as following 3 groups, 1) top 10% mutants with high lipid fluorescence intensity after 4-week cultivation, 2) top 10% mutants with large increase in lipid fluorescence intensity between culture after 1 week and 4 weeks, 3) top 10% mutants with high chlorophyll fluorescence intensity and high optical density after 3-week cultivation. From these groups, we selected 4 candidates (①~④) which have high oil accumulation ability as shown in Fig. 2. Finally, we selected 61 strains (5 strains in group ①, 16 strains in group ②, 40 strains in group ③).

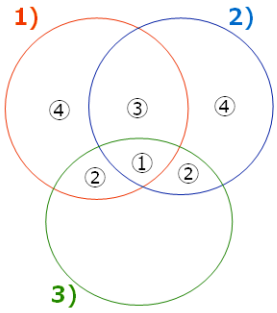

Fig. 2. Venn diagram for selection. ①: Mutants included in all groups 1) , 2) and 3). ②: Mutants included in groups 1) and 3), or groups 2) and 3). ③: Mutants included in groups 1) and 2) but not 3). ④ Mutants included in group 1) but neither 2) nor 3), or group 2) but neither 1) nor 3).

Irradiation doses and cerulenin concentrations for obtaining the selected mutants were shown in Fig 3. The ratio of selected mutants was 2.3%. Interestingly, it was suggested that a mutant with high oil accumulation may be obtained only by addition of cerulenin.

In the future, we plan to analyze how much lipids, especially alkenones, are accumulated in the 61 selected mutants. In particular, we are interested in selected mutants without heavy ion beam irradiation when adding cerulenin.

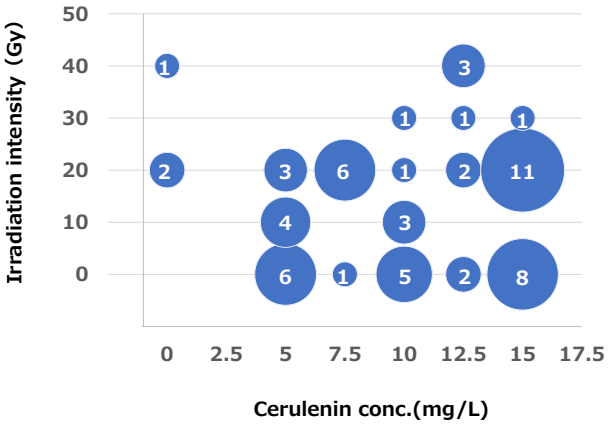

Fig. 3. Conditions for obtaining the selected mutants. Number in the circle shows numbers of selected mutants.

References

[1] O'Neil *et al.*, Energy Fuels **29**, 922 (2015).
[2] Endo *et al.*, Sci. Rep. **8**, 11230 (2018).
[3] Carrier *et al.*, Algal Res. **29**, 1 (2018).
[4] Masubuchi *et al.*, Bioindustry **30**, 65 (2013).

2 - 13 Isolation of non-urea producing candidates from Gunma KAZE3 yeast by ion-beam mutagenesis

T. Watanabe[a)], M. Yanagisawa[a)], K. Satoh[b)] and Y. Oono[b)]

[a)]Gunma Industrial Technology Center
[b)]Department of Radiation-Applied Biology Research, TARRI, QST

Gunma KAZE yeasts, bred for *ginjyo*-sake brewing, are utilized in many sake-manufactures of Gunma prefecture. Urea is a main precursor in Japanese sake of ethyl carbamate which is classified in the group 2A "probably the cause of cancer" by International Agency for Research on Cancer. Kitamoto et al. reported that CAO medium containing canavanine (analog of arginine), arginine and ornithine easily selected non-urea producing mutants [1]. We previously bred non-urea producing Gunma KAZE1 yeast (KAZE1-Arg) by natural mutation and Gunma KAZE2 yeast (KAZE2-Arg) by ion-beam irradiation [2]. However, the growth of Gunma KAZE3 yeast (KAZE3), the second most utilized strain in Gunma prefecture, could not be suppressed on modified CAO medium. On the other hand, we improved the viability of sake yeasts prepared for ion-beam mutagenesis [3]. Thus, in this year, we attempted to improve the medium condition to suppress cell growth and isolate non-urea producing candidates from KAZE3.

Previously, by modifying the concentration of CAO medium we succeed to obtain the non-urea producing candidates from Gunma KAZE2 yeast [2]. Thus, we first changed the concentration of CAO medium to suppress the cell growth of KAZE3. However, KAZE3 grew on the medium containing 4 times higher concentration of canavanine than that of described by Kitamoto et al [1]. Fortunately, we found that glycerol was used as carbon source to avoid growing multi-drug resistant mutants on cerulenin containing medium [4]. Cerulenin is an inhibitor of fatty acid synthase used as high ethyl caproate producing mutants. Gunma KAZE yeasts were bred using cerulenin containing medium. Thus, we changed carbon source of CAO medium from glucose to glycerol. As the results, the growth of KAZE3 was clearly suppressed.

Following air-dried samples were prepared as described previously [3], KAZE3 cells were irradiated with carbon ion beams ($^{12}C^{5+}$, 220 MeV, 200 - 300 Gy) accelerated by using the AVF cyclotron at TIARA, TARRI, QST. Twenty-two candidates were obtained after 5 weeks cultivation on the medium. From these 22 candidates, 17 arginase-inactivate mutants were selected as non-urea producing mutants (Fig. 1). To investigate fermentation ability, *ginjyo*-aroma productivity and urea-productivity, laboratory scale sake brewing experiment was performed using 200 g of total rice. While the parent strain of KAZE3 produced 6.1 mg/L of urea, all mutants did not produce urea (Table 1). However, several mutants changed the brewing profiles (such as fermentation ability, ethyl caproate productivity and isoamyl acetate productivity). Six mutants (KAZE3-2-2, 3-3-1, 3-3-6,3-7-2, 3-7-4 and 3-8-1) were selected for future experiments (shown in red fonts in Table 1).

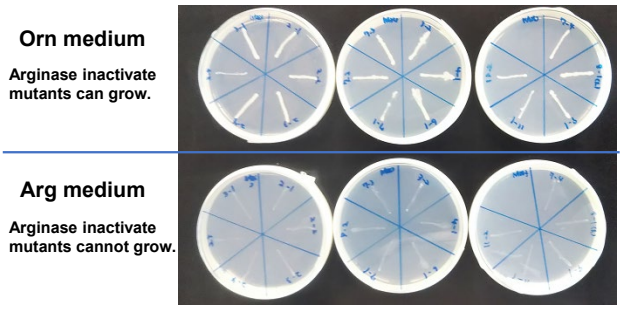

Fig. 1. Growth of arginase-inactive mutants on ornithine (Orn) and arginine (Arg) medium.

Table 1
Summary of laboratory sake brewing experiments

	Alcohol (%(v/v))	Acidity (mL)	Ethyl caproate (ppm)	Isoamly acetate (ppm)	Urea (mg/L)
KAZE3	17.5	2.3	7.4	7.1	6.1
KAZE3-2-1	16.2	2.4	5.7	6.0	ND
KAZE3-2-2	17.4	2.4	6.4	8.9	ND
KAZE3-2-3	13.3	2.3	5.7	5.3	ND
KAZE3-2-4	14.8	2.1	4.7	5.3	ND
KAZE3-2-5	15.4	2.1	4.7	4.6	ND
KAZE3-3-1	17.2	2.3	5.7	8.9	ND
KAZE3-3-2	14.6	2.0	1.4	8.7	ND
KAZE3-4-1	15.3	2.4	9.0	4.6	ND
KAZE3-6-1	15.5	2.7	8.9	8.7	ND
KAZE3-7-1	16.0	2.3	11.7	7.7	ND
KAZE3-7-2	17.2	2.4	10.2	8.2	ND
KAZE3-7-3	18.1	2.3	2.3	23.1	ND
KAZE3-7-4	16.4	2.2	6.6	10.3	ND
KAZE3-8-1	16.7	2.2	8.0	11.1	ND
KAZE3-9-1	13.4	1.8	9.8	2.6	ND
KAZE3-11-1	15.3	2.3	8.4	6.1	ND
KAZE3-11-2	14.8	1.9	1.9	7.2	ND

ND: not detected

Acknowledgments

We thank Prof. T. Fujii for technical advice on isolation of non-urea producing mutants from KAZE3. This study was supported by Dr. Yoshifumi Jigami Memorial Fund, The Society of Yeast Scientists and the grant of *Kenkyuukaihatsu- suishinhi* from Gunma prefecture.

References

[1] K. Kitamoto *et al*., J. Brew. Soc. Japan **87**, 598 (1992).
[2] T. Watanabe *et al*., QST Takasaki Annu. Rep. 2017, **QST-M-16**, 97 (2018).
[3] T. Watanabe *et al*., QST Takasaki Annu. Rep. 2019, **QST-M-29**, 98 (2020).
[4] N. Goto-Yamamoto *et al*., J. Brew. Soc. Japan **95**, 533 (2000).

2 - 14 Evaluation of damage and growth inhibition of *Bacillus subtilis* spores by analysis of their growth curves after irradiation of gamma-rays and high-LET ion beams

H. Den[a)], K. Tatsumoto[a)], A. Futenma[a)], N. Maeda[a)], R. Asada[a)], H. Sakamoto[b)], T. Tsuchido[b)], M. Furuta[a)], K. Satoh[c)] and Y. Oono[c)]

[a)]Quantum Radiation Engineering, Graduate School of Osaka Prefecture University
[b)]Research Center of Microorganism Control, Organization for Research Promotion, Osaka Prefecture University
[c)]Department of Radiation-Applied Biology Research, TARRI, QST

Introduction

Bacterial spores of the genus *Bacillus* are more resistant to physical and chemical stresses than their vegetative cells due to their unique layered and dehydrated interior structure. In order to use radiation sterilization effectively for food and medical products, it is essential to clarify the effect of radiation on resistant spores and to clarify the characteristics of radiation irradiation in comparison with other sterilization methods, in order to improve the sterilization method and to combine it with other sterilization methods. In particular, it has not yet been studied whether damaged bacteria, *i.e.*, cell populations that are damaged by sterilization but regain viability under certain conditions, are still generated after radiation treatment.

In this study, we investigated the role of DNA repair in the resistance of *Bacillus subtilis* spores to gamma-irradiation and ion beam irradiation of different LETs, and the mechanism and developmental dynamics of damaged spores. *sspAsspB* (acid-soluble low molecular weight protein: SASP) and DNA repair enzymes, which are thought to be related to spore resistance, after gamma-irradiation was measured by the flat plate method and the change in turbidity (OD_{650}) with time using a microplate reader, and the presence of damaged bacteria was evaluated by the differential viability method (DiVSaL method) [1].

Experimental method

Bacillus subtilis 168 strain (*trpC2*) and its deficient strains including SASP deficient strain, *recA* (homologous recombination repair: HR) deficient strain, and *ykoUV* (non-homologous end joining repair: NHEJ) deficient strain were used. All spores were formed in Schaefer medium and obtained according to the method of Koshikawa [2]. Spores were suspended in 50 mM potassium phosphate buffer (KPB) containing 0.1% Tween 80 and irradiated with ^{60}Co gamma-rays (0-6 kGy) at the Radiation Research Center, Osaka Prefecture University, and with $^{4}He^{2+}$ (50 MeV; 19.4 keV/μm), $^{12}C^{6+}$ (190 MeV; 148.7 keV/μm), and $^{20}Ne^{8+}$ (350 MeV; 440.8 keV/μm) ion beams were irradiated at TIARA, TARRI, QST. The number of surviving spores (CFU) was determined by the plate counting method, in which the spores were appropriately diluted in KPB, incubated on LB agar plates and the colonies generated were counted. The difference between the two was compared by the DiVSaL method [2] to estimate the quantity of the damaged bacteria.

Results and Discussions

The killing effect of ion beam irradiation of spores with different LETs showed a LET-dependent loss of colony forming ability as previously reported [3]. Analysis by DiVSaL method, an evaluation method of injured cell population based on comparison of time before starting vegetative growth of irradiated cells with unirradiated cells, indicated the increase of injured cell population with increasing dose as well as CPU. The ratio of the injured cell population tends to increase with increasing RBE according to ion species and energies used for irradiation as shown in Fig. 1.

Gamma-irradiation of the spores of SASP and DNA double-strand break repair (DSB) deficient *B. subtilis* strains showed more sensitivity than the wild type sand the rate of injured population also increased in the deficient strains by the analysis of DiVSaL method, indicating that DNA damages might increase the injured cell population. These results suggest that capacity of repairing the DNA damages within the spores would prevent injured cell formation during the recovering process from the both ion beams and gamma irradiation.

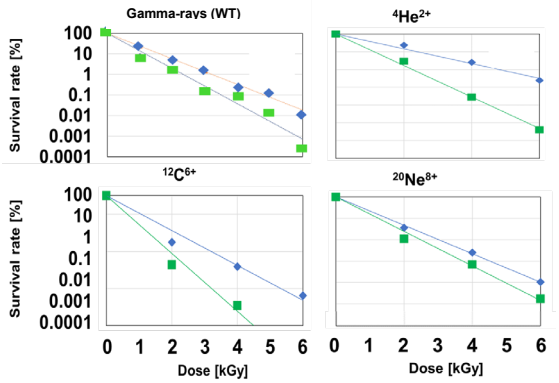

Fig. 1. Evaluation of injured fraction of survivors of *B. subtilis* following ^{60}Co- and high LET ion-beam irradiation by DivSaL method. ◆: Surviving and recovered cell fractions from injured state by CPU. ■: Surviving cell without injured cells determined by DivSaL methods.

References

[1] T. Tsuchdo, Biocontrol. Sci. **22**, 131 (2017).
[2] F. Koshikawa, RADIOISOTOPES **43**, 710 (1994).
[3] H. Den *et al.*, QST Takasaki Annu. Rep. 2019, **QST-M-29**, 100 (2021).

2 - 15 Characterization of ABC transporter which cause the delayed contact-dependent RED production in *Streptomyces coelicolor*

S. Asamizu[a,b], Y. Lei[a], T. Ishizuka[a], M. Yanagisawa[a], K. Satoh[c], Y. Oono[c] and H. Onaka[a,b]

[a]Graduate School of Agricultural and Life Sciences, The University of Tokyo
[b]Collaborative Research Institute for Innovative Microbiology, The University of Tokyo
[C]Department of Radiation-Applied Biology Research, TARRI, QST

Actinomycetes, filamentous Gram-positive bacteria, are a major source of bioactive natural products which can be drug candidates. Genome analyses of actinomycetes have revealed the huge number of "cryptic" secondary metabolite biosynthetic gene clusters, indicating the potential of actinomycetes for the production of far more diverse secondary metabolites than previously thought. We have studied about the bacterial interaction induced production of secondary metabolites by actinomycetes. *Tsukamurella pulmonis* TP-B0596 (here after Tp) had been shown to possess ability to induce production of secondary metabolites by *Streptomyces* species, which are not detected or poorly produced in a mono-culture [1]. Until now, more than 30 new compounds had been isolated from the co-culture with various actinomycetes and Tp (the method named combined-culture) [2]. Object of this study is to elucidate the gene(s) which are involved in the regulation of secondary metabolism caused by bacterial interaction. Elucidation of the mechanism can lead to the fundamental understanding of bacterial interaction induced secondary metabolism, as well as application for genetic tools to discover novel bioactive natural products from untapped genes.

Streptomyces species are suggested to respond to stimuli caused by mycolic acid-containing bacteria via a contact of cells, which led to production of secondary metabolism [1,3]. We had employed carbon ion beams ($^{12}C^{5+}$), accelerated by using the AVF cyclotron at TIARA, induced mutation to investigated the gene(s) responsible for the responsive production of secondary metabolism induced by Tp. Using *Streptomyces coelicolor* JCM4020, random spore mutant library was generated. Undecylprodigiosin (RED) production deficient mutants was screened by mixing with Tp on agar plates using red / white phenotype of the colonies as indication. Through this screening, 59 mutants from around 152,000 tested spores were obtained [8]. 16 mutants were first genome re-sequenced by Miseq and 44 mutations were identified [4, 5, 8]. Gene complementation was performed and glutamate synthase, elongation factor G, and putative membrane protein was revealed to cause the RED deficient phenotypes [6, 8]. Further 26 mutants were genome re-sequenced by Hiseq and gene complementation study revealed that molybdopterin biosynthetic enzyme, and TetR-like transcriptional regulator are also responsible for the phenotype [7]. We further analyzed the involvement of TetR-like transcriptional regulator by targeted gene disruption in *S. coelicolor* A3(2) and confirmed the delayed production of RED [7]. EMSA analysis showed that TetR-like protein bound to the 5'-UTR of adjacent ABC transporter genes. RT-qPCR showed that ABC transporter genes were overexpressed in the disruptant. Therefore, ABC transporter was indicated to efflux the unknown small molecule(s) thereby reduce the accumulated stress inside the cell. Tp was suggested to induce the accumulation of stress molecule(s) that can be a trigger to cause the production of RED (Fig. 1).

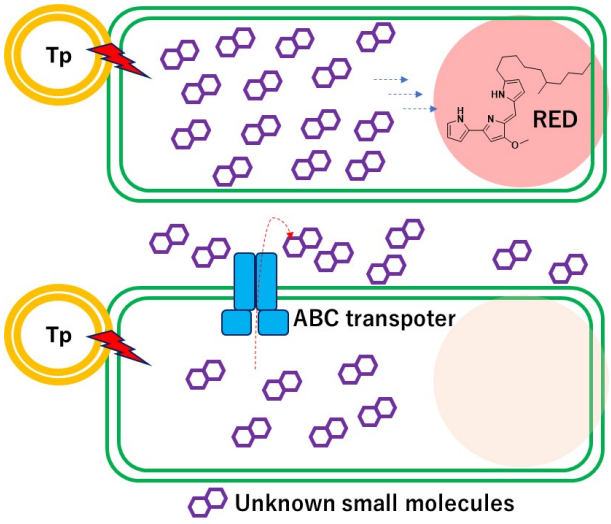

Fig. 1. Hypothetical schematic model of Tp induced RED production by *S. coelicolor*.

References

[1] H. Onaka *et al.*, Appl. Environ. Microbiol. **77**, 400-6 (2011).
[2] H. Onaka *et al.*, Comprehensive Natural Products III, (2019). DOI: 10.1016/B978-0-12-409547-2.14692-X
[3] S. Asamizu *et al.*, PLos One **10**, e0142372 (2015).
[4] M. Yanagisawa *et al.*, QST Takasaki Annu. Rep. 2016, **QST-M-8**, 97 (2018).
[5] S. Asamizu *et al.*, QST Takasaki Annu. Rep. 2017, **QST-M-16**, 106 (2019).
[6] S. Asamizu *et al.*, QST Takasaki Annu. Rep. 2018, **QST-M-23**, 88 (2020).
[7] S. Asamizu *et al.*, QST Takasaki Annu. Rep. 2019, **QST-M-29**, 101 (2021).
[8] S. Asamizu *et al.*, IFO Res. Commun. **32**, 95 (2018).

2 - 16 Mutation analysis of the DNA damage response regulator protein PprI in the radioresistant bacterium *Deinococcus radiodurans*

K. Satoh[a)], T. Sanzen[a, b)], Y. Oono [a)] and I. Narumi[b)]

[a)]Department of Radiation-Applied Biology Research, TARRI, QST
[b)]Graduate School of Life Sciences, Toyo University

Introduction

Deinococcus radiodurans is a representative strain of radioresistant bacteria and has extremely high resistance to various DNA damaging agents such as gamma rays, ultraviolet rays, desiccation, free radical-generating substances, and DNA cross-linkers. The previous studies revealed that the expression of a unique DNA repair-related protein, PprA, was up-regulated by a regulatory protein, PprI, following DNA damage in *D. radiodurans* [1]. The radiation/desiccation response (RDR) motif was found in the upstream regions of the radiation-inducible genes (RDR regulons) by comparative genome sequence analysis of *Deinococcus* [2]. The RDR motif serves as an operator sequence in the unique DNA repair response system [3]. The PprI consists of three domains, namely metalloprotease, DNA binding and GAF-like binding domains. Another regulatory protein DdrO binds the RDR motif and serves as a repressor. Following DNA damage, the metalloprotease activity of PprI cleaves DdrO, resulting in derepression of the RDR regulon [4]. In this study, to delineate the functional site of PprI in regard to the DNA damage response mechanism, we constructed several *pprI*-expression plasmids carrying mutations which cause a single amino acid substitution.

Experimental procedures

The site-directed mutagenesis was performed to introduce the following mutations (E119Q and E149Q) into the wild-type *pprI* expression plasmid [5]. The wild-type and mutated *pprI* expression plasmids were introduced into the *pprI*-deleted mutant strain SXPI [5] (designated PIPW, PIM_E119Q, PIM_E149Q) and the luciferase reporter strain SIRP [6] (designated DAW, DAM_E119Q and DAM_E149Q). The strains PIPW, PIM_E119Q and PIM_E149Q were subjected to complementation test to gamma rays. The strains DAW, DAM_E119Q and DAM_E149Q were subjected to the luciferase reporter assay following gamma irradiation. The gamma irradiations were performed at Food Irradiation Facility, TARRI, QST.

Results ad discussion

The *pprI*-deleted mutant strains carrying the mutated *pprI* genes (PIM_E119Q and PIM_E149Q) showed significant sensitivity to gamma rays as same as the strain XP (Fig. 1). On the other hands, the resistance to gamma rays in strain PIPW was restored to the wild-type level (Fig. 1). Moreover, unlike the strain DAW carrying the wild-type *pprI* gene, the enhances of luciferase reporter activity in the luciferase reporter strains carrying the mutated *pprI* genes (DAM_E119Q and DAM_E149Q) were not observed following irradiation (Fig. 2). These results suggest that E119Q and E149Q at metalloprotease domain of PprI play a critical role in the DNA damage response mechanism.

Acknowledgments

This work was supported by JSPS KAKENHI Grant Number JP18K05423 to K. Satoh.

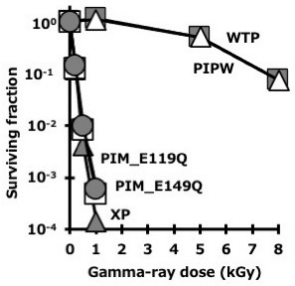

Fig. 1. Complementation tests to gamma rays. Symbols: ■, WTP (wild-type); ▲, XP (*pprI*-deletion); △, PIPW (wild-type *pprI*); □, PIM_E119Q (mutated *pprI*); ●, PIM_E149Q (mutated *pprI*).

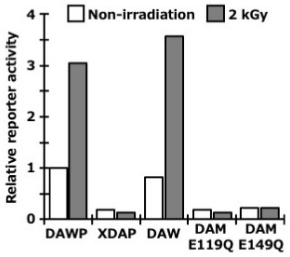

Fig. 2. Changes in luciferase reporter activity following irradiation (2 kGy) in the reporter strains DAWP (wild-type), XDAP (*pprI*-deletion), DAW (wild-type *pprI*), DAM_E119Q (mutated *pprI*) and DAM_E149Q (mutated *pprI*). Cells were irradiated (■) or mock irradiated (□) with gamma rays, incubated for 2 h and then subjected to the reporter assay. Strain DAWP Values represent the relative reporter activity normalized in relation to the mock-irradiated DAWP value of 1.

References

[1] Y. Hua *et al.*, Biochem. Biophys. Res. Commun. **306**, 354 (2003).
[2] K.S. Makarova *et al.*, PLoS One **2**, e955 (2007).
[3] M. Ludanyi *et al.*, Mol. Microbiol. **94**, 434 (2014).
[4] H. Lu *et al.*, DNA Repair **11**, 139 (2012).
[5] K. Satoh *et al.*, QST Takasaki Annu. Rep. 2018, **QST-M-23**, 83 (2020).
[6] K. Satoh *et al.*, QST Takasaki Annu. Rep. 2019, **QST-M-29**, 96 (2021).

2 - 17 Resistance to gamma- and ultraviolet-rays of *Rubrobacter* sp. AA3-22

K. Izumi[a)], K. Satoh[b)], Y. Oono[b)], K. Miyazaki[c)] and I. Narumi[a)]

[a)]Faculty of Life Sciences, Toyo University
[b)]Department of Radiation-Applied Biology Research, TARRI, QST
[c)]Bioproduction Research Institute, AIST

Introduction

Rubrobacter belong to the phylum "Actinobacteria" while *Deinococcus* that are well known as the radioresistant bacteria belong to the distinct phylum "Deinococcus-Thermus". To date, 11 species of *Rubrobacter* have been reported, and radiation resistance data are described for 3 species, namely *Rubrobacter radiotolerans* [1,2], *Rubrobacter xylanophilus* [2] and *Rubrobacter taiwanensis* [3]. The strain AA3-22 isolated from Arima Onsen is a moderate thermophile with an optimum growth temperature of 58 °C, and it has been reported from genome sequence analysis that it is most related to *R. xylanophilus* [4]. In this study, we compared the survival curves of the strain AA3-22, the *R. radiotolerans* and *R. xylanophilus* type strains in order to clarify the resistance to gamma- and ultraviolet-rays.

Materials and Methods

The type strains of *R. radiotolerans* (JCM 2153) and *R. xylanophilus* (JCM 11954) were obtained from RIKEN BioResource Research Center. JCM 2153 was cultivated at 37 °C for 72 h in R2 broth. JCM 11954 was cultivated at 60 °C for 48 h in Thermus medium. AA3-22 was cultivated at 60 °C for 24 h in Marine broth. For gamma irradiation, cultured cells suspended in 10 mM sodium phosphate buffer (pH 7.0) were exposed to ^{60}Co gamma-rays at the gamma-ray irradiation facility, TARRI, QST, and the survived cells were counted using the serial dilution spotting method. For ultraviolet irradiation, diluted cell suspension spotted on agar plates was exposed to ultraviolet C (UVC) light, and the survived cells were counted after incubating the plates at a constant temperature.

Results and Discussion

AA3-22 showed the lowest resistance to gamma-rays among the three strains tested. The survival curve of AA3-22 resembled that of the wild-type strain of *Deinococcus radiodurans* [5] (Fig. 1). The gamma-ray resistance of *R. radiotolerans* JCM 2153 was in good agreement with the previous literature value [1]. On the other hand, the gamma-ray resistance of *R. xylanophilus* JCM 11954 was lower than the previous literature value [2], which seemes to be due to the difference in cell density subjected to irradiation.

Regarding ultraviolet resistance, AA3-22 exhibited the highest resistance among the three strains tested, and *R. xylanophilus* JCM 1195 unexpectedly showed significant sensitivity to ultraviolet-rays (Fig. 2).

In the future, we would like to consider the difference in gamma-ray and ultraviolet-ray resistances between these strains from the genome sequence information.

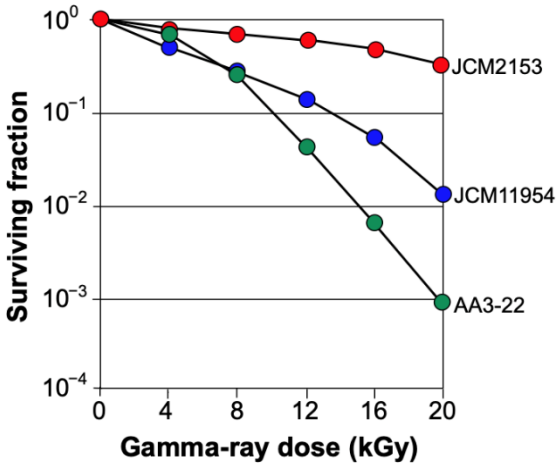

Fig. 1. Survival curves of JCM 2153, JCM 11954, and AA3-22 following gamma irradiation.

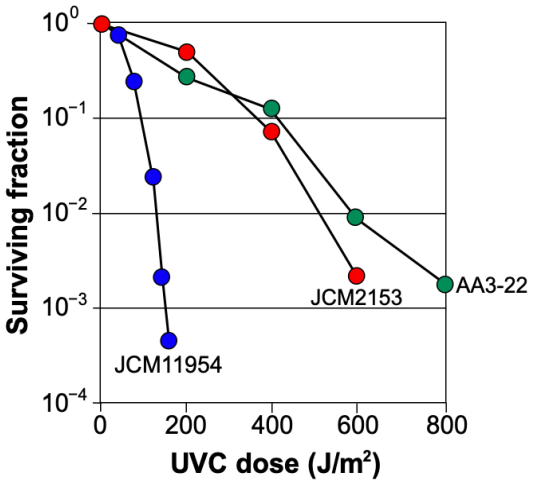

Fig. 2. Survival curves of JCM 2153, JCM 11954, and AA3-22 following UVC irradiation.

References

[1] T. Yoshinaka *et al.,* Agric. Biol. Chem. **37**, 2269 (1973).
[2] A. C. Ferreira *et al.*, Extremophiles **3**, 235 (1999).
[3] M.-Y. Chen *et al.*, Int. J. Syst. Evol. Microbiol. **54**, 1849 (2004).
[4] N. Tomariguchi and K. Miyazaki, Microbiol. Resour. Announc. **8**, e00818-19 (2019).
[5] Y. Yang *et al.*, Int. J. Syst. Evol. Microbiol. **60**, 776 (2010).

2 - 18 Radioresistance of double-strand break repair-deficient mutants in *Physcomitrium patens*

Y. Yokota and A.N. Sakamoto

Department of Radiation-Applied Biology Research, TARRI, QST

Ionizing radiation (IR) endangers organisms through the induction of DNA damage by reactive oxygen species. Compared to other types of DNA damage DNA double-strand breaks (DSBs) are the most difficult to repair accurately. The moss *Physcomitrium patens* has a unique characteristics among multicellular eukaryotes, as it exhibits high rates of homology-based knockout (KO) of a given target gene. *P. patens* cells also show more than 100- and 10-fold IR resistance compared to mammalian cells and tobacco BY-2 cells, respectively [1]. These facts suggest that *P. patens* has a particularly efficient DSB repair mechanism.

The homologous recombination (HR), canonical non-homologous end-joining (C-NHEJ), and alternative end-joining (Alt-EJ) pathways are known to be used for DSB repair. We used CRISPR/Cas9 technology to create KO strains of the *PpRAD51B*, *PpLIG4*, and *PpPOLQ* genes, which play major roles in the HR, C-NHEJ, and Alt-EJ pathways, respectively. Based on the nucleotide sequences of *Rad51B*, *Lig4* and *PolQ* obtained from public database [2], the guide RNAs (sgRNAs) for recruiting the Cas9 to the target sites were designed, and the templates for sgRNA synthesis were subcloned. Three kinds of plasmids, which carry CAS9, an sgRNA, and the geneticin-resistant genes, were co-introduced into *P. patens* protoplasts to express these genes transiently. The cells were screened on geneticin-containing plates for ~3 weeks. Sequencing analysis of the target alleles confirmed the KO strains, in which an immature stop codon occurred due to a deletion or insertion in the open reading frame.

To investigate the roles of HR, C-NHEJ, and Alt-EJ pathways in the radioresistance, we compared the sensitivity to gamma rays of the *PpRAD51B*-, *PpLIG4*-, and *PpPOLQ*-KO strains to that of the wild type. Protonema tissues of *P. patens* were irradiated with ~400 Gy of gamma rays, and the dry weight was measured. The result showed that the protonema cells of the wild type, *lig4-1*, *lig4-2*, *polq-1*, and *polq-2* strains continued growing at 200 or 400 Gy, whereas those of *rad51b-1* and *rad51b-2* stopped growing at 40 Gy. In all the strains, the dry weight tended to decrease with an increasing dose of gamma rays (Fig. 1). The doses at which the dry weight was reduced by half were disributed at 350 - 590 Gy in both wild type and mutants (Table 1). The dry weight of the *rad51b-1* and *rad51b-2* mutants was reduced by half at 9 Gy and 10 Gy, respectively. Thus, in *P. patens*, the absence of *RAD51B*, which plays a major role in the HR pathway, leads to a strong inhibition of vegetative growth after irradiation compared to the wild type.

In a growth assay, even if some cells are fatally damaged and stop growing, remaining healthy cells may increase their growth thanks to obtaining additional nutrients. To investigate the cell-killing effect of IR on individual cells, we are going to perform the colony-forming ability of irradiated protoplasts. We are also going to measure the DSB repair kinetics of the knockout strains by pulse-field gel electrophoresis assay.

Acknowledgments

We thank F. Nogué for providing materials. We also thank the operators of the Cobalt-60 irradiation facility for their technical support.

References

[1] Y. Yokota and A.N. Sakamoto, Genes **9**, 76 (2018).
[2] https://phytozome.jgi.doe.gov/pz/portal.html.

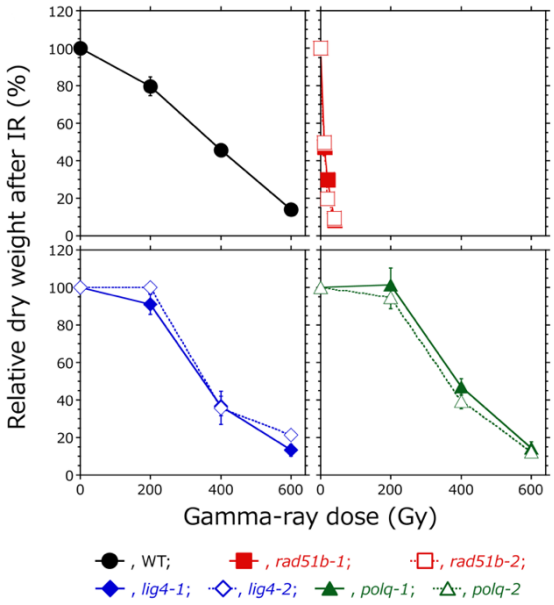

Fig. 1. Inhibition of vegetative growth in the wild type and KO strains after gamma-ray irradiation. Each point represents the mean ± standard error (SE) of 3 or more independent experiments.

Table 1
Doses that reduce the dry weight to 50%.

Strain	50% DW dose (Gy)	Strain	50% DW dose (Gy)
WT	375	*lig4-1*	352
rad51B-1	9	*lig4-2*	356
rad51B-2	10	*polq-1*	388
		polq-2	362

2 - 19 Raman-activated directed evolution of *Euglena gracilis* with quantum-beam mutagenesis

J. Gala de Pablo[a)], M. Lindley[a)], K. Hiramatsu[a)], K. Goda[a)], K. Sato[b)] and Y. Oono[b)]

[a)]Department of Chemistry, School of Science, The University of Tokyo
[b)]Department of Radiation-Applied Biology Research, TARRI, QST

Biomaterials derived from microalgae are promising as a source of biofuels, drugs, cosmetics, and foods. Among different microalgae, *Euglena gracilis* has attracted attention for biomaterials production due to its high productivity of paramylon, a potential drug for HIV and colon cancer [1]. To enhance the productivity of paramylon in *E.gracilis*, directed evolution is a promising approach. In general, directed evolution consists of three key steps: mutagenesis, selection, and amplification. For applying it to the enhancement of the paramylon productivity of *E.gracilis,* mutagenesis and selection steps are challenging because altering nuclear genome of *E.gracilis* is difficult due to its polyploid nature and no biomarker such as fluorescent dyes is available for quantifying paramylon. In this study, we tackle these difficulties by combining quantum-beam irradiation for mutagenesis and high-throughput Raman-activated cell screening for label-free selection.

Raman spectroscopy is a method to measure molecular vibrations through inelastic light scattering. Although Raman spectroscopy can characterize various molecules without staining, its application to high-throughput cell screening has been limited mainly due to small Raman scattering cross-section. Recently, we have overcome this difficulty by combining high-speed (24,000 spectra/s) broadband Fourier-transform coherent anti-Stokes Raman scattering (FT-CARS) spectrometer and on-chip flow cytometer based on an acoustofluidic-focusing microfluidic chip (Fig. 1) [2]. This collaboration study aims to establish a framework to create *E.gracilis* strains with high paramylon productivity by repeating quantum-beam-based mutagenesis and FT-CARS flow cytometer-based selection multiple times.

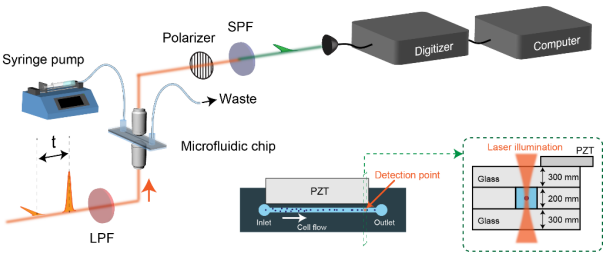

Fig. 1. Schematic of our high-throughput FT-CARS flow cytometer. Cells rapidly flowing the microfluidic chip are interrogated by pairs of ultrashort pulses. The first pulses coherently excite molecular vibrations, whose temporal evolution is characterized by the second pulses through their blue shift. Raman spectra are obtained by Fourier transforming time-domain interferograms, which are obtained by measuring the blue-shifted component at various pulse intervals t. In our setup, the pulse-interval-scan rate is 24,000 scans/s, which results in high Raman spectral acquisition rate of 24,000 spectra/s. LPF: Long-pass filter, SPF: Short-pass filter, PZT: Piezoelectric transducer.

This year, for checking the feasibility of Raman-based selection of *E.gracilis* based on paramylon productivity, we performed quantification of paramylon in *E.gracilis* with our high-throughput Raman flow cytometer irradiating γ-ray at various doses. Fig. 2 shows the distribution of paramylon amount in irradiated *E.gracilis* cells (N = 12,519 in total). The data show that the paramylon amount of the sample irradiated at 1000 Gy shows higher distribution from the control sample (0 Gy). On the other hand, the 2000-Gy sample shows almost zero distribution of paramylon, presumably because most of the cells are dead.

As a next step, we will perform paramylon quantification with different ion beams and different culturing conditions. Also, we will integrate the FT-CARS flow cytometer with an on-chip cell sorter to enable the collection of highly productive cells after mutagenesis.

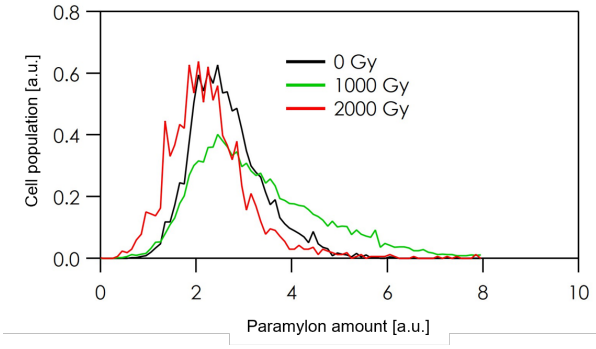

Fig. 2. Dose-dependent distribution of paramylon content in *E.gracilis* cells evaluated by our high-throughput FT-CARS flow cytometer.

Acknowledgments

This work was supported by KISTEC and Nakatani foundation.

References

[1] T. Watanabe, *et al.*, Food Funct. **4**, 1685 (2013).
[2] K.Hiramatsu, *et al.*, Sci. Adv. **5**, eaau0241 (2019).

2 - 20 Preliminery examination of soft agar colony formation assay for PC12 pheochromocytoma cells

T. Sakashita, Y. Ohshima, Y. Yokota and N. S. Ishioka

Department of Radiation-Applied Biology Research, TARRI, QST

Introduction

Pheochromocytomas (PCCs) are rare neuroendocrine tumors with malignant progression. Clinical improvement of malignant PCCs with β-emitting *meta*-^{131}I-iodo-benzylguanidine (^{131}I-MIBG) constitutes a stage of partial remission in metastatic PCC [1]. Recently, we reported strong anti-tumor effects of α-emitting *meta*-^{211}At-astato-benzylguanidine (^{211}At-MABG) in a PCC mouse model, suggesting a potential option for targeted α therapy (TAT) for patients with malignant PCC [2]. We also found that the gene expression profiles of cell cycle checkpoints displayed similar modes of cell death via the p53-p21 signaling pathway after ^{211}At-MABG treatment and γ-ray irradiation [3]. This p53-dependent pathway would induce reproductive cell death, *e.g.* cell cycle arrest. However, we have not yet checked for reproductive cell death in PCC (PC12) cells by colony formation assays because PC12 cells showed strong aggregation. Last year, we employed the soft-agar colony formation assay of PC12 cells by modifying the previously reported method [4]. Here, we preliminary reported the surviving fraction of γ-ray irradiated PC12 cells using the soft-agar colony formation assay.

Materials and methods

Cell culture. PC12 cells were cultured in RPMI1640 medium (Wako, Osaka, Japan) supplemented with 5% v/v fetal bovine serum (FBS), 10% horse serum (HS), 100 U/ml penicillin and 100 μg/ml streptomycin in a humidified 5% CO_2, 37 ºC incubator.

Cell irradiation. PC12 cell suspension was irradiated by ^{60}Co γ-rays at the absorbed dose of 1, 3, 5 and 10 Gy.

Cell detachment. PC12 cell suspension was centrifuged at 200 rcf for 3 min, and supernatant was removed. Cell pellet was gently resuspended in 1 ml accutase (Nacalai tasque, Kyoto, Japan), and incubated for 30-40 minutes in a humidified 5% CO_2, 37 ºC incubator.

Remove small aggregates. Detached cells were filtered using a Flowmi tip strainer (40 μm, Scienceware, Wayne, NJ, USA) to remove small aggregates from single cells.

Cell count. Passed cells through cell strainer were manually counted under microscope with a Burker-Turke hemocytometer equivalent to 10^4 cells/ml.

Soft agar colony formation assay. Single cells were diluted to obtain appropriate number of colonies after culture in a soft agarose. Cells were suspended in the RPMI1640 medium with 0.3% w/v agar and the cell suspension was overlaid onto the RPMI1640 medium with 0.7% bottom agar in 6 well plates. Cells were allowed to grow for 4-5 weeks at the 5% CO_2, 37 ºC incubator. Finally, cells were stained with MTT (3-(4,5-dimethylthiazol-2-yl)-2,5-diphenyltetrazolium-bromide, Roche AB) for 1 hour and colonies were manually counted under the microscope. We counted a colony with 50 or more cells, except for abortive colonies with 2–49 cells (Fig. 1(a)).

Preliminary results

We measured surviving fraction (SF) of soft-agar colony formation assay for PC12 **PCC** cells (Fig. 1 (b)). The SFs decreased with absorbed dose and showed a relationship close to a straight line in a semi-logarithmic plot. We will continue an examination of soft agar colony formation assay for γ-ray irradiated PC12 cells, and compare ^{211}At-MABG treatment with ^{60}Co γ-rays irradiation on the reproductive cell death.

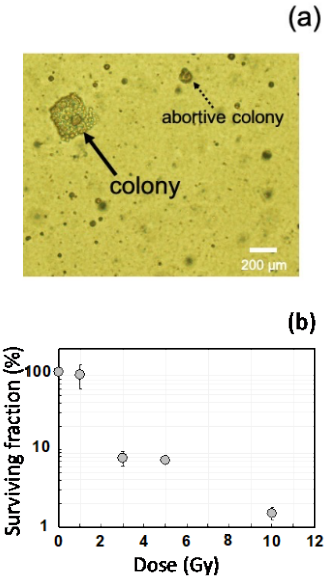

Fig. 1. (a) Colony image of normal colony with 50 or more cells and abortive colony with 2–49 cells. Scale bar indicates 200 μm. (b) Surviving fraction (gray circle) of γ–irradiated PC12 cells. Error bars indicate the standard deviation (n = 3).

Acknowledgments

We would like to thank Prof. Y. Matsumoto of Tokyo Institute of Technology for his advice of soft-agar colony assay.

References

[1] J.A. Carrasquillo *et al.*, Semin. Nucl. Med. **46**, 203 (2016).
[2] Y. Ohshima *et al.*, Eur. J. Nucl. Med. Mol. Imag. **45**, 999 (2018).
[3] Y. Ohshima *et al.*, Theranostics **9**, 1538 (2019).
[4] J. Geli *et al.*, Endocr. Relat. Canc. **14**, 125 (2007).

2 - 21 Preclinical evaluation of new α-radionuclide therapy targeting LAT1: 2-[^{211}At]astato-α-methyl-L-phenylalanine in tumor-bearing model

Y. Ohshima[a)], H. Suzuki[b)], H. Hanaoka[c)], I. Sasaki[a)], S. Watanabe[a)], H. Haba[d)], Y. Arano[b)], Y. Tsushima[c)] and N. S. Ishioka[a)]

[a)]Department of Radiation-applied Biology Research, TARRI, QST
[b)]Graduate School of Pharmaceutical Science, Chiba University
[c)]Gunma University Graduate School of Medicine
[d)]Nishina Center for Accelerator-Based Science, RIKEN

Targeted α-radionuclide therapy has attracted attention as a promising therapy for refractory cancers. However, the application is limited to certain types of cancer. Since L-type amino acid transporter 1 (LAT1) is highly expressed in various human cancers, radiopharmaceuticals targeting LAT1 would enable the wider use of targeted α-therapy. We previously developed fluorine-18 (^{18}F)- or bromine-76 (^{76}Br)-labeled amino acid tracers targeting LAT1. Among them, 2-[^{18}F]- or 2-[^{76}Br]-labeled α-methyl-L-phenylalanine analog was specifically taken up by tumor via LAT1, while they were rapidly cleared from body and excreted into urine [1,2]. Since ^{18}F and ^{76}Br belong to radiohalogen, astatine-211 (^{211}At), an α-emitting halogen, labeled α-methyl-L-phenylalanine is expected to show high tumor accumulation and preferred pharmacokinetics. In this study, we newly synthesized 2-[^{211}At]astato-α-methyl-L-phenylalanine (2-[^{211}At]AAMP) (Fig.1(a)), and evaluated its potential as a therapeutic agent [3].

^{211}At was produced via the ^{209}Bi(α,2n)^{211}At reaction and isolated by the dry distillation. 2-[^{211}At]AAMP was prepared from the stannyl precursor. Stability of 2-[^{211}At]AAMP was evaluated both *in vitro* and *in vivo*. Cell studies using an LAT1-expressing human ovarian cancer cell line, SKOV3, were performed to evaluate cellular uptake and cytotoxicity of 2-[^{211}At]AAMP. Biodistribution and therapeutic studies in SKOV3-bearing mice were performed after intravenous injection of 2-[^{211}At]AAMP.

When injected into mice, 2-[^{211}At]AAMP exhibited peak accumulation in the tumor at 30 min postinjection, and radioactivity levels in the tumor were retained up to 60 min. The majority of the radioactivity was rapidly eliminated from the body into urine in an intact form immediately after injection, indicating that 2-[^{211}At]AAMP remained stable *in vivo*. Cellular uptake of 2-[^{211}At]AAMP was rapid and sodium-independent, and significantly inhibited with LAT1 selective inhibitors. After 24 h incubation, 2-[^{211}At]AAMP suppressed clonogenic growth at 10 kBq/ml, and induced cell death and DNA double-strand breaks (DNA-DSB) at 25 kBq/ml (Fig. 1 (b)). These results indicate that 2-[^{211}At]AAMP was taken up via LAT1, and caused α-radiation-dependent cellular growth inhibition. Furthermore, 2-[^{211}At]AAMP (2 MBq/head) significantly improved the survival of mice ($P < 0.05$) without serious side effects (Fig. 2). These findings suggest that 2-[^{211}At]AAMP would be useful for the treatment of LAT1-positive cancer. This is the first report of an LAT1-targeting radiopharmaceutical for α-radionuclide therapy; this agent would be applicable for the treatment of various types of cancer. However, the clearance of 2-[^{211}At]AAMP from tumor might be too rapid for suppressing tumor growth. Therefore, modification of 2-[^{211}At]AAMP itself or combination with other compound to improve tumor retention of 2-[^{211}At]AAMP would constitute a strategy for better therapeutic effect. We will plan to apply pre-injection of probenecid, an organic anion transporter inhibitor, to enhance tumor accumulation levels of 2-[^{211}At]AAMP in tumor-bearing mice.

Acknowledgments

The authors thank the staff in the cyclotron operation section for the cyclotron operation.

References

[1] H. Hanaoka *et al*., J. Nucl. Med. **56**, 791 (2015).
[2] H. Hanaoka *et al*., Mol. Pharm. **16**, 3609 (2019).
[3] Y. Ohshima *et al*., Nucl. Med. Biol. **90-91**, 15 (2020).

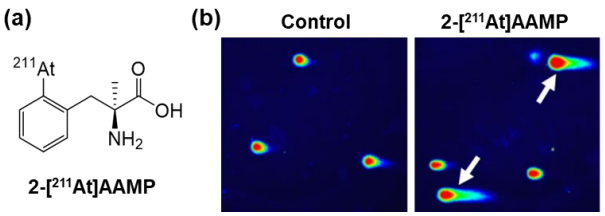

Fig.1. (a) Structure of 2-[^{211}At]AAMP. (b) Cells with DNA-DSB after treatment with 25 kBq/ml of 2-[^{211}At]AAMP. The arrows indicate the representative comets with DNA-DSB.

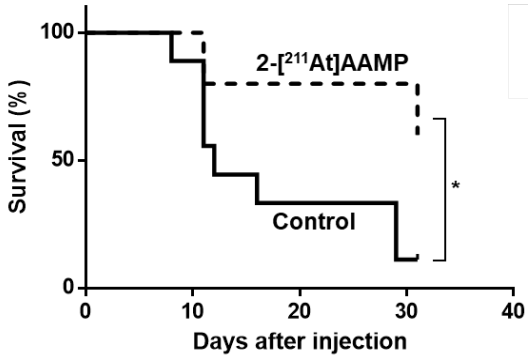

Fig. 2. Kaplan-Meier survival curves. The group treated with 2 MBq of 2-[^{211}At]AAMP showed significantly better survival than the control group (* $P < 0.05$ vs. control).

2 - 22 Preparation of no-carrier-added ^{211}At solutions by a simple dry distillation method in the ^{209}Bi(^{4}He,2n)^{211}At reaction

I. Nishinaka[a,b], N. S. Ishioka[b], S. Watanabe[b], I. Sasaki[b] and A. U. Azim[c]

[a]Tokai Quantum Beam Science Center, TARRI, QST
[b]Department of Radiation-Applied Biology, TARRI, QST
[c]National Institute of Nuclear Medicine & Allied Sciences, Bangladesh Atomic Energy Commission

An α radioactive nuclides, ^{211}At, with half-life of 7.2 h is one of the prospective candidates for target alpha therapy. This nuclide is generally produced in the ^{209}Bi(^{4}He,2n)^{211}At reaction and separated from the irradiated bismuth target by dry-distillation. A simple method, based on dry distillation, has recently developed to separate $^{207\text{-}211}$At from irradiated lead targets [1]. This method effortlessly and successfully afforded no-carrier-added astatine solutions with high chemical purities and yields. In this work, thus, we studied the applicability of the simple dry distillation method, which was developed for the preparation of ^{nat}Pb(^{7}Li,xn)$^{nat-x}$At, to the general production of ^{211}At from ^{209}Bi(^{4}He,2n)^{211}At.

The production of ^{211}At was conducted by irradiating a stack of bismuth targets with ^{4}He beams that were supplied from an AVF-930 cyclotron at the TIARA facility of QST. The beam energy was adjusted to 28 MeV. A beam current of ~3 μA was maintained during irradiations of 10 min, 30 min and 4 h. After irradiation, the radioactivity of ^{211}At (3.7 – 156 MBq) was measured by a Currie meter.

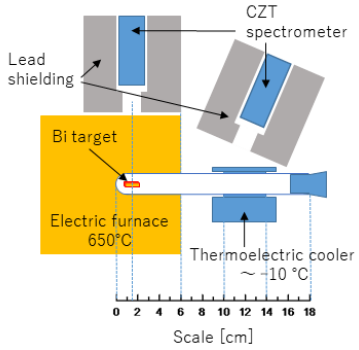

Fig. 1. Schematic view of the experimental setup for dry distillation.

Dry distillation was performed as described by Nishinaka et al. [1 - 3]. As shown in Fig.1, however, two cadmium zinc telluride (CZT) gamma-ray spectrometers (GR-1, Kromek) were introduced to study the heating time required to separate astatine from the irradiated bismuth target. The target at the bottom of a test tube (length, 18 cm; outer diameter, 18 mm) was heated for 15 min, at 650 °C, with an electric furnace. The temperature of the outer wall of test tube was measured with a thermocouple. After heating and removing the target from the test tube, the distribution of the astatine radioactivity was measured across the length of the test tube with CZT collimated with shielding. Astatine, which was attached to the inner wall of the test tube, was recovered by rinsing it with 1.6 mL of eluents. The obtained astatine solutions were subjected to thin-layer chromatography (TLC) and high-performance liquid chromatography (HPLC).

From the results of the time dependence of dry distillation, as show in Fig. 2a, astatine was released from the melted bismuth after 1 min and the separation was accomplished within 6 min of heating. Large amounts of ^{211}At were adsorbed on the inner wall of test tube in the range of 7 - 13 cm, as shown in Fig.2b. The adsorption temperature of astatine on the glass was estimated at 20 °C.

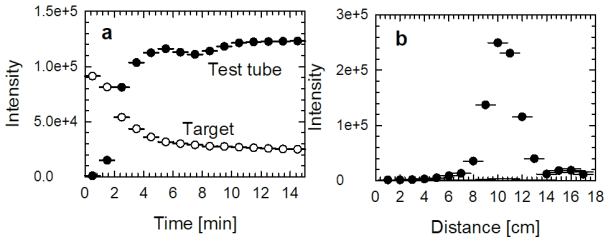

Fig. 2. a Heating-time dependence and **b** distribution of ^{211}At radioactivity.

The no-carrier-added astatine solutions were obtained in high yields (26 – 75%) only by rinsing with eluents, such as distilled water, ethanol, methanol, and chloroform. As an application of this simple dry distillation method, chloroform and *N*-chlorosuccinimide methanol solution of ^{211}At were employed for the labeling of aromatic amino acids; the aimed amino acid was obtained with high radiochemical yields [4].

TLC analysis revealed that astatine forms stable anions, At^-, AtO_3^-, and AtO_4^-, in ethanol and aqueous solutions, and these anions are readily oxidized and/or reduced between them in dynamic equilibria owing to the more electropositive character of astatine than other halogens. The results of HPLC analysis were reported in [5].

These results indicate that the method is suitable from the viewpoint of production, as well as of utilization.

Acknowledgments

The authors thank the crew of the TIARA for cyclotron operation. This work was supported by JSPS KAKENHI Grant Number JP18K11939.

References

[1] I. Nishinaka *et al.*, J. Radioanal. Nucl. Chem. **304**, 1077 (2015).
[2] I. Nishinaka *et al.*, J. Radioanal. Nucl. Chem. **318**, 897 (2018).
[3] I. Nishinaka *et al.*, J. Radioanal. Nucl. Chem. **322**, 2003 (2019).
[4] S. Watanabe *et al.*, Org. Biomol. Chem. **17**, 165 (2019).
[5] I. Nishinaka *et al.*, J. Radioanal. Nucl. Chem. **326**, 743 (2020).

2 - 23 Development of the positron-emitting ^{127}Cs tracer for non-invasive imaging of radiocesium dynamics *in vivo*

N. Suzui[a)], T. Shibata[b)], Y.-G. Yin[a)], Y. Funaki[c)], K. Kurita[a)], H. Hoshina[d)], M. Yamaguchi[a)], S. Fujimaki[e)], N. Seko[d)], H. Watabe[a,c,f)] and N. Kawachi[a)]

[a)]Department of Radiation-Applied Biology Research, TARRI, QST
[b)]Quantum Beam Science Center, JAEA
[c)]Cyclotron and Radioisotope Center, Tohoku University
[d)]Department of Advanced Functional Materials Research, TARRI, QST
[e)]Institute for Quantum Life Science, QST
[f)]Graduate School of Biomedical Engineering, Tohoku University

Since the accident at Tokyo Electric Power Company's Fukushima Daiichi Nuclear Power Station in March 2011, the public interest in the dynamics of radiocesium in animals, plants, and humans has increased. To elucidate the mechanism of radiocesium transport in living organisms, it is necessary to visualize the dynamics of radiocesium *in vivo* in more detail. In this study, we aimed to develop the production and purification methods of the positron-emitting nuclide ^{127}Cs (half-life of 6.25 h) and also to verify the suitability of ^{127}Cs as a tracer for non-invasive imaging of radiocesium dynamics *in vivo*.

^{127}Cs was produced by the ^{127}I (α, 4n)^{127}Cs reaction. A sodium iodide (NaI) target plate was irradiated with a $^{4}He^{2+}$ beam from an AVF cyclotron at the Takasaki Ion Accelerators for Advanced Radiation Application (TIARA). The incident beam energy on the target plate was set to 55 MeV. Under these irradiation conditions, ^{129}Cs was also produced by the ^{127}I (α, 2n)^{129}Cs reaction. Fig. 1A shows the gamma spectrum of the mother solution, in which the irradiated NaI target was dissolved. The production yields of ^{127}Cs and ^{129}Cs at the end of irradiation were 80.1 ± 6.5 and 1.3 ± 0.04 MBq/μAh, respectively (n = 6). Additionally, ^{24}Na, ^{124}I, and ^{126}I were also produced as by-products.

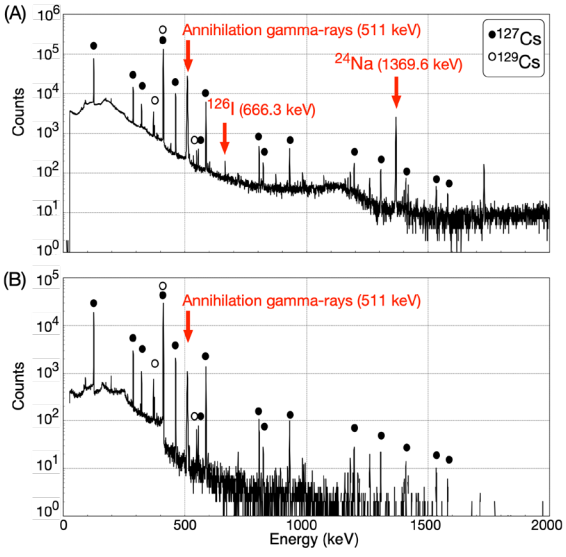

Fig. 1. Gamma spectrum of the mother and purified solutions. (A) Gamma-ray spectrum of the mother solution. Black and white circles indicate the gamma-ray peaks emitted from ^{127}Cs and ^{129}Cs, respectively. (B) Gamma-ray spectrum of the purified solution.

To purify ^{127}Cs tracer, we first loaded the mother solution onto an anion-exchange column. The results showed that ^{124}I and ^{126}I were not detected in the effluent solution from the column. Next, to separate ^{127}Cs from sodium ions, we used fibrous Cs adsorbent, which was synthesized by radiation-induced graft polymerization to introduce ammonium 12-molybdophosphate (AMP) as an adsorption ligand onto a polyethylene trunk fabric. This material has been reported to adsorb Cs specifically [1]. We passed the effluent solution through the Cs adsorbent column. The results showed that 98% ± 2% (n = 6) of ^{127}Cs was adsorbed on the Cs adsorbent packed into the column. Finally, we passed 10 mL of 1 mM $(NH_4)_2SO_4$ through the Cs adsorbent column. The results showed that 55% ± 4% (n = 6) of ^{127}Cs was eluted from the adsorbent but ^{24}Na was not detected in the eluted solution, which indicated that sodium ions derived from the NaI target plate were removed. Fig. 1B shows the gamma spectrum of the purified solution, which also indicated that the peaks of ^{24}Na and ^{126}I had disappeared in the solution.

The purified ^{127}Cs tracer solution was injected into the tail vein of a living rat, and the dynamics of ^{127}Cs were visualized using PET (Fig. 2). The result indicated that ^{127}Cs passed or accumulated in the salivary glands, heart, small intestine, and kidney, which was consistent with the report of the goat dissection experiment administered with ^{134}Cs. These results in this study indicate that the ^{127}Cs tracer is useful for the non-invasive investigation of radiocesium *in vivo* [2].

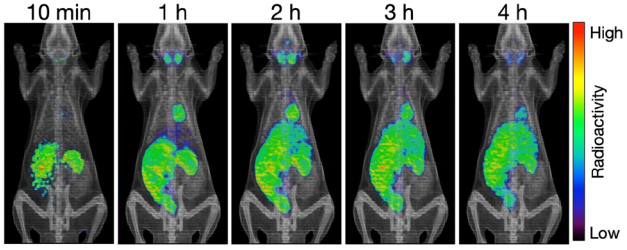

Fig. 2. PET-CT fusion images in a living rat at 10 min and every hour after injection of ^{127}Cs tracer.

References

[1] T. Shibata *et al.*, Radiat. Phys. Chem. **119**, 247 (2016).
[2] N. Suzui *et al.*, Sci. Rep. **10**, 16155 (2020).

2 - 24 Visualizing and characterizing carbon release from root to soil using $^{11}CO_2$ and a positron-emitting tracer imaging system

Y.-G. Yin[a)], N. Suzui[a)], K. Kurita[b)], Y. Miyoshi[a)], Y. Unno[c)], S. Fujimaki[d)], T. Nakamura[e)], T. Shinano[f)] and N. Kawachi[a)]

[a)]Department of Radiation-Applied Biology Research, TARRI, QST
[b)]Materials Sciences Research Center, JAEA
[c)]Department of Radioecology, Institute for Environmental Sciences
[d)]Institute for Quantum Life Science, QST
[e)]Agro-environmental Research Division, Hokkaido Agricultural Research Center, NARO
[f)]Research Faculty of Agriculture, Hokkaido University

Plant roots release a wide variety of carbon (C) compounds into the rhizosphere, which extends several millimeters from the roots into the surrounding soil. These compounds have important roles to enhance the plant's ability to cope with soil environmental conditions. On the other hand, the C release occurs at cost to limited photosynthates, therefore, the process must be strictly regulated by the plant. However, such regulatory mechanisms have not been fully elucidated owing to experimental technical difficulties to identify where is the rhizosphere. The positron-emitting tracer imaging system (PETIS) is an advanced imaging method used for the quantitative analysis of photosynthate movements from leaves to sink organs (e.g., roots and fruits) in intact plant bodies [1, 2]. The objectives of this study were to develop a new method to identify the rhizosphere by using the PETIS and $^{11}CO_2$ as a tracer to visualize and evaluate the movement of photosynthates into the root system and release of C into the soil coupled with positional information.

To separate the root and surrounding soil noninvasively, a rhizobox was specifically designed for the imaging experiment (Fig. 1). The soybean [*Glycine max* (L.) Merr. 'Jack'] and white lupin (*Lupinus albus* L. 'Energy') plant roots were sandwiched between the two soil boxes to form a flat sheet after growth for 10 d (Fig. 2 left) in a growth chamber with day/night temperatures of 25/25 ºC (12/12 h). The $^{11}CO_2$ was produced by irradiation of pure N_2 gas using an azimuthally varying field cyclotron located at the Takasaki Ion Accelerators for Advanced Radiation Application (TIARA), TARRI, QST (Gunma, Japan). The $^{11}CO_2$ gas was fed to the aerial part of a test plant and the PETIS imaging was started immediately to monitor the ^{11}C-photosynthates movement into the root system in real time (Fig. 2 middle). When the ^{11}C signal reached the root tips at 65 min (or 80 min) after $^{11}CO_2$ feeding, the whole test plant with intact root system was quickly removed from the rhizobox. Then, the rhizobox was reassembled and the PETIS imaging resumed to visualizing the distribution of ^{11}C signals released into the soil (Fig. 2 right). The PETIS imaging data were prepared using Image J ver. 1.51J8 software (https://imagej.nih.gov/ij/).

The root system and the two soil boxes can easily separate, because they were each covered with a fitted nylon-mesh bag which allowed to distinguish a small amount of ^{11}C signals of the soil from a large amount of that of roots (Fig. 1). The red square in the photograph and the yellow square in the image data indicated the rhizobox area (Fig. 2). The ^{11}C-photosynthates translocated from the leaves reached the root base within 20 min after $^{11}CO_2$ feeding and were then gradually delivered to the whole root system in white lupin and soybean plants. The distribution of soybean released ^{11}C was comparatively uniform in the soil. In contrast to the soybean, the white lupin ^{11}C released into the soil showed a hotspot of locally high ^{11}C-activity levels. The release density in the hotspots was greater than the average of the rhizobox area by approximately 5–12 times. Our results visually clarified for the first time that white lupin and soybean plants have different strategies for the release of ^{11}C into the soil. This method is sufficiently able to characterize the diversity in the release of assimilated C into the surrounding soil from different portions of the root system to define as the rhizosphere [3].

References

[1] N. Kawachi *et al.*, Nucl. Instrum. Meth. Phys. Res. A **648**, S317 (2011).
[2] K. Hidaka *et al.*, Front. Plant Sci. **9**, 1946 (2019).
[3] Y.-G. Yin *et al.*, Sci. Rep. **10**, 844 (2020).

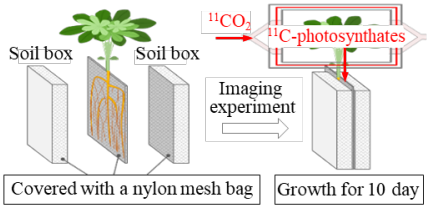

Fig. 1. Configuration of a new rhizobox for imaging experiment.

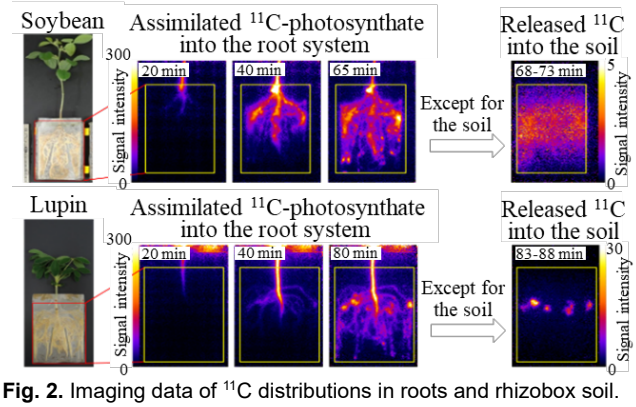

Fig. 2. Imaging data of ^{11}C distributions in roots and rhizobox soil.

2 - 25 Effects for distribution of elements and inhibition of demineralization by low concentration of titanium fluoride

K. Okuyama[a)], Y. Matsuda[b)], H. Yamamoto[c)], K. Naito[c)], M. Sakurai[b)], T. Saito[b)], M. Hayashi[c)], Y. Tamaki[a)], T. Satoh[d)], N. Yamada[d)] and R. Yamagata[d)]

[a)]Asahi University School of Dentistry
[b)]School of Dentistry, Health Sciences University of Hokkaido
[c)]Graduate School of Dentistry, Osaka University
[d)]Department of Advanced Radiation Technology, TARRI, QST

Introduction

The previous report said that 1% of titanium fluoride (TiF_4) solution showed higher fluorine (F) and titanium (Ti) distribution into the tooth structure and lower demineralization depth than 0.1% of TiF_4 solution [1]. The purpose of this study was to assess the effects of a low concentration (from 0.1 to 1%) of TiF_4 on F and Ti distribution and demineralization of root dentin surfaces.

Materials and methods

Extracted human teeth were sliced (200 μm thickness) longitudinally, coated with wax except for the buccal dentin surface. Sample preparation was carried out on pH cycling (pH 4.5 and 7.0, 6 cycles/day) for 8 weeks to prepare artificial caries. During this cycle, specimens were soaked into 0.1 (0.1T), 0.25 (0.25T), 0.5 (0.5T), 0.75 (0.75T), or 1% (1T) of TiF_4 solution for 5 minutes once a week, respectively. Control (Cont) involved no TiF_4 treatment during test periods. After cycling, each specimen was observed with a polarizing microscope, and the demineralization depth was measured. Also, calcium, F, and Ti distribution were analyzed by an in-air micro-PIXE/PIGE system with a 1.7-MeV $^1H^+$ microbeam at TIARA. Then, the cumulative concentration of F or contents of Ti in each specimen was calculated as an area of 100 μm from the superficial surface. The obtained data were analyzed by a Kruskal–Wallis test and Steel–Dwass test ($\alpha = 0.05$).

Results

Figure 1 shows the demineralization depth of each group. 1T or Cont indicated the lowest or highest depth in all groups, respectively. There was no significantly different depth among the other groups. Figure 2 and 3 show the distributions of F and Ti, respectively. For F, 1T indicated a higher value than 0.1T and 0.25T. There was no significant difference among groups of 0.1T, 0.25T, 0.5T and 0.75T (the conc. of TiF4 less than 1T). For Ti, 1T or 0.75T indicated a higher value than 0.1T and 0.25T. 0.1T indicated lower than other Ti-treated groups. Cont showed the significantly lowest F and Ti distributions in all groups.

Discussion

The F and Ti distributions depended on the concentration of the solution, especially for Ti. For demineralization depth, the trend of the depth was the same as that of F distribution, indicating that the effect of F on the demineralization depth was greater than that of Ti. This limited our results would be suggested that the effect of Ti concentration is small for inhibition of demineralization. Considering our results, it can be inferred that 0.5% concentration of TiF_4 is the minimum concentration that can effect on caries prevention and elements distribution.

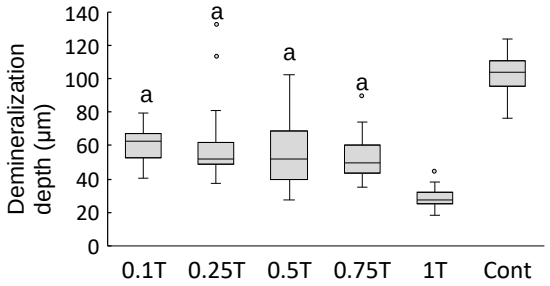

Fig. 1. Demineralization depth of each specimen. Same letters indicate no significant differences ($p > 0.05$).

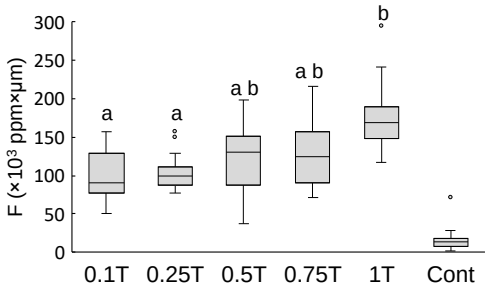

Fig. 2. Concentration of distributed F into dentin at 100 μm depth area from superficial surface. Same letters indicate no significant differences ($p>0.05$).

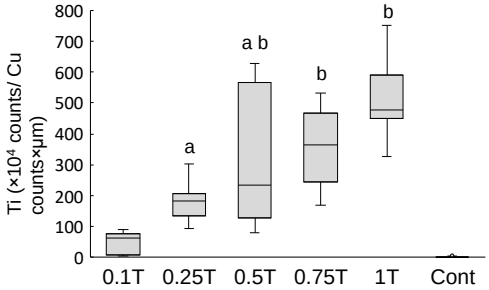

Fig. 3. Counts of distributed Ti into dentin at 100 μm depth area from superficial surface. Same letters indicate no significant differences ($p > 0.05$).

Reference

[1] K. Okuyama *et al.*, Dent. Mater. J. **40**, 736 (2021).

2 - 26 Comparative elemental analysis in lungs between control and collagen-vascular associated lung disease by in-air micro-PIXE

Y. Koga[a)], T. Satoh[b)], N. Yamada[b)], R. Yamagata[b)], T. Hisada[c)] and K. Dobashi[d)]

[a)]Department of Respiratory Medicine, Gunma University Graduate School of Medicine
[b)]Department of Advanced Radiation Technology, TARRI, QST
[c)]Gunma University Graduate School of Health Sciences
[d)]Jobu Hospital for Respiratory Diseases

Introduction

Collagen disease is a systemic disease in which connective tissue abnormalities of systemic organs such as the skin, kidneys, lungs, and lymph nodes are caused by abnormal functions of the immune system. The cause of collagen disease has not been clarified yet, but it has been suggested that exposure to heavy metals and silica may be the cause of vasculitis and scleroderma.

Materials and methods

From 2008 to 2014, elemental analysis of lung tissue specimens of 5 cases of scleroderma and 3 cases of dermatomyositis surgically resected by thoracoscopic lung biopsy was performed. Elemental analysis in the lung using paraffin sections was performed by in-air microparticle induced X-ray emission (micro-PIXE) [1], and elements of Al, Mg, Si, S, P, Fe, Ca and Zn in the paraffin sections. The concentration was measured. Elemental analysis of the normal lung part of 8 cases of early-stage lung cancer was also performed as a control. The elemental distributions of collagen disease lungs and control lungs were statistically compared using Graphpad Prism software.

Results

In elemental analysis using In-air micro-PIXE, among the 8 cases of collagen disease lung, the element concentration of Si was significantly higher than that of the control lung among Al, Mg, Si, Fe, Zn, etc. (Fig. 1). In addition, 5 of the collagen disease lungs had scleroderma. Analysis of 5 cases of scleroderma lung showed that the Si concentration was significantly higher than that of the control lung (Fig. 2).

Discussion

In collagen-vascular associated lung disease, especially scleroderma lungs, it was suggested that the deposition of silica in lung tissue may be involved in the pathogenesis of collagen disease lungs.

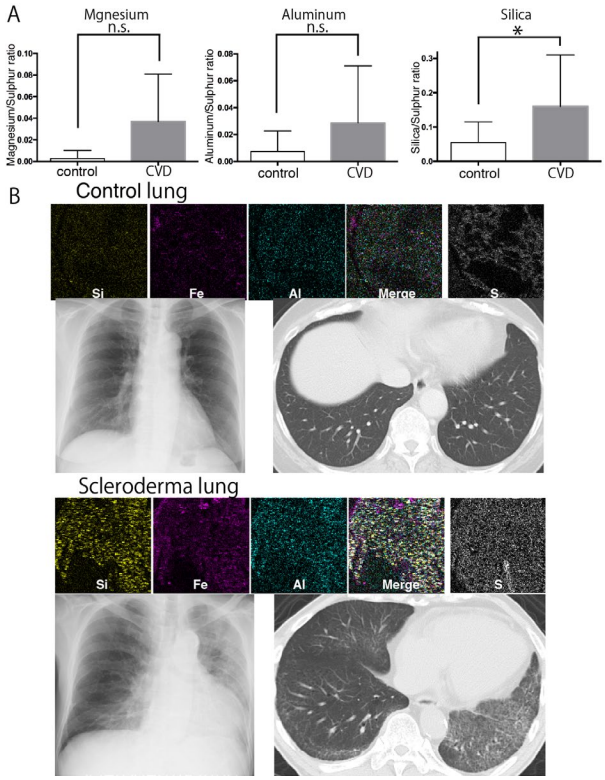

Fig. 1. A. Comparison of aluminum, magnesium, and silica in the lungs between control (n=8) and collagen-vascular associated lung disease (CVD) lung (n=8).
B. Typical elemental deposition and radiograph imaging in control (up) and CVD lung (down).

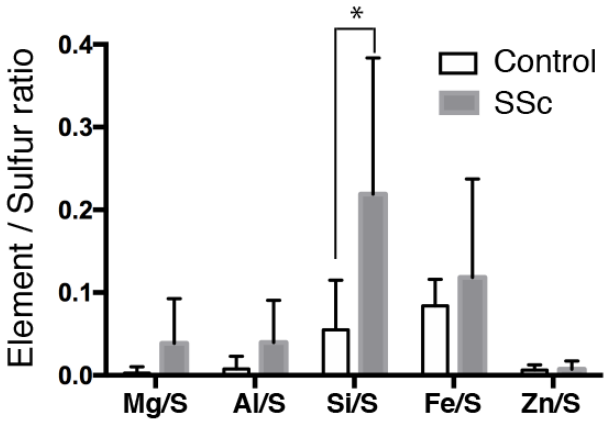

Fig. 2. Significant difference between control and scleroderma (SSc) lungs in the relative ratio of silica (Si) to sulfur (S).

Reference

[1] Y. Koga *et al.*, Environ. Health Prev. Med. **21**, 492 (2016).

2 - 27 Application of micro-PIXE/PIGE analysis for two biological researches: boron analysis for neutron capture therapy, and targeted anticancer drug delivery directed by radiation

S. Harada[a)], K. Nakai[b)], E. Sakurai[c)] and T. Satoh[d)]

[a)]School of Medicine, Iwate Medical University
[b)]School of Medicine, University of Tsukuba
[c)]Faculty of Pharmacy, Iryo Sosei University
[d)]Department of Advanced Radiation Technology, TARRI, QST

With the aim of improving radiotherapy, the micro particle-induced X-ray emission (PIXE) camera has been used to study: 1) feasibility of micro PIXE camera in applying to Boron Neutron Capture Therapy (BNCT); and 2) targeted delivery of carboplatin using particles that release their contents upon radiation.

Study of the utility of micro-PIXE camera in boron neutron capture therapy (BNCT)

Imaging of intracellular and extracellular Boroncaptate Sodium(BSH) in human glioma U251 cells was tested IN VITRO. Micro PIXE camera successfully imaged the boron distribution in U252 cell (Fig. 1). And count rate of PIGE strongly correlated with intracellular boron concentration by ICP-AES (r^2 = 0.9964) (Fig. 2) [1].

Study of delivery of carboplatin using particles that release their contents upon radiation

To confirm the targeted delivery of carboplatin in MM46 tumor model, which was observed in the study of 2019, we added the MM48 tumor model to the 2015 study [2, 3]. The nanoparticles (1×10^{10}), which were the same as 2019 study, were injected intravenously (Fig. 3-A). They accumulated around MM46 and MM48 tumors. Maximum accumulations

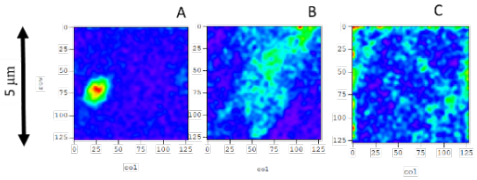

Fig. 3. Morphological change of particles by radiation (40 Gy).

were observed 9 hours after injection in both MM46 and MM48 tumors. Subsequently, 10 – 40 Gy radiation was administered. The accumulated nanoparticles released the carboplatin and gelatinized their outer shells (Fig. 3-B or C, green speckles), which prolonged the intra-tumor concentration of carboplatin and increased the antitumor effect via a synergistic effect with radiation in MM46 (Fig. 4-A ~ D green line) and MM48 (Fig. 4-E ~ F green line) tumors.

References

[1] K.Nakai *et al.* Appl. Radiat. Isot. **165**, 109334 (2020).
[2] S.Harada *et. al.* Biomed. Pharmacother. **70**, 196 (2015).
[3] T. Segawa *et al.* Radiat. Res. **193**, 263 (2020).

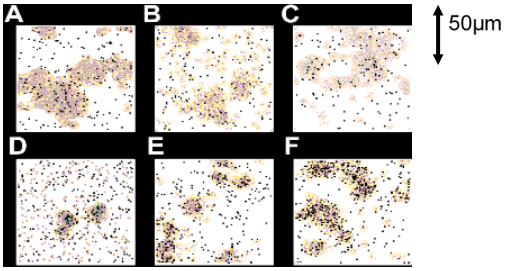

Fig. 1. Boron distribution in U252 cells by Micro-PIXE/PIGE camera.

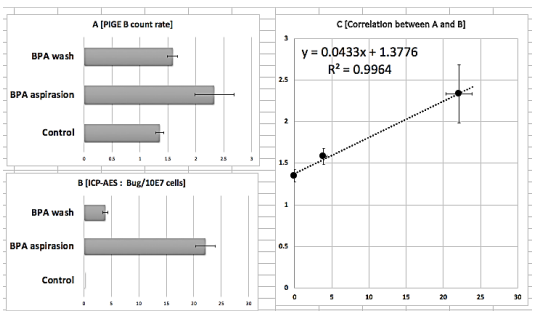

Fig. 2. Correlation between count rate of PIGE and boron concentration measured by ICP-AES.

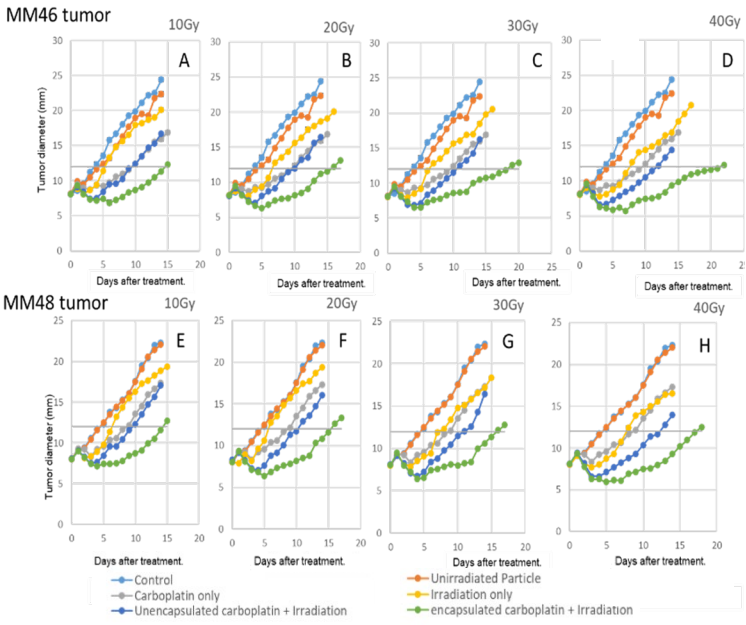

Fig. 4. Antitumor effect, expressed by the alteration of tumor diameter over time.

2 - 28 Evaluation for acid resistance of root dentin using a fluoride varnish containing tricalcium phosphate

H. Yamamoto[a)], R. Uemura[a)], K. Naito[a)], K. Okuyama[b)], Y. Matsuda[c)], M. Sakurai[c)], T. Saito[c)], M. Hayashi[a)], T. Satoh[d)], N. Yamada[d)] and R. Yamagata[d)]

[a)]Graduate School of Dentistry, Osaka University
[b)]Asahi University School of Dentistry
[c)]School of Dentistry, Health Sciences University of Hokkaido
[d)]Department of Advanced Radiation Technology, TARRI, QST

Introduction

In this study, we evaluated the fluorine (F) concentration and penetration depth in dentin applied with a fluoride varnish containing tricalcium phosphate (WV) by using in-air μ-PIXE/PIGE method. The acid resistance was also evaluated by using μ-CT.

Materials and methods

Three blocks of exposed human root dentin surface were cut from each tooth, and tricalcium phosphate-containing fluoride varnish (WV-G) and F varnish (FV-G) were applied to the exposed dentin surfaces of two blocks. One block with no material was used as the control (Con-G)[1], and these were designated as sound samples (SD). Demineralized dentin samples (DD) prepared by immersion in a pH 5.0 demineralizing solution for 3 days were also prepared using the same technique as for SD.

After immersion of both SD and DD in saline at 37 °C for one month, F and calcium (Ca) concentrations were analyzed from the root dentin surface to the inner dentin using in-air μ-PIXE/PIGE method, and the integrated amount of F concentration taken up within 200 μm from the surface was compared (Kruskal-Wallis, Mann-Whitney's U-test, $\alpha = 0.05$).

The samples were subjected to μ-CT (SMX-100CT; Shimadzu) before and after immersion in the demineralization solution for 3 days, and the mineral loss and demineralization depth were analyzed from the values before and after demineralization (Kruskal-Wallis, Mann-Whitney's U-test, $\alpha = 0.05$). Furthermore, the correlation between the amount of F concentration taken up and the mineral loss and demineralization depth was tested.

Results and discussion

The F concentration and penetration depth in WV and FV-Gs were significantly different from those in Con-G in both SD and DD. Moreover, the total F uptake in DD was significantly higher in both the WV and FV-Gs than in SD (Fig.1).

For mineral loss, the FV-G was significantly different from the Con-G in SD. Both the WV and FV-Gs were significantly different from the Con-G in DD. In terms of demineralization depth, the WV and FV-Gs were significantly different from the Con-G in SD though there was a little difference between the WV and FV-Gs (Fig.2).

The correlations between the total F concentration and mineral loss, demineralization depth were negative for both SD and DD (SD = r: -0.50, -0.49, DD = r: -0.44, -0.59).

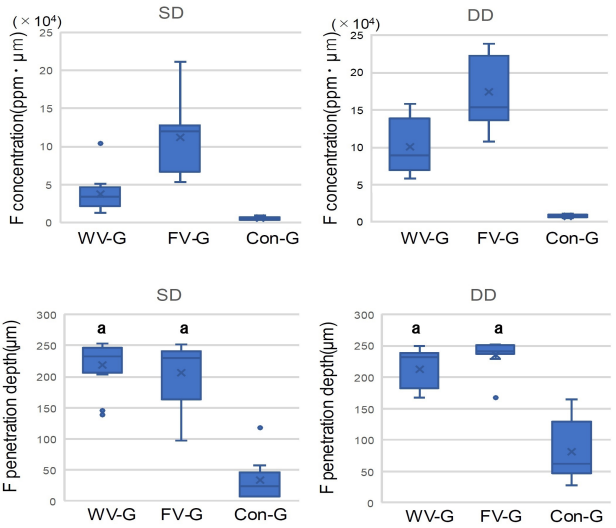

Fig. 1. Integrated concentration of F penetrated dentin at 200 μm depth area and F penetration depth from superficial surface. Same letters show no significant differences ($p > 0.05$).

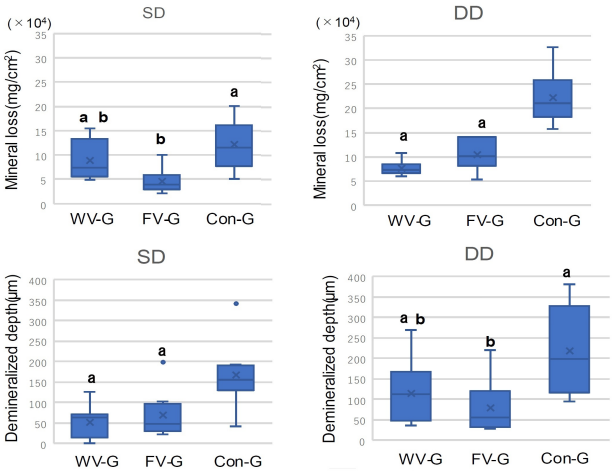

Fig. 2. Mineral loss and demineralized depth in SD and DD. Same letters show no significant differences ($p > 0.05$).

WV applied to the root surface dentin for one month showed less F penetration into the dentin than the fluoride alone, but was as effective as the fluoride alone in reducing demineralization and increasing acid resistance. The fluoride varnish with tricalcium phosphate was found to be useful as a new caries prevention and control material.

Reference

[1] K.Yagi *et al.*, Sci. Rep. **7**, 13450 (2017).

2 - 29 Lethality and energy deposition profile of proton cluster beams in *Bacillus subtilis* spores

Y. Hase[a,b], K. Satoh[a,b], A. Chiba[c], Y. Hirano[c], K. Moribayashi[a] and K. Narumi[c]

[a]Institute for Quantum Life Science, QST
[b]Department of Radiation-Applied Biology Research, TARRI, QST
[c]Department of Advanced Radiation Technology, TARRI, QST

Cluster ion beams show unique irradiation effects that cannot be achieved by monomer ion beams. This is largely attributed to the incidence of multiple atoms that are in close proximity, although their biological effects are largely unknown. We have developed an experimental method in order to examine the cluster ion-specific biological effects using bacterial spores as a model organism [1]. Here, we considered the lethality and energy deposition profile of proton cluster beams in the spores.

The spore samples were prepared and irradiated in a vacuum chamber connected to the 3-MV single-ended accelerator and the 400-keV ion implanter [1, 2]. Three kind of monomer ions (340-keV H (LET 75.0 keV/μm), 500-keV H (58.9) and 1-MeV H (37.7)) and cluster ions (2-MeV H_2) were used. The LET value of 2-MeV H_2 is 75.4 keV/μm, if we assume it is twice that of 1-MeV H.

The lethal effect of monomer ions depended on the LET, and the 340-keV H showed the highest effect (Fig. 1). The lethality of 2-MeV H_2 was similar to that of 500-keV H per particle. The 2-MeV H_2 showed clearly lower lethality than 340-keV H, even though both have a similar LET value per particle. This could be due to the difference in the spatial energy deposition profile.

A 2-MeV H_2 ion dissociates into a couple of 1-MeV H at the spore surface by losing bonding electrons. We considered the internuclear distance between the two protons of a 2-MeV H_2 ion while passing through the spore. We assume a 2-MeV H_2 ion with an initial internuclear distance of 0.108 nm incident into the spore of 0.48 μm thickness. If a 2-MeV H2 ion dissociates into a horizontal direction and a pair of 1-MeV H travel 0.48 μm in the vacuum, the internuclear distance broadens to 2.3 nm by Coulomb repulsion. In addition, calculation using the SRIM code suggested that the trajectory of the 1-MeV H ions deviates by multiple scattering from the center of the trajectory by 1.1 ± 2.1 nm (mean ± SD) while passing through the spore. In sum, the internuclear distance between the two protons of the 2-MeV H_2 ion broadens but is thought to be mostly within several nanometers while passing through a spore.

These results suggest that a single atom of 340-keV H has a higher lethality than a pair of 1-MeV H spaced within several nanometers. The radial dose distribution calculated by assuming water as a target, as described elsewhere [3], suggests that both the 340-keV H and the 1-MeV H give a high dose, particularly within a 1-nm radius from the center of the trajectory; moreover, the dose in this area is more than three times higher in 340-keV H than in 1-MeV H (Fig. 2). These facts suggest that energy density rather than total energy greatly contributes to lethality. Our result first demonstrates experimentally that the split of deposited total energy into two places separated only by up to several nanometers diminishes the lethality considerably.

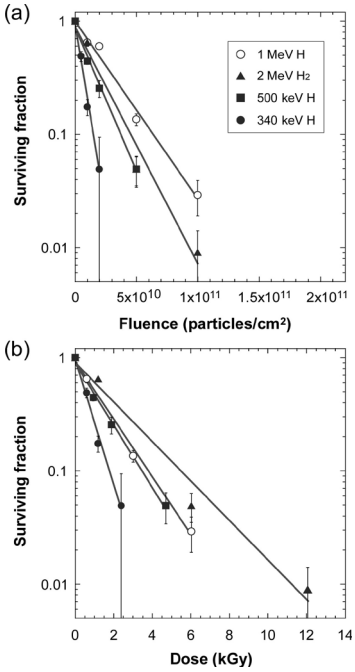

Fig. 1. Surviving fraction of irradiated *B. subtilis* spores as a function of particles/cm^2 (a) and kGy (b).

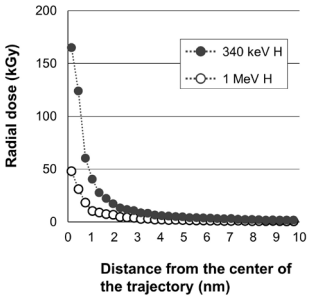

Fig. 2. Calculated radial dose distributions.

Acknowledgments

This study was partially supported by JSPS KAKENHI Grants JP17K05133 and JP20K12489.

References

[1] Y. Hase *et al.*, Quantum Beam Sci. **3**, 8 (2019).
[2] Y. Hase *et al.*, QST Takasaki Ann. Rep. 2019, **QST-M-29**, 94 (2021).
[3] K. Moribayashi, Jpn. J. Appl. Phys. **59**, SH0801 (2020).

2 - 30 Estimation of DNA damage localization of $^{4}He^{2+}$ and $^{12}C^{6+}$-irradiated DNA in a cell-mimetic condition

K. Akamatsu, N. Shikazono and K. Satoh

Institute for Quantum Life Science, QST

Introduction

Ionizing radiation-induced DNA damage can cause mutation and carcinogenesis. In particular, "clustered damage", that is a DNA region with two or more lesions within a few helical turns, is believed to be hardly repaired. This damage is considered to be induced around high-LET ionizing radiation tracks. However, detail of the damage is unknown. We have already developed a method for estimating localization of apurinic/apyrimidinic sites (APs) on DNA using fluorescence resonance energy transfer (FRET) occurring between different fluorescent dyes (Alexa350 and Alexa 488) (*hetero*-FRET). The FRET efficiency (*E*) was calculated from Alexa350 fluorescence intensities before/after enzymatic digestion of the labeled DNA with APs [1]. We succeeded in estimating qualities of clustered APs produced in $^{4}He^{2+}$-, $^{12}C^{5+}$-, and ^{60}Co γ-irradiated dry DNA film to study "direct" radiation effects using the method [2]. We also applied the method to aqueous DNA solution to study "indirect" radiation effects in a cell-mimetic condition. However, there are some problems of the complex protocol and of the sensitivity due to the low extinction coefficient of Alexa350. We have, therefore, developed "*homo*-FRET" occurred between two or more Alexa488 molecules. We will obtain magnitude of FRET also from "fluorescence anisotropy" of *homo*-FRET between Alexa488 molecules [3]. The new protocol using *homo*-FRET enables us to estimate DNA damage localization without any enzymes and improves sensitivity to detect a clustered damage.

Experiments

●Sample preparation and irradiation

PUC19 digested by Sma I was used (linear formed) for DNA samples to be irradiated. The DNA was dissolved in 0.2 M Tris-HCl buffer (pH 7.5), which is a cell-mimetic condition, to be ~10 g/L. Eight microliters of the DNA solution was mounted on a 10 mmϕ glass plate (thickness: ~0.1 mm), and was irradiated with $^{4}He^{2+}$ (LET: 17, 44 keV/μm) and with $^{12}C^{6+}$ (LET: 80, 230 keV/μm) at several doses up to 40kGy. Moreover, ^{60}Co γ-rays (LET: ~0.2 keV/μm) were also used as a standard radiation source.

●Preparation of fluorophore-labeled irradiated DNA and FRET observation [3]

The irradiated DNA (10 μL in water) and 10 μL of 100 mM Tris-HCl (pH 7.5) were mixed in a microtube. Two microliters of Alexa488/DMSO was added to the DNA solution and was incubated for 24 h at 35 °C. The fluorophore-labeled DNA was purified by ethanol-precipitation followed by ultrafiltration. The fluorescence anisotropy was measured at 525 nm (ex. 470 nm).

The anisotropy, $< r >$, is defined as follows:

$$< r > = (I_{VV} - G \cdot I_{VH}) / (I_{VV} + 2 \cdot G \cdot I_{VH})$$

where I_{VV} is the fluorescence intensity when the excitation and emission polarizers are both vertically oriented. I_{VH} is one when the excitation/emission polarizers are vertically/horizontally oriented. G is the grating factor defined as I_{HV}/I_{HH}.

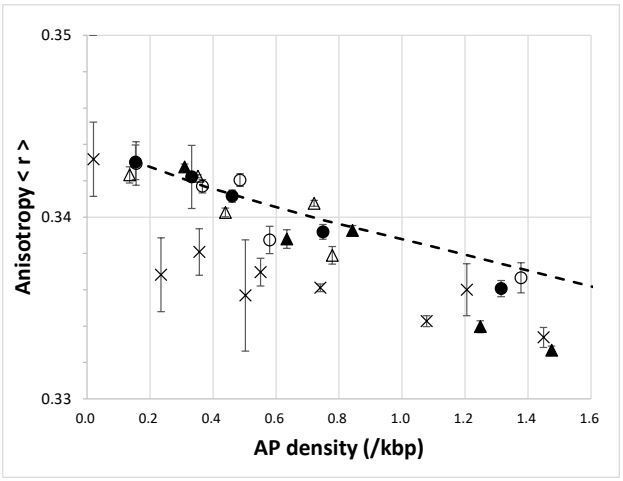

Fig.1. Fluorescence anisotropy of DNA irradiated with ^{60}Co γ-rays (×), $^{4}He^{2+}$ (LET:17 keV/μm) (○), $^{4}He^{2+}$ (44) (●), $^{12}C^{6+}$ (80) (Δ), and $^{12}C^{6+}$ (230) (▲) as a function of averaged AP density. The broken line indicates a theoretical one when APs are randomly distributed on DNA.

Results and discussion

Figure 1 shows relationships between averaged AP density and fluorescence anisotropy, <*r*>, for He-, C-, and ^{60}Co γ-irradiated DNA. This indicates that all of the radiation sources tested tend to produce almost randomly distributed APs in the cell-mimetic condition. Contrary to the results, in the solid state (using dry DNA sample) AP distribution clearly depended on LET as well as radiation sources tested (He, C, γ-rays) [4] (data not shown), that is, the higher LET radiation produces more clustered damaged sites by the direct effects. These findings suggest that indirect effect (e.g., by OH radical) would not be responsible for DNA damage clustering in the cell-mimetic condition.

Acknowledgments

We would like to gratefully thank Dr. Takeshi Saito of Institute for Integrated Radiation and Nuclear Science at Kyoto University for supporting ^{60}Co γ-ray irradiation.

References

[1] K. Akamatsu *et al.*, Anal. Biochem. **433**, 171 (2013).
[2] K. Akamatsu *et al.*, Radiat. Res. **183**, 105 (2015).
[3] K. Akamatsu *et al.*, Anal. Biochem. **536**, 78 (2017).
[4] K. Akamatsu *et al.*, Anal. Bioanal. Chem. **413**, 1185 (2021).

Part Ⅱ

3. Advanced Quantum-Beam Technology

3 - 01 Numerical estimation of water equivalent thickness through the spectroscopy of secondary-electron bremsstrahlung for the trajectory of therapeutic particle beam

M. Yamaguchi[a)], R. Satori[b)], S. Yamamoto[c)], M. Sakai[b)], Y. Nagao[a)], W. Kada[b)], T. Kamiya[b)] and N. Kawachi[a)]

[a)]Department of Radiation-Applied Biology Research, TARRI, QST
[b)]Graduate School of Medicine, Nagoya University
[c)]Graduate School of Medicine, Gunma University

Monitoring methods of therapeutic ion beams based on measurement of secondary particles (annihilation gamma rays, prompt gamma rays and secondary electron bremsstrahlung (SEB)) have been studied worldwide. Generally, these secondary particles are attenuated by substances within patients' body. Recently, we proposed a numerical estimation method of the water-equivalent thickness of the secondary particle tracks [1], which is required for the accurate attenuation correction. This method is based on the observation of energy distribution of SEB [2, 3]. Since the SEB is emitted simultaneously with the beam injection, there is no decrease in the accuracy of the attenuation correction accompanying the change in the position or shape of the organs or tissues in the body. Moreover, this method is cost-effective owing to the use of simple apparatuses compared to the computed tomography. In this study, we experimentally verified the feasibility of this estimation method of the water-equivalent thickness proposed in Ref. 1.

The experiment was performed at Gunma University Heavy Ion Medical Center. A diagram of the experimental setup was shown in Fig. 1. A carbon-ion beam having the energy of 278 MeV/u was injected into an acrylic block and the SEB emitted from the beam trajectory in the acrylic block was measured using a cadmium telluride (CdTe) semiconductor detector placed at 53.4 cm from the beam. The thickness of acrylic substance existing between the beam trajectory and the detector was 2.5 cm. The intensity distribution of the beam along the transversal direction was Gaussian one with a full width at a half maximum of 3.49 cm. To prevent charged particles such as protons and helium, which are generated by nuclear spallation reactions of the carbon ions, from entering the detector, a tungsten material (an X-ray camera) was placed upstream of the detector as a shield.

The energy spectrum of the detector was measured for 6.3×10^{10} carbon-ion injections. In addition, we added acrylic plates to the side of the acrylic block to change the thickness of the acrylic substance between the beam and the detector. The thickness of the acrylic plate was changed in three different thicknesses (1.0, 2.0 and 4.0 cm), and energy spectrum was measured for each thickness.

The acquired energy spectra were summarized in Fig. 2. A decreasing trend in the number of counts was observed in the low energy region (10-80 keV) as the acrylic thickness increased, while no change was observed in the high energy region (80-130 keV). This trend indicates that it is possible to estimate the water equivalent thickness from the shape of the energy spectra.

Acknowledgments

We would like to thank the staff at the Gunma University Heavy Ion Medical Center for allowing us beam time for our experiments. This work was partly funded by JSPS KAKENHI Grant Number JP18K12124.

References

[1] M. Yamaguchi *et al.*, Nucl. Instrum. Meth. Phys. Res. A **954**, 161607 (2020).
[2] M. Yamaguchi *et al.*, Jpn. J Appl. Phys. **59**, 087001 (2020).
[3] S. Yamamoto *et al.*, Phys. Med. Biol. **65**, 105008 (2020).

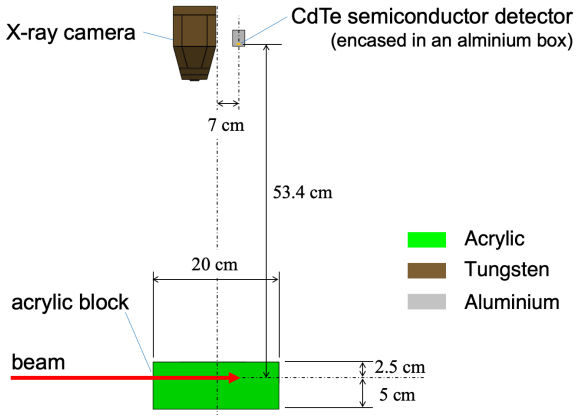

Fig. 1. A diagram of the experimental setup.

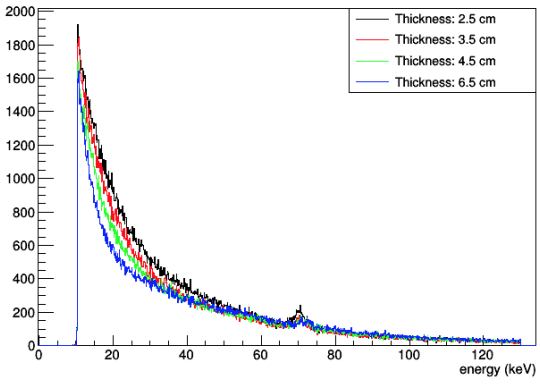

Fig. 2. Experimental energy spectrum of CdTe detector.

3 - 02 Investigation on the beam injection method and sextupole focusing effect for the hollow beam formation

H. Kashiwagi, T. Yuyama, T. Ishizaka and Y. Yuri

Department of Advanced Radiation Technology, TARRI, QST

We recently demonstrated, as a proof of concept, that a hollow beam with different cross-sectional shapes can be formed through nonlinear focusing with octupole magnets [1]. Further research and development studies related to the hollow beam formation have been performed at the TIARA cyclotron toward the irradiation application of hollow beams [2, 3]. In this report, latest results are shown.

Investigation of the beam injection method for the hollow beam formation

Particles in a Gaussian-like beam are kicked strongly by the nonlinear forces for the formation of a hollow beam. Therefore, unwanted "beam halos" of overfocused particles are also generated outside the main part of the hollow beam. These halo particles eventually hit a beam duct, which unintendedly causes radioactivation. Although the beam halo can be reduced by removing outer particles with slits before multipole magnets, this significantly reduces the available beam current. In order to solve the problem, we aim to suppress the generation of the beam halo by beam matching at the beam injection to the cyclotron.

Regarding the phase-space region of the beam injected to the cyclotron, if the region reaching the main hollow beam part is different from that reaching the beam halo part, the beam loss might be able to be decreased by properly injecting most of the beam into the phase-space region reaching the hollow beam region. We, therefore, investigated the feasibility of the above scheme. For simplicity, the two-dimensional real space in the four-dimensional transverse phase space was considered.

Systematic experiments were performed with a 10-MeV proton beam to reveal the final arrival part (hollow beam part and beam halo part) for each real-space coordinate of the beam to be injected into the cyclotron. Small beamlets of various horizontal and vertical coordinates were cut out from the injection beam (3.1 keV) by slits and injected into the cyclotron one by one. For each beamlet, the beam current of the hollow beam part was measured using the Faraday cup and that of the beam halo part was measured using the slits which remove outer particles. As shown in Fig. 1, it was found that there was a difference in the real-space region of the injection beam reaching the hollow beam part and the halo part.

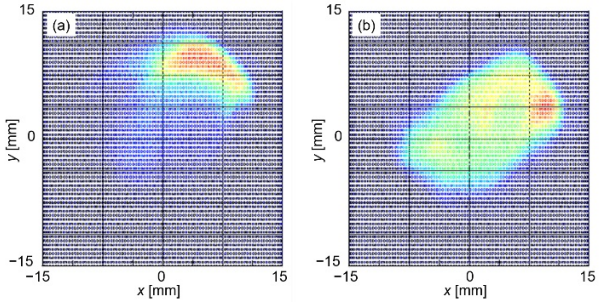

Fig. 1. Example of the real-space region of the injection beam reaching (a) the hollow beam part and (b) beam halo part.

This measurement result indicates that the beam loss induced through nonlinear focusing can be reduced by appropriate beam matching in the low-energy beam transport line before the cyclotron.

Formation of hollow beams using sextupole magnets

So far, the third-order nonlinear force of octupole magnets has been employed for the formation of hollow beams [1, 2]. Here, we explored the effect of the second-order focusing force of sextupole magnets [3].

Figure 2 shows the beam profiles measured on the target of the LB course. A hollow beam could be formed with an approximately elliptical or round cross-sectional profile by adjusting the strengths of two sextupole magnets. As explained above, the striated beam halo was generated. The centroid position of the beam shifted horizontally (while no shift occurred in the vertical direction) because of the deflecting effect of a sextupole magnet. The intensity along the beam edge was not even but maximized around the three points due to the three-fold symmetry of sextupole magnets. The contrast (the intensity ratio between the edge and center) was 3~15 and the width of the edge was about 1~2 mm in the present cases. These characteristics were about the same as the case of octupole focusing.

Acknowledgments

One of the authors (Y.Y.) would thank Prof. M. Fukuda for useful discussions on the beam dynamics and application of hollow ion beams. This work was supported in part by JSPS KAKENHI (JP18K11934).

References

[1] Y. Yuri *et al.*, Prog. Theor. Exp. Phys. **2019**, 053G01 (2019).

[2] T. Yuyama *et al.*, Proc. 17th Annual Meeting of Particle Accelerator Society of Japan, 2020, pp. 449-452.

[3] Y. Yuri *et al.*, High Energy Density Phys. **36**, 100839 (2020).

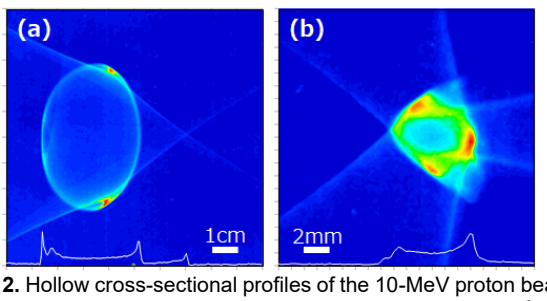

Fig. 2. Hollow cross-sectional profiles of the 10-MeV proton beam. The field gradients of two sextupole magnets are (a) (120 m^{-3}, −37 m^{-3}) and (b) (−330 m^{-3}, 130 m^{-3}).

3 - 03 Development of simultaneous multi-element data analysis software for micro-PIXE spectra obtained from hourly-collected aerosol samples

K. Usui[a)], W. Kada[a)], N. Yamada[b)], R. Yamagata[b)], T. Satoh[b)] and Y. Ishii[b)]

[a)]Faculty of Science and Technology, Gunma University
[b)]Department of Advanced Radiation Technology, TARRI, QST

A focused proton beam is a high-sensitivity analytical probe for the characterization of the elemental composition of microscopic targets. Microprobe is especially effective for the environmental research field, where limited numbers or amounts of specimens are available for characterization. Particle-induced X-ray emission (PIXE) analysis is recognized as a useful tool for such applications, and we have utilized such a probe for air-borne particle analysis [1]. It is commonly discussed that the elemental and chemical composition of particulate matter (PM) change depends on its origin and human activity. Therefore, their evaluation is indispensable not only for estimating the source of particles but also for elucidating the boundary dynamics of transboundary air pollutions. For such evaluation, it requires us to process a large number of samples, which are necessary for detailed analysis of an environmental event that occurred in long time spans. The non-negligible human cost would be an issue for such a series of spectral data analyses. That can reduce the reproductivity of micro-PIXE analysis for such applications. This study aimed to develop software for simultaneous multi-element analysis for hourly collected PM using micro-PIXE analysis to reduce the effort involved in the evaluation of PM.

Input data was obtained by micro-PIXE analysis and imaging utilizing a 3-MV single-ended accelerator at TIARA. An external microbeam probe was being used for the research with a typical beam energy of 3 MeV and a diameter of approximately around 1 μm. The PM samples were continuously obtained at Gunma Prefectural Institute of Public Health and Environmental Sciences with a collection interval of 1 hour by the automatic measuring unit. The sample was prepared in a regular manner for micro-PIXE analysis and imaging. Obtained PIXE spectra were analyzed by our house-made data analysis software made with Python language. The background noise was estimated by the SNIP method [2] using pymca, a Python library, and the fitting used the nonlinear least-squares method by the Levenberg-Marquardt method.

Figure 1 shows the elemental transition of hourly-collected PM samples obtained from 0:00-11:59, 18th March 2020. Characteristic X-ray signals were separated from the backgrounds by the house-made data analysis software. The changes in elemental composition were well illustrated for each time span by utilizing the same software. In some cases, it revealed that there are elemental compositions affected by coarse particles. For such cases, the software can distinguish the contribution of such accumulations from the major matrix. Data analysis software performed testing for the goodness of fit on the distribution of whole scanning area and distribution of accumulated particulate area, as shown in Fig.2. Results in data analysis suggested that house-made software successfully visualized differences in elemental composition for hourly collected PM samples. Further development and improvement of data processing code are expected to be implemented for more detailed characterization of PM samples, including estimation of the origins and trajectory analysis.

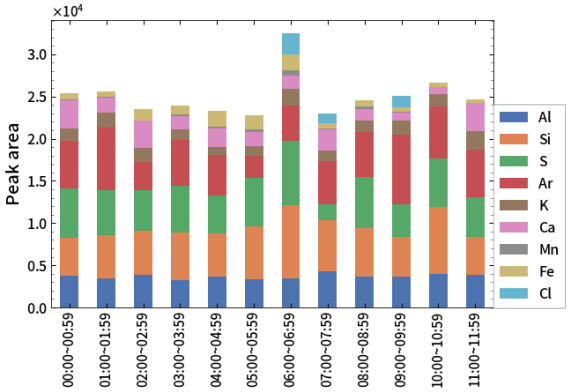

Fig. 1. Comparison of elemental composition of hourly collected PM samples obtained through micro-PIXE analysis.

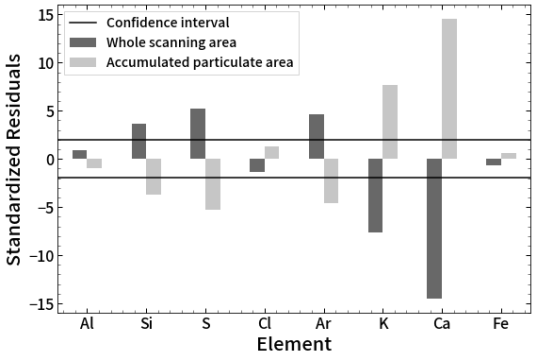

Fig. 2. Example of statical evaluation of the origin of each elemental compositions from whole scanning area and particular region of interest (accumulated particulate area).

Acknowledgments

The authors deeply thank Dr. Kumagai and Dr. Tago of Gunma Prefectural Institute of Public Health and Environmental Sciences for PM sampling.

References

[1] W. Kada *et al.*, Nucl. Istrum. Meth. Phys. Res. B **477**, 133 (2020).
[2] G. C. Ryan *et al.*, Nucl. Istrum. Meth. Phys. Res B **34**, 396 (1988).

3 - 04 Micro-structured surface of PVDF-TrFE film by proton beam writing for tactile sensing

Y. Nojiri[a)], Y. Ishii[b)] and H. Nishikawa[a)]

[a)]Department of Electrical Engineering, Shibaura Institute of Technology
[b)]Department of Advanced Radiation Technology, TARRI, QST

Polyvinylidene fluoride trifluoroethylene (PVDF-TrFE) is suited for dynamic applications such as tactile sensors built into wearable devices [1]. A previous report [2] shows that the increase of the open-circuit voltage can be expected for piezo-electric pillar arrays with high-aspect-ratio. As one of the processing methods for the microstructures with high aspect ratio, we propose proton beam writing (PBW).

We report a study of proton beam writing for micro-structuring of the PVDF-TrFE for sensing applications. Utilizing the unique feature of PBW as a lithographic tool, we patterned the surface of PVDF-TrFE film with three-dimensional structures. We investigated the dependence of the processing width and depth on the proton fluence and etching time for the pattern development.

Powder of PVDF-TrFE (composition rate: 75:25, Kureha Co. Ltd.) was dissolved in N,N-Dimethylformamide with a weight ratio of 20%. This solution is then spin-coated to a thickness of about 80 μm on the silicon. Two steps of heat treatment were then performed: first, at 40 °C for 2 h, followed by a 140 °C for 1 h. The PVDF-TrFE film is patterned by irradiation with a single-ended accelerator (beam energy: 1.7 MeV, beam size:1.0 μm, fluence: 1.0 to 7.0 μC/mm^2). After PBW, wet etching is performed by immersing the patterned film in a mixture of 9.0 mol/L potassium hydroxide (KOH) solution with 0.25 mol/L potassium permanganate ($KMnO_4$) at 80 °C for 1 to 5 h. The surface was observed either by a laser microscope (OLYMPUS, OLS4000) or a scanning electron microscope (SEM, JEOL, JSM-6010LV).

In Fig 1, we show the SEM image for PVDF-TrFE with the proton beam fluence at 3.0 μC/mm^2 after an etching of 1 h, where a grid pattern appears on the surface. Here the remaining structure of the PVDF-TrFE represents 4 × 4 pillar arrays which are expected for use as tactile sensing elements. The pillar arrays have almost collapsed away after etching for more than 5 h.

Figure 2 shows the dependence of the patterned linewidth on the etching time. With increased etching time, the grid linewidth increases and becomes larger by 50 to 150% than the irradiation linewidth of 10 μm. For increased fluence from 1.0 to 7.0 μC/mm^2, the increase in the linewidth is in the range of 10 to 20%. The depth of the grid structure also depends on the etching time. The patterned depth of 40 μm, which is almost equivalent to the projected range of 1.7 MeV protons, was achieved by etching for 3h (data not shown).

In summary, the patterned linewidth on the PVDF-TrFE film was mainly determined by etching time. Excessive fluence and etching time (such as 3.0 μC/mm^2 for 5 h) results in the collapse of the remaining pillar arrays. We were able to fabricate 4 × 4 arrays of pillars with 40 μm in height and 8 μm in width, which has an aspect ratio of about 5. For sensing applications, we have to check the effects of PBW and etching conditions on the piezoelectricity of PVDF-TrFE. Application of the PVDF-TrFE pillar arrays to sensing elements for tactile sensing is underway.

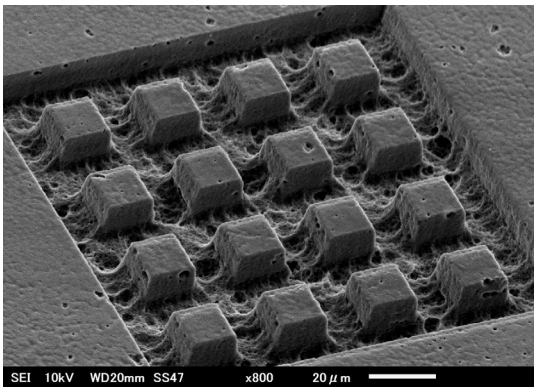

Fig. 1. A SEM image PVDF-TrFE tilted at 45° after PBW at 1.7 MeV with fluence of 3.0 μC/mm^2 and etching for 1 h.

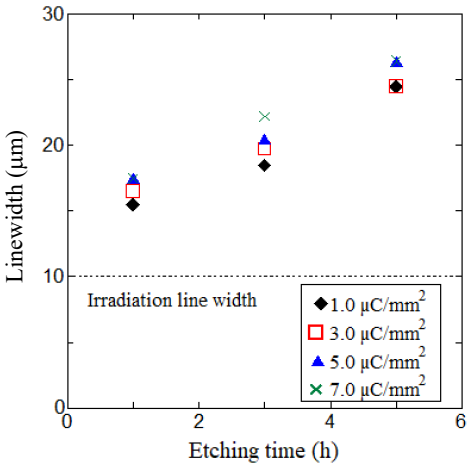

Fig. 2. Dependence of the linewidth of grid pattern on the etching time by PBW with beam energy of 1.7 MeV.

References

[1] H. Yousef *et al.*, Sens. Actuator A Phys. **167**, 171 (2011).
[2] H. Miki *et al.*, J. Micromech. Microeng. A **25**, 035026 (2015).

3 - 05 Development of convenient wide-field optical microscope for the visualization of microscopic pattern in diamond created by PBW technique

N. Kosuge[a)], S. Masuko[a)], N. Yamada[b)], R. Yamagata[b)], Y. Ishii[b)] and W. Kada[a)]

[a)]Faculty of Science and Technology, Gunma University
[b)]Department of Advanced Radiation Technology, TARRI, QST

Growing interests are being paid for fluorescent defects in wideband gap semiconductors, i.e., nitrogen-vacancy complex defect (Nitrogen-Vacancy: NV) center in diamond, for their magneto-optical characteristics and properties being ideal for quantum information elements and quantum sensing. Research and development on defect engineering for such centers are thus essential for the investigation of better properties. Several interesting fluorescence defects are created in diamond and SiC utilizing proton/particle beam writing (PBW) techniques [1, 2]. Defect engineering by high-energy ions is an effective tool for the creation of centers with high efficiency. However, sometimes it takes enormous exploring time to create the fluorescent defects, especially when a substrate with a wide area is irradiated by the particle beam. Often there could be mismatches in the region of observation and irradiation. In most cases, confocal laser scanning fluorescence microscope (CFM), which is often utilized for fluorescent defect observation, has a limited observation area compared to the area of charged particle irradiation for defect creation. These limitations are mainly relying on the photon detector utilized in the CFM. If we could utilize a CCD or CMOS camera for the detection of fluorescent defects, it would be possible to develop a total internal reflection fluorescence (TIRF) microscope that can be utilized in the so-called wide-field observation of fluorescent defects for fast screening.

In this study, we have demonstrated the development of a TIRF microscope for the observation of fluorescent defects created by the PBW technique. TIRF microscope system consists of CMOS camera and general-purpose LED and allowed us to be the rapid and convenient observation of a relatively large-scale pattern of fluorescence center distribution formed over a wide area in a diamond.

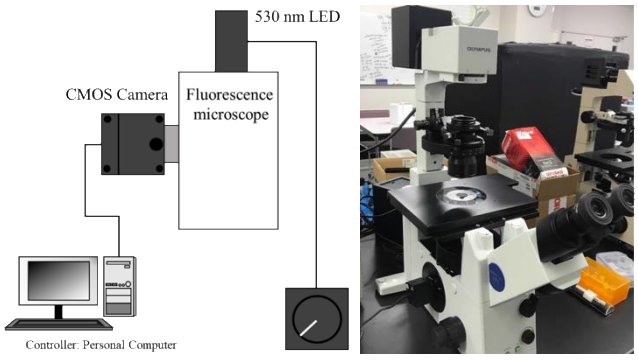

Fig. 1. (Left)Schematic illustration and (right) picture of convenient TIRF microscope designed for observation of fluorescent defect in diamond.

A simple observation system of TIRF microscope was developed for the observation of the PBW layer in a wide bandgap semiconductor. Figure 1 shows the schematic illustration of the developed TIRF microscope. TIRF microscope system was developed by utilizing a wide-field fluorescence microscope (Olympus IX71) with a general-purpose green LED light source (Thorlabs M530 L4) and a general-purpose CMOS camera (HOZAN L-836) or a scientific-grade CMOS camera (Andor Zyla 4.2 Plus).

For the evaluation of the developed TIRF microscope designed for the observation of the PBW process on a diamond, a commercially available chemical vapor deposition (CVD) diamond with a thickness of 300 μm was employed. Micrometer scaled patterns were formed in the diamond at microbeam lines of 3 MV tandem accelerator and 3MV single-ended accelerator. Figure 2 shows an example of a TIRF microscope image of the PBW pattern by 1.75 MeV H^+. A pattern of QR code-shaped fluorescence defects was created in the size of 600 μm × 600 μm by focused proton microbeam. CFM observation takes more than three days to visualize the whole structure. In contrast, the pattern was visualized under this TIRF microscope in several milli-seconds that is the readout time of CMOS. At this moment, the TIRF microscope is optimized for fluorescent ensemble defects for rapid screening over the sample. Further, improvement of the sensitivity is necessary for the investigation of low-density fluorescent defects created by charged ion impact.

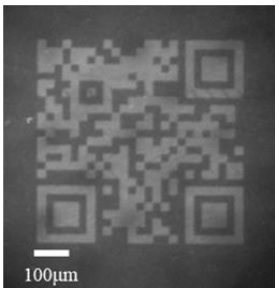

Fig. 2. Example of TIRF image of QR pattern written in diamond by PBW technique.

Acknowledgments

The authors deeply thank Dr. S. Onoda of QST for the support and advice on photoluminescence measurement and evaluation of diamond irradiated by PBW.

References

[1] H. Kraus *et al.*, Nano Lett. **17**, 2865 (2016).
[2] M. Haruyama *et al.*, Key Eng. Mater. **790**, 48 (2018).

3 - 06 Ion species analysis generated by a duoplasmatron-type ion source for a compact ion microbeam system

Y. Ishii and T. Ohkubo

Department of Advanced Radiation Technology, TARRI, QST

MeV ion microbeam, as referred to 'microbeam', is a useful tool for ion beam analyses and microfabrications. The microbeam has, so far, been produced by a large microbeam system that is comprised of an accelerator, a beam line, and a focusing lens system. The length of the microbeam system reaches to 30 m. That is one of the reasons why the system is not widely used in many laboratories of university and industries. Thus, a compact MeV ion microbeam system with the size drastically reduced is required to overcome the obstacle. A proto-type compact microbeam system with maximum beam energy of 120 kV, referred to as Prototype-IMB, is developed in Beam Engineering Section at TARRI.

Prototype-IMB consists of a dedicated duoplasmatron-type ion source, as referred to 'Duoplasmatron-IS', and a two-stage acceleration lens to obtain the reduced size. The total length of Prototype-IMB from Duoplasmatron-IS to the two-stage acceleration lens is about 90 cm. Prototype-IMB has, so far, produced a beam width of 1.8 μm at 120 keV hydrogen ion beam [1] which demonstrated the effectiveness of the Prototype-IMB.

Duoplasmatron-IS was developed for generating hydrogen ion beams with low energy and small energy spread that were required to form the microbeam. Especially a beam energy spread was studied to be reduced because it caused chromatic aberration at a beam focusing point, whereas the ion source cannot generate large beam current. Therefore, the ion source was specialized for the Prototype-IMB as compared to many ion sources used for accelerators. In addition, analysis of ion species had not been studied because ion beam including different ion species was focused on the same point when the two-stage acceleration lens was used. However, the analysis is needed when the ion microbeam is irradiated to various samples. Different ion species affect different kinds of interaction, such as penetration depth and spattering into the samples.

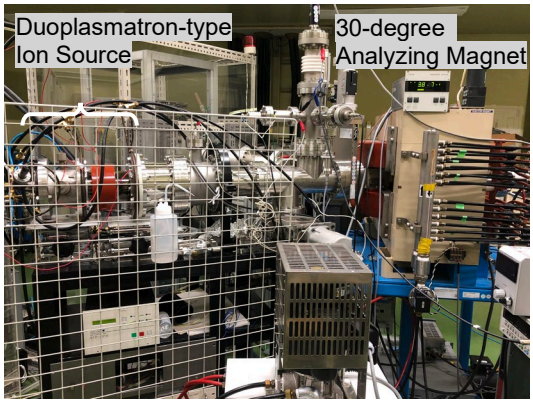

Fig. 1. Photograph of the duoplasmatron-type ion source set by an ion-source test bench with a 30-degree-analyzing magnet.

The generation rate of different ion species was studied on the basis of the analysis of hydrogen ion beams using another duoplasmatron-IS of the same concept, installed in the Prototype-IMB, on a test bench with an analyzing magnet.

Figure 1 shows the duoplasmatron-IS set in an ion-source test bench with a 30-degree-analyzing magnet. The pressure of hydrogen gas injected into the duoplasmatron-IS was controlled by a needle. The analyzing magnet was controlled by a current power supply connected by a PC. In the experiments, the pressure, the magnetic field and analyzed beam current were measured by Pirani gauge, a gauss meter, and a pico-ammeter, respectively.

Figure 2 shows an example of the measured data. Duoplasmatron-IS generated protons, diatomic ions, and triatomic ions. The generation rate of their ions depended on the hydrogen gas pressure from repeating the same experiments. This result indicates the molecular hydrogen ion beams could be selectively irradiated to samples by only controlling the gas pressure.

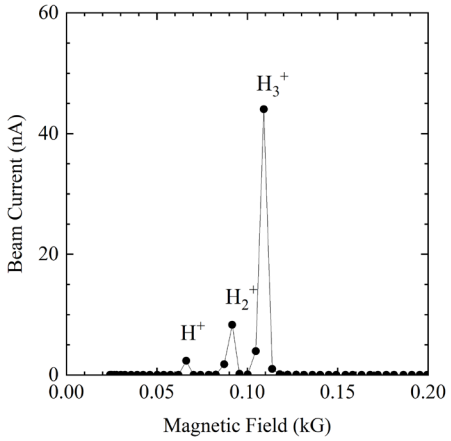

Fig. 2. An example of ion species separated by an analyzing magnet.

Acknowledgments

This work was partially supported by JSPS KAKENHI Grant Number 20H02673.

Reference

[1] T. Ohkubo and Y. Ishii, Physics Procedia **90,** 79 (2017).

3 - 07 Comparison of magnification between two electrostatic focusing lenses for a single-ion-irradiation system

Y. Ishii, T. Ohkubo and K. Narumi

Department of Advanced Functional Materials Research, TARRI, QST

Current-day society is worldwide in the information-oriented one. As long as the society is continued, the amount of the information could be increased in the future. In such a society, computer technologies are crucial to manage the information. However, it is said that the calculation speed of mainstream computers is close to the limitation. Therefore, the high-speed-calculation computers are powerfully developed in the world. The computer using quantum entanglement, namely “quantum computer”, is one of the candidates for such computers.

Some techniques of CPU with quantum entanglement are under-development to be used in such a quantum computer. In most of the techniques, ultralow temperature based on liquid helium is used to keep the quantum entanglement. That is an obstacle due to quantum computers being widely used in many places.

The entanglement between Nitrogen-vacancy centers (NVC) can be expressed by placing NVCs at the interval of about 10 nm in a substrate, which doesn’t need the ultralow temperature. The CPU applying this entanglement phenomena is proposed for the quantum computer. However, the technique of the high-precision positioning of NVC has not, so far, been developed in the world.

Single-ion injection of several tens keV with the accuracy of nano-meter scale is a method to fit the condition. A single-ion irradiation technique is developed by the combination of generating single-ion, forming several tens keV ion beam with nano-meter width and irradiating single-ions individually with the interval of 10 nm as a single-ion irradiation system. The single-ion can be generated using a Paul trap laser cooling technique. Thus a focusing system of the single-ion with small magnification needs to be developed to form the nano-meter width.

In this report, Einzel lens and acceleration lens are compered to obtain the small magnification to focus ion beam size within 10 nm as a focusing lens. The Einzel lens is commonly employed for focused-ion-microbeam systems. On the other hand, the acceleration lens is used for a submicron-ion-microbeam system [1]. develop at TARRI. The comparison was performed using numerical simulation based on the MUNRO code [2]. Figure 1 shows the schematic images (A) and (B) of an Einzel lens and an acceleration lens, respectively. Ion beam is injected into each lens from left side. The ion beam is focused on the right side. Ion beam energy is not increased by passing through an Einzel lens, whereas it is increased by an acceleration lens.

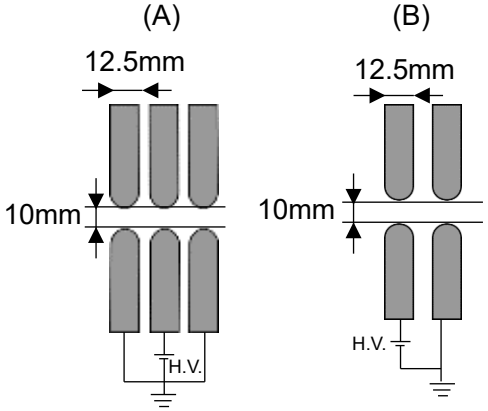

Fig. 1. Schematic drawings used for the calculation of magnification. (A) and (B) are an Einzel lens and an acceleration lens, respectively

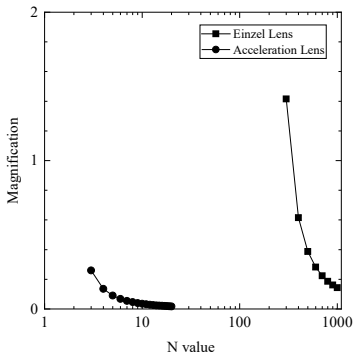

Fig. 2. A comparison of magnification of an Einzel lens and an acceleration lens as a function of N value based on the results of numerical simulation of lens parameters. The N value is defined as accelerated beam energy/injected beam energy.

Figure 2 shows the calculation result of magnification as a function of acceleration ratio of accelerated beam energy to injected beam one, namely N value. From Fig. 2, the Einzel lens needs the large N value compared to the acceleration lens to obtain the same magnification. A small magnification is required to focus ion beam on a nano-meter ranges by the single-ion injection system. Therefore, the acceleration lens was selected as the focusing lens for the single-ion injection system.

Acknowledgments

This work was partially supported by JSPS- 20H00145.

References

[1] Y. Ishii *et al.*, Nucl. Instrum. Meth. Phys. Res. B **210**, 70 (2003).

[2] E. Munro, “A set of computer programs for calculating the properties of electron lenses”, University of Cambridge, Engineering Department, 1975.

3 - 08 Feasibility study of high-sensitivity beam intensity measurement using a phase probe

H. Kashiwagi, N. Miyawaki and S. Kurashima

Department of Advanced Radiation Technology, TARRI, QST

In the TIARA AVF cyclotron, we are developing a beam injection tuning method based on the measurement of the emittance of the injection beam and the acceptance of the cyclotron for efficient beam injection [1]. The acceptance is measured by cutting out a small phase space region from the injection beam with slits and measuring the beam intensity of the region after acceleration to reveal whether the region is accelerated or not.

The accelerated ion current of the region is typically several tens of picoamperes to several nanoamperes. However, the beam current measurement probe (magnetic channel probe) in the cyclotron has a low signal-to-noise ratio (SNR) in the low current range due to the noise caused by the cooling water and other factors, making it difficult to measure the beam current below nanoamperes. Therefore, only low precision measurements of acceptance were possible by expanding the region injected into the cyclotron to be measurable by the probe. In this study, we have investigated the feasibility of high-sensitivity beam intensity measurement using a phase probe, which is a non-destructive measurement device that is used for beam phase measurement inside the cyclotron.

The phase probes [2] are 10 pairs of non-water-cooled parallel plate electrodes aligned radially from the center of the cyclotron (nine of them are currently available). A voltage signal proportional to the beam intensity is obtained when the beam bunch passes between these electrodes. High-sensitivity measurements can be made using a lock-in amplifier to remove noise including signals induced by the radio-frequency electric field for beam acceleration from the voltage signal of the phase probe.

In order to extract only the beam signal with high SNR, the optimum lock-in reference frequency must be determined. The frequency spectra of the phase probe output signals were measured using a spectrum analyzer (Tektronix RSA230) by switching the beam on and off without changing the acceleration conditions. The outermost available phase probe (No. 9) was used because the accelerated beam should be detected in the acceptance measurement. The frequency spectrum without the beam showed a high peak at 15.11 MHz, corresponding to the acceleration frequency, and the signal intensity decreases rapidly at higher frequencies. With the beam, the intensity was high around 6 times (90.11 MHz) and 7 times (105.77 MHz) the acceleration frequency. By subtracting the spectrum without the beam from the one with the beam, the frequencies of 6 times and 7 times showed a high SNR.

To verify the feasibility of measuring the beam intensity below nanoamperes with the phase probe, the output voltage signal of the phase probe was measured by a lock-in amplifier (SR844 from Stanford Research Systems) at different beam currents. The lock-in reference frequency was set to 90.11MHz (6×). The beam current was controlled by a beam chopper installed in the injection beamline of the cyclotron. The beam chopper changes the average injection current to the cyclotron by adjusting the pulse width of the square wave applied to its beam-deflecting electrodes. The correlation between the chopper pulse width and the beam current in this experimental condition was obtained by measurements with the current measurement probe, and the beam current below nanoamperes, which is not measurable with the current probe, was calculated by the chopper pulse width. The results from 47 nA to 70 pA are shown in Fig. 1. The lock-in amplifier amplitude output was almost proportional to the beam current. It was found that the relative beam intensity was able to be measured in the cyclotron down to about 70 pA even below the nanoampere order.

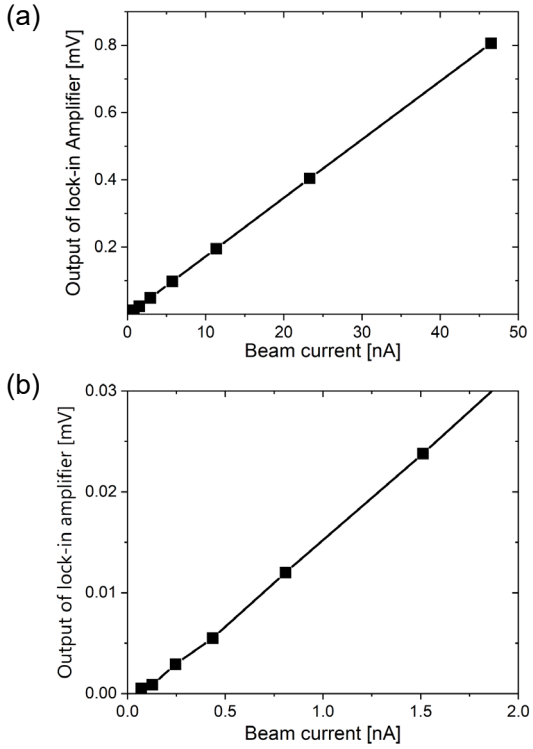

Fig. 1. Results of beam intensity measurements using a lock-in amplifier at beam currents from 47 nA to 70 pA (a) All measurements (b) Enlarged view below 2nA.

References

[1] H. Kashiwagi *et al*., Rev. Sci. Instrum. **8**, 02A735 (2014).
[2] K. Arakawa *et al*., JAEA-Technology **024**, (2008).

3 - 09 Irradiation energy dependence of Si surface structure irradiated with fast C_{60} cluster ion beams

N. Nitta[a)], N. Oishi[a)], H. Tsuchida[b)], S. Tomita[c)], K. Sasa[d)], K. Hirata[e)], H. Shibata[f)], Y. Hirano[g)], K. Yamada[g)], A. Chiba[g)], Y. Saitoh[g)], K. Narumi[g)] and Y. Hoshino[h)]

[a)]School of Environmental Science and Engineering, Kochi University of Technology
[b)]Quantum Science and Engineering Center, Kyoto University
[c)]Institute of Applied Physics, University of Tsukuba
[d)]Tandem Accelerator Complex, University of Tsukuba
[e)]National Metrology Institute of Japan, AIST
[f)]The Institute of Scientific and Industrial Research, Osaka University
[g)]Department of Advanced Radiation Technology, TARRI, QST
[h)]Department of Mathematics and Physics, Kanagawa University

Ion beam irradiation of Si induces the formation of structures on the surface by sputtering. Many studies have been reported on monatomic ion beam irradiation [1, 2]. In this study, structures formed by the fast C_{60} cluster ion beam were investigated by electron microscopy. The sputtering rate of a cluster ion beam is larger than that of a monatomic ion beam. It has also been reported that there exists a phenomenon unique to cluster irradiation called lateral sputtering [3]. The damage depth is proportional to 1/3 power of the incident energy (in the region of cluster size up to 10-200) [3]. We focused on the energy of the incident and examined its effect.

The mirror-polished Si(001) single crystal substrates were irradiated with C_{60} cluster ion beam using an ion implanter (NH40SR, Nissin Electric, QST) and a tandem Pelletron accelerator (9SDH-2, National Electronic Corporation, QST). A well-collimated C_{60} projectile with incident energy of 100 keV (C_{60}^{2+}) and 1 MeV (C_{60}^{+}) was incident at 0°and 60° to the surface normal of samples. The fluence of the C_{60} ion beams was set to 5×10^{12} and 2×10^{14} ions cm^{-2}. The irradiation temperature was room temperature. The evaluation of the surface was performed with a SEM (SU8020, Hitachi, KUT).

Figure 1 shows SEM images of Si surface irradiated with energies of 100 keV and 1 MeV, and angles of 0° and 60°. The irradiation fluence was 2×10^{14} cm^{-2}. The structure of each surface was confirmed. Surface roughness was observed at an angle of 0°, which increased with the increasing energy. At 100 keV energy, the surface roughness structure had an average of less than 10 nm. At 1 MeV energy, the structure became larger with a size of about 30 nm. It can be attributed to the increased sputtering rate at higher energies. The ripple structure was formed at an angle of 60°. The structure was formed perpendicular to the direction of incidence. As the incident energy increased, the ripple structure changed to a wave-like structure with strings. We also thought that this was due to the higher sputtering rate, in addition to the effect of the thermal annealing. Figure 2 shows SEM images of Si surface irradiated with an energy of 9 MeV and an angle of 60°. The irradiation fluence was 5×10^{12} to 1×10^{14} cm^{-2}. When irradiation fluence was low, fish scale structures were formed. The structure changed to a wave-like structure with increasing fluence. The ripple structure was not formed. In the future, we would like to perform monatomic ion beam irradiation to clarify the cluster effect.

References

[1] E. Iacb *et al.*, Microelectron. Eng. **155**, 50 (2016)
[2] S. Bhattacharjee *et al.*, Thin Solid Films **645**, 265 (2018).
[3] Cluster Ion Beam Basics and Applications, I. Yamada ed., the Nikkan Kogyo Shimbun, Ltd. (2006).

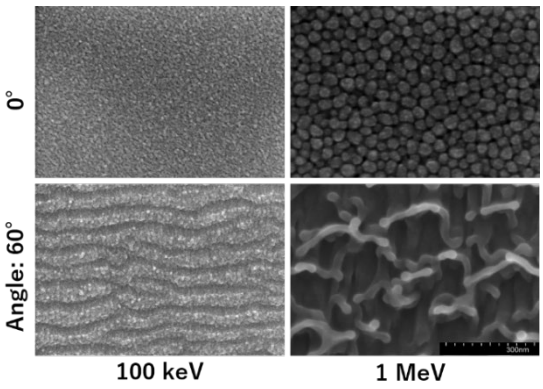

Fig. 1. Surface SEM images of Si irradiated with C_{60} cluster ion beam (Fluence: 2×10^{14} cm^{-2}).

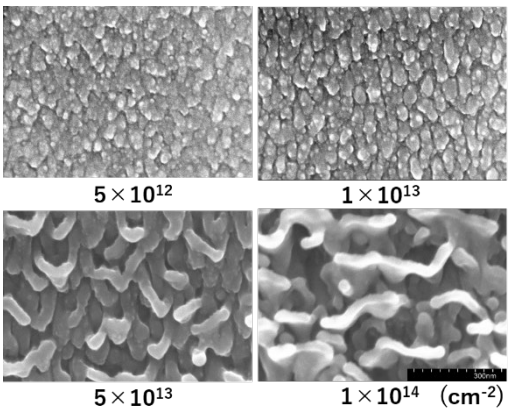

Fig. 2. Surface SEM images of Si irradiated with C_{60} cluster ion beam (Energy: 9 MeV, Angle: 60°).

3 - 10 Ion track formation in crystalline silicon under MeV C_{60} ion irradiation with much lower energy deposition than the threshold

H. Amekura[a)], K. Narumi[b)], A. Chiba[b)], Y. Hirano[b)], K. Yamada[b)], S. Yamamoto[c)] and Y. Saitoh[b)]

[a)]Center for Green Research on Energy and Environmental Materials, NIMS
[b)]Department of Advanced Radiation Technology, TARRI, QST
[c)]Department of Advanced Functional Materials Research, TARRI, QST

Damaged regions of cylindrical shapes called ion tracks, typically in nano-meters wide and longer than micro-meters, are formed along the ion trajectories in many materials, when high energy ions in the electronic stopping regime are injected [1]. In most cases, the ion tracks were assumed as consequences of dense electronic energy deposition from the high energy ions, except some cases where the synergy effect with the nuclear energy deposition plays an important role [2, 3]. In crystalline Si (c-Si), no tracks have been observed with any monomer ions up to GeV [4]. Tracks are formed in c-Si under 40 MeV fullerene (C_{60}) cluster ion irradiation [5, 6], which provides much higher energy deposition than monomer ions. The track diameter decreases with decreasing the energy until they disappear at an extrapolated value of ~17 MeV. However, here we report the track formation of 10 nm in diameter under C_{60} ion irradiation at 6 MeV, i.e., much lower than the extrapolated threshold of ~17 MeV [7]. Figures 1(a) and (b) show planar and cross-sectional transmission electron microscopy (TEM) images of Si samples irradiated with 6 MeV C_{60} ions, respectively. Judging from the images, cylindrical damaged regions of ~10 nm in diameter and ~66 nm in length in average were formed. The track diameters were comparable to those formed by 40 MeV C_{60} irradiation. Furthermore, the tracks formed by 6 MeV C_{60} irradiation were defective crystalline [7], while those formed by 40 MeV C_{60} irradiation were amorphous [6]. The track formation was observed down to 1 MeV (and probably lower), while the mean diameter decreases with decreasing the energy. These track formations at such low energy deposition cannot be explained by the conventional purely electronic energy deposition mechanism, indicating another origin, e.g., the synergy effect between the electronic and nuclear energy depositions, or efficient recrystallization in Si and inactivation by collisional damage of S_n.

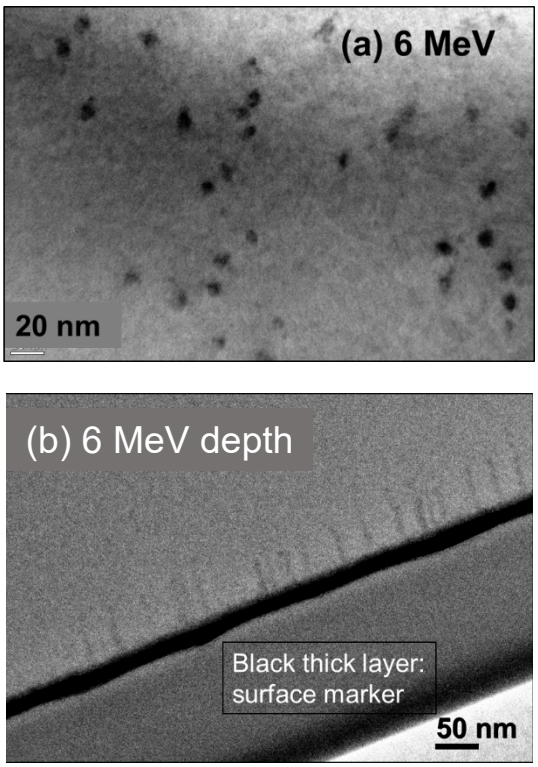

Fig. 1. Bright field transmission electron microscopy (TEM) images of crystalline silicon irradiated with 6 MeV C_{60} ions, in (a) planar and (b) cross-sectional configurations [7]. A black thick layer in (b) is a Pt layer for surface marker deposited after the irradiation.

References

[1] F. Chen *et al*., Chap. 5 “Shape Elongation of Nanoparticles Induced by Swift Heavy Ion Irradiation” in Ion Irradiation of Dielectrics for Photonic Applications (Springer-Nature Singapore) 2020.
[2] M. Toulemonde *et al*., Phys. Rev. B **83,** 054106 (2011).
[3] W.J. Weber *et al*., Sci. Rep. **5,** 7726 (2015).
[4] P. Mary *et al.*, Nucl. Instrum. Meth. Phys. Res. B **62**, 391 (1992).
[5] A. Dunlop *et al*., Nucl. Instrum. Meth. Phys. Res. B **146**, 302 (1998).
[6] B. Canut *et al*., Nucl. Instrum. Meth. Phys. Res. B **146**, 296 (1998).
[7] H. Amekura *et al*., Sci. Rep. **11**, 185 (2021).

3 - 11 Nonlinear effect on Au sputtering yield by C_{60}- and C_{70}-ion bombardment

K. Narumi, K. Yamada, Y. Hirano, A. Chiba, Y. Yuri and Y. Saitoh

Department of Advanced Radiation Technology, TARRI, QST

One of the most remarkable characteristics of molecular- or cluster-ion bombardment of condensed matter is huge sputtering [1]; for example, the characteristic has been applied to Secondary-Ion Mass Spectrometry (SIMS) [2]. It has been reported that sputtering yield by cluster ions is not proportional to the number of the constituent atoms. One of the typical cases is Au sputtering yield by Au_n-ion bombardment ($n \leq 13$) [1]: The sputtering yield is proportional to n^2. Such an effect is called nonlinear effect on sputtering yield. In the present report, we will discuss nonlinear effect on Au sputtering yield by C_{60}- and C_{70}-ion bombardment. Such fullerene ions have much more constituent atoms but a much smaller atomic number than the above Au_n ions. Thus, it draws the interest how nonlinear effect on sputtering yield by fullerene ions is. For this purpose, we have measured Au sputtering yields by 0.03-to-9-MeV C_{60}- and C_{70}-ion bombardment.

Au sputtering yields were measured with a quartz-crystal microbalance technique. An Au thin film, which was one of the electrodes on a quartz crystal, was used as a target as it is and was bombarded with C_{60} or C_{70} ions, which were accelerated to 0.03 to 1.08 MeV and to 1.08 to 9 MeV with the 400-kV ion implanter and the 3-MV tandem accelerator of TIARA, respectively. Those by 18-to-150-keV C^+ ions were also measured. Typical beam current was 1 nA and 20 nA for C_{60} and C_{70} ions, and C^+ ions, respectively.

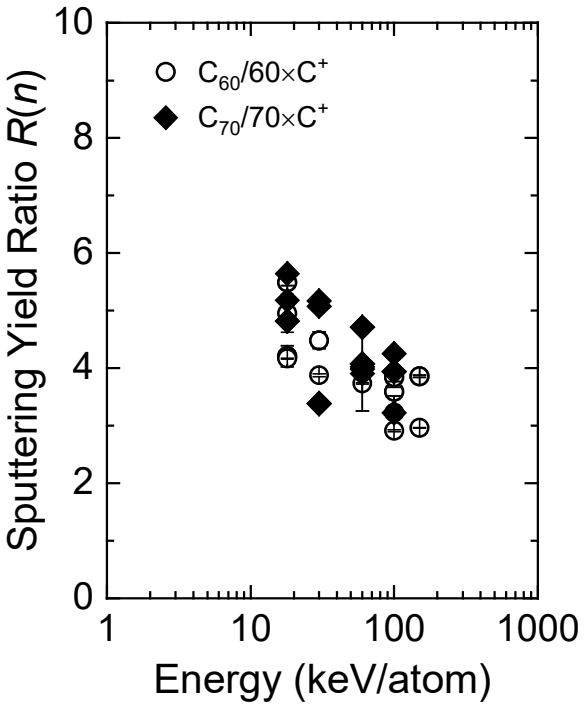

Fig. 1. Ratio between Au sputtering yields per carbon atom by C_{60} or C_{70} ions and by C ions.

Figure 1 shows Au-sputtering-yield ratio $R(n)$, which is defined by $Y(n)/nY(1)$, where $Y(n)$ is Au sputtering yield by C_n-ion bombardment. $R(n)$ is a kind of indicator of the nonlinear effect; specifically speaking, $R(n) = 1$ means that the effect is not observed. The figure tells us 3 results: $R(n) = 3 \sim 6$, $R(60) \approx R(70)$, and $R(n)$ slightly decreases with the ion velocity. First, $R(n) = 3 \sim 6$, *i.e.*, $R(n) > 1$, demonstrates obviously that the nonlinear effect is observed; however, the effect is not so much as Au_n ions on a Au target [1] because $R(n)$ is not proportional to n^2. Secondly, $R(60) \approx R(70)$ means that $R(n)$ hardly depends on n, or that the increase in $R(n)$ stops around $n \approx 60$. Thirdly, the slight velocity dependence of $R(n)$ suggests that the effect is qualitatively dependent on nuclear stopping powers of Au for C_n ions, because the nuclear stopping power of Au for C ions decreases monotonously in these range of the velocity [3]. Further study, however, is needed on the velocity dependence of the nonlinear effect.

Acknowledgments

This work was supported in part by JSPS KAKENHI Grant Number JP18K05005, and also partially supported by the Inter-organizational Atomic Energy Research Program in an academic collaborative agreement among JAEA, QST and the Univ. of Tokyo.

References

[1] H.H. Andersen *et al.*, Phys. Rev. Lett. **80**, 5433 (1998). S. Bouneau *et al.*, Phys. Rev. B **65**, 14106 (2002).
[2] K. Nakajima *et al.*, Appl. Phys. Lett. **104**, 114103 (2014).
[3] J.F. Ziegler, SRIM code version 2008.

3 - 12 Improved sample structure for transmission SIMS imaging with 9 MeV C_{60}^{2+} primary ions

K. Morimoto[a)], K. Nakamura[a)], K. Nakajima[a)], A. Chiba[b)], K. Yamada[b)], Y. Hirano[b)], K. Narumi[b)] and Y. Saitoh[b)]

[a)]Department of Micro Engineering, Kyoto University
[b)]Department of Advanced Radiation Technology, TARRI, QST

Molecular imaging by secondary ion mass spectrometry (SIMS) is a powerful analysis tool for visualizing the localization of constitutive molecular species in various samples. Although it provides better lateral resolution than imaging by matrix-assisted laser desorption/ionization (MALDI), it has a shortcoming of lower sensitivity to high molecules. Our group has recently found that transmission SIMS (T-SIMS) using MeV C_{60} primary ions can improve the sensitivity to biomolecules such as amino acids [1] and peptides [2]. Then we have built a system for T-SIMS imaging with energetic C_{60} primary ions [3]. This system includes a secondary electron microscope to determine the position of secondary-ion emission from the magnified image of the corresponding secondary-electron emission. This allows us to obtain a high-resolution image irrespective of the beam size of primary ions. For imaging with this system, however, it is essential to prepare an extremely thin sample (up to several hundred nm in thickness) with sufficient conductivity to avoid its electric charging. Therefore, optimal sample structure for our system was sought in this work.

Two different samples were prepared by vacuum evaporation of metallic and organic thin films on amorphous Si-enriched silicon nitride (SiN) membranes (50 nm in thickness). An amino acid, phenylalanine (Phe) was used as the organic target, and a two-dimensional micropattern of Phe and aluminum (Al) was fabricated on the one side (side-A) of both the membranes. An Al single layer, or a double layer composed of an Al underlayer and a gold (Au) ultrathin overlayer was deposited on the other side (side-B) of the membrane for the sample #1 and #2, respectively. These samples were irradiated from the surface on the side-B at the incident angle of 45° with 9 MeV C_{60}^{2+} ions from the 3 MV tandem accelerator of TIARA. Secondary electrons ejected from the surface on the side-B were extracted into the microscope and detected with a micro-channel plates (MCP)/phosphor screen detector. They make a bright spot on the screen, the position of which corresponds to the position on the sample surface irradiated with a C_{60} ion. The picture of the screen was taken with a high-speed CMOS camera in synchronization with detection of the corresponding transmitted ions. Simultaneously, the positively-charged secondary ions from the surface on the side-A were mass-analyzed with a linear-type time-of-flight (TOF) mass spectrometer. The signals of the transmitted ions, the secondary ions and the picture of the screen induced by incidence of a C_{60} ion were recorded event by event (list mode) with their individual time stamp. Thus, the coupled data of the irradiated position and the mass-to-charge ratio of the secondary ions were acquired for each detection of the transmitted ions.

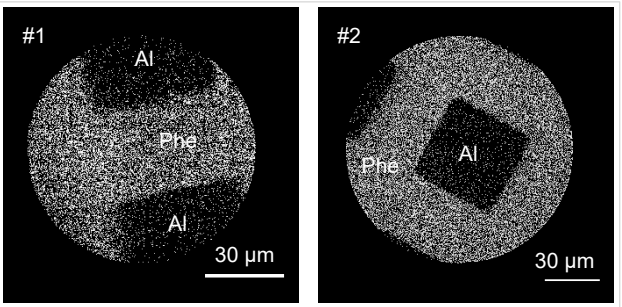

Fig. 1. The obtained images of lateral distribution of phenylalanine for the sample #1 and #2, respectively.

Figure 1 shows the obtained images of phenylalanine in the sample #1 and #2, respectively. These images were produced by plotting the center-of-mass position of the bright spot in the pictures that were taken in coincidence with the detection of phenylalanine-specific secondary ions at *m*/z 120,166, etc. Dark square regions in the images correspond to the surface on the side-A covered with Al micropattern, indicating that the micropattern of both the samples was clearly visualized. However, the boundary of the imaged pattern of the sample #1 is slightly blurred compared to that of the sample #2. This is due to electric charging of the sample #1 during the measurement, suggesting that the Al layer on its side-B was significantly oxidized by exposure to the atmosphere and that the Au overlayer of the sample #2 effectively inhibited oxidation of the underlying Al layer.

The lateral resolution of our system was estimated from the obtained image for the sample #2. In the estimation procedure, the intensity profile across an imaged pattern boundary was fitted with a complementary error function. The width of the boundary was about 1.4 μm. This value should overestimate the lateral resolution of our system because the actual pattern boundary was not completely abrupt. The present result suggests that the lateral resolution was about 1 μm or less.

References

[1] K. Nakajima *et al*., Appl. Phys. Lett. **104**, 114103 (2014).
[2] K. Nakajima *et al*., QST Takasaki Annu. Rep. 2015, **QST-M-2**, 177 (2017).
[3] S. Kitamura *et al*., QST Takasaki Annu. Rep. 2019, **QST-M-29**, 131 (2021).

3 - 13 Standing organic nanowires formed through polymerization of small molecules via irradiation with cluster ions

S. Sakaguchi[a)], K. Kamiya[a)], M. Nobuoka[a)], M. Kawata[a)], T. Sakurai[b)], Y. Hirano[c)], A. Chiba[c)], Y. Saitoh[c)], K. Narumi[c)] and S. Seki[a)]

[a)]Department of Molecular Engineering, Kyoto University
[b)]Faculty of Molecular Chemistry and Engineering, Kyoto Institute of Technology
[c)]Department of Advanced Radiation Technology, TARRI, QST

High energy particles of ion beams give their kinetic energy to materials when interacting each other. The linear trajectories of high energy heavy ion particles yield nanowires via irradiation into organic films [1 – 4]. The nanowires can be isolated on the supporting substrate by development–immersion in organic solvents to remove the unirradiated area of the initial films. Quite recently, we have demonstrated that a sublimation process instead of development enables vertically-oriented, standing nanowire arrays with desired number density and length from ubiquitous organic molecules (Fig. 1(a)) [5]. The extent of vertical alignment is related to the reaction efficiency of the polymerization/crosslinking reactions, and thus single swift heavy ions have been utilized so far. Here we have tried the use of aluminum cluster ion beams with a single MeV energy region. The morphological characteristics were visualized by scanning electron microscopy (SEM) technique.

1,6,7,12-Tetrachloroperylene tetracarboxylic acid dianhydride (PTCDA-Cl_4; Fig. 1(b)) was purchased from TCI Co., and used without further purification. The PTCDA-Cl_4 films were fabricated on silicon substrates by vacuum deposition of the powder form under vacuum at elevating the temperature. The film thickness was ~200 nm. The 3 mm-diameter sized circle spot beams of cluster ions–1.5 MeV Al^+, 3.0 MeV Al_2^+, 4.5 MeV Al_3^+, 6.0 MeV Al_4^+– were irradiated to the PTCDA-Cl_4 films at the fluence of 1.0×10^{11} cm^{-2}. After irradiation, the sublimation process and following SEM observation was carried out.

The typical SEM images after the sublimation were shown as Fig. 2, where wire-shaped objects or their

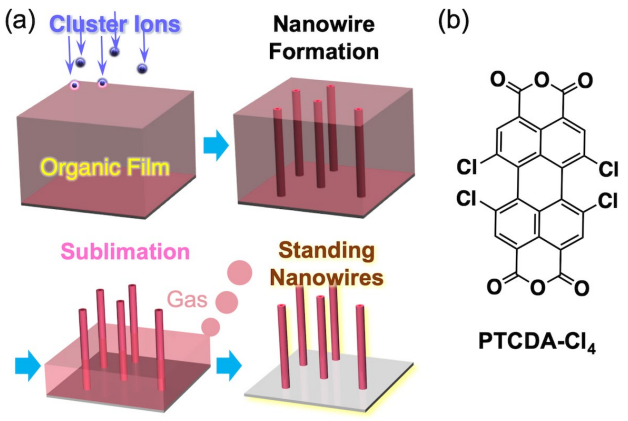

Fig. 1. (a) Schematic illustration of standing nanowire formation via cluster ion beam irradiation and isolation by sublimation. (b) Chemical structure of PTCDAI-Cl_4.

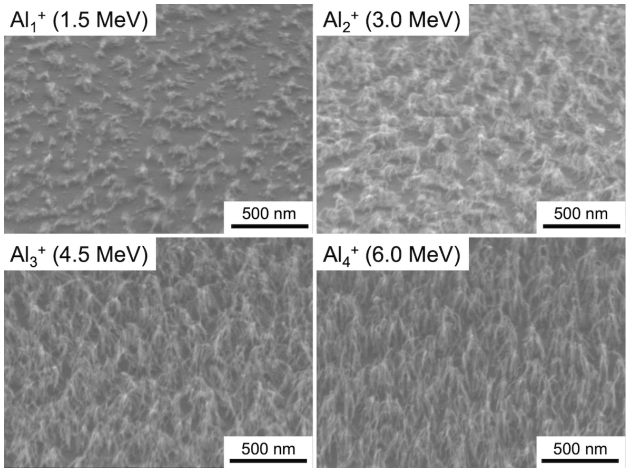

Fig. 2. Side perspective view of scanning microscopy images of vertically-aligned nanowires fabricated by irradiation of PTCDA-Cl_4 film (thickness: 200 nm) with 1.5 MeV Al_1^+, 3.0 MeV Al_2^+, 4.5 MeV Al_3^+, 6.0 MeV Al_4^+ cluster ion beams at fluence of 1.0×10^{11} cm^{-2}.

fragments were observed. Although the energy per single ion is equal, the obvious “cluster” effect was seen in these experiments. The vertical orientation of nanowires was confirmed for the irradiation with 6.0 MeV Al_4^+, while the nanowires upon 1.5 MeV Al^+ or 3.0 MeV Al_2^+ irradiation fall down. The spatial size of cluster ions with larger n size may be the key for cylindrical ion tracks with larger diameters, which would keep the standing feature of the obtained nanowires. The similar experiment with 6.0 MeV C_{60}^+ irradiation afforded further stiff nanowire arrays, supporting our hypothesis.

Acknowledgments

This work was partly supported by a Grant-in-Aid for Scientific Research (B) (19KK0134) from JSPS, Yazaki Memorial Foundation for Science and Technology, Mizuho Foundation for the Promotion of Sciences, the Ogasawara Foundation for the Promotion of Science & Engineering, and Kangenkon. Cluster ion beam irradiation was carried out using a tandem accelerator at Takasaki Advanced Radiation Research Institute, QST, Japan.

References

[1] A. Horio *et al.*, Nanoscale, **8**, 14925 (2016).
[2] S. Sakaguchi *et al.*, J. Phys. Chem. B **122**, 8614 (2018).
[3] T. Sakurai *et al.*, ACS Appl. Nano Mater. 3,6043 (2020).
[4] S. Sakaguchi, *et al.*, Quantum Beam Sci. **4**, 7 (2020).
[5] K. Kamiya *et al.*, Nature Commun. **12**, 4025 (2021).

3 - 14 Electron excitation in production and penetration of cluster ions

T. Kaneko[a)], Y. Saitoh[b)], A. Chiba[b)] and K. Narumi[b)]

[a)]Department of Applied Physics, Okayama University of Science
[b)]Department of Advanced RadiationTechnology,TARRI, QST

In order to obtain high-intensity cluster ion beams using tandem accelerator, the gas pressure of a charge- changing gas is set to maximize the ion yield for the chosen gas species. As basic research for this purpose, we estimated the electron-loss cross section and the destruction cross sections for swift carbon cluster ions composed of a few carbon atoms, penetrating through the rare gas region. This is one of basic problems in a field of cluster – atom collision. In addition, we also estimated the energy loss per unit passage of a carbon cluster C_{60} with a few MeV, penetrating a carbon foil as an example, since we have not known a direct estimation of the electronic stopping power data on a C_{60} projectile.

Production of C_n^+ cluster ion

On the basis of the rate equation on the charged fraction of a carbon cluster ion $C_n^+ (n=2-4)$ in collision with a rare gas atom, we described the singly charge fraction by six cross sections [1], i.e., three electron-loss cross sections, $\sigma_{-10}, \sigma_{-11}, \sigma_{01}$, and three destruction cross sections, $\sigma_{-1d}, \sigma_{0d}, \sigma_{1d}$. Here σ_{ik} denotes the cross section for change-state change from $i(=-1,0)$ to $k(=0,1)$, and σ_{id} $(i=-1,0,1)$ is the destruction cross section for a cluster ion in charge state i. These quantities were calculated under the assumption of the binary collision model between one of an atom/ion of a cluster and a rare gas atom as a function of impact parameter. In addition, we assumed the independent- atom and –electron picture so that the ionization probability of individual electrons bound on a given atom/ion is independently taken into account. First we calculated the orientation-dependent cross sections, i.e., those for a fixed linear cluster aligned on an orientation axis, and after that those cross sections are averaged over the orientation angle (angle between cluster axis and the incident direction of a gas). Figure 1 shows the calculated values of $\sigma_{-10}, \sigma_{-11}, \sigma_{01}$ for the 1.2 MeV/atom $C_n^+ (n=1-4)$ cluster ions in collision with He gas. Roughly speaking, three cross sections display a linear dependence on n as $\sigma(4)=\sigma(2)[1+\alpha(n-2)]$, where $\sigma(n)$ denotes the cross section for C_n^+ as a representative. The value of α ranging $0<\alpha<0.5$ means the sub-linear dependence on n. In this case, $\alpha \approx 0.13-0.22$ for σ_{ik} and $\alpha \approx 0.34-0.36$ for σ_{id}. Using three cross sections with the destruction ones, we finally obtained the singly- charged fraction of a carbon cluster penetrating charge- changing rare gas region. In particular, the gas pressure dependences of the normalized fraction of the 2.5 MeV C_2^+ and C_4^+ produced using Ne gas are in good agreement with the experimental data obtained at TIARA.

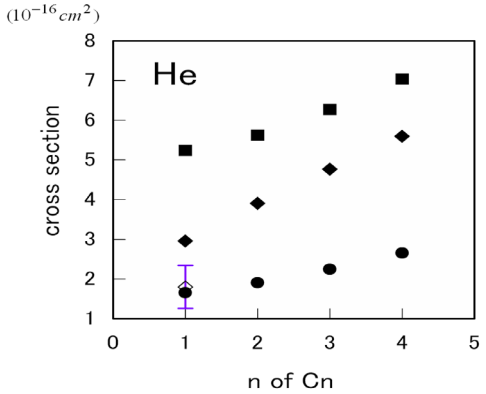

Fig. 1. The size dependence of the cross sections: σ_{-10} (■), σ_{01} (◆), σ_{-11} (●) for 1.2 MeV/atom C_n colliding with He.

The theoretical investigation on the fraction of the 3.75 MeV C_3^+ in linear and ring structures produced using He and Ne gases were also performed [2]. It was found that the structure dependence is not so large.

Energy loss of C_{60} cluster ion

As an interaction between a cluster ion and material, we presented several reports on the energy-loss and the average charge per atom as the so-called cluster effects [3-5]. In addition, in case of relatively higher energies (E >18 MeV, v > v_0), we calculated the electronic energy-loss of a C_{60} cluster moving in an electron gas on the basis of the electron gas model and the dielectric function method [6]. We performed calculation newly for a C_{60} with the kinetic energy of 2-10 MeV. The spatial structure of C_{60} is a fullerene where 60 atoms are on a sphere with radius $d=3.5\times10^{-8} cm$. Here the reduction of the average charge in cluster impact is taken into account [3]. In addition, each atom is assumed to have bound electrons, determined by a statistical approach. The calculated results show that the average charge per atom is about 0.80 of the single ion at equivalent speed, and that the electronic stopping power is also about 48 times the single-ion stopping at equivalent speed. Thus it is concluded that both quantities are about 80 percent in magnitude of the single ion at equivalent speed.

References

[1] T. Kaneko *et al*., Nucl. Instrum. Meth. Phys. Res. B **478**, 218 (2020).
[2] T. Kaneko, Bull. Okayama. Univ. Sci. **56 A**, 21 (2020).
[3] T. Kaneko, Phys. Rev. A **66**, 052901-1 (2002).
[4] T. Kaneko, Phys. Rev. A **86**, 012901-1 (2012).
[5] T. Kaneko *et al*., Nucl. Instrum. Meth. Phys. Res. B **315**, 76 (2013).
[6] T. Kaneko, Bull. Okayama. Univ. Sci. **53 A**, 1 (2017).

3 - 15 Measurements of total yields of positive secondary ions emitted by energetic carbon cluster impacts on a poly(methyl methacrylate) target

K. Hirata[a)], K. Yamada[b)], A. Chiba[b)], Y. Hirano[b)], K. Narumi[b)] and Y. Saitoh[b)]

[a)]National Metrology Institute of Japan, AIST
[b)]Department of Advanced Radiation Technology, TARRI, QST

When a primary ion impacts a solid target, secondary ions (SIs) are emitted from the target surface due to energy transfer from the primary ion to the target. As their emission yields strongly depend on various parameters of the target and incident ions, quantitative investigation of the parameter dependence of SI emission yields is important. We quantitatively measured the mean numbers of emitted positive SIs (P-SIs) for energetic carbon cluster C_n (n: cluster number) impacts on a poly(methyl methacrylate) (PMMA) target, based on primary ion beam current I_o and P-SI current I_p measurements [1, 2].

C_n^{q+} ions (q: incident ion charge number) with energies of 0.12 to 6.0 MeV, supplied by ion accelerators at QST/Takasaki, impact on a PMMA film target, which was produced by spin-coating a chlorobenzene solution of PMMA (Wako Pure Chemical Industries, Ltd.) on a silicon wafer, with an incident angle of 45° to the target normal. I_o and I_p were measured with electrometers connected to a Faraday cup and a movable metal plate with a grid, respectively, as described elsewhere [1, 2]. As the major peaks observed in the P-SI mass spectra can be attributed to singly charged ions [3], the value of qI_p/I_o gives the mean number of emitted P-SIs per C_n ion impact.

Figure 1 summarizes the impact energy dependence of the mean number of emitted P-SIs per C_n ion impact on the PMMA target for primary ion incidence on the target at an angle of 45° to the target surface [2]. In the experiment, two accelerators, a 400 kV ion accelerator and a 3 MV tandem accelerator at QST/Takasaki, were used to measure the qI_p/I_o values in a wide C_{60} energy range; the 400 kV and 3 MV accelerators provided C_{60} ion beams in impact energy ranges from 0.12 to 1.08 MeV and from 1.08 to 6.0 MeV, respectively. (Ion beams supplied by the 3 MV tandem accelerator were used for C_1 and C_8 ion impacts.) Therefore, demonstrating the equivalency of the qI_p/I_o values obtained from the two accelerators is important. In Fig. 1, the qI_p/I_o value for 1.08 MeV C_{60}^{3+} (400 kV accelerator) is almost equal to that for 1.08 MeV C_{60}^{+} (3 MV accelerator), showing that an equivalent qI_p/I_o value can be obtained for the same cluster ion species (C_{60}) with the same impact energy (1.08 MeV) and with the different q numbers ($q = 1$, 3), from the two accelerators (400 kV and 3 MV accelerators).

The figure also clearly demonstrates that the qI_p/I_o value increases with increasing n and, also with increasing impact energy for the same C_n species. Thus, energetic larger cluster impacts are advantageous for enhancing SI emission yields for organic materials. It should be noted that impacts of energetic C_{60} in sub MeV – MeV range produce as many as several tens of P-SIs per impact. These high qI_p/I_o values indicate that use of energetic C_{60} ions as primary ions for secondary ion mass spectrometry is advantageous for highly sensitive surface chemical structure analysis.

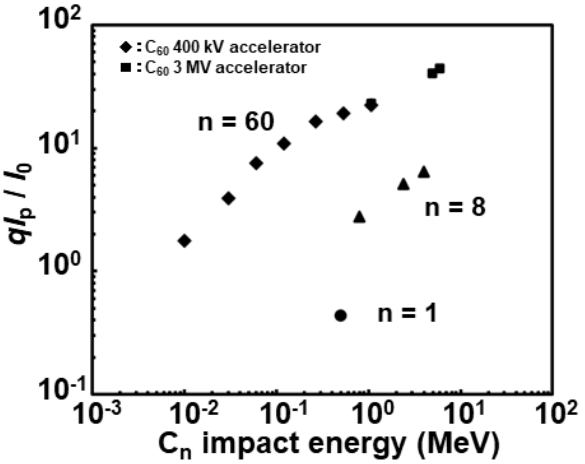

Fig. 1. Impact energy dependence of the mean number of emitted P-SIs per carbon cluster C_n^{q+} ion (n: cluster number, q: incident ion charge number) impact on a PMMA target.

Acknowledgments

This work was partially supported by JSPS KAKENHI (Grant No. 17H02819) and by the Inter-organizational Atomic Energy Research Program in an academic collaborative agreement among JAEA, QST, and the University of Tokyo.

References

[1] Hirata *et al.*, Appl. Phys. Lett. **86**, 044105 (2005).
[2] K. Hirata *et al.*, Nucl. Instrum. Meth. Phys. Res. B **479**, 240 (2020).
[3] K. Hirata *et al.*, J. Chem. Phys. **145**, 234311 (2016).

3 - 16 Status report on technical developments of electrostatic accelerators

Y. Hirano, A. Chiba, K. Yamada and S. Kurashima

Department of Advanced Radiation Technology, TARRI, QST

Formation of MeV-energy C_{60} ion microbeam

We are developing a molecular imaging technique using C_{60} ion beams of MeV energy accelerated by the tandem accelerator in TIARA/QST Takasaki. The irradiation effect characteristic of cluster ions such as C_{60}, which are never observed by any irradiation with monatomic ions, is considered to be very effective also for surface analysis of various materials. The analysis method of the secondary ion mass spectrometry using the swift C_{60} ions as the primary ions enables highly sensitive detection of the constitutive molecules of the materials such as biopolymers as well as organic-inorganic hybrid materials. In order to achieve the surface analysis with spatial resolution of a few microns, the C_{60} ion microbeam must be focused to a diameter of 1 μm or less. The beam intensity of C_{60} ions required to form the microbeam with this size was estimated to be at least 500 nA at the ion source. It has been difficult to transport the C_{60} ion beams with intensities above this value to the tandem accelerator from the existing ion sources. Therefore, in order to generate the high-intensity beam required for C_{60} ion microbeam formation, we have developed a negative ion source with the world's highest level of C_{60} ion beam intensity and introduced it as an ion source dedicated for fullerene ion generation to the tandem accelerator [1]. Figure 1 shows the location of the new ion source, an electrostatic deflector, and the C_{60} microbeam line. This ion source produced negative C_{60} ion beam up to 1.3 μA, and the electrostatic deflector equipped with lens function efficiently transports the fullerene ions to the accelerator.

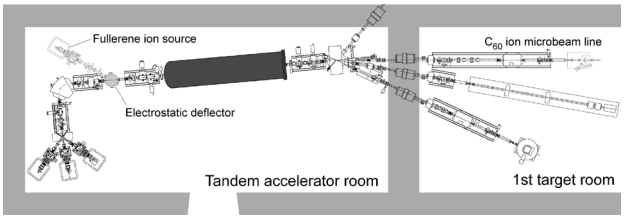

Fig. 1. The location of a new fullerene ion source and an electrostatic deflector.

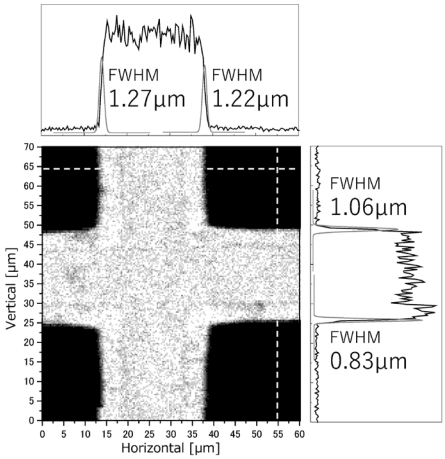

Fig. 2. Evaluation of C_{60} ion microbeam size. Secondary ion image of metal mesh and intensity distributions at the dashed line on the image. The results of the rise distance measurements showed that the microbeam size was approximately 1μm.

So far, we have designed and manufactured a high-definition electrostatic quadrupole lens, modified the existing beamline, installed a microbeam forming device, and constructed a microbeam size evaluation system. An example of the microbeam size evaluation is shown in Fig. 2. It consists of a secondary ion image and its intensity distributions obtained by irradiating a metal mesh grid (400 mesh/inch) with the 5-MeV C_{60} microbeam scanned vertically and horizontally. As a result of evaluating the beam size from the rise distances of the intensity distributions, it was 0.95 μm and 1.25 μm in the vertical and horizontal directions, respectively. In this case, the focusing rate of the entire system was 21.1 (vertical) and 16.0 (horizontal).

Production of $C_{32}H_{18}N_8$ ion beams by the ion implanter

The 3-qubits caused by triple NV center interaction had been generated by implantation of adenine ($C_5N_5H_5$) ions into diamond [2]. An ion beam of phthalocyanine ($C_{32}H_{18}N_8$) containing more nitrogen atoms than $C_5N_5H_5$ was requested to obtain more qubits. $C_{32}H_{18}N_8$ has a very vivid blue color that can be used as a pigment for road signs and body color of Shinkansen, etc. Therefore the inside of the ion source after long-time ion production is dyed blue. In the mass spectrum of ion beams produced and accelerated by the oven method of the freeman ion source at the oven temperature of 340 °C, it can be seen that many fragment ions based on phthalic acid were produced (Fig.3). On the other hand, about 20 nA of $C_{32}H_{18}N_8$ ion beam, which was enough to carry out the experiments of multi-qubits generation, was also obtained.

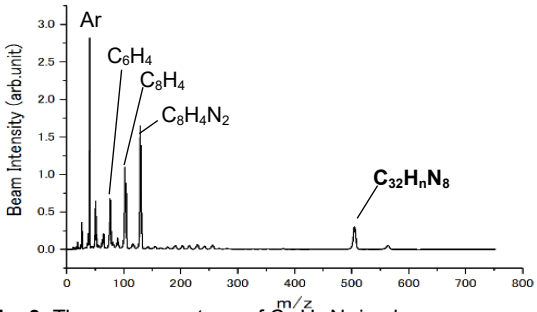

Fig. 3. The mass spectrum of $C_{32}H_{18}N_8$ ion beams.

References

[1] A. Chiba *et al.*, Quantum Beam Sci. **4**, 13 (2020).
[2] M. Haruyama *et al.*, Nat. Commun. **10**, 2664 (2019).

3 - 17 EB-irradiation conditions for production of low molecular weight PTFE

H. Seito[a)], S. Yamasaki [a)], A. Oshima [b)] and N. Nagasawa [a)]

[a)]Department of Advanced Radiation Technology, TARRI, QST
[b)]Graduate School of Engineering, Osaka University

Low molecular weight polytetrafluoroethylene (PTFE) micro-powder is a powerful additive used in diverse industrial applications. With its high surface lubricity and anti-blocking properties, its micropowder is becoming accepted in industries that include food, textiles, pharmaceuticals, and electronics, and its global market was worth US$ 400 million in 2018 [1].

PTFE micro-powder is produced industrially by the chain scission of its polymerised powder or moulded scraps induced by ^{60}Co gamma-rays, electron beam (EB) from accelerator or EB conversion X-rays irradiation in air. However, the radiation-induced oxidative degradation products (RODP) is produced at concentrations of more than 25 ppb as a by-product of radiation processing. For this reason, PTFE micropowder does not comply with regulations such as Registration, Evaluation, Authorisation and Restriction of Chemical (REACH) legislation in the European Union (EU) [2] and may cause serious problems in industrial applications. Therefore, to comply with regulations, a method for the manufacture of low molecular weight PTFE with low RODP contents (< 25 ppb) is required. Oshima et al. have reported a manufacturing process for a novel low molecular weight PTFE with < 25 ppb RODP contents [3]. In the previous report, we reported the results of examining the use of gamma-rays irradiation for mass production of the new method [4].

In the world, modification of PTFE by EB irradiation is expected instead of gamma-rays irradiation from ^{60}Co sources from the viewpoint of RI protection. Therefore, in this study, in order to evaluate the mass production of low molecular weight PTFE by EB irradiation, a vessel for EB irradiation was manufactured, the dose distribution in the vessel was measured, and the dose uniformity was evaluated by simulation, and the optimum irradiation conditions were examined to obtain basic knowledge of PTFE micro powder.

The EB irradiation vessel was manufactured with reference to the previous report [5] as showed in Figure 1. The vessel container can circulate an inert gas or keep in vacuum, it was possible illuminated at uniform temperature. As a dose measurement, the EB was irradiated under the conditions of an acceleration voltage of 2.0 MV, an electric current of 0.50 mA, a distance under the window of 300 mm, and an irradiation time of 240 s. The dose on sample support in the vessel was measured using a CTA firm dosimeter FTR-125 (Fujifilm Co. Japan). As a result, the average dose rate on the sample support table in the vessel was 0.634 to 0.664 kGy/s. The dose distribution on the sample table in the vessel was estimated based on the Monte Carlo simulation code of PHITS [6]. The dose distribution obtained from the simulation is compared to that obtained by the film dosimeter. They were mostly in agreement. This result implies that uniform dose distribution can be attained.

Homopolymerized PTFE fine powder was used in the experiments. The EB was irradiated under the conditions of an acceleration voltage of 2.0 MV, an electric current of 0.50 mA, a distance under the window of 300 mm, and an irradiation time of 600 s while ventilating nitrogen gas to obtain low molecular weight PTFE micro-powder. Since the low molecular weight PTFE obtained by EB irradiation was a substance of the same viscosity obtained by the previous gamma-rays irradiation, it was expected that gamma-rays and EB irradiation technology could be used in mass production processes.

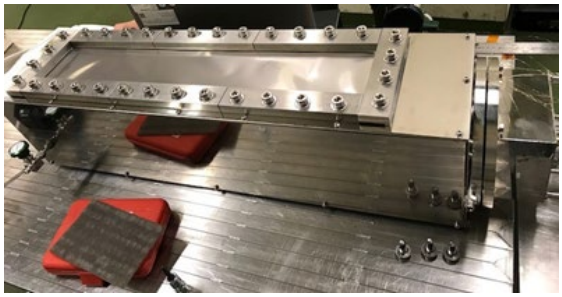

Fig. 1. Photograph of manufactured electron beam irradiation vessel.

Acknowledgments

The authors would like to thank Mr. S. Uno, Mr. Y. Haruyama and Mr. M. Takagi (QST) for their advice and assistance concerning EB and gamma-ray irradiation and Mr. H. Matsukawa (Osaka University) for sample preparation.

References

[1] Persistence Market Research, https://www.persistencemarketresearch.com/market-research/micronized-ptfe-market.asp. Accessed April 14, 2020.
[2] European Chemicals Agency (ECHA), https://echa.europa.eu
[3] A. Oshima *et al*., Sci. Rep. **10**, 13940 (2020).
[4] A. Oshima *et al*., QST-Takasaki Ann. Rep. 2019, **QST-M-23**, 62 (2020).
[5] Y. Haruyama *et al*., JAERI-Tech 95-003 (1995).
[6] T. Sato *et al.* J. Nucl. Sci. Technol. **50**, 913 (2013).

Part Ⅱ

4. Status of Quantum-Beam Facilities

4 - 01 Utilization status at the TIARA facility

H. Hanaya[a)], I. Ishibori[a)], H. Takizawa[a)], S. Watanabe[a)],
H. Kaneko[b)], S. Kaneya[b)] and T. Shimizu[b)]

[a)]Department of Advanced Radiation Technology, TARRI, QST
[b)]Takasaki Establishment, Radiation Application Development Association

Research & industrial use

Four kinds of accelerators, a cyclotron and three electrostatic accelerators (tandem accelerator, single-ended accelerator and an ion implanter), are used at the TIARA facility to meet various researchers' needs. The activities of research fields that the cyclotron was used for the past 5 fiscal years are shown in Fig. 1. Total utilization time of each fiscal year (FY) was in the range of 1,200 to 1,300 hours except FY 2018. The utilization time of FY 2018 was reduced to about 500 hours because of repairing of the main coil of the cyclotron. The utilization time of "Material Science" and "Life Science" accounted for more than about 60% of the total time. On the other hand, for the three electrostatic accelerators, as shown in Fig. 2, the utilization time of "Material Science" and "Basic Technology of Quantum Beam" accounted for more than about 65% of the total time.

The trend of the number of users in the past 5 years is shown in Fig. 3. The total number of users was in the range of 560 to 770 per year.

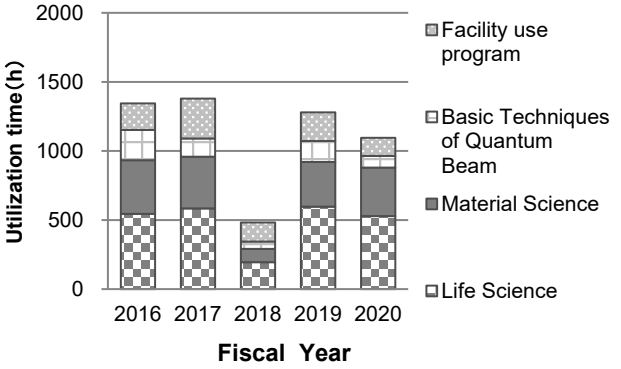

Fig. 1. Research activities for the cyclotron for the past 5 years.

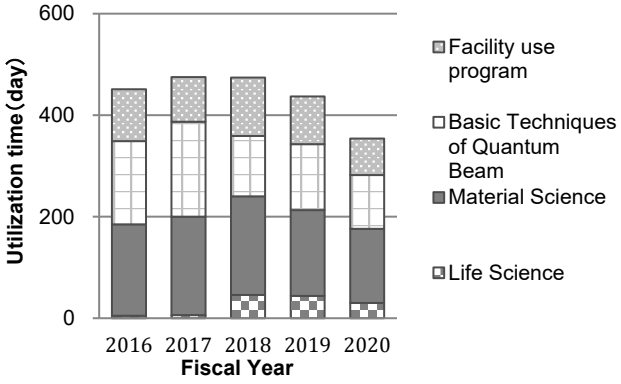

Fig. 2. Research activities for the three electrostatic accelerators for the past 5 years.

The trend of the number of project category (Internal use, Joint research, Cooperation priority research, Funded research and Facility use program) for the past 5 years is shown in Fig. 4. The total number of projects was in the range of 60 to 70 per year.

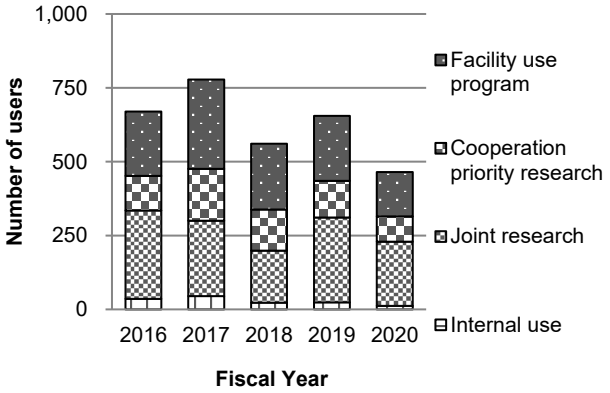

Fig. 3. The number of users for the past 5 years.

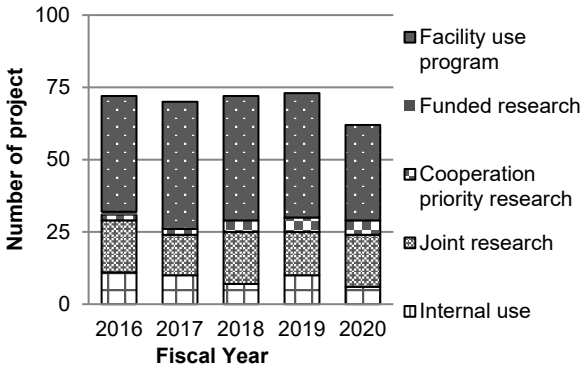

Fig. 4. The number of projects for the past 5 years.

Influence of COVID-19

The operation of the TIARA facility was stopped from April 17th to May 31th in fiscal year 2020 for the COVID-19 state of emergency in Gunma prefecture, and 49 experiments were cancelled. Consequently, the utilization time, the number of users and the number of projects decreased in FY 2020 as shown in Fig. 1 to 4.

4 - 02 Operation of the AVF Cyclotron

K. Yoshida[a)], T. Yuyama[a)], T. Ishizaka[a)], S. Hosoya[a)], I. Ishibori[a)], N. Miyawaki[a)], H. Kashiwagi[a)], T. Nara[a)], S. Kurashima[a)], To. Yoshida[b)], S. Ishiro[b)], Tu. Yoshida[b)], S. Kanou[b)], K. Takano[b)], H. Saitoh[b)] and T. Atobe[b)]

[a)]Department of Advanced Radiation Technology, TARRI, QST
[b)]Beam Operation Co., Ltd.

Operation

In fiscal year of 2020, the operation of the AVF cyclotron was started in April 6. Since the Japanese government declared the COVID-19 state of emergency, the operation of the cyclotron had been stopped from April 16 to May 25. Although 50 scheduled experiments were cancelled for the stopped period, most of these experiments were compensated in the second half of the fiscal year. Moreover, eight experiments were cancelled due to the second time of the emergency that was declared only to the metropolitan area from January 8 to March 21. The total operation time of the AVF cyclotron eventually amounted to 1880 h, and the number of experiments of the year was 194. The accumulative operation time and the total number of experiments had reached to 87424 h and 12490 since the first beam extraction in 1991 to March, 2021, and the first beam irradiation for the experiment uses, respectively.

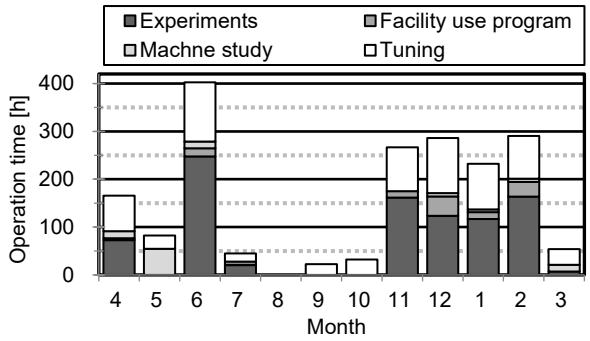

Fig. 1. Monthly operation times in fiscal 2020

Table 1
Statistics for cyclotron operation.

Fiscal year	2020	2019
Beam service time	1035 h	1196 h
Beam tuning	722 h	1113 h
Machine study	123 h	113 h
Total operation time	1880 h	2422 h
Change of particle and/or energy	152 times	199 times
Change of beam course	135 times	179 times
Change of harmonic number	67 times	87 times
The number of experiments	194	246
Cancellation due to machine trouble	0	0

Monthly operation times are shown in Fig. 1. The scheduled maintenances were carried out from the middle of July to October and in March. Table 1 shows the contents of the cyclotron operation of the fiscal year of 2020 with the previous year. The percentages of the operation time of the FY 2020 used for the regular experiments, facility use program and promotion of shared use program, beam tuning, and beam development are 48.6%, 6.4%, 38.4%, and 6.5%, respectively. Table 2 shows each operation time of three ECR ion sources, NANOGAN, OCTOPUS, and HYPERNANOGAN. NANOGAN is used to produce three species of ion beam, H, D, and He. For the production of ion beam heavier than He, HYPERNANOGAN is used. OCTOPUS is mainly used for the cocktail beam of M/Q = 5. Figure 2 shows the pie chart of the ion beams used for the experiments. The tendency of the statistics is similar to those of the past years.

Table 2
Operation times of ion sources.

ECR Ion source	Operation time	Ratio
NANOGAN	530 h	26.0 %
OCTOPUS	365 h	17.9 %
HYPERNANOGAN	1143 h	56.1 %

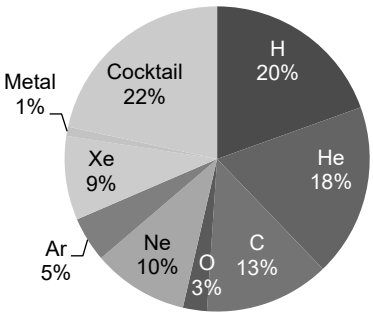

Fig. 2. Ion species used for experiments in the fiscal year of 2020.

Machine trouble and maintenance

The number of the machine troubles of the year was 99. Nineteen out of those troubles needed repair. The number of the maintenance of the year was 131. The preamplifier of the RF system of the cyclotron was replaced from the vacuum tube type to the solid-state one in summer. After the replacement, the operational parameters of the RF system were optimized. Since the body current of the klystron for OCTOPUS reached over 40mA, the klystron was replaced by the used one. The other major items of the maintenance were as follows: 1) Replacement of all capacitors in the main RF power supply. 2) Replacements of the connector pins of the inflector electrode and the contact fingers in the CH1 RF resonator. 3) Removal of unnecessary ion pumps from the beam lines. 4) Update of the gas leakage detection system in the ion-source room. 5) Inspection of the power supplies and the main RF system. 6) Change of lubricating oil for about 55 rotary vacuum pumps. 7) Replacements of internal power supplies and cooling fans used in the device controller of the cyclotron.

4 - 03 Operation of electrostatic accelerators in TIARA

A. Chiba[a)], K. Yamada[a)], A. Yokoyama[a)], Y. Hirano[a)],
T. Takayama[b)], S. Kanai[b)], Y. Aoki[b)], M. Hashizume[b)],
Y. Takahashi[b)], M. Hasegawa[b)] and S. Kurashima[a)]

[a)]Department of Advanced Radiation Technology, TARRI, QST
[b)]Beam Operation Co., Ltd.

In FY2020, the operation times of three electrostatic accelerators (the 3-MV tandem accelerator, the 3-MV single-ended accelerator and the 400-kV ion implanter) in TIARA decreased not a little due to the influence of COVID 19 pandemic. In particular, the operation times decreased significantly between April and May, when a state of emergency was declared by the national government to all over Japan. On the other hand, no irradiation experiment had been canceled due to troubles with the accelerators or related equipment. The annual operation times of the tandem accelerator, the single-ended accelerator and the ion implanter were 1,629 h, 1,637 h and 1,555 h, respectively. The transitions of the annual operation time since the start of operation and the monthly operation times of FY2020 for each electrostatic accelerator are shown in Fig. 1 and Fig. 2, respectively. With the revision of the management structure of the electrostatic accelerators, the daily operation time of the accelerators, which used to be until 22:00, will be until 17:00 from next fiscal year. Needless to say, annual operation times in FY 2021 are expected to be significantly lower than this fiscal year.

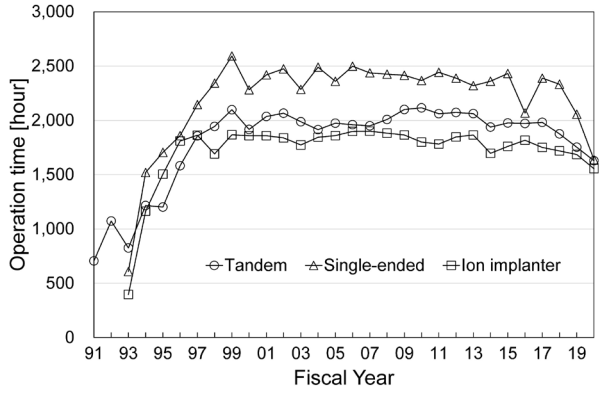

Fig. 1. Transitions of annual operation time.

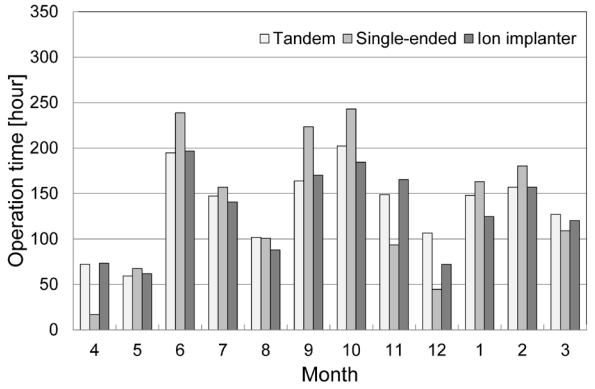

Fig. 2. Monthly operation time.

Figure 3 shows the utilization rates of ion species in each electrostatic accelerator. Fullerene ion beams such as the C_{60} were most frequently used in the tandem accelerator. A new ion source dedicated to fullerene ions installed in the tandem accelerator last year started operation this fiscal year and further improved the intensity and stability of the beam current [1]. In ion implanter, ion beams of adenine ($C_5H_5N_5$) and phthalocyanine ($C_{32}H_{18}N_{18}$) were developed for multiqubit formation experiments on the development of quantum sensing technology.

Table 1 shows the number of major troubles occurred in each accelerator in FY2020. There were no serious problems that the experiment had to be stopped. In the regular maintenance, the chain motor of the tandem accelerator was replaced, and the NMR controller of the single-ended accelerator and the steerer power supply of the ion implanter were repaired.

Reference

[1] Y. Hirano *et al.*, QST Takasaki Annu. Rep. 2019, **QST-M-29**, 129 (2021).

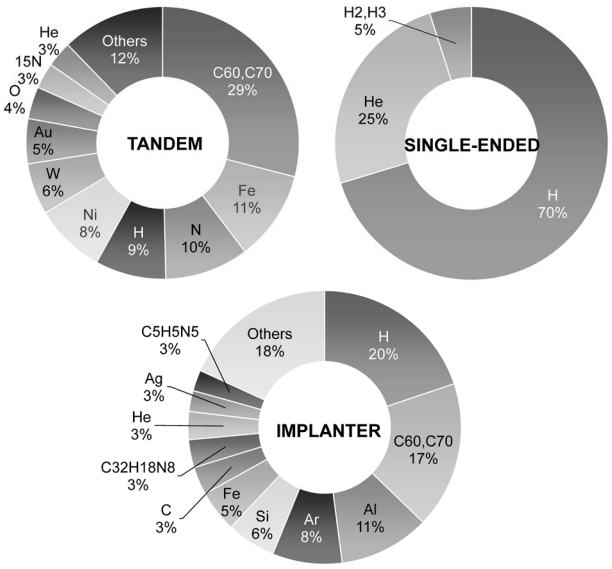

Fig. 3. Utilization rates of ion species.

Table 1
Number of troubles and maintenance.

	Tandem	Single-ended	Ion implanter
Minor trouble	27	19	15
Serious trouble	1	4	0
Maintenance	36	11	18

4 - 04 Operation status of the electron accelerator and the gamma-ray irradiation facilities

S. Uno[a)], H. Seito[a)], Y. Nagao[a)], S. Yamasaki[a)], T. Agematsu[a)], M. Hosono[a)], N. Nagasawa[a)], N. Yagi[b)], M. Takagi[b)], K. Imai[b)] and K. Akaiwa[b)]

[a)]Department of Advanced Radiation Technology, TARRI, QST
[b)]Takasaki Establishment, Radiation Application Development Association

Operation

The electron accelerator and the ^{60}Co gamma-ray irradiation facilities in TARRI were operated almost smoothly in Fiscal Year (FY) 2020.

In FY 2020, the use of irradiation facilities was forced to be suspended due to the state of emergency to prevent the spread of novel coronavirus disease-2019 (COVID-19), and the users from inside and outside the Takasaki Advanced Radiation Research Institute decreased significantly for stay-at-home order.

The annual operation time of the electron accelerator in FY 2020 was 1,015 h, including 141 h of conditioning operation to keep the good condition of accelarator during the suspension period due to the state of emergency . The operation times in recent years are shown in Fig. 1. Although there was a trouble about the high frequency power supply unit of the accelerator, the annual operation time increased in FY 2016 and 2017 because long-time irradiation increased. The annual operation time increased in FY 2018 and 2019 because long-time irradiation increased. Despite the influence of COVID-19, the annual irradiation time did not decrease in FY 2020 due to the long-term irradiation experiment conducted by the in-house users.

The ^{60}Co gamma-ray irradiation facilities consisting of three buildings with eight irradiation rooms cover a wide dose-rate range from 2×10^{-1} Gy/h to 0.9×10^{4} Gy/h as of March 2021. The annual operation times of the first and the second cobalt irradiation facilities and the food irradiation facility were 10,134 h, 11,972 h and 6,725 h, respectively, as shown in Fig. 2. The annual operation time increased until FY 2017 because long-time irradiation increased. However, the annual operation time decreased from FY 2018 because long-time irradiation experiments by the in-house users decreased. Furthermore, due to the influence of COVID-19, the use of irradiation experiments by users inside and outside the QST decreased. As a result, the operation time decreased significantly in FY 2020.

Maintenance

As a measure against COVID-19, in order to shorten the user's experiment preparation time and enable remote monitoring of the measuring device, devices called smart boxes that takes out signals and various pipes outside the irradiation rooms were installed in the electron beam vertical irradiation room and gamma-irradiation rooms.

・*Electron accelerator*

The trouble of the horizontal beam line occurred at the beginning of December 2017, and generation of the horizontal beam came to a halt. We found that this trouble was due to trouble at the capacitor on the power supply circuit for the electron gun, not to trouble at the filament by the maintenance in 2018. This repair was performed during the maintenance inspection conducted in 2019, 2020 and we confirmed that the electron beams were generated from the horizontal beamline. Since the opening and closing problem of shield door occurred and risky human assistance was required, the shield door control panels in the accelerator room, vertical irradiation room, and horizontal irradiation room, which were the causes of the problems, were updated in FY 2020.

・*Gamma-ray irradiation facilities*

The periodical maintenance check mainly on mechanical systems for radiation source transportation is performed every year on one of the three gamma-ray irradiation facilities in turn. The maintenance check of the ^{60}Co second facility was done in August and September 2020 with suspension of operation for 23 days. In preparation for the shutdown of the food irradiation facility, the manipulators for handling the ^{60}Co sources were repaired. Simulation analysis revealed that the ^{60}Co first facility could cover a wide dose-rate range of 0.2 ~ 5000 Gy/h and thus could be an alternative to the food irradiation facility.

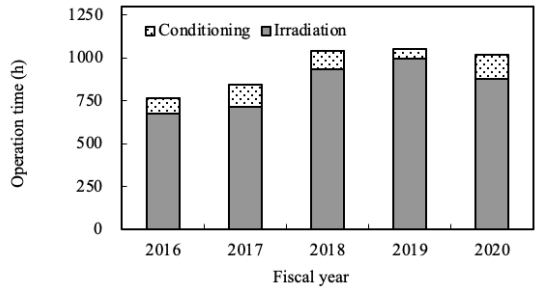

Fig. 1. Annual operation time of the electron accelerator.

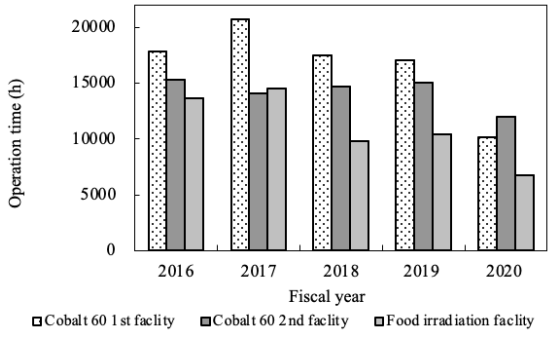

Fig. 2. Annual operation time of the ^{60}Co gamma-ray irradiation facilities.

4 - 05 Utilization status of the electron accelerator and the gamma-ray irradiation facilities

H. Seito[a)], S. Uno[a)], Y. Nagao[a)], S. Yamasaki[a)], T. Agematsu[a)], M. Hosono[a)], N. Nagasawa[a)], N. Yagi[b)], M. Takagi[b)], K. Imai[b)] and K. Akaiwa[b)]

[a)]Department of Advanced Radiation Technology, TARRI, QST
[b)]Takasaki Establishment, Radiation Application Development Association

The electron accelerator and the three gamma-ray irradiation facilities were operated for various research subjects according to the operation plans of fiscal year (FY) 2020. Their research fields were classified to 'Materials science', 'Life science' and 'Quantum beam science'.

Figure 1 shows the total number of irradiation experiments of the three research fields and facility use program in each FY 2016 - 2020. The accelerator was mainly used for materials science such as NV-center process in diamonds, novel catalyst materials, graft-polymerization for new absorbent material and so on.

The first cobalt gamma-irradiation facility was mainly employed for long-term radiation resistance tests of materials, such as polymeric parts used for accelerators, cables used in nuclear power plants and nuclear reactor facilities. The second cobalt gamma-irradiation facility, including the irradiation room No.6 operated on hourly schedule, was mainly used for development of new functional polymeric materials, such as biocompatible protein hydrogels and fuel cell separator membrane and hydrogen fuel tube, radiation resistance tests of ITER products, and other research subjects. The third gamma-ray irradiation facility named 'food irradiation facility,' which has a lower-dose-rate field, was used for radiation-resistant tests of electric devices and Li battery at wide dose-rate ranges to simulate the space environment and research for radiation effects of organisms such as microorganisms and plants.

Figure 2 shows the total irradiation time of experiments of the three research fields and facility use program in each FY 2016 - 2020. The EB-irradiation time increased in FYs 2017 to 2019 due to smoother operation than in FY 2016. The reasons of the time shortages in FY 2016 are that we had troubles with high-voltage transformers and current control systems. The irradiation time of material science of in-house users in FYs 2018 - 2020 increased because of increase in long-term irradiation for research in developing techniques of NV-center process in diamonds and novel catalyst. But the irradiation time of the facility use program in FY 2020 was dramatically reduced by the increases of irradiation fee and impact of COVID-19.

The gamma-irradiation time has been decreasing year by year for the past five years except FY 2019. This is because the one of the in-house researches on long-term radiation resistance tests was finished. Furthermore, since there are financial difficulties to purchase cobalt sources to increase the radiation intensity in the gamma-irradiation facilities, research on the creation of novel functional materials that can be synthesized in a short time using high dose rates of gamma-rays has decreased.

Especially in the cobalt gamma-irradiation facilities, radiation resistance experiments of various devices used in the accident of the Fukushima Daiichi Nuclear Power Station of Tokyo Electric Power Company were carried out mainly in the facility use program.

Due to the large impact of COVID-19 during FY2020, the use of electron beam irradiation and gamma-irradiation facilities by outside users decreased dramatically.

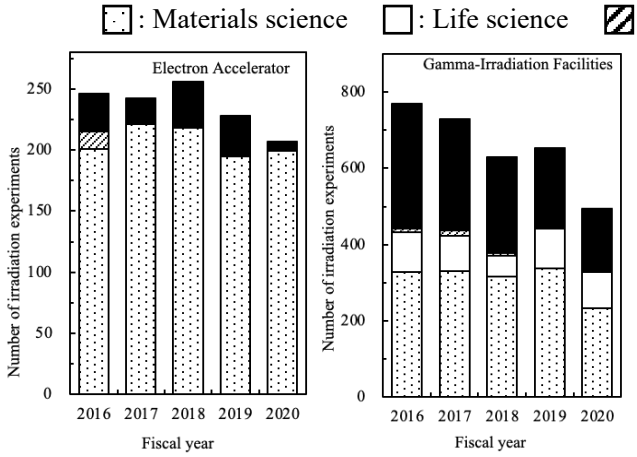

Fig. 1. The number of irradiation experiments (FY 2016-2020).

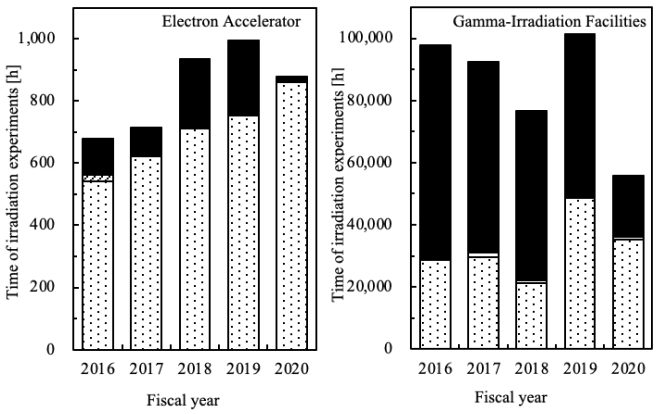

Fig. 2. The time of irradiation experiments (FY 2016-2020).

4 - 06 Radiation monitoring in TIARA

Safety Management Section

Department of Administrative Services, TARRI, QST

Individual monitoring

(1) Individual monitoring for the radiation workers

Table 1 shows a distribution of effective dose of the radiation workers in FY 2020. The effective dose values of almost all radiation workers were below the detection limit of 0.1 mSv.

The maximum dose of the radiation worker was 0.4 mSv/y by the purification work of positron-emitting radionuclide. Compared to 2019, the effective dose value was found to be 0.1 mSv/y higher.

Table 1

Distributions of the effective dose of the radiation workers in FY 2020.

Items		Number of persons in each periods				
		1st quarter	2nd quarter	3rd quarter	4th quarter	Annual
Distribution range of effective dose HE:Effective dose *1 (mSv)	HE ＜ 0.1	402	467	569	570	739
	0.1 ≦ HE ≦ 1.0	1	1	2	3	5
	1.0 ＜ HE ≦ 5.0	0	0	0	0	0
	5.0 ＜ HE ≦ 15.0	0	0	0	0	0
	15.0 ＜ HE	0	0	0	0	0
Total number of persons (A)		403	468	571	573	744
Exposure above 1mSv	Number of persons (B)	0	0	0	0	0
	(B)/(A)×100(%)	0	0	0	0	0
Mass effective dose (Person･mSv)		0.1	0.2	0.3	0.4	1.0
Mean dose (mSv)		0.00	0.00	0.00	0.00	0.01
Maximum dose (mSv)		0.1	0.2	0.2	0.2	0.4

*1 The dose by the internal exposure was not detected.

(2) Individual monitoring for the visitors and others

Table 2 shows the number of people who temporarily entered the radiation controlled areas. The effective doses of all people were less than 0.1 mSv.

Table 2

The number of people who temporarily entered the radiation controlled areas in FY 2020.

Periods	1st quarter	2nd quarter	3rd quarter	4th quarter	Total
Number of persons	119	230	419	256	1,024

Monitoring of radioactive gases and dusts

Table 3 shows the maximum radioactive concentrations and total activities for radioactive gases released from the stack of TIARA, during each quarter of FY 2020.

Small amounts of ^{41}Ar, ^{11}C, ^{77}Br and ^{131}I were detected occasionally during the operation of the cyclotron or experiments, but the particulate substances (^{65}Zn, etc.) were not detected.

Table 3

Monitoring results of released radioactive gases and dust in FY 2020.

Nuclide	Periods / Items	1st quarter	2nd quarter	3rd quarter	4th quarter	Total
^{41}Ar	Maximum concentration	$<1.2\times10^{-4}$	$<1.2\times10^{-4}$	$<1.2\times10^{-4}$	$<1.2\times10^{-4}$	
	Activity	0	0	0	9.1×10^{7}	9.1×10^{7}
^{11}C	Maximum concentration	$<1.2\times10^{-4}$	—	$<1.2\times10^{-4}$	$<1.2\times10^{-4}$	
	Activity	7.7×10^{7}	—	1.9×10^{8}	2.4×10^{8}	5.1×10^{8}
^{77}Br	Maximum concentration	—	—	—	3.8×10^{-9}	
	Activity	—	—	—	6.4×10^{4}	6.4×10^{4}
^{131}I	Maximum concentration	1.0×10^{-8}	—	—	—	
	Activity	1.7×10^{5}	—	—	—	1.7×10^{5}
^{65}Zn	Maximum concentration	$<6.5\times10^{-10}$	$<9.4\times10^{-10}$	$<6.5\times10^{-10}$	$<6.9\times10^{-10}$	
	Activity	0	0	0	0	0

Unit : Bq/cm^3 for Maximum concentration, Bq for Activity.

Monitoring for external radiation and surface contamination

The monitoring for external radiation and surface contamination was routinely performed in/around the radiation controlled areas. Neither anomalous value of dose equivalent rate nor surface contamination was detected.

Figure 1 shows a typical example of distribution of the dose equivalent rate in the radiation controlled area of the cyclotron building.

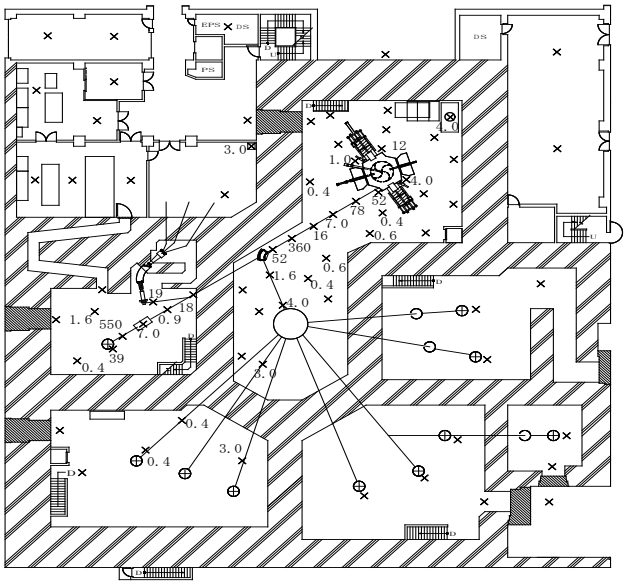

Fig. 1. Dose equivalent rate distribution in the radiation controlled area of the cyclotron building.
Measurement date : 9th and 23th March 2021,
Measuring position : Indicated with × (1 m above floor),
Unit : μSv/h.(The values are not indicated if less than 0.2 μSv/h.)

4 - 07 Radioactive waste management in TIARA

N. Higuchi

Department of Administrative Services, TARRI, QST

Radioactive waste management

The radioactive waste generated in TIARA is managed by Utilities and Maintenance Section. The main radioactive waste is the solid waste generated from research experiments and the maintenance of the cyclotron. Other radioactive waste is the liquid waste such as inorganic waste fluids generated from research experiments and the air-conditioning machines in the radiation controlled area. These wastes are managed according to their properties. Radioactive waste is stored in a storage facility and handed over to the Japan Radioisotope Association for disposal.

Solid radioactive waste

Table 1 shows the amounts of various types of solid waste generated in each quarter of FY 2020. Combustible waste consists of papers and clothes, and so on. Flame-retardant waste consists of rubber gloves, plastic articles, and polyethylene articles. Incombustible waste consists of metal pieces, the glasses, and contaminated parts. Solid waste emitting α, β, and γ is classified according to the properties.

Liquid radioactive waste

Table 2 shows the amounts of liquid waste generated in each quarter of FY 2020. Most of liquid waste was inorganic waste water generated from chemical experiments and others were condensed water going out of the air-conditioner installed in the radiation controlled area. The largest amount of waste water in summer season (2nd quarter) was the condensed water. After the treatment of evaporation of the waste water, inorganic water is reused in the radiation controlled area. Only small amounts of concentrated liquid were generated by the treatment.

Table 1
Radioactive solid waste generated in FY 2020.

Items \ Amounts	Amounts of generation in each period (m^3)					Number of package /drum
	1st quarter	2nd quarter	3rd quarter	4th quarter	Total	
Category β, γ*	0	0	0.26	0.32	0.58	14 **
Combustible	0	0	0.08	0.08	0.16	4 **
Flame-retardant	0	0	0.12	0.12	0.24	6 **
Incombustible(Compressible)	0	0	0.06	0.12	0.18	4 **
〃 (Incompressible)	0	0	0	0	0	0
Laboratory animal	0	0	0	0	0	0
Filters	0	0	0	0	0	-
Category α*	0	0	0	0.14	0.14	0
Combustible	0	0	0	0.02	0.02	0
Flame-retardant	0	0	0	0.08	0.08	0
Incombustible(Compressible)	0	0	0	0.02	0.02	0
〃 (Incompressible)	0	0	0	0	0	0
Laboratory animal	0	0	0	0.02	0.02	0
Filters	0	0	0	0	0	-

* defined by amount in Bq (β, γ): ≤2 GBq , (α) : ≤37 MBq,
** 50-liter drum.

Table 2
Radioactive liquid waste generated in FY 2020.

Items \ Amounts	Amounts of generation in each period (m^3)					Number of package /drum
	1st quarter	2nd quarter	3rd quarter	4th quarter	Total	
Category β, γ*	15.56	20.06	4.76	2.66	43.04	-
1)Inorganic	15.56	20.06	4.76	2.66	43.04	-
Inorganic	15.56	20.06	4.76	2.66	43.04	treatment
Sludge, Evaporation residue	0.00	0.00	0.00	0.00	0.00	0
2)Organic	0.00	0.00	0.00	0.00	0.00	0
Organic	0.00	0.00	0.00	0.00	0.00	0
Oil	0.00	0.00	0.00	0.00	0.00	0
Category α*	0.00	0.00	0.00	0.00	0.00	0

* defined by concentrations in Bq/mL (β, γ Inorganic) : ≤200 kBq, (Organic) : <2 kBq, (α) : ≤1.85 kBq.

4 - 08 Facility Use Program in Takasaki Advanced Radiation Research Institute

S. Nozawa, H. Hanaya and M. Seki

Department of Research Planning and Promotion, QuBS, QST

Irradiation facilities in Takasaki Advanced Radiation Research Institute (TARRI) has been opened to many researchers in universities, public institutes, R&D divisions of private companies (hereafter 'external users'), under Facility Use Program.

Under this program, external users can use the gamma-rays, electron beams, and ion beams provided from facilities of Co-60 gamma-ray, electron accelerator, TIARA's four ion accelerators, and off-line analytical instruments. When using these facilities, external users are required to bear the operating costs of irradiation equipment.

Facility Use Program in FY2020

In Pricing system of Facility Use Program, experimental costs have been calculated from the total amount of service charge, irradiation charge, and extra-costs (ex. additional consumable goods and human support).

Research-and-development's (R&D's) users, who disclose the experiment results by publication, had been partially discounted for the experimental costs. To receive this discount, users were required to submit a research proposal to Research Planning and Promotion Office in TARRI. The proposals were reviewed by the expert committee members in terms of the effectiveness of experimental designs. The approved proposals have been implemented under Facility Use Program with the partially discounted cost. In FY2020, this discount was not applied at gamma-ray irradiation facilities and electron accelerator.

Number of irradiation experiments under Facility Use Program

Number of irradiation experiments under Facility Use Program in FY2020 were shown in Table 1. The number of experiments in Co-60 gamma-ray irradiation facilities was much higher than other facilities. The number of experiments aggregated by user's affiliation were shown in Table 2. AVF cyclotron and 3 MV tandem accelerator were mainly used by researchers who belonging to universities. On the other hand, most of the users of the Co-60 gamma ray irradiation facilities were private companies.

Additional information about this program is available at the following QST website:

https://www.qst.go.jp/site/qubs/1954.html

Table 1

Number of irradiation experiments under the Facility Use program in FY2020.

Irradiation Facility \ Pricing System		Public Disclosure	Non Disclosure	Total
TIARA	AVF cyclotron	10	10	20
	3 MV tandem accelerator	11	18	29
	3 MV single-ended accelerator	5	1	6
	400 kV ion implanter	13	7	20
Co-60 gamma-ray irradiation facilities		-*	185	185
Electron accelerator		-*	9	9
Total		39	230	269

*: Discounting by public disclosure was not applied

Table 2

Number of irradiation experiments by user's affiliations.

Irradiation Facility \ User's affiliation		University	Public Institute	Private Company	Total
TIARA	AVF cyclotron	14	2	4	20
	3 MV tandem accelerator	19	6	4	29
	3 MV single-ended accelerator	0	6	0	6
	400 kV ion implanter	7	12	1	20
Co-60 gamma-ray irradiation facilities		32	22	131	185
Electron accelerator		6	0	3	9
Total		78	48	143	269

Appendices

Appendix 1 Publication List

Items in gray show the works in collaboration with other projects of QST.
Bold letters and **numbers** at the last of each item mean as follows.
Letter : Accelerators or irradiation facilities used for the work.
C : Cyclotron, **T** : Tandem accelerator, **S** : Single-ended accelerator, **I** : Ion implanter,
E : Electron accelerator, **G** : Gamma-ray irradiation facilities, **N** : Not used.
Number with hyphen: Serial number of the related paper in Part II.

P1-1 Project "Functional Polymer"

Papers

1) T. D. Tap, L. L. Nguyen, S. Hasegawa, S. Sawada, L. Q. Luan and Y. Maekawa, "Internal and interfacial structure analysis of graft-type fluorinated polymer electrolyte membrane by small angle X-ray scattering in the high-q range", J. Appl. Polym. Sci. **137**, 49029 (2020). **G, 1-02**

2) Y. Maekawa, M. Washio, "Quantum beams applying to innovative industrial materials", Quantum Beam Science **4**, 27 (2020). **N**

3) S. Hasegawa, S. Sawada, S. Azami, T. Hagiwara, A. Hiroki and Y. Maekawa, "Development of hydrogen-permselective porous membranes using radiation-induced graft polymerization", Quantum Beam Science **4**, 23 (2020). **G, 1-01**

4) Y. Zhao, K. Yoshimura, A. M. S. Mahmoud, H. C. Yu, S. Okushima, A. Hiroki, Y. Kishiyama, H. Shishitani, S. Yamaguchi, H. Tanaka, Y. Noda, S. Koizumi, A. Radulescu and Y. Maekawa, "A long side chain imidazolium-based graft-type anion-exchange membrane: novel electrolyte and alkaline-durable properties and structural elucidation using SANS contrast variation", Soft Matter **16**, 8128-8143 (2020). **G, 1-02**

5) M. M. Schiavone, D. H. Lamparelli, Y. Zhao, F. Zhu, Z. Revay and A. Radulescu, "The effects of temperature and humidity on the microstructure of sulfonated syndiotactic–polystyrene ionic membranes", Membranes **10**, 00187 (2020). **N**

6) A. M. A. Mahmoud, K. Yoshimura and Y. Maekawa, "Alkaline fuel cells consisting of imidazolium-based graft-type anion exchange membranes: Optimization of fuel cell conditions to achieve high performance and durability", J. Membr. Sci. **620,** 118844 (2021). **G, 1-02**

7) Beom-Seok Ko, K. Yoshimura, A. Hiroki and Y. Maekawa, "Mechanistic study on radiation-induced grafting into fluorinated polymer solid films using a swelling-induced detachment of grafted polymers", J. Polym. Sci. **59**, 108-116 (2021). **G, 1-02**

8) S. Sawada, T. Kimura, H. Nishijima, T. Kodaira, N. Tanaka, S. Kubo, S. Imabayashi, M. Nomura and T. Yamaki, "Overvoltage reduction in membrane Bunsen reaction for hydrogen production by using a radiation-grafted cation exchange membrane and porous Au anode", Int. J. Hydrogen Energy **45**, 13814-13820 (2020). **G**

9) S. Sawada, T. Yamaki and H. Koshikawa, "Creation of Nanostructured-Controlled Functional Membranes Using High-Energy Ion Beams", Salt Seawater Sci. Technol. **1**, 61-73 (2021). **C, 1-13**

10) M. Ishino, T. Dinh, Y. Hosaka, N. Hasegawa, K. Yoshimura, H. Yamamoto, T. Hatano, T. Higashiguchi, K. Sakaue, S. Ichimaru, M. Hatayama, A. Sasaki, M. Washio, M. Nishikino and Y. Maekawa, "Soft x-ray laser beamline for surface processing and damage studies", Applied Optics **59**, 3692-3698 (2020). **N**

Proceedings

1) 澤田 真一, 坂本 有希子, 田中 健一, 船津 公人,前川 康成, "機械学習法によるグラフト型電解質膜の導電率・含水率の予測", 第 69 回高分子討論会, [オンライン] 要旨集, 3G07 (2020). **G, 1-02**

2) 長谷 川 伸, 廣木 章博, 吉村 公男, ザオ ユエ, 町田 晃彦, 大和田 謙二, 前川 康成, "溶媒アニールによるポリエーテルエーテルケトン膜のモルフォロジー制御と 放射線グラフト重合反応加速機構", 第69回高分子討論会, [オンライン] 要旨集, PA0803 (2020). **G, 1-02**

3) 髙松 治文, 吉村 公男, 廣木 章博, 前川 康成, "アルカリ耐性アニオン伝導電解質膜の創製研究", 第 63 回放射線化学討論会, [オンライン] 要旨集, 2P-11 (2020). **G, 1-02**

4) 坂本有希子, 澤田真一, 廣木章博, 前川康成, "機械学習に基づくグラフト型電解質膜の機能性評価", 令和 2 年度日本化学会関東支部群馬地区研究交流発表会, [オンライン] 要旨集, P006 (2020). **G, 1-02**

5) 阿部 聖賢, 吉村 公男, 廣木 章博, 前川 康成, "フッ素系高分子基材へのビニルモノマーの放射線グラフト重合 ～機械学習に基づく重合予測～", 令和 2 年度日本化学会関東支部群馬地区研究交流発表会, [オンライン] 要旨集, P021 (2020). **G, 1-02**

6) 髙松 治文, 吉村 公男, 廣木 章博, 前川 康成, "アルカリ耐性アニオン伝導電解質膜の創製研究", 令和 2 年度日本化学会関東支部群馬地区研究交流発表会, [オンライン] 要旨集, P036 (2020). **G, 1-02**

7) 柴田 康瑛, 長谷川 伸, 廣木 章博, 木下 基, 前川 康成, "ポリフェニレンスルフィドを基材とした放射線グラフト重合における基材膜の結晶モルフォロジーと重合性・機能", 令和2年度日本化学会関東支部群馬地区研究交流発表会, [オンライン] 要旨集, P047 (2020). **G, 1-02**

8) 髙松 治文, 吉村 公男, 廣木 章博, 前川 康成, "イミダゾリウム基を有する放射線グラフト型アニオン伝導膜の電解質膜特性と階層構造の関係", 第 101 回日本化学会春季年会, [オンライン] 要旨集, P02-2vn-23 (2021). **G, 1-02**

P1-2 Project “Advanced Catalyst”

Papers

1) N. Tanaka, S. Sawada, T. Yamaki, T. Kodaira, T. Kimura and M. Nomura, “Improvement of HI concentration performance for hydrogen production iodine-sulfur process using crosslinked cation-exchange membrane”, Chem. Eng. Sci. **237**, 116575 (2021). **E, G, 1-12**

2) S. Sawada, T. Yamaki and H. Koshikawa, “Creation of nanostructure-controlled functional membranes using high-energy ion beams”, Salt Seawater Sci. Technol. **1**, 61-73, (2021). **C, 1-13**

3) A. Yabuuchi, T. Ozaki, H. Sakane, H. Okazaki, H. Koshikawa, S. Yamamoto and T. Yamaki, “Characterization of the effect of ion irradiation on industrially produced $GdBa_2Cu_3O_{7-\delta}$ superconducting tapes using a slow positron beam”, Appl. Phys. Express **13**, 123004, (2021). **T, 1-09**

4) T. Sakurai, S. Sakaguchi, Y. Takeshita, K. Kayama, A. Horio, M. Sugimoto, T. Yamaki, A. Chiba, S. Yuuichi, L.B.V.S. Garimella, D.K. Avasthi and S. Seki, “Porphyrin nanowire bundles for efficient photoconductivity, photoemission and generation of singlet oxygens toward photodynamic therapy”, ACS Appl. Nano Mater. **3**, 6043-6053 (2020). **C, 1-07**

5) Y. Shimizu, H. Koshikawa, M. Imbe, T. Yamaki and K. Amemiya, “Large-area perfect blackbody sheets having aperiodic array of surface micro-cavities for high-precision thermal imager calibration”, Opt. Exp. **28**, 22606-22616 (2020). **C, 1-11**

6) S. Sawada, N. Tanaka, S. Kubo, S. Imabayashi, M. Nomura and T. Yamaki, “Overvoltage reduction in membrane Bunsen reaction for hydrogen production by using a radiation-grafted cation exchange membrane and porous Au anode”, Int. J. Hydrogen Energy **45**, 13814-13820 (2020). **E, G**

7) N. Nakagawa, H. Ishitobia, S. Abe, M. Kakinuma, H. Koshikawa, S. Yamamoto and T. Yamaki, “A novel method to enhance the catalytic activity of PtRu on the support using CeO_2 by high-energy ion-beam irradiation”, Catal. Today **364**, 118-124 (2021). **C, 1-04**

8) S. Chauhan, T. Mori, T. Kobayashi, S. Yamamoto, S. Ito, G. Auchterlonie, R. Wepf, S. Ueda and F. Ye, “Surface layer of Pt-O-Ce bonds on CeO_x nanowire with high ORR activity converted by proton beam irradiation”, J. Am. Ceram. Soc. **104**, 1945-1952 (2021). **T, S**

9) T. Taguchi, S. Yamamoto and H. Oba, “Synthesis and formation mechanism of novel double-thick-walled silicon carbide nanotubes from multiwalled carbon nanotubes”, App. Surf. Sci. **551**, 149421 (2021). **I, 1-30**

10) H. Amekura, M. Toulemonde, K. Narumi, R. Li, A. Chiba, Y. Hirano, K. Yamada, S. Yamamoto, N. Ishikawa, N. Okubo and Y. Saitoh, “Ion tracks in silicon formed by much lower energy deposition than the track formation threshold”, Sci. Rep. **11**, 185 (2021). **T, 3-10**

11) K. Kamiya, K. Kayama, M. Nobuoka, S. Sakaguchi, T. Sakurai, M. Kawata, Y. Tsutsui, M. Suda, A. Idesaki, H. Koshikawa, M. Sugimoto, G.B.V.S. Lakshmi, D.K. Avasthi and S. Seki, “Ubiquitous organic molecule-based free-standing nanowires with ultra-high aspect ratios”, Nat. Commun. **12**, 4025 (2021). **C, 1-07**

Proceedings

1) 小牟田 啓子, 八巻 徹也, 澤田 真一, 越川 博, 垣花 百合子, 安川 政宏, 比嘉 充, “イオン飛跡グラフト重合法を用いて作製したイオン交換膜の特性評価”, 日本膜学会第 42 年会, [web], P-20S (2020). **C**

2) 宮下 太志, 野村 幹弘, 澤田 真一, 越川 博, 八巻 徹也, “重イオンビームによる低膨潤イオン交換膜の開発”, 日本膜学会第 42 年会, [web], P-37S (2020). **C, 1-13**

3) 尾崎 壽紀, 柏原 卓弥, 久保 友幸, 千星 聡, 末吉 哲郎, 岡﨑 宏之, 越川 博, 山本 春也, 八巻 徹也, 坂根 仁, “低エネルギーAu イオン照射した $GdBa_2Cu_3O_y$ 線材の超伝導特性”, 第 81 回応用物理学会秋季学術講演会, [web], 9a-Z27-1 (2020). **T, 1-09**

4) 薮内 敦, 木野村 淳, 尾崎 壽紀, 坂根 仁, 岡﨑 宏之, 越川 博, 山本 春也, 八巻 徹也, “イオン照射 $GdBa_2Cu_3O_{7-\delta}$超伝導テープ線材の低速陽電子ビームによる評価”, 第 81 回応用物理学会秋季学術講演会, [web], 9a-Z27-2 (2020). **T, 1-09**

5) 宮下 太志, 野村 幹弘, 澤田 真一, 越川 博, 八巻 徹也, “イオン飛跡グラフト重合法によるヨウ化水素濃縮用カチオン交換膜の開発”, 化学工学会第 51 回秋季大会, [web], S321 (2020). **C, 1-13**

6) H. Okazaki, A. Idesaki, H. Koshikawa, S. Yamamoto, D. Matsumura and T. Yamaki, “The electronic state of Pt nanoparticles on an ion-beam-irradiated carbon support”, Pacific Rim Meeting on Electrochemical and Solid State Science (PRiME) 2020, [web], I01D-2330 (2020). **I, 1-15**

7) T. Yamaki, “Ion beam technology: development of functional nanomaterials for future hydrogen energy and fuel cells”, The 2020 International Conference on Nuclear Science, Technology, and Application, [web], Keynote Speaker 05 (2020). **I, S, C, E, G, 1-13, 1-15**

8) T. Ozaki, T. Kashihara, T. Kubo, S. Semboshi, T. Sueyoshi, H. Okazaki, H. Koshikawa, S. Yamamoto, T. Yamaki and H. Sakane, “Critical current properties in $GdBa_2Cu_3O_y$ superconducting films irradiated with low-energy Au-ions”, The 30th Annual Meeting of MRS-J, [web], F-O10-003 (2020). **T, 1-09**

9) N. Nakagawa, H. Ishitobi, S. Abe, M. Kakinuma, H. Koshikawa, S. Yamamoto and T. Yamaki, “Activation of electrode catalyst for direct methanol fuel cells by high-energy ion-beam irradiation”, The 30th Annual Meeting of MRS-J, [web], F-O10-005 (2020). **C**

10) T. Miyashita, M. Nomura, S. Sawada, H. Koshikawa and T. Yamaki, “Development of cation exchange membranes for electrodialysis by ion beam technology”, The 30th Annual Meeting of MRS-J, [web], F-O10-006 (2020). **C, 1-13**

11) H. Okazaki, S. Yamamoto, H. Koshikawa, T. Taguchi, A. Idesaki and T. Yamaki, “The suppression of oxidative corrosion of carbon by structural change due to ion irradiation”, The 30th Annual Meeting of MRS-J, [web], F-O10-008 (2020). **I, 1-15**

12) S. Yamamoto, H. Koshikawa, T. Taguchi, A. Idesaki, H. Okazaki and T. Yamaki, “Synthesis of precious metal nanoparticles inside ion-track-etched capillaries formed in polyimide films”, The 30th Annual Meeting of MRS-J, [web], F-P10-001 (2020). **C,E,G, 1-05**

13) A. Idesaki, S. Yamamoto, M.Sugimoto and T. Yamaki, "The study of multi energy-ion implantation technique for uniform introduction of fine Fe nanoparticles into a phenolic resin", The 30th Annual Meeting of MRS-J, [web], F-P10-003 (2020). **I**

14) H. Okazaki, A. Idesaki, H. Koshikawa, D. Matsumura, S. Yamamoto and T. Yamaki, "The interaction changes of between Pt nanoparticle catalyst and the carbon support by the ion irradiation", The QST International Symposium －Innovation from Quantum Materials Science－, [web], 4-11 (2020). **I, 1-15**

15) K. Takeuchi, T. Yamaki, S. Sawada, K. Koshikawa, Y. Yasukawa, Y. Kakihana and M. Higa, "Preparation and characterization of charged mosaic membranes by two-step ion-track graft polymerization method", 12th International Congress on Membranes and Membrane Processes (ICOM 2020), [web], P3.024 (2020). **C**

16) K. Komuta, M. Goto, T. Yamaki, S. Sawada, H. Koshikawa, A. Kitamura, Y. Kakihana, M. Yasukawa and M. Higa, "Preparation and characterization of ion-exchange membranes by ion-track graft polymerization technique", 12th International Congress on Membranes and Membrane Processes (ICOM 2020), [web], P3.025 (2020). **C**

17) 岡崎　宏之, 出崎　亮, 松村 大樹, 越川 博, 山本 春也, 八巻 徹也, "イオン照射カーボン担持 Pt ナノ粒子の弱い酸素吸着", 第 34 回日本放射光学会年会・放射光科学合同シンポジウム, [web], 6B002 (2021). **I, 1-15**

18) 岡崎 宏之, 出崎 亮, 越川 博, 松村 大樹, 山本 春也, 八巻 徹也, "イオン照射カーボン担持 Pt ナノ粒子触媒の in situ XAFS 測定 ～酸素吸着状態の変化～", 電気化学会第 88 回大会, [web], 2K02 (2021). **I, 1-15**

19) 亀田 菜摘, 中村 将志, 出崎 亮, 山本 春也, 星 永宏, "金属ドープ TiO_2 単結晶電極上の酸素還元反応の活性化因子", 電気化学会第 88 回大会, [web], 2K05 (2021). **I**

Book

1) 根来 誠, 八巻 徹也, "序章 第二次量子革命における量子センシング", 量子センシングハンドブック ～量子科学が切り拓く新たな領域～, (株) エヌ・ティー・エス, 1-7 (2021).

Patent

1) 山本 春也, 齋藤 寛之, 田口 富嗣, 八巻 徹也, "合金、水素取出システム、水素吸蔵材、および合金の製造方法", 出願 2020-183096 (2020.10.30).

Press・TV

1) "熱利用水素製造の主反応の大幅な省エネルギー化に成功 ～国家プロジェクトの目標値である水素製造効率 40%の達成に見通し～", 2020.04.17, プレス発表: 日刊工業新聞, 電気新聞, 原子力産業新聞, 新エネルギー新聞, OPTRONICS ONLINE, fabcross for エンジニア, テック・アイ技術情報研究所に掲載 **E, G**

P1-3 Project "Positron Nanoscience"

Papers

1) M. Maekawa, K. Wada, A. Miyashita and A. Kawasuso, "Construction of a Spin-Polarized Positronium Time-of-Flight Measurement Apparatus", Acta Physica Polonica A **137**, 105-108 (2020). **N**

2) A. Miyashita, S. Li, S. Sakai, M. Maekawa and A. Kawasuso, "Spin polarization of graphene on Co2FeGe0.5Ga0.5(001) observed by spin-polarized surface positronium spectroscopy", Phys. Rev. B **102**, 045425 (2020). **N**

3) M. Maekawa, A. Miyashita, S. Sakai and A. Kawasuso, "Gadolinium-implanted GaN studied by spin-polarized positron annihilation spectroscopy", Phys. Rev. B **102**, 054427 (2020). **I, 1-17**

4) K. Wada, M. Maekawa, I. Mochizuki, T. Shidara, A. Kawasuso, M. Kimura and T. Hyodo, "A pulse stretcher for a LINAC-based pulsed slow-positron beam providing a quasi-continuous beam with an energy of 5.2 keV", Nucl. Instrum. Meth. Phys. Res. A **975**, 164161 (2020). **N**

5) T. Yamada, A. Takano, K. Sugita, A. Iwase, M. Maekawa and A. Kawasuso, "Effect of dual implantation with Ag and Ni ions on the optical absorption of silica glass", Transactions of the Materials Research Society of Japan **45**, 138 (2020). **I, 1-16**

6) M. Maekawa, K. Wada and A. Kawasuso, "Development a new positron source for spin-polarized positron beam generation", Nucl. Instrum. Meth. Phys. Res. B **240**, 49 (2020). **N**

7) A Kawasuso, K. Wada A. Miyashita M. Maekawa H. Iwamori, S. Iida and Y Nagashima, "Positronium formation at 4H SiC(0001) surfaces", J. Phys.: Condens. Matter **33**, 035006 (2021). **N**

8) M. Maekawa, A. Miyashita, S. Sakai S. Li, S. Entani, A. Kawasuso and Y. Sakuraba, "Spin-Polarized Positronium Time-of-Flight Spectroscopy for Probing Spin-Polarized Surface Electronic States", Phys. Rev. Lett. **126**, 186401 (2021). **N**

Proceedings

1) A. Kawasuso, "Spintronics Materials Studied by Spin-polarized Positron Beam", **【Invited talk】**, QST Intetnational Symposium, November 4-6, 2020, Takasaki, Japan (WEB) **N**

2) M. Maekawa, A. Miysshita and A. Kawasuso, "Development of spin-polarized positronium time-of-flight spectroscopy", QST Intetnational Symposium, November 4-6, 2020, Takasaki, Japan (WEB) **N**

3) K. Wada, T. Shirasawa, I. Mochizuki, M. Maekawa, A. Kawasuso and T. Hyodo, "Development of a low-energy positron diffraction apparatus with a three-layer delay-line anode detector", QST Intetnational Symposium, November 4-6, 2020, Takasaki, Japan (WEB) **N**

4) 河裾 厚男, "偏極陽電子を用いたスピントロニクス関連物質の評価"、公益社団法人日本磁気学会第 75 回スピントロニクス専門研究, (2020.07.22) **N**

5) 前川 雅樹, 宮下 敦己, 河裾 厚男, "スピン偏極ポジトロニウム放出エネルギー測定による表面電子スピンのエネルギー分解", 日本物理学会 2020 年秋季大会, (2020.09.08). **N**

6) 山田 智子, 前川 雅樹, 河裾 厚男, 千星 聡, 正橋 直哉, 岩瀬 彰宏, 松井 利之, 田口 昇, 田中 真悟, 堀 史説, "Ag および Ni イオンの二重照射による SiO_2 中のナノ粒子の形成",日本物理学会 2020 年秋季大会, (2020.09.08). **I, 1-16**

7) 堀 史説, 鷹野 陽弘, 金野 泰幸, 和田 武, 加藤 秀実, 石川 法人,喜多村 茜, 河裾 厚男, 前川 雅樹、“重イオン照射による Zr 系金属間化合物の非晶質化”, 日本物理学会 2020 年秋季大会, (2020.09.09). **I, 1-16**

8) 河裾 厚男、宮下 敦巳, 前川 雅樹, 和田 健, 飯田 進平, 岩森 大直, 長嶋 泰之, “半導体表面におけるポジトロニウム生成”, 京都大学複合原子力科学研究所専門研究会「陽電子科学とその理工学への応用」, (2020.12.11). **N**

9) 宮下 敦巳, 前川 雅樹、河裾 厚男, “第一原理バンド計算による表面ポジトロニウム分光解析”、京都大学複合原子力科学研究所専門研究会「陽電子科学とその理工学への応用」, (2020.12.11). **N**

10) 前川 雅樹, 宮下 敦巳, 河裾 厚男, “スピン偏極ポジトロニウム放出エネルギー測定法によるエネルギー分解表面電子スピン測定”, 京都大学複合原子力科学研究所専門研究会「陽電子科学とその理工学への応用」, (2020.12.11). **N**

P1-4 Project “Semiconductor Radiation Effects”

Papers

1) V. Ivády, H. Zheng, A. Wickenbrock, L. Bougas, G. Chatzidrosos, K. Nakamura, H. Sumiya, T. Ohshima, J. Isoya, D. Budker, I. A. Abrikosov and A. Gali, “Photoluminescence at the ground-state level anticrossing of the nitrogen-vacancy center in diamond: A comprehensive study”, Phys. Rev. B **103**, 035307-1-13 (2021). **E**

2) Z. Shang, Y. Berencén, M. Hollenbach, S. Zhou, H. Kraus, T. Ohshima and G.V. Astakhov, “Microwave-assisted spectroscopy of vacancy-related spin centers in hexagonal SiC”, Phys. Rev. Appl. **15**, 034059-1-9 (2021). **E**

3) K. Miyanishi, T. F. Segawa, K. Takeda, I. Ohki, S. Onoda, T. Ohshima, H. Abe, H. Takashima, S. Takeuchi, A. I. Shames, K. Morita, Y. Wang, F. T.-K. So, D. Terada, R. Igarashi, A. Kagawa, M. Kitagawa, N. Mizuochi, M. Shirakawa and M. Negoro, “Room-temperature hyperpolarization of polycrystalline samples with optically polarized triplet electrons: pentacene or nitrogen-vacancy center in diamond?”, Magn. Reson. **2**, 33-48 (2021). **E**

4) Y. Masuyama, K. Suzuki, A. Hekizono, M. Iwanami, M. Hatano, T. Iwasaki and T. Ohshima, “Gradiometer using separated diamond quantum magnetometers”, Sensors **21**, 977-1-11 (2021). **E**

5) T. Kitaizumi, A. Kuwahata, K. Saichi, T. Sato, R. Igarashi, T. Ohshima, Y. Masuyama, T. Iwasaki, M. Hatano, F. Jelezko, M. Kusakabe, T. Yatsui and M. Sekino, “Magnetic field generation system of the magnetic probe with diamond quantum sensor and ferromagnetic materials for the detection of sentinel lymph nodes with magnetic nanoparticles”, IEEE Trans. Magnetics **57**, 5100405-1-5 (2021). **E**

6) T. Narahara, S.-i. Sato, K. Kojima, Y. Hijikata and T. Ohshima, “Influences of hydrogen ion irradiation on $N_CV_{Si}^-$ formation in 4H-silicon carbide”, Appl. Phys. Express **14**, 021004-1-4 (2021). **C, I, T**

7) T. M. Hoang, H. Ishiwata, Y. Masuyama, Y. Yamazaki, K. Kojima, S.-Y. Lee, T. Ohshima, T. Iwasaki, D. Hisamoto and M. Hatano, “Thermometric quantum sensor using excited state of silicon vacancy centers in 4H-SiC devices”, Appl. Phys. Lett. **118**, 044001-1-5 (2021). **S, I, E**

8) Y. Hatano, J. Shin, D. Nishitani, H. Iwatsuka, Y. Masuyama, H. Sugiyama, M. Ishii, S. Onoda, T. Ohshima, K. Arai, T. Iwasaki and M. Hatano, “Simultaneous thermometry and magnetometry using a fiber-coupled quantum diamond sensor” Appl. Phys. Lett. **118**, 034001-1-6 (2021). **E**

9) Y. Yamazaki, Y. Chiba, S.-i. Sato, T. Makino, N. Yamada, T. Satoh, K. Kojima, Y. Hijikata, H. Tsuchida, N. Hoshino, S.-Y. Lee and T. Ohshima, “Carrier dynamics of silicon vacancies of SiC under simultaneous optically and electrically excitations”, Appl. Phys. Lett. **118**, 021106-1-6 (2021). **S, I**

10) S. Castelletto, J. Maksimovic, T. Katkus, T. Ohshima, B. C. Johnson and S. Juodkazis, “Color centers enabled by direct femtosecond laser writing in wide bandgap semiconductors”, Nanomaterials **11**, 72-1-17 (2021). **E**

11) R. Bernat, I. Capan, L. Bakrač, T. Brodar, T. Makino, T. Ohshima, Ž. Pastuović and A. Sarbutt, “Response of 4H-SiC Detectors to Ionizing Particles”, Crystals **11**, 10-1-14 (2021). **E**

12) F. M. Sturner, A. Brenneis, T. Buck, J. Kassel, R. Rolver, T. Fuchs, A. Savitsky, D. Suter, Jens Grimmel, S. Hengesbach, M. Fortsch, K. Nakamura, H. Sumiya, S. Onoda, J. Isoya and F. Jelezko, “Integrated and Portable Magnetometer Based on Nitrogen-Vacancy Ensembles in Diamond”, Adv. Quantum Technol. **10**, 2000111-1-11 (2021). **E**

13) L. Q. Zhou, R. L. Patel, A. C. Frangeskou, A. Nikitin, B. L. Green, B. G. Breeze, S. Onoda, J. Isoya and G. W. Morley, “Imaging Damage in Steel Using a Diamond Magnetometer”, Phys. Rev. Appl. **15**, 024015-1-10 (2021). **E**

14) S. R. Nair, L. J. Rogers, X. Vidal, R. P. Roberts, H. Abe, T. Ohshima, T. Yatsui, A. D. Greentree, J. Jeske and T. Volz, “Amplification by stimulated emission of nitrogen-vacancy centres in a diamond-loaded fibre cavity”, Nanophotonics **9**, 4505 (2020). **E**

15) V. Guarino, I. Cruz-Maya, P. Reineck, H. Abe, T. Ohshima, K. Fox, A. D. Greentree, B. C. Gibson, L. Ambrosio, “Fluorescent Nanodiamonds Embedded in Poly-ε-Caprolactone Fibers as Biomedical Scaffolds”, ACS Appl. Nano Mater. **3**,10814 (2020). **E**

16) J. Coutinho, V. J.B. Torres, I. Capan, T. Brodar, Z. Ereš, R. Bernat, V. Radulović, K. Ambrožič, L. Snoj, Ž. Pastuović, A. Sarbutt, T. Ohshima, Y. Yamazaki, T. Makino, “Silicon Carbide Diodes for Neutron Detection”, Nucl. Instrum. Meth. Phys. Res A **986**, 164793-1-15 (2020). **N**

17) A. I. Shames, A. Dalis, A. D. Greentree, B. C. Gibson, H. Abe, T. Ohshima, O. Shenderova, A. Zaitsev and P. Reineck, “Near-infrared fluorescence from silicon- and nickel-based color centers in high-pressure high-temperature diamond micro- and nanoparticles”, Advanced Optical Materials **8**, 2001047 (2020). **E**

18) P. Reineck, A. N. Abraham, A. Poddar, R. Shukla, H. Abe, T. Ohshima, B. C. Gibson, C. Dekiwadia, J. J. Conesa, E. Pereiro, A. Gelmi and G. Bryant, “Multimodal Imaging and Soft X-Ray Tomography of Fluorescent Nanodiamonds in Cancer Cells”, Biotechnology J. **16**, 2000289-1-8 (2021). **E**

19) S.-W. Jeon, J. Lee, H. Jung, Sa.-W. Han, Y.-W. Cho, Y.-S. Kim, H.-T. Lim, Y. Kim, M. Niethammer, W. C. Lim, J. Song, S. Onoda,

T. Ohshima, R. Reuter, A. Denisenko, J. Wrachtrup and S.-Y. Lee, "Bright nitrogen-vacancy centers in diamond inverted nanocones", ACS Photonics **7**, 2739 (2020). **T**

20) S.-I. Sato, M. Deki, H. Watanabe, S. Nitta, Y. Honda, T. Nishimura, B. C. Gibson, A. D. Grenntree, H. Aamano and T. Ohshima, "Optical properties of neodymium ions in nanoscale regions of gallium nitride", Optical Materials Express 10, 2614-2623 (2020). **I, 1-19**

21) T. Brodar, L. Bakrac, I. Capan, T. Ohshima, L. Snoj, V. Radulovic and Z. Pastuovic, "Depth profile analysis of deep level defects in 4H-SiC introduced by radiation", Crystals **10**, 845-1-16 (2020). **N**

22) A. Bourassa, C. P. Anderson, K. C. Miao, M. Onizhuk, H. Ma, A. L. Crook, H. Abe, J. Ul-Hassan, T. Ohshima, N. T. Son, G. Galli and D. D. Awschalom, "Entanglement and control of single nuclear spins in isotopically engineered silicon carbide", Nat. Mater. **19**, 1319-1325 (2020). **E**

23) I. Capan, T. Brodar, Y. Yamazaki, Y. Oki, T. Ohshima, Y. Chiba, Y. Hijikata, L. Snoj and V. Radulovic, "Influence of neutron radiation on majority and minority carrier traps in n-type 4H-SiC", Nucl. Instrum. Meth. B **478**, 224 (2020). **N**

24) K. C. Miao, J. P. Blanton, C. P. Anderson, A. Bourassa, A. L. Crook, G. Wolfowicz, H. Abe, T. Ohshima and D. D. Awschalom, "Universal coherence protection in a solid-state spin qubit", Science **369**, 1493-1497 (2020). **E**

25) D. M. Lukin, A. D. White, R. Trivedi, M. A. Guidry, N. Morioka., C. Babin, Ö. O. Soykal, J. Ul-Hassan, N. T. Son, T. Ohshima, P. K. Vasireddy, M. H. Nasr, S. Sun, J.-P. W. MacLean, C. Dory, E. A. Nanni, J. Wrachtrup, F. Kaiser and J. Vučković, "Spectrally reconfigurable quantum emitters enabled by optimized fast modulation", npj Quantum Infor. **6**, 80-1-9 (2020). **E**

26) A. L. Crook, C. P. Anderson, K. C. Miao, A. Bourassa, H. Lee, S. L. Bayliss, D. O. Bracher, X. Zhang, H. Abe, T. Ohshima, E. L. Hu and D. D. Awschalom, "Purcell enhancement of a single silicon carbide color center with coherent spin control", Nano Lett. **20**, 3427-3434 (2020). **E**

27) Y. Chiba, Y. Yamazaki, S.-I. Sato, T. Makino, N. Yamada, T. Satoh, Y. Hijikata and T. Ohshima, "Enhancement of ODMR contrasts of silicon vacancy in SiC by thermal treatment", Mater. Sci. Forum **1004**, 337-342 (2020). **S**

28) Y. Yamazaki, Y. Chiba, S.I. Sato, T. Makino, N. Yamada, T. Satoh, K. Kojima, Y. Hijikata, H. Tsuchida, N. Hoshino, S.-Y. Lee and T. Ohshima, "Optically detected magnetic resonance study of 3D arrayed silicon vacancies in SiC pn diodes", Mater. Sci. Forum **1004**, 343-348 (2020). **S, I**

29) T. Narahara, S.-I. Sato, K. Kojima, Y. Yamazaki, Y. Hijikata and T. Ohshima, "Effects of nitrogen impurity concentration on nitrogen-vacancy center formation in 4H-SiC", Mater. Sci. Forum **1004**, 349 (2020). **I**

30) S.-i. Sato, T. Narahara, S. Onoda, Y. Yamazaki, Y. Hijikata, B. C. Gibson, A. D. Greentree and T. Ohshima, "Near infrared photoluminescence of $N_CV_{Si}^-$ centers in high-purity semi-insulating 4H-SiC irradiated with energetic charged particles", Mater. Sci. Forum **1004**, 355 (2020). **I**

31) Y. Abe, T. Umeda, M. Okamoto, S. Harada, Y. Yamazaki and T. Ohshima, "The effect of γ-ray irradiation on optical properties of single photon sources in 4H- SiC MOSFET", Mater. Sci. Forum **1004**, 361-366 (2020). **G**

32) A. Takeyama, K. Shimizu, T. Makino, Y. Yamazaki, S.-I. Kuroki, Y. Tanaka and T. Ohshima, "Radiation hardness of 4H-SiC JFETs in MGy Dose Ranges", Mater. Sci. Forum **1004**, 1109 (2020). **G**

33) N. T. Son, Q. D. Ho, K. Goto, H. Abe, T. Ohshima, B. Monemar, Y. Kumagai, T. Frauenheim and P. Deak, "Electron paramagnetic resonance and theoretical study of gallium vacancy in ß-Ga_2O_3", Appl. Phys. Lett. **117**, 032101-1-5 (2020). **E**

34) V. Radulovic, Y. Yamazaki, Z. Pastuovic, A. Sarbutt, K. Ambrozic, R. Bernat, Z. Eres, J. Coutinho, T. Ohshima, I. Capan and L. Snoj, "Silicon carbide neutron detector testing at the JSI TRIGA reactor for enhanced border and port security", Nucl. Instrum. Methods A **972**, 164122-1-8 (2020). **N**

35) S-i. Sato, M. Deki, T. Nishimura, H. Okada, H. Watanabe, S. Nitta, Y. Honda, H. Amano and T. Ohshima, "Photoluminescence properties of implanted praseodymium into gallium nitride at elevated temperatures", Nucl. Instrum. Meth. Phys. Res. B **479**, 7 (2020). **I, 1-19**

36) N. Morioka, C. Babin, R. Nagy, I. Gediz, E. Hesselmeier, D. Liu, M. Joliffe, M. Niethammer, D. Dasari, V. Vorobyov, R. Kolesov, R. Stohr, J. U-Hassan, N. T. Son, T. Ohshima, P. Udvarhelyi, G. Thiering, A. Gali, J. Wrachtrup and F. Kaiser, "Spin-controlled generation of indistinguishable and distinguishable photons from silicon vacancy centres in silicon carbide", Nat. Commun. **11**, 2516-1-8 (2020). **E**

37) P. Udvarhelyi, G. Thiering, N. Morioka, C. Babin, F. Kaiser, D. Lukin, T. Ohshima, J. U-Hassan, N. T. Son, J. Vuckovic, J. Wrachtrup and A. Gali, "Vibronic states and their effect on the temperature and strain dependence of silicon-vacancy qubits in 4H-SiC", Phys Rev. Appl. **13**, 054017-1-10 (2020). **E**

38) H. Zheng, Z. Sun, G. Chatzidrosos, C. Zhang, K. Nakamura, H. Sumiya, T. Ohshima, J. Isoya, J. Wrachtrup, A. Wickenbrock and D. Budker, "Microwave-free vector magnetometry with nitrogen-vacancy centers along a single axis in diamond", Phys. Rev. Appl. **13**, 0044023-1-9 (2020). **E**

39) K. Hayashi, Y. Matsuzaki, T. Ashida, S. Onoda, H. Abe, T. Ohshima, M. Hatano, T. Taniguchi, H. Morishita, M. Fujiwara and N. Mizuochi, "Experimental and theoretical analysis of noise strength and environmental correlation time for ensembles of nitrogen-vacancy centers in diamond", J. Phys. Soci. Jpn. **89**, 054708-1-6 (2020). **C**

40) C. Kasper, D. Klenkert, Z. Shang, D. Simin, A. Gottscholl, A. Sperlich, H. Kraus, C. Schneider, S. Zhou, M. Trupke, W. Kada, T. Ohshima, V. Dyakonov and G. V. Astakhov, "Influence of irradiation on defect spin coherence in silicon carbide", Phys. Rev. Appl. **13**, 044054-1-11 (2020). **E**

41) A. Kuwahata, T. Kitaizumi, K. Saichi, T. Sato, R. Igarashi, T. Ohshima, Y. Masuyama, T. Iwasaki, M. Hatano, F. Jelezko, M. Kusakabe, T. Yatsui and M. Sekino, "Magnetometer with nitrogen vacancy center in a bulk diamond for detecting magnetic nanoparticles in biomedical applications", Sci. Reports **10**, 2483-1-9 (2020). **E**

42) H. Zhou, J. Choi, S. Choi, R. Landig, A. M. Douglas, J. Isoya, F. Jelezko, S. Onoda, H. Sumiya, P. Cappellaro, H. S. Knowles, H. Park and M. D. Lukin, "Quantum metrology with strongly interacting spin systems", Phys. Rev. X **10**, 031003-1-9 (2020). **E**

43) S. Castelletto, F. A. Inam, S.-I. Sato and A. Boretti, "Hexagonal boron nitride: a review of the emerging material

platform for single-photon source and the spin-photon interface", Beilstein J. Nanotechnol. **11**, 740 (2020). **N**

44) K. Akiba, K. Tamehiro, K. Matsui, H. Ikegami and H. Minoda, "Cathodoluminescence of green fluorescent protein exhibits the redshifted spectrum and the robustness", Sci. Rep. **10**, 17342 (2020). **N**

Proceedings

1) M. Imaizumi, Y. Okuno, T. Takamoto, S.-I. Sato, T. Ohshima and T. Okamoto, "Displacement Damage Dose Analysis of Alpha-ray Degradation on Output of an InGaP Solar Cell", Proc. 47th IEEE Photovoltaic Specialists Conference (47th PVSC), [Online] (2020.06). **T, I, E, 1-23**

2) K. Takeuchi, T. Kato, K. Sakamoto, K. Yukumatsu, K. Watanabe, Y. Tsuchiya, H. Matsuyama, A. Takeyama, T. Ohshima, S. Kuboyama and H. Shindo, "Characteristic Charge Collection Mechanism Observed in FinFET SRAM cells", Proc. Radiation and its Effects on Components and Systems 2020 (RADECS 2020), [Online], (2020.09). **I**

3) Y. Yamazaki, S. Onoda and T. Ohshima, "Color Centers in Wide-Gap Semiconductors for Quantum Technology", Chapter 4 of "Defects in Functional Materials", Edited by F. C.-C. Ling, S. Zhou, A. Kuznetsov, World Scientific, 93-116 (2020).

Patents

1) 佐藤 真一郎, 出来 真斗, 西村 智朗, "温度検出装置、温度センサ、温度検出方法、および温度検出プログラム",特願 2021-032894 (2021.03.02) **I, 1-19**

2) 佐藤 真一郎, 出来 真斗, 西村 智朗, "温度センサ、温度検出装置、温度検出方法、温度検出プログラム、および温度センサの製造方法",特願 2021-032895 (2021.03.02) **I, 1-19**

3) 山﨑 雄一, 増山 雄太, 境 誠司, 李 松田, 平山 祥郎, 大島 武, 新田 淳作, "光スピンデバイス、これを用いた情報保持装置、及び光スピンデバイスの動作方法",特願 2020-165535 (2020.09.30) **N**

P1-5 Project "Environmental Polymer"

Papers

1) R. Kakuchi, R. Tsuji, K. Fukasawa, S. Yamashita, M. Omichi and N. Seko, "Polymers of lignin-sourced components as a facile chemical integrant for the Passerini three-component reaction", Polym. J., **53**, 523–531 (2021). **G, 1-26**

2) H. Hoshina, J. Chen, H. Amada and N. Seko, "Chain Entanglement of 2-Ethylhexyl Hydrogen-2-Ethylhexyl -phosphonate into Methacrylate-Grafted Nonwoven Fabrics for Applications in Separation and Recovery of Dy (III) and Nd (III) from Aqueous Solution", Polymers, **12**, 2656:1–12 (2020). **E, 1-24, 1-25**

3) N. A. F. Othman, S. Selambakkannu, H. Azian, C. T. Ratnam, T. Yamanobe, H. Hoshina and N. Seko, "Synthesis of surface ion-imprinted polymer for specific detection of thorium under acidic conditions", Polym. Bull., **78**, 165–183 (2021). **G, 1-24**

4) N. Suzui, T. Shibata, Y. Yin, Y. Funaki, K. Kurita, H. Hoshina, M. Yamaguchi, S. Fujimaki, N. Seko, H. Watabe and N. Kawachi, "Non-invasive imaging of radiocesium dynamics in a living animal using a positron-emitting 127Cs tracer", Sci. Rep., **10**, 16155:1–9 (2020). **E, 1-24, 1-25**

5) Y. Arai, S. Watanabe, S. Ohno, K. Nomura, F. Nakamura, T. Arai, N. Seko, H. Hoshina, N. Hagura, T. Kubota, "Microscopic analyses on Zr adsorbed IDA chelating resin by PIXE and EXAFS", Nucl. Instrum. Meth. Phys. Res. B **477**, 54 (2020). **E, 1-26**

6) 植木 悠二, "汎用素材を機能性材料へ改良", ケミカルエンジニヤリング, 65(6), 329–335 (2020). **E, 1-24, 1-25**

Proceedings

1) 阿部 美波, 坂口 綾, 瀬古 典明, 保科 宏行, 山崎 信哉, 末木 啓介, "海水中の極微量 233U-236U の海水循環デュアルトレーサー利用に向けた U 濃縮法の検討", 福島大学環境放射能研究所第7回成果報告会, [オンライン] (2021.03.18). **E, 1-24, 1-25**

2) 瀬古 典明, "量子ビームを活用した機能性高分子材料の開発", **【招待講演】**, 第 3 回産学官連携交流会(第 115 回複合材料懇話会), [オンライン] (2021.03.15). **E, 1-24, 1-25**

3) 阿部 美波, 坂口 綾, 瀬古 典明, 保科 宏行, 山崎 信哉, 末木 啓介, "極微量人工放射性核種 233U と 236U の海洋循環デュアルトレーサー利用に向けた海水中 U 濃縮法の検討", 第 22 回環境放射能研究会, [オンライン] (2021.03.10). **E, 1-24, 1-25**

4) 瀬古 典明, "量子ビームを用いた高分子材料の創製と評価", **【招待講演】**, 第 63 回放射線化学討論会, [オンライン] (2020/12/13). **E, 1-24, 1-25**

Patents

1) 保科 宏行, 植木 悠二, 瀬古 典明, "固体組成物及び固体組成物の製造方法", 特許第 6744538 号 (2020.08.04). **E, 1-24, 1-25**

2) 瀬古 典明, 保科 宏行, 笠井 昇, "溶解物除去装置及びこれに用いられるろ過助剤並びに溶解物除去方法", 特許第 6695542 号 (2020/04/24). **E, 1-24, 1-25**

Press・TV

1) 鈴井 伸郎, 柴田 卓弥, 尹 永根, 船木 善仁 栗田 圭輔, 保科 宏行, 山口充孝, 藤巻 秀, 瀬古 典明, 渡部 浩司, 河地 有木, "体内に取り込まれたセシウムの動きが見える！～PET で撮像できるポジトロン放出核種セシウム-127 トレーサの開発に世界で初めて成功～", 2020.10.15, プレス発表: 上毛新聞、日刊工業新聞、福島民友新聞、福島民報新聞、日経産業新聞、科学新聞に掲載 **E, 1-24, 1-25**

P1-6 Project "Biocompatible Materials"

Papers

1) Kotaro Oyama, Mizuho Gotoh, Yuji Hosaka, Tomoko G. Oyama, Aya Kubonoya, Yuma Suzuki, Tomomi Arai, Seiichi Tsukamoto, Yuki Kawamura, Hideki Itoh, Seine A. Shintani, Toshiko Yamazawa, Mitsumasa Taguchi, Shin'ichi Ishiwata and Norio Fukuda, "Single-cell temperature mapping with

fluorescent thermometer nanosheets", The Journal of General Physiology, 152(8), e201912469 (2020). **N**

2) Shuya Ishii, Kotaro Oyama, Seine A. Shintani, Fuyu Kobirumaki-Shimozawa, Shin'ichi Ishiwata and Norio Fukuda, "Thermal activation of thin filaments in striated muscle", Frontiers in Physiology, 11, 278 (2020). **N**

3) Tomoko Gowa Oyama, Kotaro Oyama and Mitsumasa Taguchi, "A simple method for production of hydrophilic, rigid, and sterilized multi-layer 3D integrated polydimethylsiloxane microfluidic chips", Lab on a Chip **20**, 2354 (2020). **E, G**

4) Masato Yamawaki, Naoya Uesugi, Toshitaka Oka, Naotsugu Nagasawa, Hirokazu Ando, Brain E. O' Rourke and Yoshinori Kobayashi, "Development of a method for positron annihilation lifetime measurement in thin polyethylene films using a Na-22 source", Jpn. J. Appl. Phys. **59**, 116504 (2020). **G**

5) Charito T. Aranilla, Bin Jeremiah D. Barba, Lorna S. Relleve and Naotsugu Nagasawa, "Properties and Potential Applications of Carboxymethyl-kappa-carrageenan Hydrogels Crosslinked by Gamma Radiation", The Philippine Journal of Science **150**, 85 (2020). **G**

6) Masanori Koshimizu, Atsushi Kimura, Satoshi Kurashima, Mitsumasa Taguchi, Takayuki Yanagida, Yutaka Fujimoto and Keisuke Asai, "Effect of linear energy transfer on the scintillation properties of Ce-doped Ca3B2O6 crystals", Nucl. Instrum. Meth. Phys. Res. B **471**, 59 (2020). **C**

7) John patrick Mc grady, Shinichi Yamashita, Sho Kano, Huilong Yang, Atsushi Kimura and Hiroaki Abe, "H2 Generation at Metal Oxide Particle Surfaces under γ-Radiation in Water", Journal of Nuclear Science and Technology, in press. **G**

8) Atsushi Kimura, Fumiya Yoshida, Miho Ueno and Mitsumasa Taguchi, "Application of radiation crosslinking technique to development of gelatin scaffold for tissue engineering", Radiat. Phys. Chem. **180**, 109287 (2021). **G, 1-27**

9) Atsushi Kimura, Jun-ichiro Jo, Fumiya Yoshida, Zhang Hong, Yasuhiko Tabata, Akira Sumiyoshi, Mitsumasa Taguchi and Ichio Aoki, "Ultra-small size gelatin nanogel as a blood brain barrier impermeable contrast agent for magnetic resonance imaging", Acta Biomater. **125**, 290 (2021). **G**

10) Atsushi Kimura, Miho Ueno, Tadashi Arai, Kotaro Oyama and Mitsumasa Taguchi, "Radiation crosslinked smart peptide nanoparticles: A new platform for tumor imaging", Nanomaterials **11**, 714 (2021). **G, 1-28**

11) Minami Fukuchi, Kotaro Oyama, Hiroaki Mizuno, Akihisa Miyagawa, Kazuya Koumoto and Gaku Fukuhara, "Hydrostatic Pressure-Regulated Cellular Calcium Responses". Langmuir **37**, 820-826, 2021-01. **N**

12) Ayaka Imanishi, Atsushi Kimura, Hisao Miyamoto, Akihiro Hiroki, Naotsugu Nagasawa, Fumio Yoshii, Mitsumasa Taguchi, "Human organ phantoms for catheterization using the radiation crosslinking technique", J. Appl. Polym. Sci. **138**, 50818 (2021). **G**

13) 田口 光正、廣木 章博, 大山 智子、木村 敦, 大山 廣太郎, "放射線化学反応を利用した先端医療用ゲルの開発"日本白内障学会誌 **32,** 37-36 (2020).

14) 今西 彩花、宮本 久生、吉井 文男、木村 敦、田口 光正,"量子ビーム技術を利用した新しい模擬臓器の開発" , (2020).

15) 大山 智子、田口 光正、山田 高史、小谷 卓司、小沢 幸雄、"微量検体の高速分析を可能にする多段積層マイクロ流体チップの開発"コンバーテック **571**, 48, 96～98, (2020).

16) 大山 智子, "量子ビーム一括接合による 3 次元積層マイクロ流体デバイスの実現",『UV・EB 硬化技術の最新開発動向』CMC 出版

17) 田口 光正, "タンパク質の量子ビーム架橋で作る機能性バイオデバイス",『UV・EB 硬化技術の最新開発動向』CMC 出版

Patents

1) 高山 利夫, 保科 克行, 松浦 壮平, 大山 智子, 田口 光正, 大山 廣太郎, "ゲル被覆医療用材料及びその製造方法", 特願 2020-73756 (2020.04.17)

2) 田口 光正, 大山 智子, 木村 敦, 大山 廣太郎, 石原 弘, 下川 卓志, "細胞培養用ハイドロゲル、ゲルキット、細胞培養物の製造方法、及び細胞培養用ハイドロゲルの製造方法", 特願 2020-527697 (2020.12.10)

3) 大山 智子, 田口 光正, 大山 廣太郎, "物品、物品を製造する方法、複合体、及び複合体を製造する方法", 特願 2021-18449 (2021.02.08)

P1-7 Project "Spintronics in Two-dimensional Materials"

Papers

1) J. Okabayashi, S. Li, S. Sakai, Y. Kobayashi, T. Mitsui, K. Tanaka, Y. Miura and S. Mitani, "Perpendicular magnetic anisotropy at Fe/Au(111) interface studied by Mössbauer, x-ray absorption, and photoemission spectroscopies", Phys. Rev. B **103**, 104435 (2021). **N**

2) S. Entani, M. Honda, H. Naramoto, S. Li and S. Sakai, "Synchrotron X-ray standing wave characterization of atomic arrangement at interface between transferred graphene and alpha-Al_2O_3(0001)", Surf. Sci. **704**, 121749 (2021). **N**

3) T. Mitsui, S. Sakai, S. Li, T. Ueno, T. Watanuki, Y. Kobayashi, R. Masuda, M. Seto and H. Akai, "Magnetic Friedel oscillation at Fe(001) surface: direct observation by atomic-layer-resolved synchrotron radiation ^{57}Fe Mössbauer spectroscopy", Phys. Rev. Lett. **125**, 236806 (2020) (Editor's Suggestion & Featured in Physics). **N**

4) M. Maekawa, A. Miyashita, S. Sakai and A. Kawasuso, "Gadolinium-implanted GaN studied by spin-polarized positron annihilation spectroscopy", Phys. Rev. B **102**, 054427 (2020). **N, 1-17**

5) S. Li, K. V. Larionov, Z. I. Popov, T. Watanabe, K. Amemiya, S. Entani, P. V. Avramov, Y. Sakuraba, H. Naramoto, P. B. Sorokin and S. Sakai, "Graphene/half-metallic Heusler alloy: a novel heterostructure toward high-performance graphene spintronic devices", Adv. Mater. **32**, 1905734 (2020) (Frontispiece). **N**

6) A. Miyashita, S. Li, S. Sakai, M. Maekawa and A. Kawasuso, "Spin polarization of graphene on $Co_2FeGe_{0.5}Ga_{0.5}$(001) observed by spin-polarized surface positronium spectroscopy", Phys. Rev. B **102**, 045425 (2020). **N**

7) S. Entani, K. V. Larionov, Z. I. Popov, M. Takizawa, M. Mizuguchi, H. Watanabe, S. Li, H. Naramoto, P. B. Sorokin and S. Sakai, "Non-chemical fluorination of hexagonal boron

nitride by high-energy ion irradiation", Nanotechnology **31**, 125705 (2020). **N**

8) J. Chen, Y. Sakuraba, K. Yakushiji, Y. Kurashima, N. Watanabe, J. Liu, S. Li, A. Fukushima, H. Takagi, K. Kikuchi, S. Yuasa and K. Hono, "Fully epitaxial giant magnetoresistive devices with half-metallic Heusler alloy fabricated on poly-crystalline electrode using three-dimensional integration technology", Acta Mater**. 200**, 1038-1045 (2020). **N**

9) D. G. Kvashnin, A. G. Kvashnin, E. Kano, A. Hashimoto, M. Takeguchi, H. Naramoto, S. Sakai and P. B. Sorokin, "Two-Dimensional CuO Inside the Supportive Bilayer Graphene Matrix", J. Phys. Chem. C **123**, 17459-17465 (2019). **N**

10) S. Entani, M. Takizawa, S. Li, H. Naramoto and S. Sakai, "Growth of graphene on SiO_2 with hexagonal boron nitride buffer layer", Appl. Surf. Sci. **475**, 6-11 (2019). **N**

Proceedings

1) M. Maekawa, S. Sakai, S. Hagiwara, A. Miyashita, K. Wada, A. Kawasuso, A. Yabuuchi and S. Hasegawa, "Magnetic Doppler broadening measurement on Gadolinium-doped GaN", AIP Conf. Proc. **2182**, 050007 (2019). **N, 1-17**

Press・TV

1) "鉄の磁石の「表面の謎」を解明！― 一原子層単位の深さ精度で磁性探査する新技術を開発―", 2020.12.04, プレス発表: 時事通信、日経産業新聞、日刊工業新聞、科学新聞に掲載. **C**

2) "電子スピンを自在に操ることができる積層材料の開発に成功 - 日常生活の情報化を支える超高記録密度・省エネ磁気メモリの実現に大きく前進 –", 2019.12.03, プレス発表: academist Journal 等ネット記事に掲載. **C**

P1-8 Project "EUV Ultra-fine Fabrication"

Papers

1) Y. Hosaka, H. Yamamoto, M. Ishino, T.-H. Dinh, M. Nishikino, A. Kon, S. Owada, Y. Inubushi, Y. Kubota and Y. Maekawa, "Study on irradiation effects by femtosecond-pulsed extreme ultraviolet in resist materials", J. Photopolym. Sci. Technol. **34**, 95 (2021). **N**

2) M. Ishino, T. Dinh, Y. Hosaka, N. Hasegawa, K. Yoshimura, H. Yamamoto, T. Hatano, T. Higashiguchi, K. Sakaue, S. Ichimaru, M. Hatayama, A. Sasaki, M. Washio, M. Nishikino and Y. Maekawa, "Soft x-ray laser beamline for surface processing and damage studies"**,** Applied Optics **59**, 3692 (2020). **N**

3) H. Yamamoto, G. Dawson, T. Kozawa and A. P.G. Robinson, "Lamellar orientation of a block copolymer via an electron-beam induced polarity switch in a nitrophenyl self-assembled monolayer"**,** Quantum. Beam Sci. **4**, 12-1-10 (2020). **N**

4) H. Maekawa, H. Kudo, T. Watanabe, H. Yamamoto, T. Kozawa, M. Taniguchi and A. Yokoya, "Higher sensitive extreme ultraviolet (EUV) resist materials derived from p-t-Butylcalix[n]arenes (n = 4 and 8)", J. Photopolym. Sci. Technol. **33**, 45 (2020). **N**

Proceedings

1) H. Yamamoto and Y. Maekawa, "Fundamental study on lithographic characteristics of metal oxo clusters for KrF, ArF, and electron beam lithography", Proc. of SPIE **11326**, 11326W1 (Advances in Patterning Materials and Processes XXXI XXVIII) (2020). **N**

P1-9 Project "Element Separation and Analysis"

Papers

1) R. Nakanishi, M. Saeki, I. Wakaida and H. Ohba, "Detection of Gadolinium in Surrogate Nuclear Fuel Debris Using Fiber-Optic Laser-Induced Breakdown Spectroscopy under Gamma Irradiation", Appl. Sci. **10**, 8985 (2020). **G, 1-31**

2) Y. Kurosaki, R. Nakanishi, M. Saeki and H. Ohba, "Ab initio MRCI study on potential energy surfaces for double Cl loss from the palladium tetrachloride anion PdCl42–", Chem. Phys. Lett. **764**, 138247 (2020). **N**

3) Y. Kurosaki and K. Yokoyama, "Quantum Optimal Control of Isotope-Selective Rovibrational Transitions", AIP Conf. Proc. **2343**, 020005 (2021). **N**

4) K. Tamura, H. Ohba, M. Saeki, T. Taguchi, H. H. Lim, T. Taira and I. Wakaida, "Radiation dose rate effects on the properties of a laser-induced breakdown spectroscopy system developed using a ceramics micro-laser for fiber-optic remote analysis", J. Nucl. Sci. Technol. **58**, 405 (2021). **G, 1-31**

5) M. Yoshimoto, T. Nakanoya, Y. Yamazaki, P. Saha, M. Kinsho, S. Yamamoto, H. Okazaki, T. Taguchi, N. Yamada and R. Yamagata, "Analysis of J-HBC stripper foil for the J-PARC RCS", J. Phys. Soc. of Japan, Proceeding of the J-PARC Symposium 2019 **33**, 011019 (2021). **N**

6) S. Yamamoto, H. Koshikawa, T. Taguchi and T. Yamaki, "Precipitation of Pt nanoparticles inside ion-track-etched capillaries", Quantum Beam Sci. **4**(1) 8 (2020). **N**

7) N. Ishikawa, T. Taguchi, A. Kitamura, G. Szenes and M. E. Toimil-Molares, C. Trautmann, "TEM analysis of ion-tracks and hillocks produced by swift heavy ions of different velocities in $Y_3Fe_5O_{12}$", J. Appl. Phys. **127**, 055902 (2020). **N**

8) M. Saeki, T. Yomogida, D. Matsumura, T. Saito, R. Nakanishi, T. Tsuji and H Ohba, "Application of augmentation method to MCR-ALS analysis for XAFS and Raman data matrices in structural change of isopolymolybdates", Anal. Sci. **36**, 1371 (2020). **N**

9) K. Tamura, H. Ohba, M. Saeki, T. Taguchi, H.H. Lim and T. Taira, I. Wakaida, "Development of a laser-induced breakdown spectroscopy system using a ceramic micro-laser for fiber-optic remote analysis", J. Nucl. Sci. Technol. **57**, 1189 (2020). **G, 1-31**

10) 中西 隆造, 佐伯 盛久, 大場 弘則, "パルスレーザー照射による希少金属を回収する", レーザ加工学会誌, 27(3), 159 (2020). **N**

11) Y. Kurosaki, R. Nakanishi, M. Saeki and H. Ohba, "Ab initio MRCI study on potential energy curves for a single Cl loss from the palladium tetrachloride anion $PdCl_4^{2-}$", Chem. Phys. Lett. **746**, 137288 (2020). **N**

12) 大場 弘則, 佐伯 盛久, 中西 隆造, "廃液にレーザーを照射して希少金属を回収する", ケミカルエンジニヤリング **65**, 347 (2020). **N**

13) 田村 浩司, 遠山 伸一, "レーザー法による原子炉厚板鋼材切断技術の開発", 日本原子力学会誌 **62**, 268 (2020). **N**

14) 大場 弘則, 若井田 育夫, 平等 拓範, "過酷環境下での遠隔レーザー分析技術", 日本原子力学会誌 **62**, 263-267 (2020). **G, 1-31**

15) R. Nakanishi, M. Saeki, T. Taguchi and H. Ohba, "Photoinduced gold recovery mediated by isopolymolybdate in strongly acidic HCl/NaCl solutions", J. Photochem. Photobio. A **383**, 111994 (2019). **N**

16) Y. Kurosaki and K. Yokoyama, "Quantum optimal control of rovibrational excitations of a diatomic alkali halide: one-photon vs. two-photon processes", Universe **5**, 109 (2019). **N**

17) T. Taguchi, S. Yamamoto and H. Ohba, "Synthesis of novel hybrid carbon nanomaterials inside silicon carbide nanotubes by ion irradiation", Acta Mater. **173**, 153 (2019). **I, 1-30**

18) Ayumu Matsumoto, Hironori Ohba, Masaaki Toshimitsu, Katsuaki Akaoka, Alexandre Ruas, Ikuo Wakaida, Tetsuo Sakka and Shinji Yae, "Enhancement of molecular formation in fiber-optic laser ablation with a long nanosecond pulsed laser", Spectrochim. Acta Part B At. Spectrosc. **155**, 56 (2019). **G, 1-31**

19) M. Saeki, D. Matsumura, T. Yomogida, T. Taguchi, T. Tsuji, H. Saito and H. Ohba, "In Situ Time-Resolved XAFS Studies on Laser-Induced Particle Formation of Palladium Metal in an Aqueous / EtOH Solution", J. Phys. Chem. C, **123**, 817 (2019). **N**

20) Y. Sasaki, M. Saeki and K. Yoshizuka, "Extractions and spectroscopic studies of various metals with Diglycolamide-Type Tridentate Ligands", Solvent Extr. Res. Dev., Jpn, **26**, 21-34(2019). **N**

21) 田村 浩司, 遠山 伸一, "厚板鋼材のレーザー切断技術－廃炉の時代の先端技術開発－", 日本原子力学会誌, **61**, 413 (2019). **N**

22) 若井田 育夫, 大場 弘則, 宮部 昌文, 赤岡 克昭, 大場 正規, 田村 浩司, 佐伯 盛久, "核燃料サイクルおよび福島第一原子力発電所廃炉への適用を念頭としたレーザー誘起ブレークダウン分光と関連分光技術", 光学（日本光学会機関誌）**48**, 13 (2019). **N**

Patent

1) 大場 弘則, 佐伯 盛久, 田口 富嗣, 中西 隆造, "回収装置、回収システム、及び回収方法", 特願 2019-097119

Press・TV

1) "廃液からパラジウムや金、銀", 日経サイエンス（2020 年 2 月号）掲載

2) "廃液中の金属、レーザーで回収～量研、連続処理装置開発めざす～", 2019.09.18, 日経産業新聞に掲載.

P1-10 Advanced Functional Polymer Materials Research Group

Papers

1) T. D. Tap, L. L. Nguyen, S. Hasegawa, S. Sawada, L. Q. Luan and Y. Maekawa, "Internal and interfacial structure analysis of graft-type fluorinated polymer electrolyte membrane by small angle X-ray scattering in the high-q range", J. Appl. Polym. Sci. **137**, 49029 (2020). **G, 1-02**

2) Y. Maekawa and M. Washio, "Quantum beams applying to innovative industrial materials", Quantum Beam Sci. **4**, 27 (2020). **N**

3) S. Hasegawa, S. Sawada, S. Azami, T. Hagiwara, A. Hiroki and Y. Maekawa, "Development of hydrogen-permselective porous membranes using radiation-induced graft polymerization", Quantum Beam Sci. **4**, 23 (2020). **G, 1-01**

4) Y. Zhao, K. Yoshimura, A. M. S. Mahmoud, H. C. Yu, S. Okushima, A. Hiroki, Y. Kishiyama, H. Shishitani, S. Yamaguchi, H. Tanaka, Y. Noda, S. Koizumi, A. Radulescu and Y. Maekawa, "A long side chain imidazolium-based graft-type anion-exchange membrane: novel electrolyte and alkaline-durable properties and structural elucidation using SANS contrast variation", Soft Matter **16**, 8128 (2020). **G, 1-02**

5) M. M. Schiavone, D. H. Lamparelli, Y. Zhao, F. Zhu, Z. Revay and A. Radulescu, "The effects of temperature and humidity on the microstructure of sulfonated syndiotactic–polystyrene ionic membranes", Membranes **10**, 00187 (2020). **N**

6) A. M. A. Mahmoud, K. Yoshimura and Y. Maekawa, "Alkaline fuel cells consisting of imidazolium-based graft-type anion exchange membranes: Optimization of fuel cell conditions to achieve high performance and durability", J. Membr. Sci. **620,** 118844 (2021). **G, 1-02**

7) Beom-Seok Ko, K. Yoshimura, A. Hiroki and Y. Maekawa, "Mechanistic study on radiation-induced grafting into fluorinated polymer solid films using a swelling-induced detachment of grafted polymers", J. Polym. Sci. **59**, 108-116 (2021). **G, 1-02**

8) S. Sawada, T. Kimura, H. Nishijima, T. Kodaira, N. Tanaka, S. Kubo, S. Imabayashi, M. Nomura and T. Yamaki, "Overvoltage reduction in membrane Bunsen reaction for hydrogen production by using a radiation-grafted cation exchange membrane and porous Au anode", Int. J. Hydrogen Energy **45**, 13814-13820 (2020). **G**

9) S. Sawada, T. Yamaki and H. Koshikawa, "Creation of Nanostructured-Controlled Functional Membranes Using High-Energy Ion Beams", Salt Seawater Sci. Technol. **1**, 61-73 (2021). **C, 1-13**

10) M. Ishino, T. Dinh, Y. Hosaka, N. Hasegawa, K. Yoshimura, H. Yamamoto, T. Hatano, T. Higashiguchi, K. Sakaue, S. Ichimaru, M. Hatayama, A. Sasaki, M. Washio, M. Nishikino and Y. Maekawa, "Soft x-ray laser beamline for surface processing and damage studies", Appl. Opt. **59**, 3692-3698 (2020). **N**

11) R. Kakuchi, R. Tsuji, K. Fukasawa, S. Yamashita, M. Omichi and N. Seko, "Polymers of lignin-sourced components as a facile chemical integrant for the Passerini three-component reaction", Polym. J. **53**, 523–531 (2021). **G, 1-26**

12) H. Hoshina, J. Chen, H. Amada and N. Seko, "Chain Entanglement of 2-Ethylhexyl Hydrogen-2-Ethylhexylphosphonate into Methacrylate-Grafted Nonwoven Fabrics for Applications in Separation and Recovery of Dy (III) and Nd (III) from Aqueous Solution", Polymers **12**, 2656:1–12 (2020). **E, 1-24, 1-25**

13) N. A. F. Othman, S. Selambakkannu, H. Azian, C. T. Ratnam, T. Yamanobe, H. Hoshina and N. Seko, "Synthesis of surface ion-imprinted polymer for specific detection of thorium under acidic conditions", Polym. Bull. **78**, 165–183 (2021). **G, 1-24, 1-25**

14) N. Suzui, T. Shibata, Y. Yin, Y. Funaki, K. Kurita, H. Hoshina, M. Yamaguchi, S. Fujimaki, N. Seko, H. Watabe and N. Kawachi, "Non-invasive imaging of radiocesium dynamics in a living animal using a positron-emitting 127Cs tracer", Sci. Rep. **10**, 16155:1–9 (2020). **E, 1-24, 1-25**

15) Y. Arai, S. Watanabe, S. Ohno, K. Nomura, F. Nakamura, T. Arai, N. Seko, H. Hoshina, N. Hagura and T. Kubota, "Microscopic analyses on Zr adsorbed IDA chelating resin by PIXE and EXAFS", Nucl. Instrum. Meth. Phys. Res. B **477**, 54 (2020). **E, 1-26**

16) 植木 悠二, "汎用素材を機能性材料へ改良", ケミカルエンジニヤリング, 65(6), 329–335 (2020). **E, 1-24, 1-25**

Proceedings

1) 澤田 真一, 坂本 有希子, 田中 健一, 船津 公人,前川 康成, "機械学習法によるグラフト型電解質膜の導電率・含水率の予測", 第 69 回高分子討論会, [オンライン], 要旨集, 3G07 (2020). **G, 1-02**

2) 長谷川 伸, 廣木 章博, 吉村 公男, ザオ ユエ, 町田 晃彦, 大和田 謙二, 前川 康成, "溶媒アニールによるポリエーテルエーテルケトン膜のモルフォロジー制御と 放射線グラフト重合反応加速機構", 第 69 回高分子討論会, [オンライン], 要旨集, PA0803 (2020). **G, 1-02**

3) 髙松 治文, 吉村 公男, 廣木 章博, 前川 康成, "アルカリ耐性アニオン伝導電解質膜の創製研究", 第 63 回放射線化学討論会, [オンライン], 要旨集, 2P-11 (2020). **G, 1-02**

4) 坂本 有希子, 澤田 真一, 廣木 章博, 前川 康成, "機械学習に基づくグラフト型電解質膜の機能性評価", 令和 2 年度日本化学会関東支部群馬地区研究交流発表会, [オンライン], 要旨集, P006 (2020). **G, 1-02**

5) 阿部 聖賢, 吉村 公男, 廣木 章博, 前川 康成, "フッ素系高分子基材へのビニルモノマーの放射線グラフト重合 ～機械学習に基づく重合予測～", 令和 2 年度日本化学会関東支部群馬地区研究交流発表会, [オンライン], 要旨集, P021 (2020). **G, 1-02**

6) 髙松 治文, 吉村 公男, 廣木 章博, 前川 康成, "アルカリ耐性アニオン伝導電解質膜の創製研究", 令和 2 年度日本化学会関東支部群馬地区研究交流発表会, [オンライン], 要旨集, P036 (2020). **G, 1-02**

7) 柴田 康瑛, 長谷川 伸, 廣木 章博, 木下 基, 前川 康成, "ポリフェニレンスルフィドを基材とした放射線グラフト重合における基材膜の結晶モルフォロジーと重合性・機能", 令和2年度日本化学会関東支部群馬地区研究交流発表会, [オンライン] 要旨集, P047 (2020). **G, 1-02**

8) 髙松治文, 吉村公男, 廣木章博, 前川康成, "イミダゾリウム基を有する放射線グラフト型アニオン伝導膜の電解質膜特性と階層構造の関係", 第 101 回日本化学会春季年会, [オンライン], 要旨集, P02-2vn-23 (2021). **G, 1-02**

9) 阿部 美波, 坂口 綾, 瀬古 典明, 保科 宏行, 山崎 信哉, 末木 啓介, "海水中の極微量 233U-236U の海水循環デュアルトレーサー利用に向けた U 濃縮法の検討", 福島大学環境放射能研究所第7回成果報告会, [オンライン], (2021). **E, 1-24, 1-25**

10) 瀬古 典明, "量子ビームを活用した機能性高分子材料の開発", **【招待講演】**, 第 3 回産学官連携交流会（第 115 回複合材料懇話会）, [オンライン], (2021). **E, 1-24, 1-25**

11) 阿部 美波, 坂口 綾, 瀬古 典明, 保科 宏行, 山崎 信哉, 末木 啓介, "極微量人工放射性核種 233U と 236U の海洋循環デュアルトレーサー利用に向けた海水中 U 濃縮法の検討", 第 22 回環境放射能研究会, [オンライン], (2021). **E, 1-24, 1-25**

12) 瀬古 典明, "量子ビームを用いた高分子材料の創製と評価", **【招待講演】**, 第 63 回放射線化学討論会, [オンライン] (2020). **E, 1-24, 1-25**

Patents

1) 保科 宏行, 植木 悠二, 瀬古 典明, "固体組成物及び固体組成物の製造方法"特許第 6744538 号 (2020.08.04). **E, 1-24, 1-25**

2) 瀬古 典明, 保科 宏行, 笠井 昇, "溶解物除去装置及びこれに用いられるろ過助剤並びに溶解物除去方法", 特許第 6695542 号 (2020.04.24). **E, 1-24, 1-25**

P1-11 Quantum Sensing and Information Materials Research Group

Papers

1) V. Ivády, H. Zheng, A. Wickenbrock, L. Bougas, G. Chatzidrosos, K. Nakamura, H. Sumiya, T. Ohshima, J. Isoya, D. Budker, I. A. Abrikosov and A. Gali, "Photoluminescence at the ground-state level anticrossing of the nitrogen-vacancy center in diamond: A comprehensive study", Phys. Rev. B **103**, 035307-1-13 (2021). **E**

2) Z. Shang, Y. Berencén, M. Hollenbach, S. Zhou, H. Kraus, T. Ohshima and G.V. Astakhov, "Microwave-assisted spectroscopy of vacancy-related spin centers in hexagonal SiC", Phys. Rev. Appl. **15**, 034059-1-9 (2021). **E**

3) K. Miyanishi, T. F. Segawa, K. Takeda, I. Ohki, S. Onoda, T. Ohshima, H. Abe, H. Takashima, S. Takeuchi, A. I. Shames, K. Morita, Y. Wang, F. T.-K. So, D. Terada, R. Igarashi, A. Kagawa, M. Kitagawa, N. Mizuochi, M. Shirakawa and M. Negoro, "Room-temperature hyperpolarization of polycrystalline samples with optically polarized triplet electrons: pentacene or nitrogen-vacancy center in diamond?", Magn. Reson. **2**, 33-48 (2021). **E**

4) Y. Masuyama, K. Suzuki, A. Hekizono, M. Iwanami, M. Hatano, T. Iwasaki and T. Ohshima, "Gradiometer using separated diamond quantum magnetometers", Sensors **21**, 977-1-11 (2021). **E**

5) T. Kitaizumi, A. Kuwahata, K. Saichi, T. Sato, R. Igarashi, T. Ohshima, Y. Masuyama, T. Iwasaki, M. Hatano, F. Jelezko, M. Kusakabe, T. Yatsui and M. Sekino, "Magnetic field generation

system of the magnetic probe with diamond quantum sensor and ferromagnetic materials for the detection of sentinel lymph nodes with magnetic nanoparticles", IEEE Trans. Magnetics **57**, 5100405-1-5 (2021). **E**

6) T. Narahara, S.-I. Sato, K. Kojima, Y. Hijikata and T. Ohshima, "Influences of hydrogen ion irradiation on $N_CV_{Si}^-$ formation in 4H-silicon carbide", Appl. Phys. Express **14**, 021004-1-4 (2021). **C, I, T**

7) T. M. Hoang, H. Ishiwata, Y. Masuyama, Y. Yamazaki, K. Kojima, S.-Y. Lee, T. Ohshima, T. Iwasaki, D. Hisamoto and M. Hatano, "Thermometric quantum sensor using excited state of silicon vacancy centers in 4H-SiC devices", Appl. Phys. Lett. **118**, 044001-1-5 (2021). **S, I, E**

8) Y. Hatano, J. Shin, D. Nishitani, H. Iwatsuka, Y. Masuyama, H. Sugiyama, M. Ishii, S. Onoda, T. Ohshima, K. Arai, T. Iwasaki and M. Hatano, "Simultaneous thermometry and magnetometry using a fiber-coupled quantum diamond sensor", Appl. Phys. Lett. **118**, 034001-1-6 (2021). **E**

9) Y. Yamazaki, Y. Chiba, S.-I. Sato, T. Makino, N. Yamada, T. Satoh, K. Kojima, Y. Hijikata, H. Tsuchida, N. Hoshino, S.-Y. Lee and T. Ohshima, "Carrier dynamics of silicon vacancies of SiC under simultaneous optically and electrically excitations", Appl. Phys. Lett. **118**, 021106-1-6 (2021). **S, I**

10) S. Castelletto, J. Maksimovic, T. Katkus, T. Ohshima, B. C. Johnson and S. Juodkazis, "Color centers enabled by direct femto-second laser writing in wide bandgap semiconductors", Nanomaterials **11**, 72-1-17 (2021). **E**

11) F. M. Sturner, A. Brenneis, T. Buck, J. Kassel, R. Rolver, T. Fuchs, A. Savitsky, D. Suter, Jens Grimmel, S. Hengesbach, M. Fortsch, K. Nakamura, H. Sumiya, S. Onoda, J. Isoya and F. Jelezko, "Integrated and Portable Magnetometer Based on Nitrogen-Vacancy Ensembles in Diamond", Adv. Quantum Technol. **10**, 2000111-1-11 (2021). **E**

12) L. Q. Zhou, R. L. Patel, A. C. Frangeskou, A. Nikitin, B. L. Green, B. G. Breeze, S. Onoda, J. Isoya and G. W. Morley, "Imaging Damage in Steel Using a Diamond Magnetometer", Phys. Rev. Appl. **15**, 024015-1-10 (2021). **E**

13) S. R. Nair, L. J. Rogers, X. Vidal, R. P. Roberts, H. Abe, T. Ohshima, T. Yatsui, A. D. Greentree, J. Jeske and T. Volz, "Amplification by stimulated emission of nitrogen-vacancy centres in a diamond-loaded fibre cavity", Nanophotonics **9**, 4505-4518 (2020) **E**

14) V. Guarino, I. Cruz-Maya, P. Reineck, H. Abe, T. Ohshima, K. Fox, A. D. Greentree, B. C. Gibson and L. Ambrosio, "Fluorescent Nanodiamonds Embedded in Poly-ε-Caprolactone Fibers as Biomedical Scaffolds", ACS Appl. Nano Mater. **3**, 10814-10822 (2020). **E**

15) A. I. Shames, A. Dalis, A. D. Greentree, B. C. Gibson, H. Abe, T. Ohshima, O. Shenderova, A. Zaitsev and P. Reineck, "Near-infrared fluorescence from silicon- and nickel-based color centers in high-pressure high-temperature diamond micro- and nanoparticles", Adv. Opt. Mater. **8**, 2001047 (2020). **E**

16) P. Reineck, A. N. Abraham, A. Poddar, R. Shukla, H. Abe, T. Ohshima, B. C. Gibson, C. Dekiwadia, J. J. Conesa, E. Pereiro, A. Gelmi and G. Bryant, "Multimodal Imaging and Soft X-Ray Tomography of Fluorescent Nanodiamonds in Cancer Cells", Biotechnology J. **16**, 2000289-1-8 (2021). **E**

17) S.-W. Jeon, J. Lee, H. Jung, Sa.-W. Han, Y.-W. Cho, Y.-S. Kim, H.-T. Lim, Y. Kim, M. Niethammer, W. C. Lim, J. Song, S. Onoda, T. Ohshima, R. Reuter, A. Denisenko, J. Wrachtrup and S.-Y. Lee, "Bright nitrogen-vacancy centers in diamond inverted nanocones", ACS Photonics **7**, 2739-2747 (2020). **T**

18) S.-I. Sato, M. Deki, H. Watanabe, S. Nitta, Y. Honda, T. Nishimura, B. C. Gibson, A. D. Grenntree, H. Aamano and T. Ohshima, "Optical properties of neodymium ions in nanoscale regions of gallium nitride", Opt. Mater. Express **10**, 2614-2623 (2020). **I**

19) A. Bourassa, C. P. Anderson, K. C. Miao, M. Onizhuk, H. Ma, A. L. Crook, H. Abe, J. Ul-Hassan, T. Ohshima, N. T. Son, G. Galli and D. D. Awschalom, "Entanglement and control of single nuclear spins in isotopically engineered silicon carbide", Nat. Mater. **19**, 1319-1325 (2020). **E**

20) K. C. Miao, J. P. Blanton, C. P. Anderson, A. Bourassa, A. L. Crook, G. Wolfowicz, H. Abe, T. Ohshima and D. D. Awschalom, "Universal coherence protection in a solid-state spin qubit", Science **369**, 1493-1497 (2020). **E**

21) D. M. Lukin, A. D. White, R. Trivedi, M. A. Guidry, N. Morioka., C. Babin, Ö. O. Soykal, J. Ul-Hassan, N. T. Son, T. Ohshima, P. K. Vasireddy, M. H. Nasr, S. Sun, J.-P. W. MacLean, C. Dory, E. A. Nanni, J. Wrachtrup, F. Kaiser and J. Vučković, "Spectrally reconfigurable quantum emitters enabled by optimized fast modulation", npj Quantum Inf. **6**, 80-1-9 (2020). **E**

22) A. L. Crook, C. P. Anderson, K. C. Miao, A. Bourassa, H. Lee, S. L. Bayliss, D. O. Bracher, X. Zhang, H. Abe, T. Ohshima, E. L. Hu and D. D. Awschalom, "Purcell enhancement of a single silicon carbide color center with coherent spin control", Nano Lett. **20**, 3427-3434 (2020). **E**

23) Y. Chiba, Y. Yamazaki, S.-I. Sato, T. Makino, N. Yamada, T. Satoh, Y. Hijikata and T. Ohshima, "Enhancement of ODMR contrasts of silicon vacancy in SiC by thermal treatment", Mater. Sci. Forum **1004**, 337-342 (2020). **S**

24) Y. Yamazaki, Y. Chiba, S.-I. Sato, T. Makino, N. Yamada, T. Satoh, K. Kojima, Y. Hijikata, H. Tsuchida, N. Hoshino, S.-Y. Lee and T. Ohshima, "Optically detected magnetic resonance study of 3D arrayed silicon vacancies in SiC pn diodes", Mater. Sci. Forum **1004**, 343-348 (2020). **S, I**

25) T. Narahara, S.-I. Sato, K. Kojima, Y. Yamazaki, Y. Hijikata and T. Ohshima, "Effects of nitrogen impurity concentration on nitrogen-vacancy center formation in 4H-SiC", Mater. Sci. Forum **1004**, 349-354 (2020). **I**

26) S.-I. Sato, T. Narahara, S. Onoda, Y. Yamazaki, Y. Hijikata, B. C. Gibson, A. D. Greentree and T. Ohshima, "Near infrared photoluminescence of $N_CV_{Si}^-$ centers in high-purity semi-insulating 4H-SiC irradiated with energetic charged particles", Mater. Sci. Forum **1004**, 355-360 (2020). **I**

27) Y. Abe, T. Umeda, M. Okamoto, S. Harada, Y. Yamazaki and T. Ohshima, "The effect of γ-ray irradiation on optical properties of single photon sources in 4H- SiC MOSFET", Mater. Sci. Forum **1004**, 361-366 (2020). **G**

28) N. T. Son, Q. D. Ho, K. Goto, H. Abe, T. Ohshima, B. Monemar, Y. Kumagai and T. Frauenheim, P. Deak, "Electron paramagnetic resonance and theoretical study of gallium vacancy in ß-Ga_2O_3", Appl. Phys. Lett. **117**, 032101-1-5 (2020). **E**

29) S.-I. Sato, M. Deki, T. Nishimura, H. Okada, H. Watanabe, S. Nitta, Y. Honda, H. Amano and T. Ohshima, "Photoluminescence properties of implanted praseodymium into gallium nitride at elevated temperatures", Nucl. Instrum. Meth. Phys. Res. B **479**, 7-12 (2020). **I**

30) N. Morioka, C. Babin, R. Nagy, I. Gediz, E. Hesselmeier, D. Liu, M. Joliffe, M. Niethammer, D. Dasari, V. Vorobyov, R. Kolesov, R. Stohr, J. U-Hassan, N. T. Son, T. Ohshima, P. Udvarhelyi, G. Thiering, A. Gali, J. Wrachtrup and F. Kaiser, "Spin-controlled generation of indistinguishable and distinguishable photons from silicon vacancy centres in silicon carbide", Nat. Commun. **11**, 2516-1-8 (2020). **E**

31) P. Udvarhelyi, G. Thiering, N. Morioka, C. Babin, F. Kaiser, D. Lukin, T. Ohshima, J. U-Hassan, N. T. Son, J. Vuckovic, J. Wrachtrup and A. Gali, "Vibronic states and their effect on the temperature and strain dependence of silicon-vacancy qubits in 4H-SiC", Phys Rev. Appl. **13**, 054017-1-10 (2020). **E**

32) H. Zheng, Z. Sun, G. Chatzidrosos, C. Zhang, K. Nakamura, H. Sumiya, T. Ohshima, J. Isoya, J. Wrachtrup, A. Wickenbrock and D. Budker, "Microwave-free vector magnetometry with nitrogen-vacancy centers along a single axis in diamond", Phys. Rev. Appl. **13**, 0044023-1-9 (2020). **E**

33) K. Hayashi, Y. Matsuzaki, T. Ashida, S. Onoda, H. Abe, T. Ohshima, M. Hatano, T. Taniguchi, H. Morishita, M. Fujiwara and N. Mizuochi, "Experimental and theoretical analysis of noise strength and environmental correlation time for ensembles of nitrogen-vacancy centers in diamond", J. Phys. Soc. Jpn. **89**, 054708-1-6 (2020). **C**

34) C. Kasper, D. Klenkert, Z. Shang, D. Simin, A. Gottscholl, A. Sperlich, H. Kraus, C. Schneider, S. Zhou, M. Trupke, W. Kada, T. Ohshima, V. Dyakonov and G. V. Astakhov, "Influence of irradiation on defect spin coherence in silicon carbide", Phys. Rev. Appl. **13**, 044054-1-11 (2020). **E**

35) A. Kuwahata, T. Kitaizumi, K. Saichi, T. Sato, R. Igarashi, T. Ohshima, Y. Masuyama, T. Iwasaki, M. Hatano, F. Jelezko, M. Kusakabe, T. Yatsui and M. Sekino, "Magnetometer with nitrogen vacancy center in a bulk diamond for detecting magnetic nanoparticles in biomedical applications", Sci. Rep. **10**, 2483-1-9 (2020). **E**

36) H. Zhou, J. Choi, S. Choi, R. Landig, A. M. Douglas, J. Isoya, F. Jelezko, S. Onoda, H. Sumiya, P. Cappellaro, H. S. Knowles, H. Park and M. D. Lukin, "Quantum metrology with strongly interacting spin systems", Phys. Rev. X **10**, 031003-1-9 (2020). **E**

37) S. Castelletto, F. A. Inam, S.-I. Sato and A. Boretti, "Hexagonal boron nitride: a review of the emerging material platform for single-photon source and the spin-photon interface," Beilstein J. Nanotechnol. **11**, 740-769 (2020). **N**

38) K. Akiba, K. Tamehiro, K. Matsui, H. Ikegami and H. Minoda, "Cathodoluminescence of green fluorescent protein exhibits the redshifted spectrum and the robustness", Sci. Rep. **10**, 17342 (2020). **N**

39) Y. Yamazaki, S. Onoda and T. Ohshima, "Color Centers in Wide-Gap Semiconductors for Quantum Technology", Chapter 4 of "Defects in Functional Materials" Edited by F. C.-C. Ling, S. Zhou, A. Kuznetsov, World Scientific, 93-116 (2020).

Patents

1) 佐藤 真一郎, 出来 真斗, 西村 智朗, "温度検出装置、温度センサ、温度検出方法、および温度検出プログラム"特願 2021-032894 (2021.03.02) **I**

2) 佐藤 真一郎, 出来 真斗, 西村 智朗, "温度センサ、温度検出装置、温度検出方法、温度検出プログラム、および温度センサの製造方法"特願 2021-032895 (2021.03.02) **I**

3) 山﨑 雄一, 増山 雄太, 境 誠司, 李 松田, 平山 祥郎, 大島 武, 新田 淳作, "光スピンデバイス、これを用いた情報保持装置、及び光スピンデバイスの動作方法"特願 2020-165535 (2020.09.30) **N**

P2-1 Project "Microbeam Radiation Biology"

Papers

1) M. Suzuki, Z. Soh, H. Yamashita, T. Tsuji, T. Funayama and "Targeted central nervous system irradiation of *Caenorhabditis elegans* induces a limited effect on motility", Biology **9**, 289 (2020). **C, 2-07**

2) T. Yasuda, T. Funayama, K. Nagata, D. Li, T. Endo, Q. Jia, M. Suzuki, Y. Ishikawa, H. Mitani and S. Oda, "Collimated Microbeam reveals that the proportion of non-damaged cells in irradiated blastoderm determines the success of development in Medaka (*Oryzias latipes*) Embryos", Biology **9**, 447 (2020). **C**

3) T. Oizumi, R. Ohno, S. Yamabe, T. Funayama and A. J. Nakamura, "Repair kinetics of DNA double-strand breaks induced by simulated space radiation", Life, **10**, 341 (2020). **C, 2-03**

4) S. Furukawa, A. Nagamatsu, M. Nenoi, A. Fujimori, S. Kakinuma, T. Katsube, B. Wang, C. Tsuruoka, T. Shirai, A. J. Nakamura, A. Sakaue-Sawano, A. Miyawaki, H. Harada, M. Kobayashi, J. Kobayashi, T. Kunieda, T. Funayama, M. Suzuki, T. Miyamoto, J. Hidema, Y. Yoshida and A. Takahashi, "Space radiation biology for "Living in Space"", BioMed Res. Int. **4703286**, 1-25 (2020). **C**

Proceedings

1) K. Sakamoto, H. Yamashita, Z. Soh, M. Suzuki and T. Tsuji, "Multiple regression analysis to reveal relationships between muscle activities and body bends in a transgenic *Caenorhabditis elegans*", Proc. 26th Int. Symp. Artific. Life Robotics (AROB 26th 2021), [Online], 96-100 (2021). **N**

Patents

1) 鈴木 芳代, 服部 佑哉, 齋藤 俊行, 原田 良信, "線虫トラップ用プレート、およびその利用", 国際出願 PCT/JP2020/017674 (2020.04.24).

2) 舟山 知夫, 鈴木 芳代, "生物収容容器(D20005JP.1)", 意匠登録 1660525 (2020.05.11).

3) 舟山 知夫, 鈴木 芳代, "生物収容容器(D20005JP.3)", 意匠登録 1660526 (2020.05.11).

4) 鈴木 芳代, 坂下 哲哉, 舟山 知夫, 平塚 哉, "生物試料用マイクロチップ、カバー、生物試料封入キットおよび方法", 出願 特願 2020-521272 (2020.11.09).

5) 鈴木 芳代, "線虫を用いる試験方法および線虫試験用プレート", 出願 特願 2021-046605 (2021.03.19).

Press・TV

1) “生命の不思議を“ピンポイント照射”で明らかに～マイクロビーム照射を用いて脳神経系の発生や運動機能を解明～”, 2020.12.05, プレス発表: 上毛新聞, 東京新聞群馬版に掲載. **C, 2-07**

P2-2 Project “Ion Beam Mutagenesis”

Papers

1) K. Satoh, S. Ozawa, H. Hayashi, N. Tomioka, I. Narumi and Y. Oono, “Complete genome sequence of the cesium-accumulating bacterium *Rhodococcus qingshengii* CS98, isolated from soil in Japan”, Microbiol. Resour. Announc. **9**, e01188-20 (2020). **N**

2) Y. Du, Y. Hase, K. Satoh and N. Shikazono, “Characterization of gamma irradiation-induced mutations in *Arabidopsis* mutants deficient in non-homologous end joining”, J. Radiat. Res. **61**, 639–647 (2020). **G**

3) A. Miyagi, T. Saimaru, N. Harigai, Y. Oono, Y. Hase and M. Kawai-Yamada, “Metabolome analysis of rice leaves to obtain low-oxalate strain from ion beam-mutagenised population”, Metabolomics **16**, 94 (2020). **C**

4) R. Yoshihara, Y. Mitomi, M. Okada, H. Shibata, M. Tanokami, Y. Nakajima, H. Inui, Y. Oono, H.Furudate and S.Tanaka, “Effects of *Arabidopsis* Ku80 deletion on the integration of the left border of T-DNA into plant chromosomal DNA *via Agrobacterium tumefaciens*”, Genes Genet. Syst. **95**, 173 (2020). **G**

5) Y. Shiroshita, M. Yuhazu, Y. Hase, T. Yamada, J. Abe and A. Kanazawa, “Characterization of chlorophyll-deficient soybean [*Glycine max* (L.) Merr.] mutants obtained by ion-beam irradiation reveals concomitant reduction in isoflavone levels”, Genet. Resour. Crop Evol. **68**, 1213-1223 (2021). **C**

6) A. Balestrazzi, K. O. Yoshiyama and A. N. Sakamoto, “Editorial: The maintenance of genome integrity in plants: Novel challenges in basic and applied research”, Front. Plant Sci. **11**, 585 (2020). **N**

7) M. Okamura and Y. Hase, “Advances in mutation technology to create novel carnation varieties”, The Carnation Genome, Springer Singapore, 119-134 (2020).

8) S. Hussein, A. R. Harun, J. M.Simoli, M .R. Abdul Wahab, S. Salleh, F. Ahmand, P. C. Kwai Hoe, A. Abdul Rahman, Shyful Azizi Ahmad Nazrul, L. Nordin, A. Tanaka, A. L. Pick Kiong, K. R. Yian, M. R. Yusop, A. Ilyani, K. Kogeethavani R, Y. Hase, K. Aki, N. Affendi M, N. Kamaruzaman, Rahiniza Hassan, N. Abd Aziz Shamsudin and N. Md Hashim, “Mutation breeding of rice for sustainable agriculture in Malaysia”, Achievement, Mutation Breeding of Rice for Sustainable Agriculture (FY 2013-2017), Mutation Breeding Project: Forum for Nuclear Cooperation in Asia (FNCA), 30-58 (2020).

9) H. Nakai, Y. Nara, C. Suzuki, H. Tabuchi, S. Nozawa and Y. Hase, “Trials on cross and mutation breeding of rice for adaptability to nature farming”, Achievement, Mutation Breeding of Rice for Sustainable Agriculture (FY 2013-2017), Mutation Breeding Project: Forum for Nuclear Cooperation in Asia (FNCA), 19–29 (2020).

Book

1) Y. Hase, Achievement : Sub-Project on Mutation Breeding of Rice for Sustainable Agriculture (FY 2013-2017), Mutation Breeding Project: Forum for Nuclear Cooperation in Asia (FNCA), (2020).

Patents

1) 長谷川 徹, 伊藤 健二, 新井和俊, 渡邊 孝政, 遠 山宏和, 平松 裕邦, 二村 幹雄, 奥村 義秀, 辻 孝子, 近藤 満治, 石川 高史, 青木 献, 竹内 良彦, 野村 浩二, 小久保 恭明, 山本 雅春, 西尾 譲一, 加藤 博美, 鬼頭 温文, 浅見 逸夫, 長谷 純宏, 野澤 樹, “きく品種「夢の煌めき白」”, 品種登録 28023 (2020.07.09).

2) 長谷川 徹, 伊藤 健二, 新井和俊, 渡邊 孝政, 遠山 宏和, 平松 裕邦, 二村 幹雄, 奥村 義秀, 辻 孝子, 近藤 満治, 石川 高史, 青木 献, 竹内 良彦, 野村 浩二, 小久保 恭明, 山本 雅春, 西尾 譲一, 加藤 博美, 鬼頭 温文, 浅見 逸夫, 長谷 純宏, 野澤 樹, “きく品種「夢の煌めき紫」”, 品種登録 28024 (2020.07.09).

3) 長谷川 徹, 伊藤 健二, 新井 和俊, 渡邊 孝政, 遠山 宏和, 平松 裕邦, 二村 幹雄, 奥村 義秀, 辻 孝子, 近藤 満治, 石川 高史, 青木 献, 竹内 良彦, 野村 浩二, 小久保 恭明, 山本 雅春, 西尾 譲一, 加藤 博美, 鬼頭 温文, 浅見 逸夫, 長谷 純宏, 野澤 樹, “きく品種「夢の煌めき黄」”, 品種登録 28025 (2020.07.09).

P2-3 Project “Medical Radioisotope Application”

Papers

1) T. Sakashita, S. Watanabe, H. Hanaoka, Y. Ohshima, Y. Ikoma, N. Ukon, I. Sasaki, T. Higashi, T. Higuchi, Y. Tsushima and N. S. Ishioka, “Absorbed dose simulation of *meta*-^{211}At-astato-benzylguanidine using pharmacokinetics of ^{131}I-MIBG, and the novel dose conversion method, RAP”, Ann. Nucl. Med. **35**, 121-31 (2021). **N**

2) 坂下 哲哉, 横田 裕一郎, 大島 康宏, “α線放出核種を用いたRI 内用療法と放射線生物学”, 放射線生物研究 **55**, 229-47 (2020). **N, 2-20**

3) Y. Ohshima, H. Suzuki H, H. Hanaoka, I. Sasaki, S. Watanabe, H. Haba, Y. Arano, Y. Tsushima and N. S. Ishioka, Preclinical evaluation of new α-radionuclide therapy targeting LAT1: 2-[^{211}At]astato-α-methyl-L-phenylalanine in tumor-bearing model, Nucl. Med. Biol. **90-91**, 15-22 (2020). **C, 2-21**

4) Y. Sugo, R. Miyachi, Y. Maruyama, S. Ohira, M. Mori, N. S. Ishioka and K. Toda, “Electrodialytic handling of radioactive metal ions for preparation of tracer reagents”, Anal. Chem. **92**, 14953–14958 (2020). **C**

5) I. Nishinaka, N. S. Ishioka, S. Watanabe, I. Sasaki and M. A. Azim, “Preparation of no-carrier-added ^{211}At solutions by a simple dry distillation method in the ^{209}Bi(^{4}He,2n)^{211}At reaction” J. Radioanal. Nucl., Chem. **326**, 743-751 (2020). **C, 2-22**

6) S. Watanabe, I. Sasaki, S. Watanabe, T. Higashi and N.S. Ishioka, "A Simple Isolation of ^{211}At using an Anion-Exchange Spin Column Method" J. Radioanal. Nucl. Chem. **326**, 1399-1404 (2020). **C**

Proceedings

1) 高 井俊秀, 古川 智弘, 渡辺 茂樹, 石岡 典子, "がん治療用アスタチン 211 の連続製造を可能にする液体ビスマス標的の開発(4) 標的窓候補材の低酸素分圧下ビスマス中における腐食特性", 日本原子力学会 2021 年春の大会, 要旨集 1M18, [富山大五福キャンパス・富山], (2021.03). **C**
2) 渡辺 茂樹, "At-211 の分離精製と標識法の開発", 大阪大学放射線科学基盤機構シンポジウム:核医学セラノスティックス基盤技術から臨床応用まで, 核医学(化学・薬学系)セッション, [オンライン], (2021.03). **C**
3) 坂下 哲哉, 渡辺 茂樹, 花岡 宏史, 大島 康宏, 生駒 洋子, 右近 直之, 佐々木 一郎, 東 達也, 樋口 徹也, 対馬 義人, 石岡 典子, "^{131}I-MIBG の体内動態に着目した ^{211}At-MABG の線量評価シミュレーション", 第 60 回日本核医学会学術総会, 要旨集 MP2D5, [神戸・兵庫], (2020.11). **N**
4) 貝塚 祐太,龍田 真帆, 佐々木 一郎, 渡辺 茂樹, 佐藤 由衣, 山下 紗葵, 田中 浩士, "^{211}At 標識テトラジン誘導体のプレターゲティング用薬剤としての基礎的評価", 第 60 回日本核医学会学術総会, 要旨集 MP2D5, [神戸・兵庫], (2020.11). **C**
5) 宮脇 信正, 柏木 啓次, 石岡 典子, 倉島 俊, 福田 光宏, "TIARA AVF サイクロトロンの低エネルギービーム輸送系におけるビーム輸送効率改善の検討", Proc. the 17th Annual Meeting of Particle Accelerator Society of Japan, 710-13, [オンライン], (2020.10), **C**
6) T. Furukawa, T. Takai, S. Watanabe and N. S. Ishioka, "Compatibility of Fe-Cr-Al alloys with Liquid Bismuth", Proc. NuMat2020: The Nuclear Materials Conference, PS4.08, [オンライン], (2020.10). **C**
7) 丸山 洋平, 須郷 由美, 宮地 凌摩, 山崎 直亨, 大平 慎一, 戸田 敬, 石岡 典子, 森 勝伸, "フロー電解セルとイオン抽出装置を組み合わせた医療用放射性銅(^{64}Cu)の分離精製", 日本分析化学会第 69 年会, 要旨集 F2001, [オンライン], (2020.09). **C**
8) 瀬川 麻里子, 前田 亮, 藤 暢輔, 西中 一朗, 渡辺 茂樹, 石岡 典子, "^{211}At 療法実用化に向けた高線量 ^{211}At の生成量・化学形短時間同時分析技術", 日本放射化学会第 64 回討論会, 3A08, [オンライン], (2020.09) **C**
9) 西中 一朗, 橋本 和幸, 石岡 典子, 渡辺 茂樹, 佐々木 一郎, Mohammad Anwar Ul Azim, "乾式蒸留分離精製で分かったアスタチン化学", 日本放射化学会第 64 回討論会, 1A05, [オンライン], (2020.09) **C**
10) Y. Kaizuka, H. Suzuki, H. Tanaka, N. Washiya, Y. Saito, M. Tatsuta, S. Watanabe, N. S. Ishioka, Y. Shirakami, K. Ooe, A. Toyoshima, J. Hatazawa, Y. Arano and T. Uehara, "Metabolic studies of astatine- and radioiodine-labeled neopentyl derivatives", Journal of Nuclear Medicine May 2020, 61 (supplement 1) 1100, [オンライン], (2020.06) **C**
11) 丸山 洋 平, 須郷 由美, 宮地 凌摩, 山崎 直亨, 大平 慎一, 戸田 敬, 石岡 典子, 森 勝伸, "カラム型フロー電解セルを用いた医療用放射性銅(^{64}Cu)の分離とイオン抽出デバイスによる精製", 第 80 回分析化学討論会, 要旨集 Y1028, [北海道教育大・札幌], (2020.05). **C**

Patent

1) 山田 圭一, 渡邉 早貴, 森口 朋尚, 奥 浩之, 篠塚 和夫, 渡辺 茂樹, 石岡 典子, "ペプチド化合物及びペプチド化合物の製造方法", 特許第 6707783 号 (2020.05.25). **C**

P2-4 Project "Radiotracer Imaging"

Papers

1) J.-S. Li, N. Suzui, Y. Nakai, Y.-G. Yin, S. Ishii, S. Fujimaki, N. Kawachi, H. Rai, T. Matsumoto, K. Sato-Izawa, N. O.-Ohtsu and S. Nakamura, "Shoot base responds to root-applied glutathione and functions as a critical region to inhibit cadmium translocation from the roots to shoots in oilseed rape (*Brassica napus*)", Plant Sci. **305**, 110822 (2021). **C**
2) S. Yamamoto, Y. Nagao, K. Kurita, M. Yamaguchi and N. Kawachi, "Measurements of intensity of produced light in water during irradiations of electron beams with energies above and below the Cerenkov-light threshold", J. Instrum. **16**, P01007 (2021). **E**
3) S. Yamamoto, T. Akagi, M. Yamaguchi and N. Kawachihi, "Estimation of the origins and fractions of emitted light from acrylic block during irradiation of carbon-ions", J. Instrum. **16**, P01004 (2021). **N**
4) N. Suzui, T. Shibata, Y.-G. Yin, Y. Funaki, K. Kurita, H. Hoshina, M. Yamaguchi, S. Fujimaki, N. Seko, H. Watabe and N. Kawachi, "Non-invasive imaging of radiocesium dynamics in a living animal using a positron-emitting ^{127}Cs tracer", Sci. Rep. **10**, 16155 (2020). **C, 2-23**
5) 塚本 崇志, 石井 里美, 七夕 小百合, 鈴井 伸郎, 河地 有木, 藤巻 秀, 草川 知行, "Positron-emitting Tracer Imaging System (PETIS) 法を用いたトマト果実への光合成産物の転流に果実直下の側枝葉が及ぼす影響の評価", 園芸学研究 **19**, 269-275 (2020). **C**
6) N. Sato, M. Kihira, R. Matsushita, C. Kaneko, Y. Ishii, Y.-G. Yin, N. Kawachi, H. Teramura, H. Kusano and H. Shimada, "*AtFLL2*, a member of the *FLO2* gene family, affects the enlargement of leaves at the vegetative stage and facilitates the regulation of carbon metabolism and flow", Biosci. Biotechnol. Biochem. **84**, 2466-2475 (2020). **C**
7) M. Yamaguchi, S. Yamamoto, M. Kitano, M. Sakai, T. Akagi, Y. Nagao and N. Kawachi, "Estimation of shifts of therapeutic carbon-ion beams owing to cavities in a polyethylene target by measuring prompt X-ray images", Jpn. J. Appl. Phys. **59**, 087001 (2020). **O, 3-01**
8) Y.-G. Yin, N. Suzui, K. Kurita, Y. Miyoshi, Y. Unno, S. Fujimaki, T. Nakamura, T. Shinano and N. Kawachi, "Visualising spatio-temporal distributions of assimilated carbon translocation and release in root systems of leguminous plants", Sci. Rep. **10**, 8446 (2020). **C, 2-24**
9) M. Yamaguchi, C.-C. Liu, H.-M. Huang, T. Yabe, T. Akagi, N. Kawachi and S. Yamamoto, "Dose image prediction for range and width verifications from carbon-ion induced secondary electron bremsstrahlung X-rays using deep learning workflow", Med. Phys. **47**, 3520-3532 (2020). **N, 3-01**

10) M. Sakai, R. K. Parajuli, Y. Kubota, N. Kubo, M. Yamaguchi, Y. Nagao, N. Kawachi, M. Kikuchi, K. Arakawa and M. Tashiro, "Crosstalk Reduction Using a Dual Energy Window Scatter Correction in Compton Imaging", Sensors **20**, 2453 (2020). **N**

Proceedings

1) S. Yamamoto, M. Yamaguchi, K. Okudaira, F, Kawabata, T. Nakaya and N. Kawachi, "Observation of Cerenkov-ring in water during irradiation of high-energy electron or X-ray beam", Proceedings of the Workshop on Radiation Detectors and Their Uses, [Tsukuba, Japan], KEK Proceedings 75-78 (2020). **E**

Patent

1) 中野 隆史, 荒川 和夫, 酒井 真理, 菅井 裕之, 菊地 美貴子, 山口 充孝, 長尾 悠人, 河地 有木, 神谷 富裕, "情報処理装置、イメージング方法、及び、イメージングプログラム", 登録 6781918 (2020.10.21).

Press・TV

1) "最新研究成果 中高生に配信", 2020.11.24, 上毛新聞に掲載 **C**

2) "甘さのヒミツ PET で探究", 2020.11.19, 読売新聞に掲載 **C**

3) "体内に取り込まれたセシウムの動きが見える！～PET で撮像できるポジトロン放出核種セシウム-127 トレーサの開発に世界で初めて成功～", 2020.10.15, プレス発表: 上毛新聞、日刊工業新聞、福島民友新聞、福島民報新聞、日経産業新聞、科学新聞に掲載. **C, 2-23**

4) "倉渕小学校出張授業「野菜や果物がおいしくなる仕組み」", 2020.7.21, 群馬テレビで放映, 2020.07.22, 上毛新聞、毎日新聞に掲載 **C**

5) "見えてきた！土の中のミラクルワールド:根圏 ～植物の根と微生物が土の中で繰り広げる営みを観る～", 2020.6.10, プレス発表: 読売新聞、朝日新聞、毎日新聞、上毛新聞に掲載. **C, 2-24**

6) "深層学習を用い、粒子線照射即発Ｘ線実測データから正確な線量画像の生成に成功～粒子線がん治療への応用に期待～", 2020.06.04, プレス発表: Oncology Tribune, OPTICS ONLINE, Laser Focus World JAPAN に掲載. **O, 3-01**

P2-5 Project "Generation of Radioisotopes with Accelerator Neutrons"

Papers

1) I. Nishinaka and K. Hashimoto, "Separation of astatine from irradiated lead targets based on dry distillation in a glass test tube", J. Radioanal. Nucl. Chem. **327**, 869-875 (2021). **N**

2) A. Yokoyama, E. Maeda, T. Taniguchi, K. Washiyama and I. Nishinaka, "Measurements of the excitation functions of radon and astatine isotopes from ^{7}Li-induced reactions with ^{209}Bi for development of a ^{211}Rn-^{211}At generator", J. Radioanal. Nucl. Chem. **323**, 921-926. (2020). **N**

3) M. Segawa, I. Nishinaka, Y. Toh and M. Maeda, "Analytical method for At-211 using an α-scintillation-camera system and thin-layer chromatography", J. Radioanal. Nucl. Chem. **326**, 773-778. (2020). **N**

Proceedings

1) 初川 雄一, 株木 重人, 櫛田 淳子, 幾田敦也, 木村 寛之, 浅井 雅人, 塚田 和明, "Tc-95, Tc-96 を用いた ETCC 撮像による新しい診断法の開発", 日本放射化学会第 64 回討論会(2020), [大阪、オンライン], 要旨集 3A02 (2020). **N**

2) 橋本和幸, 塚田和明, 佐伯秀也, 川端方子, 太田朗生, "重陽子照射で発生する加速器中性子によるがん治療用 ^{47}Sc の製造に関する検討", 日本放射化学会第 64 回討論会(2020), [大阪、オンライン], 要旨集 P32 (2020). **N**

3) 青井 景都, 新 裕喜, 川﨑 康平, 丸山 峻平, 鷲山 幸信, 西中 一朗, 羽場 宏光, 森 大輝, Yang Wang, 横山 明彦, "^{211}Rn/^{211}At ジェネレータシステムに必要な ^{207}Po 除去の最適化", 日本放射化学会第 64 回討論会(2020), [大阪、オンライン], 要旨集 3A05 (2020). **N**

4) 丸山 峻平, 川﨑 康平, 青井 景都, 東美里, 西中 一朗, 鷲山 幸信, 羽場宏光, 森 大輝, 横山 明彦, "薄層クロマトグラフィーを利用したアスタチン化学種同定による溶媒抽出の最適化", 日本放射化学会第 64 回討論会(2020), [大阪、オンライン], 要旨集 3A06 (2020). **N**

5) 西中 一朗, 橋本 和幸, 石岡 典子, 渡辺 茂樹, 佐々木 一郎, Anwar-UI Azim, "乾式蒸留分離精製で分かったアスタチン化学", 日本放射化学会第 64 回討論会(2020), [大阪、オンライン], 要旨集 1A05 (2020). **C, 2-22**

Press・TV

1) "革新的医療用ラジオアイソトープ製造施設整備に向け始動－DATE プロジェクトが拓く国産診断治療用アイソトープ医薬品開発", 2020.10.19, プレス発表: 日本経済新聞(電子版), 原子力産業新聞に掲載. **N**

P3-1 Project "LCS Gamma-ray"

Papers

1) M. Omer, T. Shizuma and R. Hajima, "Compton scattering of quasi-monochromatic γ-rays beam", Nucl. Instrum. Meth. Phys. Res. A **951,** 162998 (2020). **N**

2) Heamin Ko, Myung-Ki Cheoun, Eunja Ha, Motohiko Kusakabe, Takehito Hayakawa, Hirokazu Sasaki, Toshitaka Kajino, Masa-aki Hashimoto, Masaomi Ono, Mark D. Usang, Satoshi Chiba, Ko Nakamura, Alexey Tolstov, Ken'ichi Nomoto, Toshihiko Kawano and Grant J. Mathew, "Neutrino Process in Core-collapse Supernovae with Neutrino Self-interaction and MSW Effects", Astrophys. J. Lett. **891**, L24 (2020). **N**

3) Heishun Zen, Hideaki Ohgaki and Ryoichi Hajima, "High-extraction-efficiency operation of a midinfrared free electron laser enabled by dynamic cavity desynchronization", Phys. Rev. Accel. Beams **23**, 070701 (2020). **N**

4) Heishun Zen, Hideaki Ohgaki and Ryoichi Hajima, "Record high extraction efficiency of free electron laser oscillator", Appl. Phys. Express **13**, 102007 (2020). **N**

5) Khaled Ali, Hideaki Ohgaki, Heishun Zen, Toshiteru Kii, Takehito Hayakawa, Toshiyuki Shizuma, Hiroyuki Toyokawa, Yoshitaka Taira, Violeta Iancu, Gabriel Turturica, Calin Alexandru Ur, Masaki Fujimoto and Masahiro Katoh, "Selective Isotope CT Imaging Based on Nuclear Resonance Fluorescence Transmission Method", IEEE Transactions on Nucl. Sci., **67**(8), 1976 (2020). **N**

6) Akinori Irizawa, Masaki Fujimoto, Keigo Kawase, Ryukou Kato, Hidenori Fujiwara, Atsushi Higashiya, Salvatore Macis, Luca Tomarchio, Stefano Lupi, Augusto Marcelli and Shigemasa Suga, "Spatially Resolved Spectral Imaging by A THz-FEL", Condens. Matter **2020**, 38 (2020). **N**

7) Keigo Kawase, Masaya Nagai, Kazuya Furukawa, Masaki Fujimoto, Ryukou Kato, Yoshihide Honda and Goro Isoyama, "Extremely high-intensity operation of a THz free-electron laser using an electron beam with a higher bunch", Nucl. Instrrum. Meth. Phys. Res. A **960**, 163582 (2020). **N**

8) Heamin Ko, Myung-Ki Cheoun, Motohiko Kusakabe, Takehito Hayakawa, Hirokazu Sasaki, Toshitaka Kajino and Grant J. Mathews, "Neutrino Self-interaction and MSW Effects by an Equi-partitioned Fermi-Dirac Neutrino Luminosity on the Supernova Neutrino-process", JPS Conf. Proc. **31**, 011027 (2020). **N**

9) Takehito Hayakawa, Motohiko Kusakabe, Toshitaka Kajino, Myung-Ki Cheoun, Heamin Ko, Grant J. Mathews, Alexey Tolstov, Ken'ichi Nomoto, Satoshi Chiba, Toshihiko Kawano, Masa-aki Hashimoto and Masaomi Ono, "Nuclear Cosmochronometer for Supernova Neutrino Process", JPS Conf. Proc. **31**, 011028 (2020). **N**

10) 兒玉 了祐, 細貝 知直, 余語 覚文,·西内 満美子, 早川 岳人, " レーザープラズマ加速器の進展とその可能性", 原子核研究, 第 65 巻 1, 34-48 (2020). **N**

Proceedings

1) 羽島 良一, 早川 岳人, 静間 俊行, 宮本 修治, 松葉 俊哉, "回折結晶を利用したレーザー・コンプトン散乱ガンマ線のエネルギー、角度分布の再構成", Proceedings of the 17th Annual Meeting of Particle Accelerator Society of Japan, Sept. 2-4, 2020, Online Virtual Conference, 100 (2020). **N**

2) 川瀬 啓悟, 羽島 良一, 永井 良治, "差周波中赤外光源のためのファイバーレーザーの開発", Proceedings of the 17th Annual Meeting of Particle Accelerator Society of Japan, Sept. 2-4, 2020, Online Virtual Conference, 268 (2020). **N**

3) 沢村 勝, 羽島 良一, 佐伯 学行, 岩下 芳久, 頓宮 拓, 中村 哲朗, 渡邉 直久, "超伝導スポーク空洞製作のための電子ビーム溶接試験", Proceedings of the 17th Annual Meeting of Particle Accelerator Society of Japan, Sept. 2-4, 2020, Online Virtual Conference, 317 (2020). **N**

4) 川瀬 啓悟, 誉田 義英, 磯山 悟朗, "THz FEL からの単一パルスの取り出しのためのプラズマスイッチの研究", Proceedings of the 17th Annual Meeting of Particle Accelerator Society of Japan, Sept. 2-4, 2020, Online Virtual Conference, 624 (2020). **N**

5) 黒澤 歩夢, 住友 洋介, 川瀬 啓悟, 羽島 良一, 早川 恭史, 境 武志, "FEL パルス光の外部蓄積のための試験蓄積状況", Proceedings of the 17th Annual Meeting of Particle Accelerator Society of Japan, Sept. 2-4, 2020, Online Virtual Conference, 626 (2020). **N**

6) 羽島 良一, "Geant4 へのレーザー・コンプトン散乱ガンマ線源の実装", Proceedings of the 17th Annual Meeting of Particle Accelerator Society of Japan, Sept. 2-4, 2020, Online Virtual Conference, 724 (2020). **N**

7) T. Kawachi, R. Nagai, R. Hajima et al., "Generation of short wavelength radiation and energetic particles by using PW-class lasers", Proceedings of the 16th International Conference on X-ray Lasers, Springer Proceedings in Physics (2020). **N**

Press・TV

1) "長波長赤外での強光子場の実現とアト秒 X 線源の開発に大きく前進－共振器型自由電子レーザの世界最高変換効率を達成－", 2020.10.6, 日刊工業新聞紙面他に掲載。 **N**

P3-2 Beam Engineering Section

Papers

1) S. Kurashima, S. Okumura and T. Yuyama, "Temperature stabilization of a K110 variable energy cyclotron magnet", Rev. Sci. Instrum. **92**, 013303-1 – 013303-3 (2021). **C, 3-08**

2) W. Kada, S. Nakatsu, T. Imayoshi, K. Kumagai, H. Tago, T. Satoh, M. Koka, K. Miura, O. Hanaizumi and T. Kamiya, "In-air micro-particle-induced X-ray emission imaging and spectroscopy of air-borne particles collected hourly from an automated sampling unit of the atmospheric environmental regional observation system", Nucl. Instrum. Meth. Phys. Res. B **477**, 133 (2020). **S, 3-03**

3) K. Nakai, K. Endo, F. Yoshida, M. Koka, N. Yamada, T. Satoh, T. Tsurubuchi, A. Matsumura, Y. Matsumoto and H. Sakurai, "Boron analysis and imaging of cells with 2-hr BPA exposure by using micro-proton particle-induced gamma-ray emission (PIGE)", Appl. Radiat. Isot. **165**, 109334 (2020). **S**

4) K. Takayama, T. Adachi, T. Kawakubo, K. Okamura, Y. Yuri, J. Hasegawa, K. Horioka, T. Kikuchi, T. Sasaki and K. Takahashi," A massive-ion beam driver for high-energy-density physics and future inertial fusion", Phys. Lett. A **384**, 126692 (2020) **N**

5) Y. Yuri, T. Yuyama, T. Ishizaka and M. Fukuda, "Shaping ion beams into hollow profiles using sextupole magnets", High Energy Density Phys. **36**, 100839 (2020) **C, 3-02**

6) T. Segawa, S. Harada, T. Satoh and S. Ehara, "Delivery and Effectiveness of Carboplatin via Targeted Delivery Compared to Passive Accumulation of Intravenously Injected Particles Releasing Carboplatin upon Irradiation", Radiat. Res. **193**, 263-273 (2020). **S, 2-27**

7) Y. Ishii, T. Okubo, H. Kashiwagi and Y. Miyake, "Preliminary Study: Measurement of Ion Beam Energy Spreads Produced by a Penning Ionization Gauge-Type Ion Source Using Electromagnets for a Mega-electron Volt Compact Ion Microbeam System", Rev. Sci. Instrum. **91**, 043304-1-043304-5, (2020) **N, 3-06**

8) Y. Hase, K. Satoh, A. Chiba, Y. Hirano, Y. Saito and K. Narumi, "Proton-Cluster-Beam Lethality and Mutagenicity in

Bacillus subtilis Spores", Quantum Beam Sci. **5**, 25 (2021). **S, I, 2-29**

9) K. Hirata, K. Yamada, A. Chiba, Y. Hirano, K. Narumi and Y. Saitoh, "Experimental characterization of ultrafast phenomena of secondary-ion emission induced by nanoscale energy deposition processes of energetic C_{60} impacts", J. Appl. Phys. **127**, 214302 (2020). **T, I, 3-15**
10) T. Sakurai, S. Sakaguchi, Y. Takeshita, K. Kayama, A. Horio, M. Sugimoto, T. Yamaki, A. Chiba, Y. Saitoh, G.B.V.S. Lakshmi, D.K. Avasthi and S. Seki, "Porphyrin Nanowire Bundles for Efficient Photoconductivity, Photoemission, and Generation of Singlet Oxygens toward Photodynamic Therapy" ACS Appl. Nano Mater. **3**, 6043–6053 (2020). **T, 3-13**
11) H. Amekura, M. Toulemonde, K. Narumi, R. Li, A. Chiba, Y. Hirano, K. Yamada, S. Yamamoto, N. Ishikawa, N. Okubo and Y. Saitoh, "Ion tracks in silicon formed by much lower energy deposition than the track formation threshold," Sci. Rep. **11,** 185 (2021). **T, S, 3-10**
12) T. Yamada, K. Fukuda, S. Semboshi, Y. Saitoh, H. Amekura, A. Iwase and F. Hori, "Control of optical absorption of silica glass by Ag ion implantation and subsequent heavy ion irradiation," Nanotechnology **31,** 455706 (2020). **T, I**
13) T. Kaneko, R. Usami, H. Morioka, Y. Saitoh, A. Chiba and K. Narumi, "Electron-loss and destruction processes in collision of MeV/atom carbon cluster ions with rare gases", Nucl. Instrum. Meth. Phys. Res. B **478**, 218 (2020). **N, 3-14**

Proceedings

1) 松田 洋平, 伊藤 正俊, 篠塚 勉, 福田 光宏, 依田哲彦, 神田 浩樹, 中尾 政夫, 倉島 俊, 宮脇 信正, 涌井 崇志, "大強度負重水素イオン加速に向けた CYRIC930 型 AVF サイクロトロン加速器の軌道計算", 第 17 回日本加速器学会年会プロシーディング, 38-42 (2020) **N**
2) 原 隆文, 福田 光宏, 神田 浩樹, 依田 哲彦, 中尾 政夫, 安田 裕介, 篠塚 勉, 伊藤 正俊, 松田 洋平, 倉島 俊, 宮脇 信正, 涌井 崇志, "自動サイクロトロン共鳴加速法を用いた陽子加速器の概念設計", 第 17 回日本加速器学会年会プロシーディング, 43-45 (2020). **N**
3) 柏木 啓次, 宮脇 信正, 倉島 俊, "Measurement of beam intensity using a phase probe in a cyclotron", 第 17 回日本加速器学会年会プロシーディング, 707-709 (2020). **C, 3-08**
4) 湯山 貴裕, 百合 庸介, 石坂 知久, 柏木 啓次, 福田 光宏, "多重極電磁石を用いた大面積均一ビームと中空ビームの形成", 第 17 回日本加速器学会年会プロシーディング, 449-452 (2020). **C, 3-02**
5) 宮脇 信正, 柏木 啓次, 石岡 典子, 倉島 俊, 福田 光宏, "TIARA AVF サイクロトロンの低エネルギービーム輸送系におけるビーム輸送効率改善の検討", 第 17 回日本加速器学会年会プロシーディング, 710-713 (2020) **C, 3-08**
6) 宮脇 信正, 千葉 敦也, 吉田 健一, 山田 圭介, 湯山 貴裕, 石坂 知久, 横山 彰人, 平野 貴美, 細谷 青児, 柏木 啓次, 百合 庸介, 石堀 郁夫, 奥村 進, 倉島 俊, "QST 高崎イオン照射施設(TIARA)の現状報告", 第 17 回日本加速器学会年会プロシーディング, 890-892 (2020) **C, T, S, I, 3-08**

External Research Group Except for Takasaki Advanced Radiation Research Institute

Paper

1) 福地龍郎, "ESR法による活断層の絶対年代測定と活動性評価 ー 糸魚川－静岡構造線活断層系を例として ー", Radioisotopes, **70**, 131-145 (2021). **G, 1-41**

Appendix 2 Type of Research Collaboration and Facilities Used for Research

Paper No.	Type of Research Collaboration*1					Utilization of Irradiation Facility*2					
	Joint Res.	Entr. Res.	Coop. Res.	Inter. Use	Ext. Use	C	T	S	I	E	G
1-01				○		○					
1-02		○								○	○
1-03	○										○
1-04				○						○	
1-05	○					○				○	
1-06	○								○		
1-07	○					○					
1-08		○								○	
1-09	○						○				
1-10				○							○
1-11	○					○					
1-12	○					○					
1-13	○					○					
1-14	○					○					
1-15	○								○		
1-16	○						○	○	○	○	
1-17				○					○		
1-18	○								○		
1-19	○					○	○	○	○	○	○
1-20				○			○				
1-21	○					○					
1-22	○								○		
1-23	○					○	○		○	○	
1-24				○						○	○
1-25				○						○	
1-26	○									○	○
1-27	○							○		○	○
1-28	○							○		○	○
1-29		○									○
1-30				○			○		○		
1-31				○							○
1-32	○							○			
1-33	○					○		○			
1-34	○										
1-35	○						○	○	○		
1-36	○						○				
1-37				○							○
1-38				○							○
1-39					○			○			
1-40					○				○		
1-41					○						○

Paper No.	Type of Research Collaboration*1					Utilization of Irradiation Facility*2					
	Joint Res.	Entr. Res.	Coop. Res.	Inter. Use	Ext. Use	C	T	S	I	E	G
2-01	○					○					
2-02	○					○					○
2-03	○					○					
2-04	○					○					
2-05	○					○					
2-06	○					○					
2-07	○					○					
2-08	○										○
2-09	○					○					
2-10	○					○					
2-11	○										○
2-12	○					○					
2-13	○					○					
2-14	○					○					
2-15	○					○					
2-16	○										○
2-17	○										○
2-18	○										○
2-19	○										○
2-20				○							○
2-21	○					○					
2-22	○					○					
2-23			○			○					
2-24	○					○					
2-25			○					○			
2-26			○					○			
2-27			○					○			
2-28			○					○			
2-29			○					○	○		
2-30				○		○					
3-01	○										
3-02				○		○					
3-03			○					○			
3-04	○							○			
3-05	○							○	○		
3-06				○							
3-07				○							
3-08				○		○					
3-09			○				○			○	
3-10			○				○	○	○		
3-11			○				○	○	○		

Paper No.	Type of Research Collaboration*1					Utilization of Irradiation Facility*2					
	Joint Res.	Entr. Res.	Coop. Res.	Inter. Use	Ext. Use	C	T	S	I	E	G
3-12			O				O				
3-13			O				O				
3-14			O								
3-15			O				O		O		
3-16				O			O		O		
3-17	O									O	O
total	**50**	**3**	**14**	**18**	**3**	**31**	**15**	**18**	**17**	**14**	**23**

Paper No.	Type of Research Collaboration*1					Management of Irradiation Facility*2					
	Joint Res.	Entr. Res.	Coop. Res.	Inter. Use	Ext. Use	C	T	S	I	E	G
4-01	–	–	–	–	–	O	O	O	O		
4-02	–	–	–	–	–	O					
4-03	–	–	–	–	–		O	O	O		
4-04	–	–	–	–	–					O	O
4-05	–	–	–	–	–					O	O
4-06	–	–	–	–	–	O	O	O	O		
4-07	–	–	–	–	–	O	O	O	O		
4-08	–	–	–	–	–	O	O	O	O	O	O

***1 Type of Research Collaboration**

Joint Res. : Joint research with external users

Entr. Res. : Research entrusted to QST

Coop. Res. : Cooperative research with plural universities through the University of Tokyo (Paper submission is voluntary.)

Inter. Use : Internal use

Ext. Use : Facility use program for external users (Paper submission is voluntary.)

***2 Irradiation Facility**

C : AVF Cyclotron

T : 3 MV Tandem Electrostatic Accelerator

S : 3 MV Single-ended Electrostatic Accelerator

I : 400 kV Ion Implanter

E : 2 MV Electron Accelerator

G : Co-60 Gamma-ray Irradiation Facilities

Appendix 3　Abbreviation Name for National Organizations

【National Institutes for Quantum Science and Technology: **QST**】
（量子科学技術研究開発機構）

◆Directorate and Institutes of QST appearing in this report

QuBS	量子ビーム科学部門	:	Quantum Beam Science Research Directorate
TARRI	高崎量子応用研究所	:	Takasaki Advanced Radiation Research Institute
KPSI	関西光科学研究所	:	Kansai Photon Science Institute
NFI	那珂核融合研究所	:	Naka Fusion Institute
RFI	六ヶ所核融合研究所	:	Rokkasho Fusion Institute
IQMS	量子医科学研究所	:	Institute for Quantum Medical Science

◆Examples of Department and Center of QST

・量子ビーム科学部門、研究企画部
　Department of Research Planning and Promotion, QuBS, QST
・量子ビーム科学部門、高崎量子応用研究所、先端機能材料研究部
　Department of Advanced Functional Materials Research, TARRI, QST
・量子ビーム科学部門、高崎量子応用研究所、放射線生物応用研究部
　Department of Radiation-Applied Biology Research, TARRI, QST
・量子ビーム科学部門、高崎量子応用研究所、放射線高度利用施設部
　Department of Advanced Radiation Technology, TARRI, QST
・量子ビーム科学部門、高崎量子応用研究所、東海量子ビーム応用研究センター
　Tokai Quantum Beam Science Center, TARRI, QST
・量子ビーム科学部門、高崎量子応用研究所、管理部
　Department of Administrative Services, TARRI, QST
・核融合エネルギー部門、那珂核融合研究所、ITERプロジェクト部
　Department of ITER Project, NFI, QST
・核融合エネルギー部門、六ヶ所核融合研究所、核融合炉材料研究開発部
　Department of Fusion Reactor Materials Research, RFI, QST
・量子生命・医学部門、量子医科学研究所、重粒子線治療研究部
　Department of Charged Particle Therapy Research, IQMS, QST
・量子生命科学領域
　Institute for Quantum Life Science, QST

【Other national organizations appearing in this report】

AIST	産業技術総合研究所	:	National Institute of Advanced Industrial Science and Technology
JAEA	日本原子力研究開発機構	:	Japan Atomic Energy Agency
JAXA	宇宙航空研究開発機構	:	Japan Aerospace Exploration Agency
NARO	農業・食品産業技術総合研究機構	:	National Agriculture and Food Research Organization
NIMS	物質・材料研究機構	:	National Institute for Materials Science

QST Takasaki Annual Report 2020

(Ed) YAMAMOTO Hiroyuki

Date of Publishing : March 2022

Editorial committee : YAMAMOTO Hiroyuki, MAEKAWA Yasunari, OHSHIMA Takeshi, ISHIOKA Noriko S., SAITOH Yuichi, NARUMI Kazumasa, NAGAI Ryoji, OONO Yutaka and HAJIMA Ryoichi

Publication : Takasaki Advanced Radiation Research Institute
National Institutes for Quantum Science and Technology
1233 Watanuki, Takasaki, Gunma 370-1292, Japan

Tel : +81-27-346-9232

E-mail : taka-annualrep@qst.go.jp

Homepage : https://www.qst.go.jp/site/taka/

Printed in Japan

QST-M-33

https://www.qst.go.jp